

FAST TEMPERATURE CYCLING OF THE CATALYTIC CO OXIDATION USING MICROSTRUCTURE REACTORS

THÈSE N° 4050 (2008)

PRÉSENTÉE LE 9 MAI 2008

À LA FACULTÉ DES SCIENCES DE BASE
LABORATOIRE DE GÉNIE DE LA RÉACTION CHIMIQUE
PROGRAMME DOCTORAL EN CHIMIE ET GÉNIE CHIMIQUE

ÉCOLE POLYTECHNIQUE FÉDÉRALE DE LAUSANNE

POUR L'OBTENTION DU GRADE DE DOCTEUR ÈS SCIENCES

PAR

Martin LUTHER

ingénieur chimiste diplômé EPF
de nationalité suisse et originaire de Neuchâtel (NE)

acceptée sur proposition du jury:

Prof. P. Vogel, président du jury
Dr L. Kiwi, Prof. A. Renken, directeurs de thèse
Dr J. Brandner, rapporteur
Dr G. Foti, rapporteur
Prof. R. Lange, rapporteur



ÉCOLE POLYTECHNIQUE
FÉDÉRALE DE LAUSANNE

Suisse
2008

ACKNOWLEDGMENTS

This thesis has been realized between 2003 and 2008 at the Institute for Micro Process Engineering at the Karlsruhe Research Centre (Germany).

I want here to express my gratitude to the people without whom this work would never have succeeded.

- Firstly, Pr. Albert Renken and Pr. Lioubov Kiwi-Minsker, for taking me in their research group, arranging the PhD student position at the Karlsruhe Research Centre and for the liberty and confidence accorded during the accomplishment of this work.
- Dr. Klaus Schubert, for taking me in his institute and giving me the possibility to realize my doctor thesis in Germany.
- Dr. Jürgen J. Brandner, for the organization of the PhD student position at the Karlsruhe Research Centre, for his availability for discussion, for his encouragement during the difficult phases of this work, and for the correction of the first version of this thesis.
- Mr. Conrad Grehl and Mr. Helmut Schlenker, for their useful help for the numerous modifications of the experimental setup.
- All the collaborators from the Institute for Micro Process Engineering. Particularly Ms Janina Thormann, for having supported my fluctuating mood and making me believe I would one day bring this thesis to an end. All the others, for having received me cordially at their institute, among them Achim Wenka for his useful general life advice.
- My parents and sisters, for their encouragement that permitted me to always look forward.

For everybody I did not mention, Thank you.

ABSTRACT

The possibility to increase the performance (productivity or selectivity) of a chemical reactor by using periodic variations of reaction parameters (e.g. reactant concentration or temperature) has been theoretically envisaged since the beginning of the 70th. The experimental validation of the predicted positive effects was successful in the case of concentration variation but failed for temperature variation. This was mainly due to the high thermal inertia of the conventional chemical reactors used for the measurements which prevented to create variations having a sufficiently high frequency. Microstructure reactors own, at the contrary to conventional reactors, a very low thermal inertia and allow to generate temperature oscillations with an amplitude of about ten to hundred Kelvin at a frequency in the order of magnitude of 10^{-1} to 4 Hz. These properties, coupled with the possibility to introduce a catalytic active material within the devices, seem to make them well suited for the study of the effects of fast periodic temperature variations of a catalytic reaction.

The objective of this work was to demonstrate that non-stationary temperature conditions may increase the reaction rate of a heterogeneously catalyzed reaction up to values not predicted by the classical Arrhenius dependency towards the temperature.

Two different types of microstructure reactors have been used. The reaction was taking place in the first one (FTC-type 2) in microstructured channels on whose walls a catalytic layer was deposited. In the second one (FTC-type 3), the reaction was taking place on a piece of sintered metal fibres (SMF) plate placed in a reaction chamber. The catalytic active material was deposited on the SMF plate filaments. Both devices were permanently heated by electrical resistors and periodically cooled down with water flowing through cooling channels incorporated in the devices.

The test reaction chosen for the experimental measurements was the CO oxidation reaction, heterogeneously catalyzed by platinum supported on alumina ($\text{Pt}/\text{Al}_2\text{O}_3$). The reaction behaviour under stationary thermal conditions was consistent with the one predicted by the Arrhenius law. The dependency of the reaction rate with the temperature was exponential with an apparent activation energy of $104 \text{ kJ}\cdot\text{mol}^{-1}$, a negative partial reaction order for CO and a positive one for O_2 .

The measurements effectuated under quasi-stationary thermal conditions (slow temperature ramps) have shown that a temperature change rate between 7 and $14 \text{ K}\cdot\text{min}^{-1}$ was not sufficient to observe any non-trivial effect of the temperature. The reaction behaviour was always predicted by the Arrhenius law. The surface coverage of the reactive species is, in this case, always able to follow the slow temperature changes and the reaction behaves as being always under steady-state conditions.

The experiments realized under non-stationary thermal conditions using the FTC-type 2 reactor have also failed to demonstrate any non-trivial effects of the temperature oscillations. This device

allows indeed to generate temperature oscillations with an amplitude of up to 120 K with a frequency of 0.1 Hz but unfortunately correlated with a very high thermal inhomogeneity. A temperature difference of up to 80 K was measured between a cold spot and a hot spot inside the device. Due to their very low local reaction rate the colder areas of the reactor have attenuated the product concentration (CO_2) oscillations which should have been created by the temperature variations. This attenuation prevented the temperature oscillations to have any positive effect compared to the stationary thermal conditions.

The FTC-type 3 reactor allowed temperature changes of lower amplitude but the thermal homogeneity was much better. The maximal temperature difference measured between two points within the reactor was only 15 K. Under temperature oscillation conditions, the measured instantaneous CO_2 concentration was higher for any temperature within the oscillation range compared to the one recorded under stationary thermal conditions. The increase obtained in the mean CO_2 concentration was ranging from 34% for a frequency of the oscillations of 0.035 Hz to 85% for a frequency of 0.052 Hz. The amplitude of the oscillations was kept constant at approximately 40 K and the mean temperature value at 437 K.

The simulations effectuated using a theoretical model for the catalytic CO oxidation including a feed-back step in the form of the oxidation-reduction of the catalyst have shown that the experimentally observed increase may be qualitatively explained. Above a certain frequency, the temperature oscillations are fast enough compared to the characteristic time of the feedback step and are able to perturb the stationary established reactive species surface coverage. The formation of a transient surface coverage more favourable for the reaction than the surface coverage at high temperature allows during the transient period to reach an instantaneous surface reaction rate values higher than the one at high temperature. This reaction rate peak is then responsible for the increase of the mean reaction rate under non-stationary thermal conditions and, thus, for an increased yield.

Keywords

Microstructure reactor, non-stationary, temperature oscillations, catalysis, kinetics, simulation

ZUSAMMENFASSUNG

Die Möglichkeit einer Effizienzsteigerung eines chemischen Reaktors durch periodische Parametervariationen (z.B. Eduktkonzentration oder Temperatur) wurde seit Ende der 70er Jahre in Betracht gezogen. Die vorhergesagten positiven Effekte konnten für Konzentrationsvariationen erfolgreich experimentell bestätigt werden, im Gegensatz zu Temperaturvariationen. Grund hierfür war vor allem die zu große thermische Trägheit der verwendeten konventionellen chemischen Reaktoren. Es war technisch unmöglich periodische Temperaturvariationen hoher Frequenz zu erzeugen. Mikrostrukturreaktoren besitzen im Gegenteil zu konventionellen Reaktoren eine sehr geringe thermische Trägheit und erlauben es, Temperaturosillationen mit einer Amplitude von mehreren zehn Kelvin und einer Frequenz von 10^{-1} bis zu 4 Hz zu erzeugen. Diese Eigenschaft, zusammen mit der Möglichkeit katalytisch aktives Material in diese Apparate zu integrieren, lässt Mikrostrukturreaktoren ideal geeignet erscheinen, um die Effekte von schnellen periodischen Temperaturvariationen auf eine katalytische Reaktion zu studieren.

Das Ziel der vorliegenden Arbeit ist die Demonstration der Erhöhung der Reaktionsgeschwindigkeit einer heterogen katalysierten Reaktion durch instationäre Temperaturbedingungen. Es sollen dadurch Werte erreicht werden, die mit der klassischen Abhängigkeit der Temperatur gemäß dem Arrhenius-Gesetz nicht mehr beschrieben werden können.

Während dieser Studie wurden zwei unterschiedliche Reaktoren verwendet. In dem ersten Reaktor (FTC-Type 2) fand die Reaktion in Mikrokanälen statt. Die Wände der Mikrokanäle waren mit katalytisch aktivem Material beschichtet. In dem zweiten Reaktor (FTC-Type 3) fand die Reaktion auf einem Stück gesinterter Metallfolie statt. Dieses Folienstück, beschichtet mit katalytisch aktivem Material, war in die Reaktionskammer des Reaktors gelegt worden. Beide Reaktoren wurden kontinuierlich elektrisch beheizt und periodisch mit einem Wasserstrom gekühlt.

Die gewählte Testreaktion war die heterogen katalysierte CO-Oxidationsreaktion auf einem Platinkatalysator mit einer Trägerschicht aus Aluminiumoxid ($\text{Pt}/\text{Al}_2\text{O}_3$). Die Reaktion verhält sich unter thermisch stationären Bedingungen gemäß dem Arrhenius-Gesetz. Die Reaktionsgeschwindigkeit ist exponential abhängig von der Temperatur mit einer scheinbaren Aktivierungsenergie von $104 \text{ kJ}\cdot\text{mol}^{-1}$. Die Reaktionsordnung ist negativ für CO und positiv für O_2 .

Die realisierten experimentellen Messungen unter quasi-stationären Bedingungen (langsame Temperaturrampe) haben gezeigt, dass eine Temperaturänderungsgeschwindigkeit zwischen 7 und $14 \text{ K}\cdot\text{min}^{-1}$ nicht ausreichend war, um nichttriviale Effekte zu verursachen. Die Reaktion verhielt sich immer gemäß dem Arrhenius-Gesetz. Die Oberflächenbedeckung der reaktiven Spezies ist in

diesem Fall immer in der Lage den langsamen Temperaturänderungen zu folgen. Die Reaktion verhält sich, als ob sie immer unter stationären Bedingungen sei.

Die Versuche unter thermisch instationären Bedingungen mit dem FTC-Type 2 Reaktor haben ebenso keine nicht trivialen Effekte bedingt durch die Temperaturoszillationen gezeigt. Es war zwar möglich mit diesem Reaktor Temperaturoszillationen mit einer Amplitude von bis zu 120 K und eine Frequenz von 0.1 Hz zu generieren. Die Oszillationen waren jedoch leider mit einer sehr hohen thermischen Inhomogenität verbunden. Ein Temperaturunterschied von bis zu 80 K zwischen einem Hotspot und einem Coldspot ist in dem Reaktor gemessen worden. Aufgrund der niedrigen lokalen Reaktionsgeschwindigkeit sind die kalten Zonen des Reaktors verantwortlich für die Dämpfung der Konzentrationsozillationen, welche durch die Temperaturoszillationen erzeugt werden sollten. Diese Dämpfung verhindert das Erreichen eines positiven Effekts durch Temperaturoszillationen im Vergleich zum thermisch stationären Zustand.

Der FTC-Type 3 Reaktor ermöglichte Temperaturänderungen mit einer relativ kleinen Amplitude, jedoch verbesserter thermischer Homogenität. Der maximale Temperaturunterschied im Reaktor betrug nur 15 K. Unter thermisch instationären Bedingungen war die momentane CO_2 -Konzentration für alle Temperaturen höher als die im Vergleich dazu gemessenen Konzentrationen unter thermisch stationären Bedingungen. Die Erhöhung der mittleren CO_2 -Konzentration erstreckte sich von 34% für eine Oszillationsfrequenz von 0.035 Hz bis zu 85% für eine Frequenz von 0.052 Hz. Die Oszillationsamplitude wurde dabei konstant gehalten bei ungefähr 40 K mit einer mittleren Temperatur von 437 K.

Simulationen, realisiert mit einem kinetischen Modell für die katalytische CO Oxidation einschließlich der Oxidation-Reduktion des Katalysators als Feed-back Mechanismus, haben gezeigt, dass die experimentelle Erhöhung der mittleren CO_2 -Konzentration qualitativ erklärbar ist. Wenn die Temperaturoszillationen schnell genug sind im Vergleich zur charakteristischen Zeit des Feed-back Mechanismus, sind sie in der Lage, die stationär etablierte Oberflächenbedeckung zu beeinflussen. Die Bildung einer für die Reaktion günstigeren transienten Oberflächenbedeckung, im Vergleich zu der bei hohen Temperaturen erreichten stationären Oberflächenbedeckung, ermöglicht während der transienten Periode eine höhere momentane Oberflächenreaktionsgeschwindigkeit bei höherer Temperatur. Dieses Reaktionsgeschwindigkeitsmaximum ist wiederum verantwortlich für die Erhöhung der mittleren Reaktionsgeschwindigkeit unter thermisch instationären Bedingungen und damit für einen erhöhten Umsatz.

Schlagwörter

Mikrostrukturreaktor, instationär, Temperaturoszillationen, Katalyse, Kinetik, Simulation

RÉSUMÉ

La possibilité d'augmenter la productivité d'un réacteur chimique grâce à une variation cyclique forcée de paramètres réactionnels tel que la concentration des réactants ou la température a été envisagée dès la fin des années 70. Les effets positifs prévus théoriquement ont pu être validés expérimentalement dans le cas d'une variation forcée de la concentration, mais pas pour les variations de la température. Cela a été principalement dû à la grande inertie thermique des réacteurs conventionnels utilisés. En utilisant ces réacteurs, il était impossible de créer des variations cycliques de température ayant une fréquence suffisante. Au contraire, les réacteurs microstructurés possèdent eux une inertie thermique très réduite et permettent de créer des variations périodiques de la température ayant une amplitude de jusqu'à 100 K et une fréquence variant de 10^{-1} à 4 Hz. Cette propriété, couplée à la possibilité d'introduire un composé catalytique à l'intérieur de ces réacteurs, les rend idéaux pour étudier les effets d'une variation cyclique rapide de la température sur le comportement d'une réaction catalytique.

Le but du présent travail était de démontrer que des conditions thermiques non stationnaires peuvent sous certaines conditions augmenter la vitesse d'une réaction catalytique jusqu'à des valeurs non prévues par la loi d'Arrhenius.

Deux différents types de réacteurs microstructurés ont été utilisés durant ce travail. La réaction se déroulait dans le premier réacteur (FTC-type 2) à l'intérieur de canaux microstructurés. La couche catalytique était déposée sur les parois de ces canaux microstructurés. Dans le cas du deuxième réacteur (FTC-type 3), la réaction se déroulait sur un morceau de fritte métallique déposée dans la chambre de réaction du réacteur. Le composé catalytique était déposé sur les fibres de la fritte métallique. Les deux types de réacteurs étaient en permanence chauffés à l'aide de résistances électriques et périodiquement refroidis par un flux d'eau circulant à travers des canaux microstructurés incorporés dans les réacteurs.

La réaction choisie pour cette étude était l'oxydation catalytique du CO hétérogènement catalysée par du platine déposé sur une couche d'oxyde d'aluminium ($\text{Pt}/\text{Al}_2\text{O}_3$). La réaction se comportait sous conditions thermiques stationnaires comme prévu par la loi d'Arrhenius. La vitesse de réaction était exponentiellement dépendante de la température avec une énergie d'activation apparente de $104 \text{ kJ}\cdot\text{mol}^{-1}$. L'ordre partiel de réaction était négatif pour CO et positif pour O_2 .

Les expériences réalisées sous conditions thermiques quasi-stationnaires (lente rampe de température) ont montré qu'une vitesse de changement de température de l'ordre de 7 à $14 \text{ K}\cdot\text{min}^{-1}$ n'est pas suffisante pour observer des effets dus à la température qui ne soient pas prévus par la loi d'Arrhenius. Le taux de recouvrement de la surface catalytique par les espèces réactives est dans ce

cas toujours capable de suivre les changements de températures et la réaction se comporte comme étant en permanence à l'état stationnaire.

Les mesures expérimentales réalisées sous conditions thermiques non-stationnaires à l'aide du réacteur FTC-type 2 n'ont pas permis de démontrer un quelconque effet non-trivial du à la variation périodique de la température. Il était possible à l'aide de ce réacteur d'obtenir des oscillations de la température d'une amplitude allant jusqu'à 120 K et une fréquence de 0.1 Hz. Malheureusement, ces variations de la température étaient accompagnées par le développement d'un profile de température très inhomogène. Une différence de température allant jusqu'à 80 K a été mesurée entre un point chaud et un point froid du réacteur. Les zones froides du réacteur, ayant une vitesse de réaction locale très faible, ont atténués les oscillations de la concentration du produit de la réaction (CO_2) qui auraient du être générées par les oscillations de la température. Cette atténuation marquée a empêché les oscillations de la température d'avoir un effet positif sur la vitesse de réaction globale comparé aux conditions stationnaires de température.

Les changements périodiques de température réalisables à l'aide du réacteur FTC-type 3 étaient d'une fréquence et d'une amplitude plus faible mais le profil de température obtenu beaucoup plus homogène. La différence de température maximale mesurée était d'environ 15 K. La concentration instantanée de CO_2 mesurée sous conditions thermiques non-stationnaires était supérieure comparée à la concentration mesurée à l'état stationnaire pour une température identique et ceci pour toute température située à l'intérieur du domaine oscillant. L'augmentation obtenue pour la concentration moyenne de CO_2 variait de 34% pour une fréquence d'oscillation de 0.035 Hz à 85% pour une fréquence de 0.052 Hz. L'amplitude des oscillations a été gardée constante à environ 40 K et la température moyenne à 437 K.

Les simulations réalisées à l'aide d'un modèle cinétique théorique pour l'oxydation catalytique du CO incluant l'oxidation-reduction du catalyseur comme mécanisme de feed-back ont montré que l'augmentation obtenue expérimentalement peut-être qualitativement expliquée. A partir d'une certaine fréquence, les oscillations de température sont suffisamment rapides comparées au temps caractéristique du mécanisme de feed-back et elles sont capables de perturber le taux de recouvrement de la surface établi à l'état stationnaire. La formation d'un taux de recouvrement transitoire plus favorable à la réaction que celui à haute température permet d'atteindre durant la période transitoire une vitesse de réaction instantanée plus grande que celle à haute température. Le pic de vitesse de réaction ainsi obtenu est responsable de l'augmentation de la vitesse moyenne de réaction, et donc du rendement, obtenue sous conditions non-stationnaires.

Mots clés

Réacteur microstructuré, non-stationnaire, oscillations de température, catalyse, cinétique, simulation

TABLE OF CONTENTS

1.	Introduction	1
1.1.	Periodic cycling of a reactor.....	1
1.2.	Objectives.....	1
2.	Fundamentals.....	3
2.1.	Microstructure devices.....	3
2.1.1.	Definition - applications	3
2.1.2.	Limitations compared to conventional reactors.....	4
2.1.3.	Fabrication techniques	5
2.1.4.	Existing devices.....	8
2.1.4.1.	Microstructure mixers.....	8
2.1.4.2.	Microstructure heat exchangers.....	9
2.1.4.3.	Microstructure reactors	10
2.1.5.	Catalyst integration into microstructure reactors.....	12
2.1.5.1.	Catalyst integration before mounting the reaction plates in the reactor	12
2.1.5.2.	Catalyst deposition after the bonding of the reactor	15
2.1.6.	Existing possibilities for the periodic cycling of a microstructure reactor	16
2.2.	Periodic cycling of reaction parameters	16
2.2.1.	Parameters of choice	16
2.2.2.	Classification and criteria of comparison	18
2.2.3.	Trivial and non-trivial effects of temperature cycling	19
2.3.	Catalytic CO oxidation as a test reaction.....	21
3.	Experimental.....	23
3.1.	Microstructure reactor.....	24
3.1.1.	FTC-reactor type 2	24
3.1.2.	FTC-reactor type 3	27
3.2.	Experimental installation.....	29
3.2.1.	Gas supply	29
3.2.2.	Cooling water supply.....	31
3.2.3.	Voltage supply	31
3.3.	Measurements and control technology.....	32
3.3.1.	Sensors	32
3.3.1.1.	Temperature sensors.....	32
3.3.1.2.	Pressure sensors.....	32
3.3.1.3.	Mass flow controllers.....	33
3.4.	Analytics.....	33
3.4.1.	Fourier Transform Infrared Spectrometry (FTIR spectrometry)	33
3.4.1.1.	General theory of the FTIR spectrometry	34
3.4.1.2.	FTIR spectrometry stability problem	36
3.4.2.	Mass spectrometry (MS spectrometry)	38
3.4.2.1.	General theory of the mass spectrometry.....	38
3.4.2.2.	Development of an inlet setup for the mass spectrometer	40
3.4.2.3.	MS spectrometer stability problem	42
3.4.3.	Response time characterization for the FTIR and mass spectrometer.....	44
3.5.	Catalyst preparation and characterization.....	46
3.5.1.	FTC reactor type 2.....	46
3.5.2.	FTC-reactor type 3	47
3.6.	Reactants and chemicals	48
4.	Experimental results: FTC-reactor type 2	49
4.1.	Flow characterisation	49
4.1.1.	Experimental determination of the flow characteristics.....	49

4.1.2.	Theoretical calculations of the flow characteristics	51
4.2.	Thermal characterization	54
4.2.1.	Temperature profile under temperature cycling conditions	54
4.2.2.	Heat transfer characterisation	57
4.3.	CO oxidation	59
4.3.1.	Reaction conditions	59
4.3.2.	Stationary thermal conditions	59
4.3.3.	Mass transport characteristics	65
4.3.3.1.	External mass transfer rate	65
4.3.3.2.	Mears criterion	67
4.3.4.	Quasi-stationary thermal conditions	68
4.3.5.	Non-stationary thermal conditions	69
5.	Experimental results: FTC-reactor type 3	75
5.1.	Flow characterization	75
5.1.1.	Experimental determination of the flow characteristics	75
5.1.2.	Theoretical calculations of the flow characteristics	76
5.2.	Thermal characterization	77
5.2.1.	Temperature profile under temperature cycling conditions	77
5.3.	CO oxidation	83
5.3.1.	Reaction conditions	83
5.3.2.	Stationary thermal conditions	83
5.3.3.	Quasi-stationary thermal conditions	88
5.3.4.	Non-stationary thermal conditions	90
6.	Simulations and theoretical interpretation of the experimental results	101
6.1.	Monomolecular reaction	101
6.2.	CO oxidation reaction	108
7.	Conclusions and perspectives	125
7.1.	Conclusions	125
7.2.	Perspectives	126
8.	Symbols and abbreviations	129
	BIBLIOGRAPHY	131
	APPENDICES	135
	Appendix A: Calibration curves of the mass flows	135
	Appendix B: FTIR spectrometer calibration curves	136
	Appendix C: Mass spectrometer calibration curve	136
	Appendix D: Error estimation	137
	Appendix E: Simulation program for the Bodenstein number evaluation	139
	Appendix F: Concentration and reaction rate values for the kinetic study	140
	Appendix G: Simulation programs for the temperature oscillations	141

LIST OF TABLES

Tab. 3.1 Mass flow of He through the capillary leak calculated for different diameters and lengths	42
Tab. 3.2 Response time t_{50} and t_{90} of the FTIR and mass spectrometer to a CO_2 concentration step	45
Tab. 3.3 BET and chemisorption results obtained for the coated SMF foil.....	48
Tab. 4.1 Experimental values of the residence time and Bodenstein number for the FTC-type 2 microstructure reactor.....	51
Tab. 4.2 Diffusion coefficient for CO and O_2 in N_2 at different temperatures.....	53
Tab. 4.3 Schmidt number for O_2 and CO for different temperatures	53
Tab. 4.4 Reynolds, Peclet and Bodenstein number for three different temperatures	54
Tab. 4.5 Calculated apparent activation energy in function of the partial order of CO “a”	64
Tab. 4.6 Sherwood number for O_2 and CO for different temperatures and coordinates along a microchannel	65
Tab. 4.7 Overall mass transfer coefficient for O_2 and CO at different temperature	66
Tab. 4.8 Transfer rate for O_2 and CO from the bulk to the surface at different temperature.....	66
Tab. 5.1 Experimental values of the residence time τ_{reactor} and Bodenstein number for the FTC-type 3 reactor	76
Tab. 5.2 Reaction rate constant for different temperature	87
Tab. 6.1 Different kinetic parameters values found in the literature for the CO oxidation reaction	110
Tab. 6.2 Parameters used in the simulations based on the basic model.....	111
Tab. 6.3 Parameters used in the simulations based on the model with the oxidation-reduction step	117

LIST OF FIGURES

Fig. 2.1	Principle of a multilamination microstructure mixer.....	9
Fig. 2.2	Picture of a V-microstructure mixer built at the Forschungszentrum Karlsruhe	9
Fig. 2.3	Picture of a crossflow microstructure heat exchanger	10
Fig. 2.4	Picture of an electrically heated microstructure heat exchanger.....	10
Fig. 2.5	Lower part of a single-bead reactor containing catalyst before closing with the upper part (left) and anodically bonded single-bead reactor with 625 parallel microreaction chambers with different catalyst	10
Fig. 2.6	Electrically heated methanol steam reformer.....	11
Fig. 2.7	Oil heated methanol steam reformer.....	11
Fig. 2.8	Picture of the microstructure reactor designed for industrial production compared with the size of standard microstructure devices (left) and incorporate in the production set-up (right).....	11
Fig. 2.9	Picture of a microstructured stainless steel foil coated with alumina using the so-gel method. 1. Alumina layer 2. Stainless steel	14
Fig. 2.10	Reaction rate curve (plain line) with the three different mean values obtained under relaxed steady operation (cross), quasi-stationary operation (square) and intermediate periodic operation (star)	20
Fig. 3.1	Experimental set-up flow chart	23
Fig. 3.2	Picture of the whole experimental set-up. It is: 1: security valves and mass flow controllers 2: Mass spectrometer 3: FTIR spectrometer 4: Microstructure reactor (hidden by the mass spectrometer)	23
Fig. 3.3	Detailed view of the experimental set-up with the FTC-type 3 microstructure reactor...	24
Fig. 3.4	Explosion drawing of a FTC microstructure reactor type 2 with 1: microstructure foil with reaction channels 2: microstructure foil with cooling channels 3: plate with heater cartridges holes 4: adapter 5: cover plate 6: channel for thermocouples.	25
Fig. 3.5	Picture of a FTC microstructure reactor type 2. On the left, electrically powered heater cartridges used to permanently heat the device are shown. The foil in the centre is a reaction foil with meandric channels. The foil at the right is a cooling foil with linear channels. The device size is 44 mm x 33 mm x 17 mm (without adapters).	25
Fig. 3.6	Picture of a reaction foil with 3 wet chemically etched meandric channels. The foil is 44 mm long, 33 mm wide and 0.2 mm thick. The channels are 764 mm long, 0.32 mm wide and 0.13 mm deep	26
Fig. 3.7	Picture of a cooling foil.	27
Fig. 3.8	Explosion drawing of the FTC-reactor type 3 with 1: Adapters 2: top plate with microchannels for the cooling passage 3: blind foil for closing the cooling microchannels 4: base plate with reaction chamber and holes for heater cartridges 5: tightening screws.	28
Fig. 3.9	Picture of the FTC-reactor type 3. Down left is a heater cartridge used to permanently electrically heat the device. Down right is a SMF plate coated with alumina and impregnated with platinum used to perform the CO oxidation. Once screwed together, the reactor device size is 35 mm x 35 mm x 21 mm (without adapters).....	28
Fig. 3.10	Picture of the metallic gauze piece which is placed in the reaction chamber to perform the CO oxidation. The piece size is 20 mm x 20 mm x 0.4 mm	29
Fig. 3.11	SEM picture of the structure of the SMF foil with a 100 μ m scale.	29
Fig. 3.12	Infrared spectrum of CO and CO ₂	35
Fig. 3.13	CO ₂ absorbance for a constant CO ₂ concentration without correction (squares) and after the correction of the background evolution (points).....	37
Fig. 3.14	Mass spectrum of 4.5 % CO, 0.5 % CO ₂ and 25 % O ₂ obtained by electronic ionization..	39
Fig. 3.15	Schematic diagram of the developed mass spectrometer inlet set-up	40

Fig. 3.16	Picture of the developed mass spectrometer inlet set-up	41
Fig. 3.17	Picture of the orifice plate inserted in the inlet set-up (above) with the laser-drilled capillary leak (below)	41
Fig. 3.18	Mass spectrometer signal intensity for CO (m/z 28) (squares), O ₂ (m/z 32) (circles) and CO ₂ (m/z 44) (triangles) depending from the mixture composition.....	43
Fig. 3.19	Evolution of the normalized CO ₂ signal intensity recorded by the FTIR and mass spectrometer after a CO ₂ concentration step down in the gas flow	45
Fig. 3.20	SEM picture of the fibers of a SMF foil before the coating procedure (30 μm scale)	47
Fig. 3.21	SEM picture of the fibers of a SMF foil after the coating procedure (30 μm scale)	47
Fig. 4.1	Experimental curves of the residence time distribution of the set-up (squares) and of the set-up with the microstructure reactor connected (diamonds).....	50
Fig. 4.2	Thermocouples position in the microstructure reactor type 2	55
Fig. 4.3	Picture of a reaction plate with the thermocouples position.....	56
Fig. 4.4	Temperature measured by the thermocouples during temperature oscillations with a period duration of 120 seconds and a mean amplitude of 120 K.....	56
Fig. 4.5	Temperature measured by the thermocouples during temperature oscillations with a period duration of 20 seconds and a mean amplitude of 115 K.....	56
Fig. 4.6	CO ₂ concentration at the reactor outlet with respect to the temperature	59
Fig. 4.7	Plot similar to an Arrhenius one for the CO oxidation reaction.....	60
Fig. 4.8	Influence of the partial order of CO “a” on the apparent activation energy of the CO oxidation.....	64
Fig. 4.9	CO ₂ concentration measured by FTIR at the FIC-type 2 reactor outlet under stationary thermal conditions (full squares) and quasi-stationary thermal conditions (empty squares)	69
Fig. 4.10	Measured mean reactor temperature (triangles) and CO ₂ concentration (squares) under forced temperature oscillations with a period duration of 120 s and an amplitude of 120 Kelvin.....	70
Fig. 4.11	Measured mean reactor temperature (triangles) and CO ₂ concentration (squares) under forced temperature oscillations with a period duration of 120 s and an amplitude of 120 Kelvin after phase difference subtraction	71
Fig. 4.12	Comparison of the measured CO ₂ concentration under stationary thermal conditions (full squares) and non-stationary thermal conditions (empty squares).....	72
Fig. 4.13	Measured mean reactor temperature (triangles) and CO ₂ concentration (squares) under forced temperature oscillations with a period duration of 40 s and an amplitude of 120 Kelvin.....	72
Fig. 4.14	Measured mean reactor temperature (triangles) and CO ₂ concentration (squares) under forced temperature oscillations with a period duration of 20 s and an amplitude of 110 Kelvin.....	72
Fig. 4.15	Comparison of the measured CO ₂ concentration under stationary (full squares) and non-stationary conditions (empty squares).	73
Fig. 4.16	Comparison of the measured CO ₂ concentration under stationary (full squares) and non-stationary conditions (empty squares).	73
Fig. 5.1	Experimental plots of the residence time distribution for the set-up only (squares) and for the set-up including the microstructure reactor (diamonds).....	75
Fig. 5.2	Schematic drawing of the thermocouple configuration. The ends are pressed between the reactor top plate and the SMF foil to ensure a good temperature measurement.....	78
Fig. 5.3	Temperature measured by the thermocouples during temperature oscillations with a period duration of 24 seconds and a mean amplitude of 60 K	78
Fig. 5.4	Temperature measured by the thermocouples during temperature oscillations with a period duration of 16 seconds and a mean amplitude of 58 K	78
Fig. 5.5	Picture of a SMF foil with the two slots created by the clamping of the thermocouples	79
Fig. 5.6	Schematic drawing of the second configuration of the thermocouples. The ends are now simply pressed to the surface of the SMF foil.....	80

Fig. 5.7	Temperature recorded with the ends of the thermocouples pressed into the SMF foil. Period duration = 31 s, Amplitude max = 70 K.....	80
Fig. 5.8	Temperature recorded with the ends of the thermocouples pressed onto the surface of the SMF foil. Period duration = 31 s, Amplitude max = 70 K.....	80
Fig. 5.9	Temperature recorded under non-stationary thermal conditions with a maximal amplitude of 40 Kelvin and a period duration of a) 26 seconds b) 21 seconds and c) 19 seconds	81
Fig. 5.10	Evolution of the temperature measured during a period represented using a dimensionless time for three different period durations.....	82
Fig. 5.11	CO ₂ concentration measured with the FTIR spectrometer at the FTC-type 3 reactor outlet under stationary thermal conditions represented with respect to the temperature	84
Fig. 5.12	Observed reaction rate under stationary thermal conditions represented with respect to the temperature	85
Fig. 5.13	Graphic used for the determination of the partial order for CO. Reaction temperature 463 K	86
Fig. 5.14	Graphic used for the determination of the partial order for O ₂ . Reaction temperature 463 K	87
Fig. 5.15	Arrhenius plot for the determination of the apparent activation energy of the CO oxidation.....	88
Fig. 5.16	CO ₂ concentration measured by FTIR at the FTC-type 3 reactor outlet under stationary thermal conditions (full squares) and quasi-stationary thermal conditions (empty squares)	89
Fig. 5.17	Measured highest reactor temperature (triangles) and CO ₂ concentration (squares) under forced temperature oscillations with an oscillation frequency of 0.05 Hz and an amplitude of 35 Kelvin.....	90
Fig. 5.18	Comparison of the measured CO ₂ concentration with respect to the temperature under stationary (full squares) and non-stationary (empty squares) thermal conditions (Amplitude = 35 K, Frq. = 0.05 Hz).....	91
Fig. 5.19	Measured highest reactor temperature (triangles) and CO ₂ concentration (circles) under forced temperature oscillations with a period duration of 26 seconds and an amplitude of 38 Kelvin.	92
Fig. 5.20	Measured highest reactor temperature (triangles) and CO ₂ concentration (circles) under forced temperature oscillations with a period duration of 21 seconds and an amplitude of 41 Kelvin.	92
Fig. 5.21	Comparison of the measured CO ₂ concentration with respect to the temperature under stationary thermal conditions (full squares) and non-stationary thermal conditions (empty squares: Amplitude = 39 K, Frq. = 0.05 Hz; empty diamonds: Amplitude = 38 K, Frq. = 0.048 Hz).....	93
Fig. 5.22	Illustration of the method used to calculate the mean CO ₂ concentration under non-stationary conditions with temperature oscillations with a period duration of 21 seconds and an amplitude of 41 Kelvin.....	94
Fig. 5.23	Graphical illustration of the mean CO ₂ concentration obtained under quasi-stationary temperature conditions (square) and under non-stationary conditions (star).	95
Fig. 5.24	Gain obtained calculated using Eq. 5.11 for different frequencies of temperature oscillations and a constant amplitude of 39 K (± 2 K).....	96
Fig. 5.25	Mass spectrometer signals intensity for CO (stars), O ₂ (diamonds) and CO ₂ (squares) and reactor temperature (triangles) under forced temperature oscillations with an amplitude of 38 K and a period duration of 19 seconds.	97
Fig. 5.26	CO ₂ concentration measured under non-stationary thermal conditions using the FTIR spectrometer (circles) and the mass spectrometer (squares). Temperature amplitude = 39 K, Period duration = 26 seconds	98
Fig. 6.1	Periodic temperature variations of type step according to the time	103

Fig. 6.2	Reaction rate at low temperature (dash), at high temperature (short dash), instantaneous (plain), mean under stationary conditions (dash-dot) and mean under non-stationary temperature conditions (dot); $k_{0,a} = 5 \text{ m}^3 \cdot \text{mol}^{-1} \cdot \text{s}^{-1}$, $E_{a,a} = 0 \text{ kJ} \cdot \text{mol}^{-1}$, $k_{0,d} = 2 \cdot 10^{14} \text{ s}^{-1}$, $E_{a,d} = 100 \text{ kJ} \cdot \text{mol}^{-1}$, $k_{0,r} = 1.25 \cdot 10^{12} \text{ s}^{-1}$, $E_r = 90 \text{ kJ} \cdot \text{mol}^{-1}$	103
Fig. 6.3	Surface coverage of the catalyst under stationary (dash) and non-stationary (plain) temperature conditions and surface reaction rate constant k_r (dots); kinetic parameters value as in Fig. 6.2.....	104
Fig. 6.4	Reaction rate at low temperature (dash), at high temperature (short dash), instantaneous (plain), mean under stationary conditions (dash-dot) and mean under non-stationary temperature conditions (dot); kinetic parameters identical with the ones in Fig. 6.2 excepting $k_{0,a} = 50 \text{ m}^3 \cdot \text{mol}^{-1} \cdot \text{s}^{-1}$ and $k_{0,d} = 2 \cdot 10^{15} \text{ s}^{-1}$	105
Fig. 6.5	Surface coverage of the catalyst under stationary (dash) and non-stationary (plain) temperature conditions and surface reaction rate constant k_r (dots); kinetic parameters value has in Fig. 6.4.....	106
Fig. 6.6	Periodic temperature variation of exponential type according to the time	107
Fig. 6.7	Reaction rate at low temperature (dash), at high temperature (short dash), instantaneous (plain), mean under stationary conditions (dash-dot) and mean under non-stationary temperature conditions (dot); kinetic parameters identical with Fig. 6.2.....	107
Fig. 6.8	Comparison of the experimental reaction rate (circles) with the simulated one (line)...	111
Fig. 6.9	Evolution of the surface coverage of CO (dashed line), oxygen atoms (dotted line) and reaction rate (plain line) with respect to the temperature under stationary temperature conditions.....	112
Fig. 6.10	Simulated reaction rates at low temperature (dashed line), at high temperature (short dashed line), instantaneous (plain line), mean under stationary conditions (dash-dotted line) and mean under non-stationary temperature conditions (dotted line) and temperature (short-dashed line)	113
Fig. 6.11	Simulated surface coverage of CO (dashed lines) and O (dotted lines) under stationary temperature conditions, under non-stationary temperature conditions (CO dash dotted line and O dash-dot-dotted line) and reaction rate constant (short-dotted line).....	114
Fig. 6.12	Comparison of the experimental reaction rate (circles) with the simulated one (line)...	117
Fig. 6.13	Evolution of the surface coverage of CO (dash), oxygen atoms (dot), oxidized active sites (dash-dot) and reaction rate (plain) with respect to the temperature under stationary temperature conditions.....	118
Fig. 6.14	Simulated reaction rates at low temperature (dash), at high temperature (short dash), instantaneous (plain line), mean under stationary conditions (dash-dot) and mean under non-stationary temperature conditions (dot) and temperature (short-dash).....	119
Fig. 6.15	Simulated surface coverage of oxidized sites (dash) under stationary temperature conditions, CO, O and oxidized sites (dot, short-dot and short dash) under non-stationary conditions and temperature (dash-dot).....	120
Fig. 6.16	Gain obtained in the mean reaction rate with respect to the frequency of the temperature oscillations.....	121
Fig. 6.17	Evolution of the surface coverage of CO (dash) oxygen atoms (plain) and oxidized sites (dot) under non-stationary temperature conditions during one period of oscillations with respect to the dimensionless time. Freq. = a) $1 \cdot 10^{-4} \text{ Hz}$, b) $1 \cdot 10^{-2} \text{ Hz}$ c) 0.1 Hz and d) 1 Hz	122

1. Introduction

1.1. Periodic cycling of a reactor

Most of the continuously operated processes used in the chemical industry are designed and optimized for working under stationary conditions with no variation of parameters like reactant concentration, pressure or temperature. However, the possibility to increase the conversion or selectivity of a chemical reaction using forced periodic variations of one of the above mentioned parameters has been already envisaged forty years ago.

In 1967 Lin et al [1] realized a theoretical study using the example of two parallel competitive reactions. They demonstrated that under certain conditions the cycling of the temperature increased the selectivity toward the desired product compared to the optimum obtained under stationary temperature conditions. But they concluded at the end of their study that the fast switching of the temperature was not conceivable from a practical point of view.

Indeed, this statement is definitively right for conventional chemical reactors. Due to their high inertia, only periodic variations with a frequency in the order of magnitude of 10^{-4} to 10^{-3} Hz are possible. Even if the optimum cycling period depends strongly from the kinetics of the system studied, it is usually situated between below one second to around 10 seconds. Consequently, conventional chemical reactors are not adequate tools to study the effect of fast temperature variations on a chemical reaction.

The development of microsystem technology in the last decade and the emergence of microstructure reactors changed the situation. The inertia of those devices is low due to their small size, mass and high surface to volume ratio compared to even conventional lab-scale reactors. Therefore, periodic parameter changes with a frequency between 10^{-2} and 4 Hz are now feasible and the effect of these fast variations on a chemical system can be experimentally investigated.

1.2. Objectives

This thesis is the continuation of the work realized by Brandner [2] and is based on two main points:

- Confirmation of the qualitative experimental results obtained during the work of Brandner. This first work was mainly dedicated to the design and production of a microstructure reactor for Fast Temperature Cycling measurements and to the construction of an adequate set-up. Experimental measurements have been realized using the CO oxidation reaction showing an increase in the time averaged CO_2 concentration under non-stationary temperature conditions compared to those measured under stationary temperature conditions. However, these results were only qualitative and quantitative measurements have to be realized for confirmation.

- Proposition of a theoretical model for the CO oxidation reaction. A theoretical model including all the reaction steps (adsorption, desorption, surface reaction(s)) has to be developed based on the existing literature. The model can be used for simulations under non-stationary temperature conditions. A comparison between the simulated results and the experimental measurements gives an indication on the validity of the proposed model. The objective is not to obtain exact kinetic parameters but to propose a possible explanation for the experimental observations.

2. Fundamentals

2.1. Microstructure devices

Since the 90th and the first appearance of the concept of microsystem technology [3] a lot of publications have been dedicated to this topic. The basics, advantages and disadvantages of this still emerging technology have been listed, e.g., in details by Ehrfeld et al. [4] or Hessel et al. [5]. Therefore, the goal of the following chapters is not to repeat extensively some already made presentations and comments, but only to depict a short overview of the actual microsystem technology state of the art.

2.1.1. Definition - applications

The terms microstructure devices or microsystems include a very broad spectrum of apparatus having different sizes and applications. Microdevices can be heat-exchangers, reactors, valves, pumps or sensors and their external size is not always a reliable clue to assess whether the piece of equipment examined is “micro” or not. As an example, the dimensions of a microstructure reactor developed at the Forschungszentrum Karlsruhe for an industrial application are 68 cm x 33 cm x 24 cm and the device weights nearly 300 kg [6]. The prefix “micro” is much more related to the device inner structure characteristics. A general definition for the microstructure devices domain is relatively difficult to find due to the above mentioned diversity, but it is possible to consider that the “micro” definition is applicable to devices whose characteristic sizes are situated in the sub-millimetre range. Nevertheless, compared to conventional industrial reactors whose size is often ranging up to several cubic meters (CSTR) or about ten meters (tubular reactor) microstructure reactors are generally smaller by several orders of magnitude.

Microstructure devices are not expedient for every imaginable chemical or industrial application. However, in some particular domains, the use of the microsystem technique can bring some non-negligible advantages [7]:

- Very large surface to volume ratio. The extremely large microstructure surface compared to the volume allows to reach heat and mass transfer rates which are several orders of magnitudes higher compared to those obtained in conventional reactors. This permits in turn to perform chemical reactions under more aggressive conditions to obtain higher yields.
- Distributed production. The possibility to produce unstable chemical intermediates like peroxides or azides using microstructure devices directly where they are needed could solve some transport or storage problems encountered by the chemical industry. Moreover, if an accident should happen, despite the safety given by the

good heat and mass transfer control possible in microstructure devices, the small quantity of the chemical released (due to the tiny reaction volume) will restrain the damages caused to the environment or human health.

- Shortening of the “lab to production” time. Once a process is developed and optimized using a single microstructure unit, the step toward industrial production is theoretically not at all-too difficult. The simple numbering up of the lab unit allows to increase the throughput up to the desired production value. However, it appears that this procedure is not so straightforward due to the rising up of the control complexity with the increasing number of the units.
- Less inertia (absolute value) and defined flow pattern. The reduced inertia (absolute value) and well defined flow patterns (plug flow in the case of gases) in microstructure devices allow to produce sharper temperature or concentration changes compared to those obtained in conventional, even lab-size, chemical reactors. This reaction condition jumps are useful tools for the comprehension of reaction mechanisms and allow to get kinetic information which are not accessible under stationary conditions. Moreover, due to the small characteristics size of the microstructures, the kinetic measurements are less likely influenced by external transport limitations.

2.1.2. Limitations compared to conventional reactors

Microstructures devices are very versatile tools which can be successfully exploited in many applications, ranging from chemical research to commercial production, as mentioned in Chap. 2.1.1. Anyhow, this technique implies some limitations compared to standard size devices which should be taken into account before envisaging the use of microstructure devices:

- To manufacture microstructure devices some rules for design and manufacturing have to be taken in account. A detailed description of the manufacturing processes as well as the design rules can be found in [8, 9]. For the device shown in this thesis, the fabrication is relatively expensive and complicated. The manufacturing process of the devices used in this thesis is given in Chap. 3.1. In general, the production of single prototype microstructure devices implies much more expensive manufacturing processes compared to those necessary for conventional structures. The device materials must fulfil criterions like processing and welding possibilities or resistance and the machining treatments are equally more expensive due to the smaller manufacturing and processing tolerances. Generating microstructure devices in large-scale production or series production would clearly reduce the

production costs, but the commercial demand from the chemical industry is at the moment not large enough to envisage this kind of production. This might be changing in future. For other industrial technology branches like medical instrumentation or bio-tech, microstructure devices are common and commercially available for low prices. But still the most common application of microstructure technology is the semiconductor industry.

- Limited flow rates. The maximal flow rates attainable using a single microstructure devices are relatively restraint due to the small inner characteristics size. Higher flow rates are always related with increasing pressure drop which are not always supportable or suitable for the whole installation. The numbering-up of the devices (in parallel) is a possibility to reach higher total mass flows without paying it by a too high pressure drop. However, as mentioned in Chap. 2.1.1, this option increases the complexity of control and monitoring operations for the overall installation.
- Reaction choice. Due to the short residence time obtained in microstructure reactors, there use is restricted to (very) fast reactions with a space time in the (sub)second range to obtain high conversion and yield.
- Plugging risk. The characteristic size in the sub-millimetre range of the microstructure devices makes them more vulnerable to the blocking of the structures by particles present in the inflow. The use of filters with a mesh size in the order of magnitude of a few microns reduces efficiently the plugging risk but slightly increase the pressure drop of the whole system. The fouling of microstructures by the precipitation of organic or inorganic material (e.g. calcium carbonate) inside the device is also a point of concern. Different possibilities like the use of protective coatings or the application of ultrasound are actually investigated to solve this problem [10].

2.1.3. Fabrication techniques

Has mentioned above, the principal characteristic of microstructure devices is the presence of an internal structure with characteristic dimensions in the micrometer range (e.g. microchannels). Some of the most important techniques used to create the interior three dimensional structures are mentioned below [11]:

- The LIGA technology. LIGA is a German acronym for Lithographie, Galvanoformung and Abformung. This method is based on deep x-ray lithography, electroforming and moulding processes following the subsequent steps:

1. A pattern from a mask is transferred using X-rays into a resist layer deposited on an electrically conductive support.
 2. The three dimensional structure obtained on the resist polymer is transferred into a metallic structure by electroforming. This structure can be in some cases the end product of the procedure.
 3. The metal structure can then be used as a mould for the serial production of pieces using for example injection moulding or embossing.
- Wet and dry etching processes. The wet etching process is based on the dissolution of the material using an appropriate liquid. The parts of the material which must not be dissolved are protected using a mask. However, due to lateral-etching (under the protective mask) for most of the materials, only superficial structures can be generated. Three dimensional structures like microchannels with a high aspect ratio can be realized by etching completely through thin foils which are then stacked together. The microstructured foils used to build the microstructure reactor FTC-type 2 presented in Chap. 3.1.1 were manufactured using the wet etching method. These microchannels are 320 μm wide and 130 μm deep with 100 μm wide fins between the channels. The structure bottoms obtained via this method are not totally plane but with slightly rounded corners.
Anisotropic plasma etching methods are used to create microstructures of any form, mainly in silicon. As in the case of wet etching, the surface which should not be etched may be protected using a mask based on plasma resistant polymers. By using alternatively etching steps and passivation of the already etched structure, it is possible to obtain structures with a very high aspect ratio.
 - Mechanical micromachining. Progresses realized in the mechanical micromachining allow now to produce complex structures with contour accuracy in the sub-micrometer domain using milling, turning and grinding. Almost all materials can be processed using this technique with nearly no restriction concerning the shape of the structure to be produced, even if 3D-structures are relatively difficult to manufacture. Some limitations may also appear for the production of closed packed structures due to the finite size of the micromachining tools.

Once the microstructuring process of the foils is completed, they have to be assembled to build the desired microstructure device. Two different possibilities exist for the assembling of microstructure devices. The first one consists in welding the foils together by means of one of the following techniques [12]:

- Diffusion bonding. During the diffusion bonding process the microstructure foils are stacked together and placed in a vacuum furnace. Dependant from the material to be welded, a defined pressure is applied on the stack while a temperature profile is running. As a consequence of the temperature and pressure, the foil material diffuses at the contact areas between the different layers. The microstructure foils are bound together not only on their outer edges but by all the contact surfaces originated from the stacking. The result is a compact metallic block especially stable and resistant towards pressure differences.
- Electron beam or laser welding. This method uses a laser beam to heat up the edges of the microstructure foils to the material melting point. The result is again a compact metallic block but at the contrary to the diffusion bonding, the foils are only bound together at their edges and not at the core of the block. The microstructure devices produced this way are less resistant towards pressure. If a too high pressure is applied compared to the thickness of the foils, the risk exists that they arch in the middle. As a result of the arching, the heat transfer characteristics are getting worse and the microchannel closing obtained by the plate situated on top may leak.

The electron or laser beam welding method is adequate for the production of microstructure devices using welding sensitive material or when a temperature damageable material like a support layer or a complete supported catalyst has been deposited on the microstructure foils to be welded. The heat entry inside the material can be better controlled during the process than in the case of diffusion bonding, rendering this method more material sparing.

Microstructure reactors used in fast temperature cycling experiments have to be very resistant towards high pressure changes because the cooling method chosen (water cooling) leads to vapour formation which is related with pressure pulses and this in a cycling way. The stress of the devices by the periodic temperature changes is also a parameter which should not be neglected. Since the diffusion bonding method is giving the more stable devices, it is this method which is chosen for the fabrication of the FTC-reactor type 2 presented in Chap. 3.1.1. The only limitation of the diffusion bonding method is that it is not possible to deposit a supported catalyst in the microchannels of the foils before the welding process takes place. From one side the high temperature applied during the welding process would damage the catalyst. From the other side, if some of the support layer is accidentally deposited on the top of the walls between the channels, which is relatively difficult to prevent, the diffusion process will not fully take place and some area will not be completely welded together. These not welded areas will then in turn weaken the device making it less suitable for fast temperature cycling experiments. The problems generated by the

impossibility to coat the microstructure foils before the welding are presented in details in Chap. 2.1.5.

The second possibility for the assembling of a microstructure device consists in piling up the foils on top of each other and to press them together using e.g. tightening screws. This way of doing is mainly used to build microstructure reactors when the microstructured foils have to be changed easily. This type of devices is ideal for e.g. catalyst testing. However, this technique implies that the final mass of the device is higher than when the plates are welded together due to presence of the tightening screws and their corresponding threads. The microstructure reactor presented in Chap. 3.1.2 is originally designed for material testing and is consequently built using the tightening screws technique. Nevertheless, the device weight remains relatively small, allowing to realize fast temperature cycling experiments with an only slightly lower temperature change rate.

2.1.4. Existing devices

As mentioned in Chap. 2.1.1, microstructure devices are designed for a very broad spectrum of applications. This chapter will only briefly describe three different general types of apparatus designed, produced and investigated at the Forschungszentrum Karlsruhe. A more extensive description of all possible types of microstructure devices is presented in [5].

2.1.4.1. Microstructure mixers

Because of the hydraulic dimensions of the microchannels present in microstructure mixers, the flows are practically always laminar [13]. The absence of turbulences induces that the mixing happens only through molecular interdiffusion. Two different principles exist for the mixing of liquid or gas in microstructure mixers. The active mixing is realized by delivering energy from the outside to the device. The energy supplied can have different forms like ultrasound, periodic variation of the flow rate or electrokinetic instabilities. The second possibility consists in rearranging the flow in order to increase the mixing rate. This is called passive mixing. Different options exist for the flow rearrangement like the separation of the flows to be mixed in smaller lamellae, the injection of one flow in the other using nozzles or the collision of the flows. Fig. 2.1 and Fig. 2.2 show the principle and a picture of a microstructure mixer based on the principle of the creation of thin lamellae for the mixing of two flows.

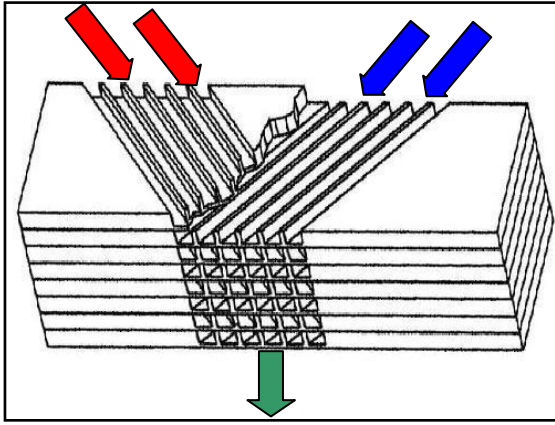


Fig. 2.1 Principle of a multilamination microstructure mixer

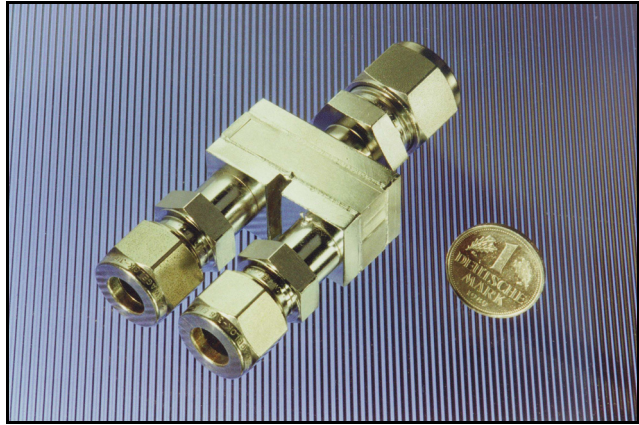


Fig. 2.2 Picture of a V-microstructure mixer built at the Forschungszentrum Karlsruhe

2.1.4.2. Microstructure heat exchangers

Microstructure heat exchangers own a clear advantage compared to the standard heat exchangers used in process engineering [14,15]. Since the volume decreases with the third power of the linear dimensions of the device and the surface decrease with the second power, the reduced size of the internal structures allows to obtain very high surface-to-volume ratio (e.g. $30000 \text{ m}^2 \cdot \text{m}^{-3}$ or more). Overall heat transfer coefficients of up to $25000 \text{ W} \cdot \text{m}^{-2} \cdot \text{K}^{-1}$ compared to about $2000 \text{ W} \cdot \text{m}^{-2} \cdot \text{K}^{-1}$ for standard tubular heat exchangers have been reported [15]. The heat transfer in microstructure devices can be realized either between two flows at different temperatures or by using electrical heating cartridges for the heating of a single flow. In the first case, the device is made of microstructured foils which are stacked and bonded together to form the central part of the exchanger. Fluid connections are then welded to the stack of foils and the flows are circulating inside the devices in alternating layers. Crossflow, co-current flow or counterflow are the three existing possibilities for the fluid circulation.

To build the electrically heated heat exchangers, the microstructured foils for the flow circulation are stacked between metal blocks containing drilled holes for the heater cartridges. The flow connections are then welded on the obtained central part. Fig. 2.3 and Fig. 2.4 present two different types of microstructure heat exchangers built at the Forschungszentrum Karlsruhe.

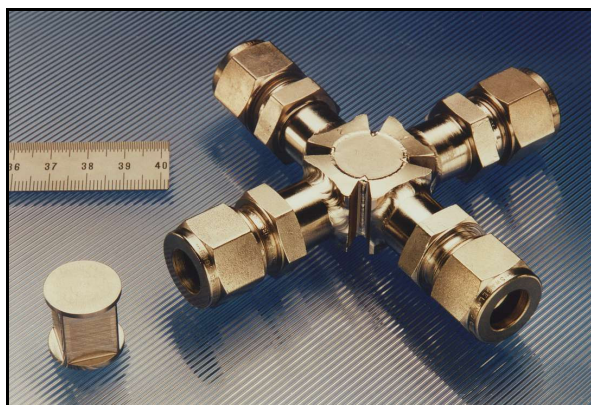


Fig. 2.3 Picture of a crossflow microstructure heat exchanger

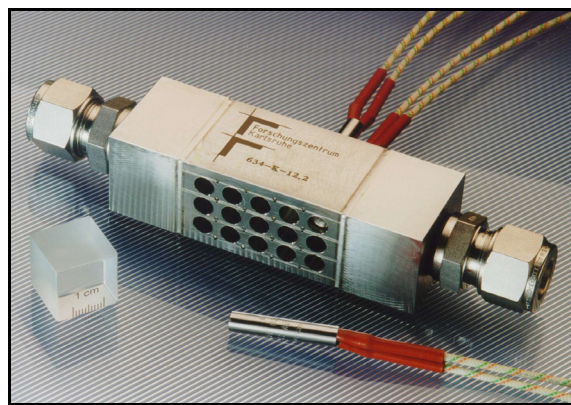


Fig. 2.4 Picture of an electrically heated microstructure heat exchanger

2.1.4.3. Microstructure reactors

Since the end of the 90th a very broad variety of microstructure reactors has been developed both for heterogeneously catalyzed gas reaction and for liquid phase reaction [16]. The application spectrum is now ranging from small devices for laboratory and research purposes to relatively large apparatus for industrial production. This chapter is only shortly presenting three devices illustrating this diversity.

On the laboratory scale, microstructure reactors can be very useful tools for the screening of catalysts. The flow conditions inside the devices are generally well defined, the reduced size diminishes the quantity of catalyst needed for the experiments and new devices allow to test simultaneously a large number of different catalysts. Fig. 2.5 present a microstructure reactor developed for catalyst testing containing 625 separated reaction chambers [17].

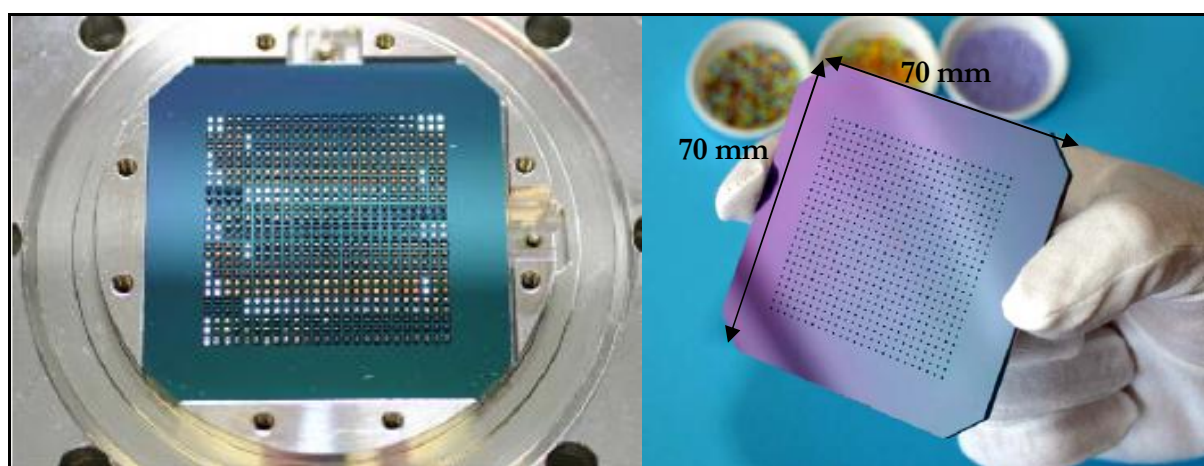


Fig. 2.5 Lower part of a single-bead reactor containing catalyst before closing with the upper part (left) and anodically bonded single-bead reactor with 625 parallel microreaction chambers with different catalyst

Another application for microstructure reactors is the domain of energy generation, namely the production of hydrogen for e.g. fuel cells through the conversion of chemicals like methanol or

gasoline. Fuel processors covering an electrical power range from less than one watt to some megawatts and based on standard engineering techniques already exist or are under investigation. However, due to their reduced size, fuel processors based on microstructure technology seem to have an important potential for e.g. mobile or portable applications. Fig. 2.6 and Fig. 2.7 show two different types of methanol steam reformers built at the Forschungszentrum Karlsruhe. These two reformers have been designed for the production of approximately 15 and 35 g of hydrogen per hour.



Fig. 2.6 Electrically heated methanol steam reformer Fig. 2.7 Oil heated methanol steam reformer

The last example of microstructure reactors presented here shows that this new technology is not only a laboratory curiosity but that real industrial production is already a reality. Fig. 2.8 presents the pictures of a microstructure reactor produced at the Forschungszentrum Karlsruhe for the chemical company DSM. The device is designed for an acidic reaction mixture throughput of $1500\text{--}1700\text{ kg}\cdot\text{h}^{-1}$ and allows the transfer of some hundreds of kilowatts at approximately 80°C while keeping the cooling fluid temperature increase below 5 K [6].

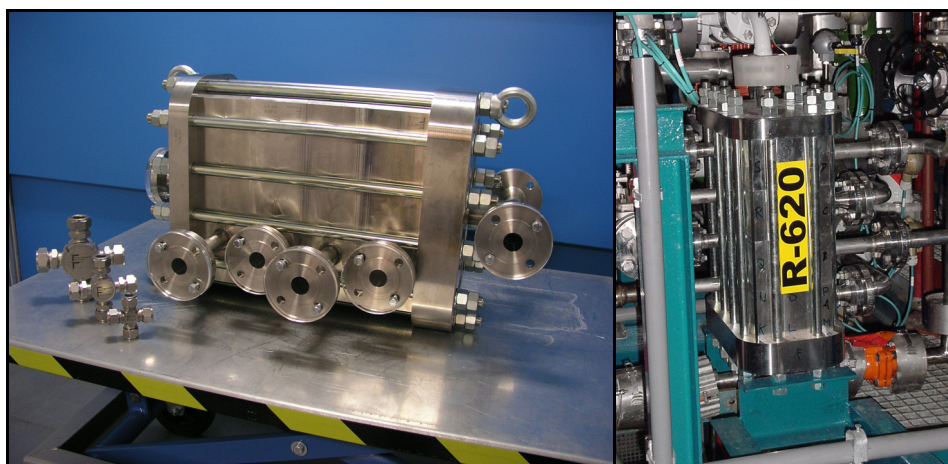


Fig. 2.8 Picture of the microstructure reactor designed for industrial production compared with the size of standard microstructure devices (left) and incorporate in the production set-up (right). The reactor length is 65 cm and the weight 290 kg.

2.1.5. Catalyst integration into microstructure reactors

There are two different possibilities to integrate a catalytic active material in a microstructure reactor. The first solution consists in depositing the layer on the reaction plates before mounting them in the reactor. The second solution is the coating of the reaction passage(s) of the reactor once all the reactor constituents have been bonded together.

2.1.5.1. Catalyst integration before mounting the reaction plates in the reactor

This way of doing is only applicable if the reactor plates are placed inside the reactor and maintained using a mechanical force. The diffusion bonding of the reactor is not anymore possible because of the limitations mentioned in Chap. 2.1.3.

Even if in some cases the material used to produce the microstructure reactor itself is catalytically active for the reaction envisaged [18], it is necessary to create a porous oxide layer on the walls of the microstructure reactor reaction channels or other internal structure of the reactor in order to increase the reaction surface. This layer may also serve as a support for an afterward deposited catalytic material. Different possibilities exist to create the porous support layer, see for example [19]. Four of them which can be used for microchannel coatings are listed below:

- anodic oxidation [20]
- chemical vapour deposition [21]
- deposition of nanoparticles [22]
- sol-gel process [23, 24]

The sol-gel process has already been used successfully by Haas-Santo et al. [23] or Brandner [2] for the coating of completely assembled microstructure reactors and it is consequently the method which has been used during this work. The description presented beneath uses specifically the formation of an alumina porous layer as example. However, the basic principles remain the same for the creation of a porous layer using another type of oxide like SiO_2 or CeO_2 .

The first step consists in the preparation of a colloidal alumina sol. This sol can be prepared either by hydrolyzing aqueous AlCl_3 following by a precipitation using NH_3 or by hydrolyzing aluminium alkoxide (Al(OR)_x with R being an alkyl group of type $\text{C}_n\text{H}_{2n+1}$) with water. An acid like for example HNO_3 , acetic or hydrochloric acid is then added to the sol as a peptizing agent [25]. To obtain surface films, the pieces which have to be coated are dipped into the sol and then withdrawn. The channels may equally be filled using a pipette. If necessary, the sol excess may be removed by gravity or by slightly blowing air. The sol on the pieces surface is then dried and solidified. The dry layer is calcined in order to obtain the desired type of alumina. Boehmite is

obtained by using a calcination temperature below 670 K, γ or δ -type is obtained between 670 and 1070 K and α -alumina at approximately 1270 K.

The surface enhancement factor ($F = \frac{S_{\text{porous alumina}}}{S_{\text{support}}}$) seems to be dependent on the calcination temperature chosen, with $F = 3$ at 670 K and $F = 152$ at 770 K. Haas-Santo et al. [23] have moreover shown that the properties of the porous layer obtained depend not only on the calcination temperature chosen but also on factors like:

- Type of stabilizer added to the solution. The choice of a good stabilizer is crucial for the adhesion of the oxide layer on the metallic surface. If no stabilizer is used and the condensation rate is too high, a bad adhesion will be obtained. Acetylacetone was found to be a good stabilizer for the coating with alumina.
- Temperature pre-treatment of the metallic support. Experiments using an Fe-based alloy containing 5% aluminium have shown that the formation of a 1 μm thick alumina layer which happens when the metallic foil is heated to 1270 K increases the adhesive strength of the alumina layer formed afterwards by sol-gel.
- Aging time of the alumina sol. The fluidity of the sol is decreasing with increasing time due to continuing condensation reactions in the sol itself. The fluidity of the sol is an important parameter because with increasing viscosity the sol produces thicker layers which are more sensitive to the formation of cracks and with lower adhesion strength. However, the use of a stabilizer like acetylacetone allows to reduce the effects of the aging of the sol.

The coating of material which can be directly dipped in the coating solution (e.g. ceramic monoliths) or onto which the solution can be deposited (e.g. microstructured stainless steel foils) is relatively straightforward and applied since several years [26]. Optimized reaction parameters and conditions result in porous layer with good mechanical properties, surface enhancement and porosity. A picture of a microstructured reaction foil coated with alumina is presented in Fig. 2.9.

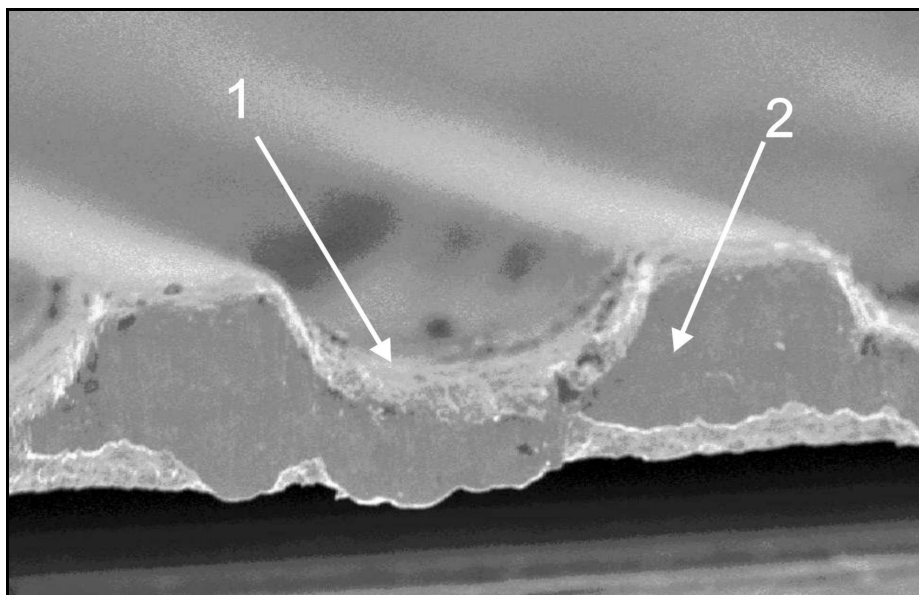


Fig. 2.9 Picture of a microstructured stainless steel foil coated with alumina using the so-gel method. 1. Alumina layer 2. Stainless steel [2]

The layer thickness obtained is typically between a couple and around 10 micrometers. The specific surface area of the coating and its pore distribution can be determined using the standard BET physisorption method [27].

Concerning the incorporation of the active material itself (generally a metal like Cu, Fe or a noble metal like Pd or Pt) in or at the surface of the porous layer, different possibilities exist. The active metal can be directly added to the sol-gel solution [28] and the porous layer is then formed as mentioned above. One other possibility is to deposit the active metal on the porous layer after it has been prepared. This step can be realized using a wet impregnation method [29]. For this purpose, the alumina layer is impregnated with a solution of the active metal, the solvent is removed by drying and the layer containing now the active metal at the surface and in the pores is again calcined.

The two steps method (sol-gel and wet impregnation) results in more surface metal atoms compared to the one step method because the metal can only be deposited on the surface and into the pores of the support layer. At the contrary, the one step method implies the incorporation of the metal atoms equally within the layer (under the surface) where they are not accessible for the reaction. Since in microstructure reactors the support surface available is relatively restrained compared to conventional reactors, it is the method delivering the most surface metal atoms (sol-gel and wet impregnation) which is generally chosen to produce the supported catalyst in microstructure reactors.

2.1.5.2. Catalyst deposition after the bonding of the reactor

As mentioned in Chap. 2.1.3, if the microstructure reactor has to be built up using the diffusion bonding method, the support layer cannot be prepared before the welding process. The device has to be coated when already welded and the procedure becomes much more complicated. The coating solution has to be introduced somehow in the microchannels where the layer must be created without blocking them with an excessive thickness. By filling a micro-heat exchanger placed in a vertical position (the solution flowing through the channels by gravity) and removing the solution excess by blowing it out, Haas-Santo et al. [23] have been able to produce a porous layer in an already welded microstructure reactor with a good adhesion to the microchannels walls. A picture of coated microchannels is shown in [23].

Beside the fact that the coating of already welded reactors is more tricky compared to the coating of single metallic foils, the characterization of the deposited layer regarding its surface, pore distribution, catalytic activity or mechanical properties is another point of concern. The conventional methods using physical or chemical adsorption are all based on the principle that the support to be characterized can be cut in small pieces. This operation can be easily realized with metallic foils but this is obviously not the case for a complete reactor. The only way to get an idea of the appearance of the support layer deposited in an already welded microstructure reactor is to cut the device in slices perpendicular to the channels. The surface of the segments obtained can then be examined using an optical method like Scanning Electron Microscopy. A picture of such a microstructure reactor slice can be found in [23]. This method is unfortunately destructive and gives only an idea of the porous layer appearance at a given point in the device and not on the whole length of the channels. The weighting of the microstructure reactors to know at least the quantity of e.g. active metal which has been deposited inside the microchannels is hardly feasible because the weight difference (some milligrams) compared to the reactor weight (some 100 grams) is negligible. To my knowledge, no applicable characterization methods of a supported catalyst deposited in an already welded microstructure have been proposed in the literature yet.

This lack of characterization possibilities is a major limitation for the use of the reactor presented in Chap. 3.1.1 as a tool for thorough catalytic investigations. This problem is solved by the use of the reactor presented in Chap. 3.1.2 which is screwed together instead of being welded. The supported catalyst deposited on a metallic gauze can be investigated before the gauze being inserted in the reactor.

2.1.6. Existing possibilities for the periodic cycling of a microstructure reactor

Two main possibilities exist to control the temperature of a microstructure reactor. The one implies the use of a fluid as heat transfer medium flowing through microchannels incorporated inside the device and the other the utilisation of electrical heating or cooling elements installed within the reactor corpus. Each method owns its particular advantages and disadvantages which have been in detail listed by Brandner [2]. Moreover, Brandner [2] envisages in extenso the different fluid/electrical combinations possible for the heating/cooling with their advantages and restrictions. Since the work presented here is based on an already existing set-up, respectively microstructure reactor, only the chosen alternative is described in details in this paragraph.

The option chosen for the periodic cooling and heating of the microstructure device used during this work is the permanent heating of the device with high power heating cartridges and the periodic cooling of the reactor by water flowing through the reactor in cooling microchannels. Using this option, the control of the electrical heating is straightforward because the voltage applied to the heating cartridges has once to be set and then simply to be kept constant. Moreover the lifetime of the heating cartridges is increased compared to a solution where fast on-off cycles are applied to the cartridges [30]. The cooling can be effectuated using pneumatically driven, electronically controlled magnetic valves for switching between the water flowing through the reactor cooling microchannels and a by-pass tube.

One problem which can appear when using a cooling fluid to cool down the device is the presence of a liquid hold-up inside the reactor. At the end of a cooling period, the cooling microchannels will be full of water which will be heated together with the whole reactor during the heating period. The possible hold-up volume is not very important (10 μ l) but could nevertheless induce a reduction of the maximal heating rate attainable. To solve this problem, a very short pulse of compressed air is injected in the cooling microchannels at the end of the cooling period. This air pulse is cleaning the microchannels from the residual water and eliminating so the potentially present hold-up.

2.2. Periodic cycling of reaction parameters

2.2.1. Parameters of choice

There are many different parameters of a chemical system which can be varied in order to modify its behaviour. The most commonly studied in both theoretical and experimental studies is the concentration or partial pressure of the reactants in the feed. Although the periodic change of this parameter is not the topic of this work, it is due to its popularity worth to shortly present it. From the practical point of view, it is relatively easy to vary the concentration of liquids or the partial

pressure of gaseous reactants by using a four way valve for switching between two reaction feeds. The oscillations obtained using this method are mostly of square-wave form. This is because square-wave functions results in most cases in the highest effects. To obtain an ideal square wave function is however not totally evident. Cutlip [31] used square-wave type oscillations in his experimental study of the CO oxidation reaction under periodic concentration changes and observed an increase in the CO₂ production rate compared to the one measured under steady-state. Other studies using for example the ammonia synthesis [32] have also demonstrated large production rate increases compared to the steady state conditions. It is therefore now commonly accepted that the periodic variation of the reactant concentration may under certain conditions increase the mean reaction rate of a chemical reaction.

The influence of the periodic variation of the temperature on a chemical system has been by far less practically investigated compared to the concentration oscillations. This lack of studies is mainly due to limitations in the available experimental set-up, respectively in the used reactors. It is relatively difficult to cycle the temperature of reactors built using conventional techniques in a fast, reproducible and homogeneous way because of the external and internal heat transfer limitations present in this type of devices. Despite the experimental difficulties linked with temperature oscillations, it is theoretically expected [33] that the periodic variation of this parameter will produce much more impressive effects on the reaction rate of a chemical system than concentration oscillations. This is due to the highly non-linear dependence of the kinetic constants of a chemical system with regard to the temperature.

In 1980 Abdul-Kareem et al. [34] realized an experimental study of the catalytic CO oxidation behaviour under temperature cycling conditions. The reaction rates they measured under non-stationary conditions were closely approximated by the ones under steady-state conditions. They therefore concluded that no advantages of temperature cycling could be awaited if it was possible to work at the highest temperature applied during the oscillations. However, the shortest oscillation period they were able to perform using their reactor was one hour. Since adsorption processes for CO and O₂ are very rapid phenomena (very low activation energy and relatively high pre-exponential factors [35]), it is doubtful that the measurements realized were really under non-stationary conditions. It is more likely that the reactor was in reality always operating under quasi-steady state conditions and, thus, no special effects of the temperature oscillations were observable.

Microstructure reactors allowing temperature cycling periods between some seconds and around ten seconds are at the contrary the ideal tools to study the behaviour of a chemical reaction under non-stationary temperature conditions. These new devices are opening new possibilities to reproduce more precisely the conditions used in the theoretical studies in order to confirm or infirm their results in an experimental way.

2.2.2. *Classification and criteria of comparison*

One of the first reviews about the topic of forced parameters oscillations published in 1973 by Bailey [36] classifies periodic operations in different branches depending on the duration of the period (t_p) and the characteristic time of the system studied (t_c). According to Renken [37], who reuses this classification, three domains can be defined:

- 1) Quasi-Steady Operation with $t_p \gg t_c$. The period of the oscillations is larger than the characteristic time of the system. The system will act like being always in steady state and the dynamics can be described using the Quasi Steady-State Approximation (QSSA).
- 2) Intermediate Periodic Operation with $t_p \approx t_c$. The period of the oscillations is in the same order of magnitude as the characteristic time of the system. The system operates in a transient regime. Under these conditions, the system performance (e.g. instantaneous reaction rate, selectivity) may strongly vary compared to the one under steady-state. This domain is thus the most interesting to study the effects of periodic operation.
- 3) Relaxed Steady-State Operation with $t_p \ll t_c$. The varied parameter changes very quickly compared to the characteristic time of the system. As a result, the reactor cannot follow the oscillations anymore and the system acts as being under steady state conditions at the average value of the varied parameter.

The results obtained under periodic parameters forcing conditions have to be compared with the ones obtained under stationary state conditions. It is therefore necessary to determine the comparison criteria. Three different criteria are proposed by Renken [37]:

- 1) The parameter values for the steady state operation are chosen randomly and used as the average for the periodic operation.
- 2) The optimal parameters for the steady-state operation are used as the time averaged value for the periodic operation.
- 3) A range of parameters is chosen for the steady-state operation and the results obtained within this parameter range are compared with the ones obtained under periodic operation. The time averaged value and the maximal and minimal values of the parameters under periodic operation must be inside the domain used for the steady state measurements.

The third criterion is the most interesting. It allows to answer the question whether better results are achieved under periodic operation compared to the steady state-operation within the same range of parameters. It is consequently this criterion which has been chosen in this work for the comparison of the results obtained under temperature stationary conditions with the non-stationary ones.

2.2.3. *Trivial and non-trivial effects of temperature cycling*

Since the general rate constant of a chemical reaction is given by the Arrhenius law

$$k_r = k_0 \cdot e^{\left(\frac{-E_a}{R \cdot T}\right)} \quad \text{Eq. 2.1}$$

with

$$\begin{array}{ll} k_0 = \text{pre-exponential factor} & [\text{s}^{-1}] \\ E_a = \text{Activation energy} & [\text{kJ} \cdot \text{mol}^{-1}] \end{array}$$

the reaction rate of a chemical reaction given by the following equation:

$$R_r = k_r \cdot \prod_i C_i^j \quad \text{Eq. 2.2}$$

is, as can be seen in Fig. 2.10, a convex function. Mathematically, a function is convex if and only if:

$$f\left(\frac{x_1 + x_2}{2}\right) \leq \frac{f(x_1) + f(x_2)}{2} \quad \text{Eq. 2.3}$$

with x_1 and x_2 being two points along the x axis.

The consequence of this convexity is shown in Fig. 2.10. The averaged reaction rate (square) under slow temperature cycling (quasi-steady-state operation) between a low and a high temperature is higher than the mean reaction rate at the mean temperature (cross). This increase is therefore trivial and results only from the exponential dependence of the reaction rate with respect to the temperature and the related convex behaviour.

A non trivial effect of temperature oscillations under intermediate regime conditions is only demonstrated if the obtained averaged value of the reaction rate (star) is higher than the averaged value under quasi-steady-state conditions (square).

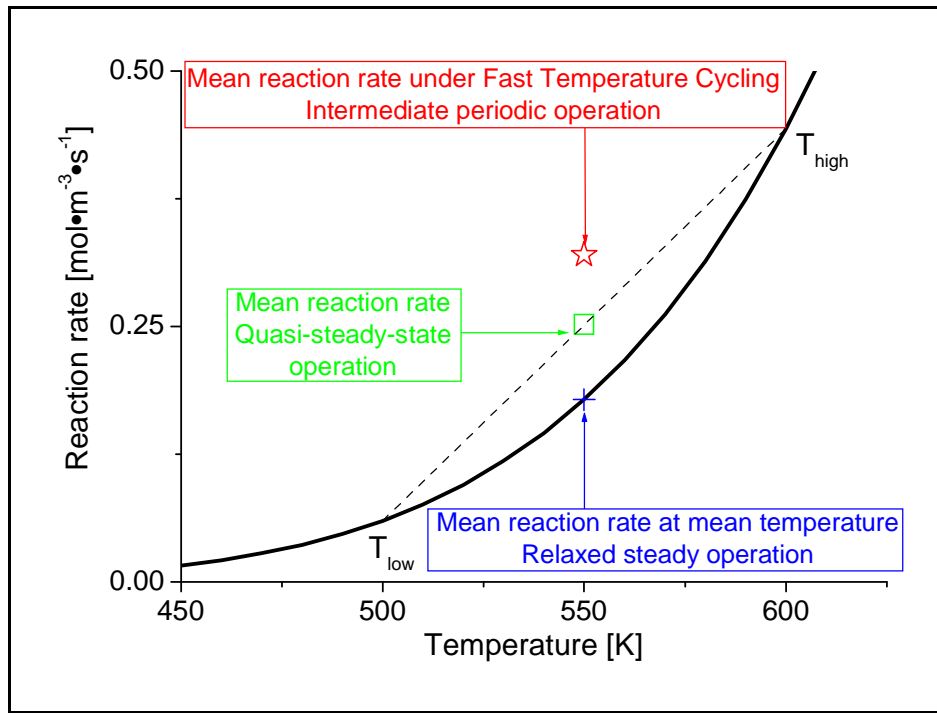


Fig. 2.10 Reaction rate curve (plain line) with the three different mean values obtained under relaxed steady operation (cross), quasi-stationary operation (square) and intermediate periodic operation (star)

If the mean reaction rate under quasi-steady-state operation is defined by using the reaction rate at low temperature ($R_{rx}(T_{low})$) and at high temperature ($R_{rx}(T_{high})$):

$$R_{rx,meanQSC} = \frac{R_{rx}(T_{low}) + R_{rx}(T_{high})}{2} \quad [\text{mol} \cdot \text{m}^3 \cdot \text{s}^{-1}] \quad \text{Eq. 2.4}$$

and the mean reaction rate under intermediate periodic cycling conditions by using the reaction rate measured at each temperature ($R_{rx}(T_i)$):

$$R_{rx,meanTC} = \frac{\sum_i R_{rx}(T_i)}{i} \quad [\text{mol} \cdot \text{m}^3 \cdot \text{s}^{-1}] \quad \text{Eq. 2.5}$$

a rate enhancement factor EF, similar to the one proposed by Hansen et al. [38], can be calculated using:

$$EF = \frac{R_{rx,meanTC}}{R_{rx,meanQSC}} \quad [-] \quad \text{Eq. 2.6}$$

Since this rate enhancement factor is based on the mean reaction rate under quasi-steady-state conditions (square in Fig. 2.10) it allows to quantify the effects of temperature cycling which are not directly due to the Arrhenius law.

In the perspective of e.g. the increase of a product concentration, the best case would be if the mean reaction rate under intermediate periodic operation (star in Fig. 2.10) is higher than the value obtainable at the highest temperature. This would give a clear advantage to periodic operation compared to the steady state operation at the highest temperature. From an industrial point of

view, the presented situation is indeed non trivial but less interesting. In this case, the periodic operation is beneficial compared to the stationary operation if it is e.g. not possible to run the reaction (or process) permanently at the highest temperature.

2.3. Catalytic CO oxidation as a test reaction

The catalytic carbon monoxide oxidation is one of the most studied reactions either under stationary state conditions or periodic operation. This chapter presents shortly some of the experimental results in the periodic operation field obtained using this reaction and the basic mechanism commonly accepted by most of the researchers. A much more extensive review about this reaction has been presented by e.g. Gulari et al. [39] in the middle of the 90th.

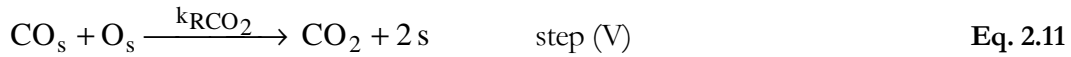
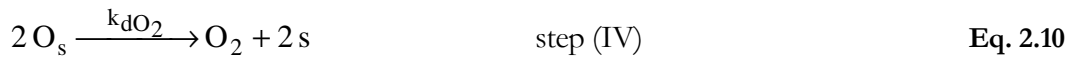
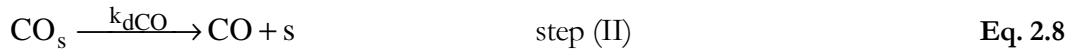
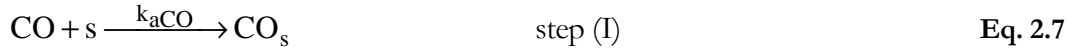
The majority of the experimental studies on periodic operation realized till yet were focused on the topic of concentration forcing for practical reasons. Temperature cycling as a forcing parameter has only been scarcely investigated with relatively limited success. Between the study of Abdul-Kareem et al. [34] who failed to demonstrate any positive effects of temperature cycling and the study of Brandner [2] who firstly demonstrated a qualitative increase in the reaction rate passed more than 20 years. The new results have woken up again the interest towards the investigation of this reaction under temperature forcing conditions and there is now the need to confirm them in a quantitative way.

The literature about the periodic operation of the CO oxidation using the concentration forcing of the reactants is at the contrary much more numerous. As mentioned in Chap. 2.2.1, Cutlip [31] switched periodically between mixtures of carbon monoxide/argon and oxygen/argon in a gradientless reactor and measured a net increase of the reaction rate compared to the stationary conditions. He attributed this reaction rate increase to changes in the surface coverage of the reactive species during the periodic operation. The following work of Abdul-Kareem et al. [40] using a vanadium based catalyst instead of a platinum one brought principally the same experimental results. Zhou et al. [41] proposed, based on FTIR studies, that the periodic cycling of the reactant prevents the formation of large reactant islands of the same species on the catalyst surface. Assuming that the surface reaction happens at the periphery of these reactant islands, smaller islands will result in a larger perimeter length and thus in an increase in the reaction rate.

If similar changes in the surface coverage can be obtained using temperature forcing instead of concentration forcing, this could essentially lead to the same increase in the reaction rate and be a possible explanation for the results obtained by Brandner [2]. Moreover, according to Nibbelke et al. [42] the CO oxidation is inhibited by the preferential adsorption of CO on the catalyst surface compared to the adsorption of oxygen. If it is possible to influence the adsorption-desorption equilibrium of the carbon monoxide and the oxygen by temperature cycling in order to increase the oxygen coverage on the surface, this could be another explanation for a reaction rate increase.

Therefore, this reaction and the possible effect of fast temperature cycling on its behaviour is worth to be investigated in details and is the test reaction chosen for this work.

The catalytic CO oxidation reaction has not only been intensively studied under forced parameter conditions but many studies have equally been concentrated on the determination of the elementary steps of this reaction. Based on the studies of e.g. Rinnemo et al. [35], Nibbelke et al. [42] or Engel and Ertl [43], the following basic mechanism can be proposed:



In this model, the adsorption of CO and O₂ is considered to be competitive. There is only one type of active site on the surface catalyst on which CO and O molecules can adsorb. The oxygen is either irreversibly adsorbed on the surface of the catalyst [44] or can associatively desorb [45]. The CO₂ formed interacts only weakly with the surface [43,46]. Consequently, it can be considered that it desorbs instantaneously from the catalyst active site. This mechanism is the simplest one which can be envisaged for this reaction.

It will be shown in Chap. 6.2 that the simple mechanism presented here is not sufficient to explain the obtained experimental results under non-stationary temperature conditions. The introduction of a slower step with a characteristic time in the order of magnitude of the period duration is necessary. Such a step could be e.g. in the form of e.g. oxidation-reduction of the catalyst or surface restructuring as envisaged by Yuranov et al. [47] or van Neer et al. [48]. A more detailed discussion is presented in Chap. 6.2.

3. Experimental

To realize this work, the set-up built by Brandner [2] to exploit microstructure reactors under temperature instationary conditions has been reused. The most notable modification is the integration of a mass spectrometer to analyze the reaction gas mixture in addition to the existing Fourier Transform Infrared spectrometer. The following chapters mention only the most important characteristics of the experimental set-up. A very detailed description is given in [2]. Fig. 3.1 presents a flowchart of the experimental set-up final state and Fig. 3.2 shows a picture of the whole experimental set-up. The flow chart parts are described in the chapters 3.1 to 3.4.

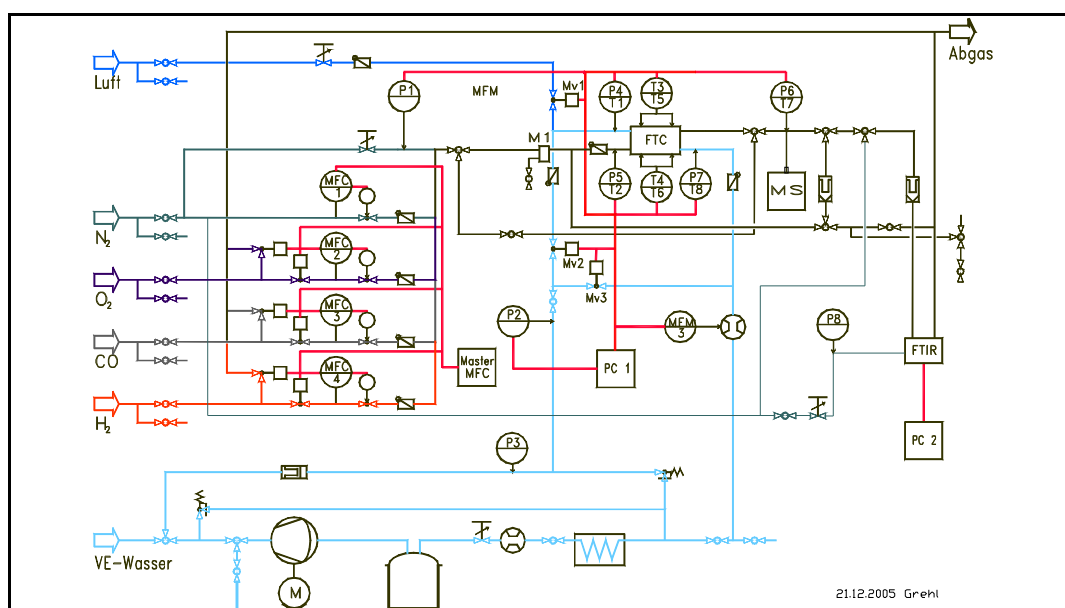


Fig. 3.1 Experimental set-up flow chart

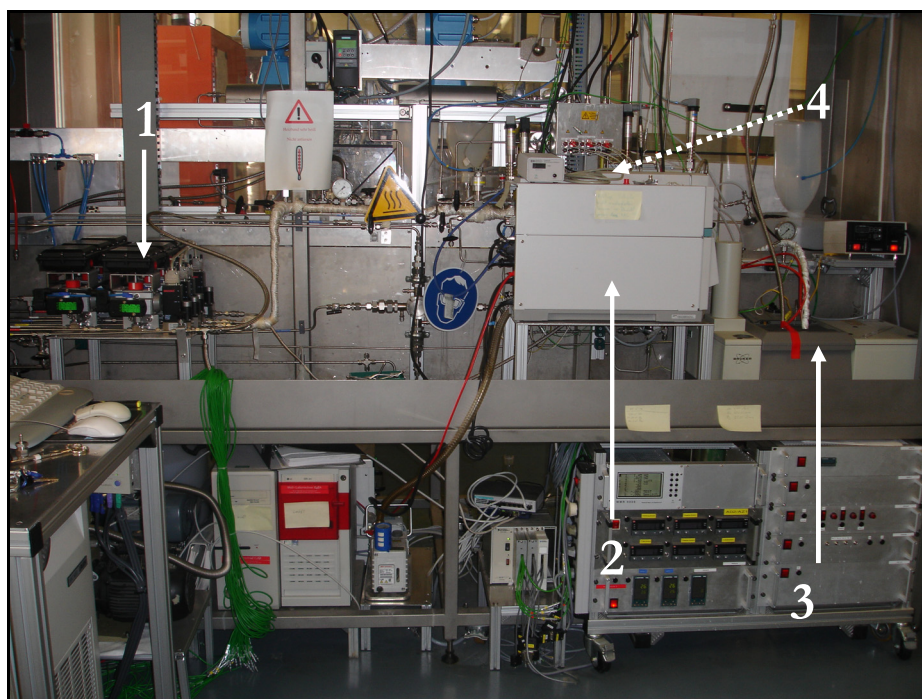


Fig. 3.2 Picture of the whole experimental set-up. It is: 1: security valves and mass flow controllers 2: Mass spectrometer 3: FTIR spectrometer 4: Microstructure reactor (hidden by the mass spectrometer)

This set-up is enclosed in a flowbox with metallic walls. The flowbox has a constant gas flow of $150 \text{ m}^3\cdot\text{h}^{-1}$ being pumped out, preventing the dissipation of any reaction gas in the laboratory if an accident should happen. In Fig. 3.2, the part of the experimental set-up where the microstructure reactor is situated is hidden by the mass spectrometer. Fig. 3.3 presents a more detailed picture where the microstructure reactor can be seen.

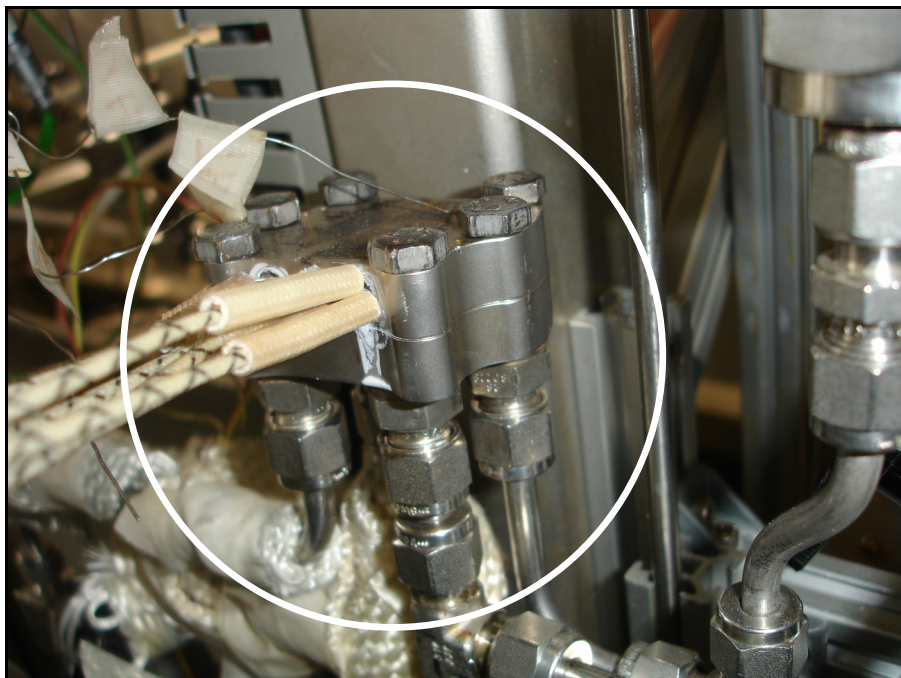


Fig. 3.3 Detailed view of the experimental set-up with the FTC-type 3 microstructure reactor

3.1. Microstructure reactor

Denoted by FTC on Fig. 3.1, this is the master piece of the experimental set-up. During this work, two different types of microstructure reactor have been used. The first one was specially designed for Fast Temperature Cycling experiments (FTC-reactor type 2). The second one was intended for material testing (FTC-reactor type 3) and has been modified to perform the CO oxidation reaction.

3.1.1. *FTC-reactor type 2*

The microstructure reactor FTC type 2 is an evolution of the type 1 presented in [2]. The modifications were realized in order to reduce the pressure drop inside the cooling part of the reactor and the maximal heating rate value. However, the reactor modified in such a way owns a nearly doubled mass and tripled external volume, which has a relatively bad influence on its thermal homogeneity (see Chap. 4.2.1).

The reactor is made of three stainless steel heating blocks providing eight holes for heater cartridges each and three holes for thermocouples. Three cooling plates and two reaction plates (described later in this chapter) are situated above and below the central heating plate. Two thin metallic cover plates are used for the bottom and the top of the microstructure reactor.

All the above mentioned plates are assembled by diffusion welding in a vacuum furnace. The technique is described in [15] in details. At the smallest side of the reactor (where the entry and exit for the gas and water are situated), four adapter pieces are fixed by electron beam welding. On these adapter pieces four standard screw fittings (Swagelok 6 mm) are welded. Fig. 3.4 shows an explosion drawing of a FTC microstructure reactor type 2 and Fig. 3.5 shows a picture of a FTC microstructure reactor type 2.

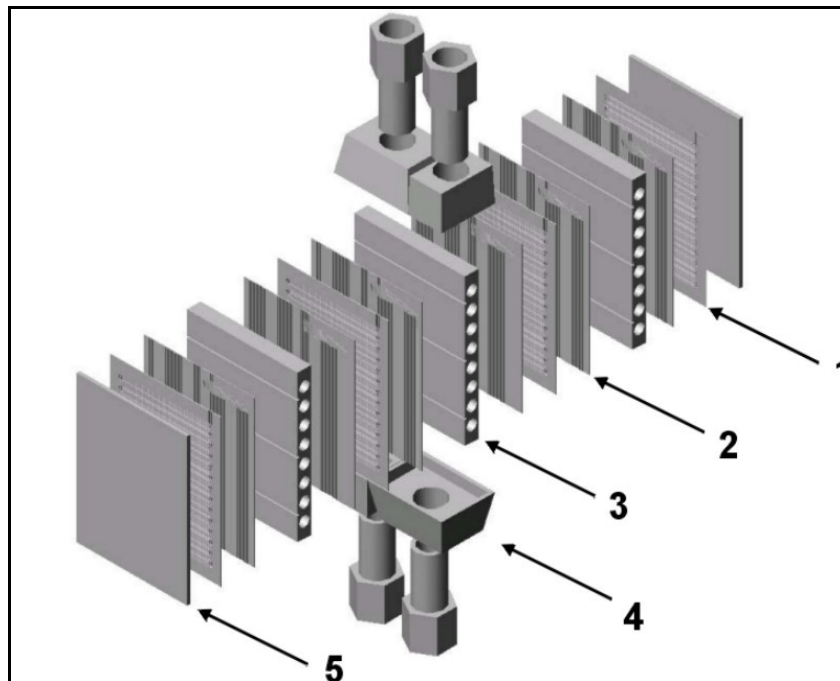


Fig. 3.4 Explosion drawing of a FTC microstructure reactor type 2 with 1: microstructure foil with reaction channels 2: microstructure foil with cooling channels 3: plate with heater cartridges holes 4: adapter 5: cover plate 6: channel for thermocouples.

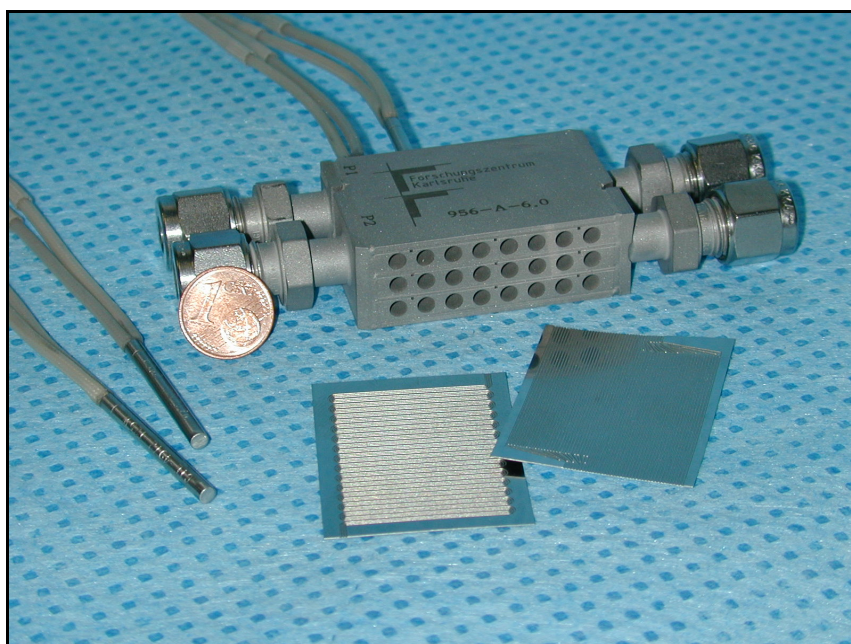


Fig. 3.5 Picture of a FTC microstructure reactor type 2. On the left, electrically powered heater cartridges used to permanently heat the device are shown. The foil in the centre is a reaction foil with meandric channels. The foil at the right is a cooling foil with linear channels. The device size is 44 mm x 33 mm x 17 mm (without adapters).

The microstructure reactor is continuously heated by electrically powered heater cartridges and periodically cooled with deionised water flowing through the cooling channels, as explained in Chap. 2.1.6.

The reaction foils are stainless steel foils 44 mm long, 33 mm wide and 0.2 mm thick, on which three meandric channels are wet chemically etched. The channels are 764 mm long, 0.32 mm wide and 0.13 mm deep. The total reaction volume given by the twelve channels is approximately 300 μl . Fig. 3.6 shows a picture of a reaction foil.

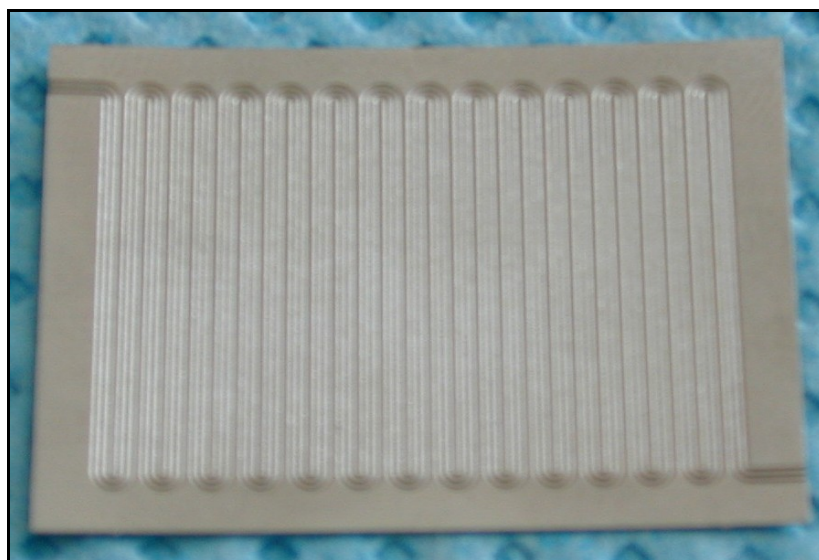


Fig. 3.6 Picture of a reaction foil with 3 wet chemically etched meandric channels. The foil is 44 mm long, 33 mm wide and 0.2 mm thick. The channels are 764 mm long, 0.32 mm wide and 0.13 mm deep

The advantage of the meandric design is to increase the length of the channels obtainable on the foil, and, therefore to increase the residence time within the reactor as well as the active surface. This increase will allow to get a non negligible conversion during the reaction despite the relatively high value of the gas flow used (between 100 and 300 $\text{ml}\cdot\text{min}^{-1}$ STP). The number of reaction foils (4) and channels per foil (3) is chosen to reduce the pressure drop generated in the channels. For a gas flow of 100 $\text{ml}\cdot\text{min}^{-1}$ (STP), the pressure drop decreases from 2.5 MPa for one foil with one channel to 0.19 MPa for four foils with three channels each (see [2] for details). Once all the parts of the reactor have been welded together, the reaction channels are coated with alumina and impregnated with platinum. The detailed coating and impregnating methods are given in Chap. 3.5.1.

The cooling foil has the same dimensions as the reaction foil. The channels are designed to allow the maximum of water to flow through while minimizing the pressure drop generated. Fig. 3.7 shows a picture of a cooling foil.

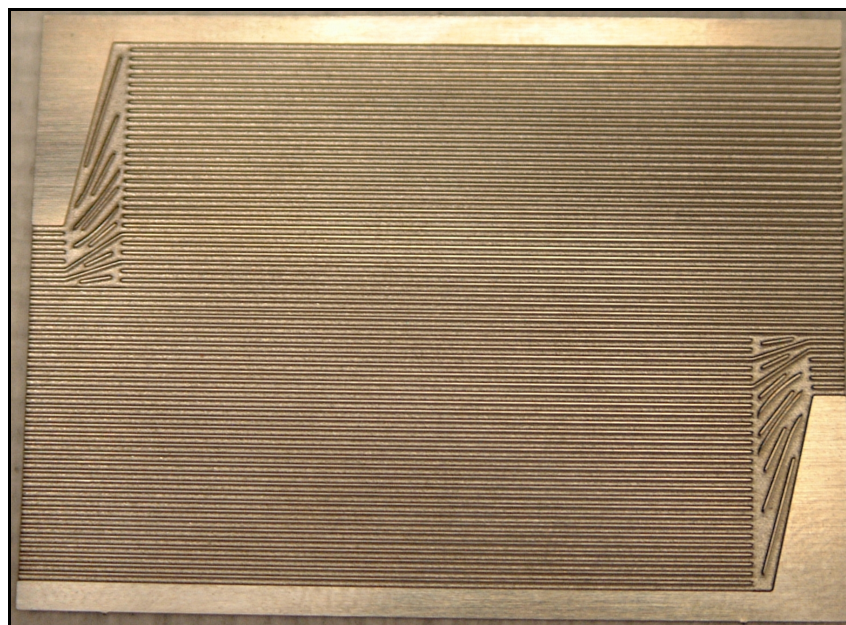


Fig. 3.7 Picture of a cooling foil.

3.1.2. FTC-reactor type 3

The FTC-reactor type 3 has been primarily designed for material testing. Some modifications were necessary to perform the CO oxidation reaction. This reactor consists mainly of two stainless steel plates fixed together with six bolts. In the bottom plate three holes for heater cartridges are drilled and a small square chamber (20 mm x 20 mm x 1mm) is machined on it. This chamber is thought to accommodate different material plates during the material testing experiments. The material type used to perform the CO oxidation reaction is a piece of sintered metal fibres (SMF) coated with alumina and impregnated with platinum (see Chap. 3.5.2 for details). The sintered metal fibres are forming a kind of metallic gauze through which the reaction gas flows. On the top plate microchannels are mechanically machined which allow the passage of a cooling water flow. The cooling channels are closed toward the reaction chamber by a blind foil welded on the plate after the channels machining. Four standard screw fittings (Swagelok 6 mm) are welded on the top plate to allow the connexion of the reactor with the gas and cooling water pipes. Fig. 3.8 shows an explosion drawing of the FTC-reactor type 3 and Fig. 3.9 shows a picture of the FTC-reactor type 3.

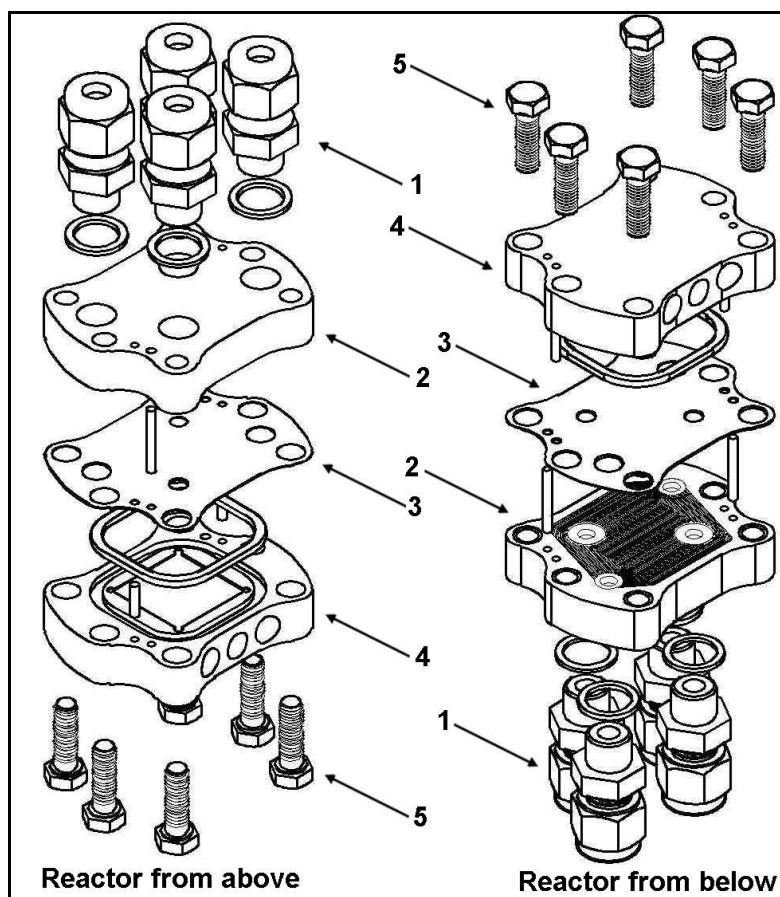


Fig. 3.8 Explosion drawing of the FTC-reactor type 3 with 1: Adapters 2: top plate with microchannels for the cooling passage 3: blind foil for closing the cooling microchannels 4: base plate with reaction chamber and holes for heater cartridges 5: tightening screws.

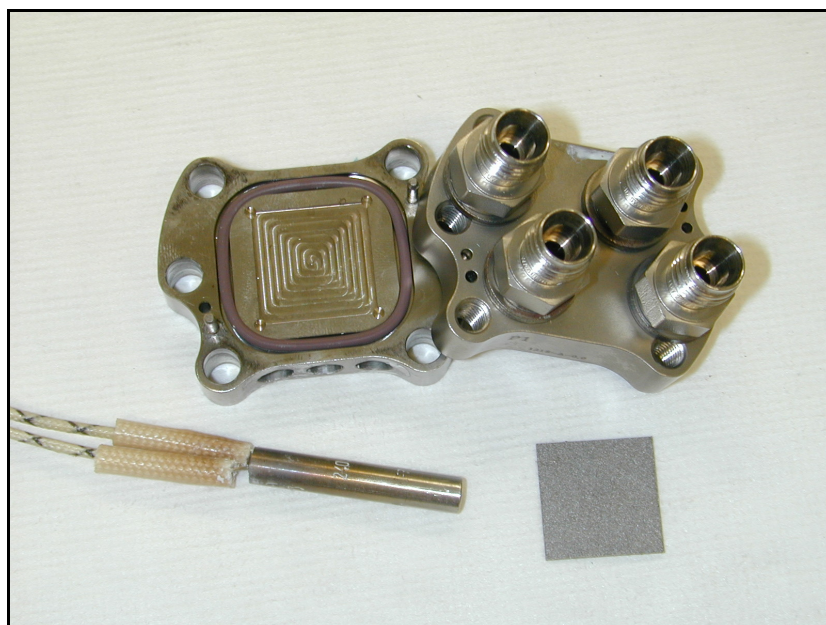


Fig. 3.9 Picture of the FTC-reactor type 3. Down left is a heater cartridge used to permanently electrically heat the device. Down right is a SMF plate coated with alumina and impregnated with platinum used to perform the CO oxidation. Once screwed together, the reactor device size is 35 mm x 35 mm x 21 mm (without adapters).

Down left on Fig. 3.9 one of the heater cartridges used to heat the device is shown. The grey foil down right is a piece of sintered metal fibres coated with alumina and impregnated with platinum used to perform the CO oxidation reaction. Fig. 3.10 presents a closer view of this plate and Fig. 3.11 a SEM picture of the structure of the SMF foil before the coating procedure.



Fig. 3.10 Picture of the metallic gauze piece which is placed in the reaction chamber to perform the CO oxidation. The piece size is 20 mm x 20 mm x 0.4 mm

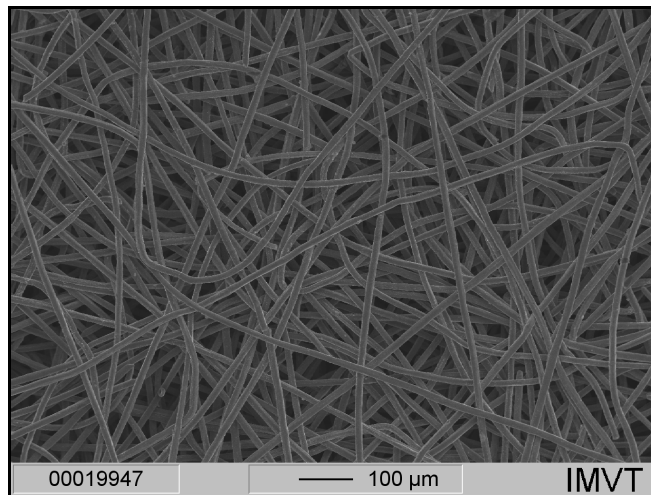


Fig. 3.11 SEM picture of the structure of the SMF foil with a 100 μ m scale.

The use of this type of material as a catalyst support as already been investigated by e.g. Yuranov et al. [49]. They used sintered metal fibres composites for the deposition of zeolites and tested the obtained catalytic active material using the benzene hydroxylation as a test reaction. The structure built by the single fibers shown in Fig. 3.11 is clearly of random type. This will have an influence on e.g. the residence time distribution as it will be shown in Chap. 5.1.1.

Due to the disposition of the gauze piece in the reaction chamber, the gas flow is flowing parallel to the weaving and not perpendicular. The temperature of the reactor is measured by two thermocouples introduced in the gas flow fittings and having their ends either pressed into the metallic gauze by the top plate or simply pressed on the surface of the SMF plate.

3.2. Experimental installation

3.2.1. Gas supply

The three reaction gases CO, O₂ and N₂ are taken from the central laboratory gas supply through pressure reducers and stainless steel pipes. A fourth line exists enabling the possibility to mix additionally H₂ (or other gases) to the reaction mixture to conduct e.g. the preferential oxidation reaction (PROX-reaction [50,51]) of CO in the presence of H₂. All the lines can be individually closed with ball valves. The three lines containing the reaction gases CO, O₂ and H₂ are connected with the pipe leading into the microstructure reactor and simultaneously with the exhaust gas pipe.

Six pneumatically driven switch-over valves are built in for the security of the experimental set-up. These valves are separated in two groups. The three ones in the reactor direction are of type “normally closed” while the other three in the exhaust gas direction are of type “normally open”. In case of a malfunction of the set-up this system prevents any reaction gas flowing further through the microstructure reactor.

The mass flow for all the four gases is controlled with mass flow controllers made by the Brooks company. These mass flow controllers are denoted by MFC1 to MFC4 on Fig. 3.1. A central mass flow control unit “Master MFC” of type Brooks WMR4008 is responsible for the regulation of the mass flow controllers. A no-return valve is situated after each mass flow controller for protection against a possible return of the reaction gas flow during operation. The different pipes come together through T-pieces and cross-pieces, providing a sufficient mixing of the different gases before they reach the microstructure reactor. The pressure sensor P5 and the thermocouple T2 measure the pressure and the temperature of the gas flow before the microstructure reactor, respectively. Before the addition of the mass spectrometer in the experimental set-up, the pressure sensor P6 and thermocouple T7 have measured the gas pressure and temperature directly at the reactor exit. This is not the case any more with the new set-up design. The two sensors are yet situated far away from the reactor and the measurements obtained, especially for the temperature, are consequently not of any relevance.

A filter situated behind the microstructure reactor blocks any particles which could arise from the catalyst layer and prevent them to go into the mass or infrared spectrometer.

Two by-passes are built in the experimental set-up. The first one avoids the reactor and goes directly into the exhaust pipe. The second one is a pipe connected directly before and behind the reactor. This second by-pass is used to effectuate calibration measurements while avoiding gas flowing through the reactor.

Two pipes related with the use of the infrared spectrometer have been added to the set-up. One is thought to purge the infrared spectrometer measurement room where the measurement cell is situated in order to get rid of the influence of the ambient CO₂. The second one is used to purge the pipe going into the FTIR spectrometer to realize a background measurement while keeping the reaction running in the reactor (see Chap. 3.4.1.2 for more details).

The gas is preheated before reaching the reactor by a heating coil wound around the gas pipe between the exit of the mass flow controllers (MFC1 to MFC4) and the entry of the reactor. The temperature of the heating coil could be varied in order to get the right gas temperature at the entry of the microstructure reactor. Typically, a heating coil temperature of 520 K is necessary to heat the gas to 400 K before the microstructure reactor.

3.2.2. Cooling water supply

The cooling of the microstructure reactor is assured by a cooling system consisting of two closed loops. The first one is designed to cool the microstructure reactor itself. This cooling loop is constituted by 50 litres of water pumped by a triple membrane pump. A frequency controller Micromaster S420 from Siemens controls the working frequency of the pump. The pump is furnished with a pulsation damper which prevents the apparition of undesirable pulsation in the experimental set-up. A metallic filter with a mesh width of 20 μm filters the potential solid particles present in the deionised water to avoid the blocking of the cooling foils microchannels.

Two overflow valves are incorporated in this cooling loop to protect it against working pressure above the value the loop was designed for. The first overflow valve opens at a pressure of 1.4 MPa, the second at 1.8 MPa. The overflow pipes are linked directly with the reservoir and any pushed-out water will run back into it, preventing any water to flow out of the experimental installation. A combination of the pneumatically driven and electronically controlled magnetic valve MV2 and MV3 direct the cooling water either through the cooling part of the microstructure reactor or in a by-pass. The MV2 valve is of type “normally closed” and the MV3 of the type “normally open”. If a problem occurs with the cooling cycle, the cooling water would only flow in the by-pass, preventing damages of the experimental set-up due to a possible too high working pressure. A no-return valve is situated in the pipe leading to the reactor cooling passage. This valve prevents the water or the steam which is produced during the cooling of the reactor to flow back in the direction of the pump.

A pipe ducting compressed air is additionally linked with this cooling loop. The compressed air is used to purge the channels of the cooling foils, as mentioned in Chap. 2.1.6. The pneumatically driven and electronically controlled magnetic valve MV1 controls the duration of the compressed air pulse programmed after each cooling period. A pulse duration of 200 ms has been found experimentally to be sufficient to purge the cooling microchannels efficiently from the residual water.

The second cooling loop is designed to cool down the water of the first cooling loop. This system is based on a mobile cooling unit Lauda W1400 with an integrated pump. This unit cools the water of the second loop to a temperature of approximately 280 K. The contact between the two water flows at different temperature is realized with a crossflow micro heat exchanger.

3.2.3. Voltage supply

An adjustable triple transformer power supply from the ELNA company is used for the electrical heating of the microstructure reactor. A control signal adjusts the position of a servo-motor which controls the grip position on three superposed iron core transformers. Each one of those

transformers is connected to one phase of a three-phase power connection and delivers a tunable voltage between 0 and 230 V DC with a maximal current of 10 A.

All the measurement sensors needing an external voltage supply are connected to a power source delivering a constant voltage of 24 V DC.

3.3. Measurements and control technology

The global control and analysis of the measurements and control electronics is based on a computer program developed in LabVIEW Version 6.1. This program has mainly been developed by Brandner during his doctoral work [2] and was improved in the work afterward.

3.3.1. Sensors

3.3.1.1. Temperature sensors

All the temperature sensors built into the experimental set-up are thermocouples of type K (NiCr/Ni combination with stainless steel mantle). Their working temperature range is from -200 to 800 K. The only difference between the thermocouples is the diameter of the external mantle and consequently their response time t_{90} (time necessary to reach 90% of the stable end-signal). The thermocouples used to measure the temperature of the microstructure reactor have an external mantle diameter of 0.5 mm and a t_{90} of 0.1 s. The temperature sensors are calibrated using a three point calibration curve using boiling water, sludge (ice-water mixture) and the ambient temperature measured with a mercury thermometer. The maximal tolerance of the thermocouples is 0.25% of the measured value what correspond to an absolute value of 2 K [2]. Moreover, it has been observed that even under perfectly stationary conditions the temperature recorded by the LabVIEW program was oscillating around a central value with an amplitude of approximately 1 Kelvin. This oscillation is due to the processing of the voltage given by the thermocouples [2]. Consequently, an absolute error of always 3 K will be taken as a realistic value for all the temperatures measured.

3.3.1.2. Pressure sensors

The pressure sensors used in the experimental installation are from the company Haenni, type ED 513/374.411/A35 with a measurement range from 0.0 to 2.0 MPa absolute pressure. The maximal deviation is 0.5% [2] of the measured value what corresponds to $5 \cdot 10^{-4}$ MPa in the range of pressure of concern.

3.3.1.3. Mass flow controllers

The mass flow controllers installed in the experimental set-up are from Brooks Instrument, type 5850S. The mass flow used for the carrier gas, O₂ and H₂ are calibrated ex factory for N₂ and the one used for CO is directly calibrated for CO. The mass flow controllers are calibrated ex factory for the diverse mass flow ranges (STP) used for the different gases during the experimental measurements. In order to increase the precision of the gas flow controlled by the mass flow controllers, new calibration curves have been realized on site before starting with the experimental measurements. These calibration measurements have been effectuated using a bubble column. The resulting calibration curves are presented in Appendix A. The error calculation for the gas flow controllers is presented in details in Appendix D. The relative uncertainty on the regulated gas flow is situated between 2 and 10 % of the measured absolute value. The mass flow controllers are controlled by a central control unit (called Master MFC in Fig. 3.1) from Brooks Instrument, type WMR4008.

3.4. Analytics

To analyze the reaction species concentration, Fourier Transform Infrared Spectrometry (FTIR) and the Mass Spectrometry (MS) are used. Those two methods are chosen for there relatively short reaction time which makes it possible to analyze fast variations of reaction species concentrations quasi-online or online.

3.4.1. Fourier Transform Infrared Spectrometry (FTIR spectrometry)

The FTIR spectrometer is mentioned as “FTIR” in Fig. 3.1. The device incorporated in the experimental installation is a Vector 22 from Bruker Optik GmbH. This spectrometer works with a Helium-Neon-laser emitting at a wavelength of 633 nm. The spectrometer is operated with the program OPUS 4.2® which enables the recording and the integration of the measured spectra. Alternatively, a LADTGS (L-Alanin doped deuterated Triglyzinsulphate or a MCT (Mercury Cadmium Tellurid) detector can be used. The MCT detector is the most sensitive and fast one but has to be cooled with liquid nitrogen. With the LADTGS detector it is possible to take a whole infrared spectrum approximately every 5 seconds while keeping the resolution at 8cm⁻¹. The MCT detector enables to measure till 8 scans per second, but the duration of each measurement series is then limited to 10 minutes by the size of the acquisition processor which cannot exceed 16 MB.

3.4.1.1. General theory of the FTIR spectrometry

The objective of this chapter is not to develop the whole theory and principles of the FTIR spectroscopy but to give an overview of the method used. Detailed explanations can be found for example in Guenzler et al [52] or in Gottwald et al [53].

The most important restriction of the infrared spectrometry is that this method is limited to substances which are infrared active. If the molecules of the substance do not absorb in the infrared region, this substance will be infrared transparent and will not be detected. While CO and CO₂ are well infrared active, this is not the case for O₂ (due to the symmetry of the oxygen molecule). This leads to the consequence that when using the FTIR method for the concentration measurements of the reaction species no calculation of mass balances is possible and the yield of the reaction has to be calculated based only of the CO and CO₂ concentration.

The infrared measurements are realized in a temperature controlled gas cell TGC-S10 from Harrick Scientific Corporation with KBr windows. The windows are sealed with Kalrez O-rings which are capable to withstand temperatures close to 570 K. This gas cell has a 10 cm optical pathlength with a volume of 17 ml and a body made entirely of stainless steel. The spectrometer is installed in the experimental installation in a way that the whole reaction gas flow is passing through the measurement cell.

Since the goal is to measure fast variations of concentration, it is necessary for the gas flow to be not too small in order to renew the gas volume present in the cell sufficiently fast. If that is not the case, the measurements taken will consist of a mean of different concentrations. Online monitoring is necessary if it is wished to resolve the concentration oscillations with respect to the time. If this type of measurement is not feasible, an integral measurement of the species concentration during a certain time period, when temperature oscillations are applied, can equally give a basis of comparison toward the thermal stationary conditions. However, the online monitoring of the concentration is the only way to investigate the effect of temperature cycling on a catalytic reaction in details. With a reaction gas flow of 300 ml·min⁻¹, the total volume of the cell is renewed approximately every 3.5 seconds. If the flow conditions within the cell are considered being of “plug flow” type, neglecting a possible mixture of the gas inside the cell, the measured concentrations can be considered being “instant concentrations”. In order to avoid the adsorption of CO on the cell walls, the cell is heated to a temperature of 350 K. This temperature is high enough to minimize the adsorption of CO while avoiding any undesirable further reaction of CO with oxygen after the gases left the microstructure reactor. The pressure inside the measurement cell is almost atmospheric, independently of the gas flow passing through.

In Fig. 3.12, a typical infrared absorbance spectrum measured between 2400 cm⁻¹ and 1800 cm⁻¹ for CO and CO₂ is shown.

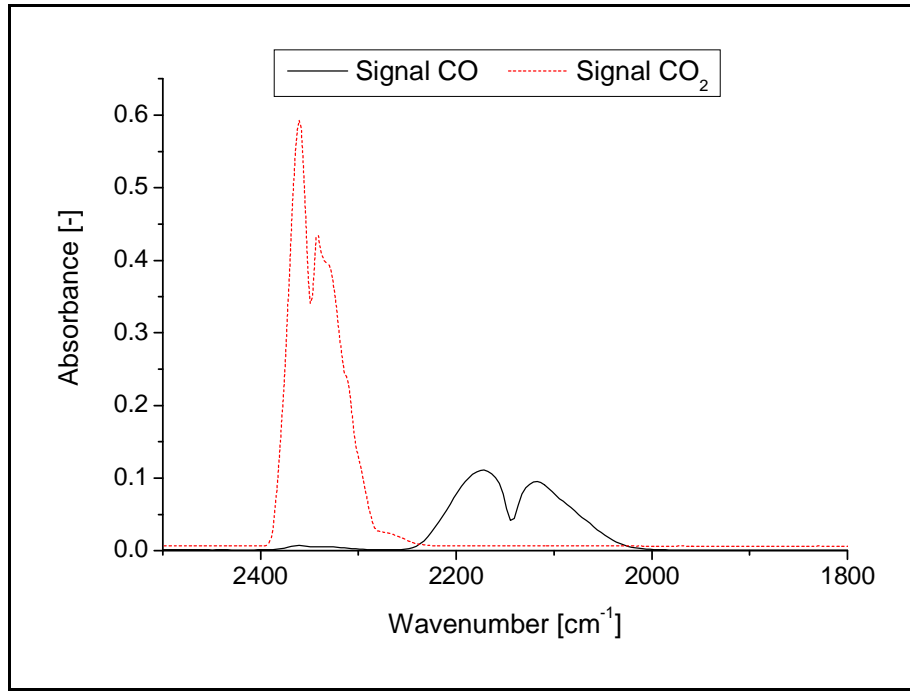


Fig. 3.12 Infrared spectrum of CO and CO₂

The plain line in Fig. 3.12 is the infrared spectrum obtained for a mixture of 5 % CO in N₂ and the dotted one for a mixture of 1% CO₂ in N₂ at a gas flow value of 300 ml·min⁻¹. The infrared range is limited to the area where CO and CO₂ are mainly active. Outside of this domain, no other peaks are useable for the determination of the composition of the reaction gas mixture considered during this work. As it can be seen in Fig. 3.12, the CO and CO₂ peaks are sufficiently well separated. They can consequently be used to determine the concentration of these two gases in a gas mixture. Gaseous water absorbs strongly only above 3000 and below 2000 cm⁻¹ [54] and has consequently no noticeable influence in the wavelength range of interest.

The Lambert-Beer law is the basis to calculate a species concentration based on its infrared absorbance spectrum. The Lambert-Beer law describes the dependence of a sample absorbance toward the sample layer thickness d , the absorption coefficient ε of the species and its concentration c . After passing through the sample, the initial radiation intensity I_0 is weakened to an intensity I :

$$I = I_0 \cdot e^{-\varepsilon \cdot c \cdot d} \quad \text{Eq. 3.1}$$

Eq.3.1 is normally, for practical use, transformed into a logarithmic form:

$$-\log\left(\frac{I}{I_0}\right) = \varepsilon \cdot d \cdot c \quad \text{Eq. 3.2}$$

By defining the absorbance as:

$$\text{Asb} = -\log\left(\frac{I}{I_0}\right) \quad \text{Eq. 3.3}$$

the Lambert-Beer can be written in its most common and simplified form:

$$Asb = \varepsilon \cdot d_1 \cdot c \quad \text{Eq. 3.4}$$

Eq. 3.1 to 3.4 contain the parameter ε , known as extinction coefficient. Because this parameter is influenced during the measurement by different factors like the scattered light or the emission radiation, a direct calculation of this factor is practically not realized. Instead of this, because the measurements are normally done with a constant sample layer thickness (or optical path) and today's spectrometers can give an absorbance spectrum directly as a measurement result, it is possible to describe the dependence of the absorbance toward the concentration empirically with a calibration curve of the form:

$$Asb = p \cdot \text{concentration} + b \quad \text{Eq. 3.5}$$

The linear dependence between the concentration and the absorbance is valid if the mixture containing the adsorbing species is not too concentrated. A quantitative analysis is performed best on bands where the absorbance peak is less than 0.7 [55].

To realize the calibration curves for CO and CO₂, different mixtures of gases containing different vol% of CO or CO₂ mixed with N₂ have been prepared using the mass flow controllers and measured under the same temperature, pressure and flow conditions as the reaction ones are. The absorbance "Asb" of a species can be calculated with different methods using the same adsorption spectrum. It is possible for example to either integrate the surface situated under the curve between two fixed wavenumbers, to take the maximal intensity of the peak between two fixed wavenumbers or to take the intensity of the signal at a fixed wavenumber. For this work, it has been chosen to use the intensity of the absorbance spectrum at a wavenumber of 2358 cm⁻¹ for CO₂ and 2170 cm⁻¹ for CO. The calibration curves measured and calculated for CO and CO₂ are given in Appendix B.

As it can be seen in Fig. 3.12, the CO₂ molecule absorbs much more IR radiation than the CO molecule. For a CO₂ concentration five times smaller than the CO concentration, the measured CO₂ absorption signal is five times higher. Due to this difference, smaller variations of the CO₂ concentration will have a greater influence on the signal measured than variations of CO, but the measured signal reaches the saturation level at much smaller concentration. For the reasons mentioned in [52] or [55], absorbance values larger than 0.9 will not be considered for the evaluation of the concentration. Consequently, using the FTIR spectrometer, it is only possible to measure a CO₂ concentration which does not exceed approximately 1.8 % (v/v).

3.4.1.2. FTIR spectrometry stability problem

During the first measurements realized using the FTIR spectrometer it appeared that the measured CO₂ signal was not constant with respect to the time, even if the regulated concentration in the gas

flow was maintained constant. This signal deviation is due to the presence of CO_2 in the ambient air at a concentration which is not totally stable. If many people are present in the laboratory, the ambient CO_2 concentration will slightly increase due to their breathing and the related reject of CO_2 . At the contrary, during e.g. the lunch break, less people are present in the laboratory and the ambient CO_2 concentration will drop.

Due to the configuration of the spectrometer, the laser beam has to travel from the source to the measurement cell and from the measurement cell to the detector through a certain length of ambient air. The measurement is then influenced by the ambient CO_2 concentration. This influence is normally eliminated by taking a background spectrum. However, if the background CO_2 concentration is changing during a measurement, the background taken at the beginning will not be valid at the end of the measurement. The attempts to purge the room where the measurement cell is situated in order to remove completely the ambient CO_2 were not successful. The chosen practical solution consists in periodically by-pass the measurement cell and to replace the flux containing the reaction products with a flux of pure N_2 (infrared inactive) and to take a new background spectrum. Two three way valves situated between the reactor and the measurement cell allow to keep the reaction running in the reactor while purging the measurement cell. If the time between two purges is below one hour, the variation in the ambient CO_2 concentration is supposed to be linear and this correction curve is subtracted from the measured CO_2 concentration.

Fig. 3.13 presents the measured CO_2 absorption for a constant CO_2 concentration without correction (squares) and after the correction with the background evolution (points).

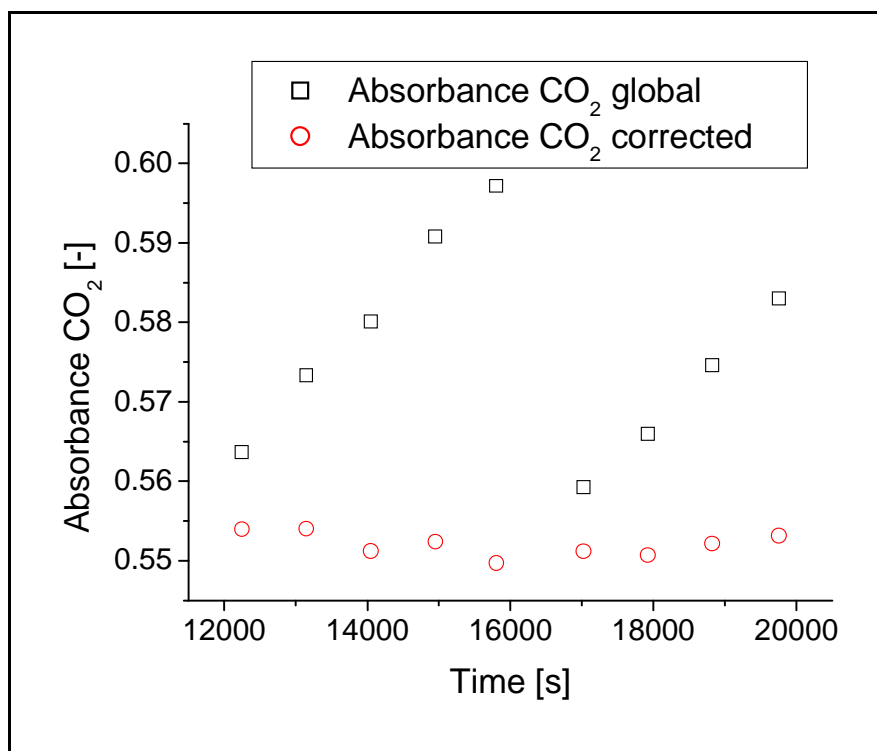


Fig. 3.13 CO_2 absorbance for a constant CO_2 concentration without correction (squares) and after the correction of the background evolution (points).

Fig. 3.13 clearly shows that the global CO₂ absorption increases with the time although the concentration of CO₂ in the gas mixture passing through the cell is maintained constant. This increase is due to the above mentioned variation of the CO₂ concentration in the ambient air and almost disappears when the correction method is applied.

To purge the measurement cell of all the reaction gas for taking a new background spectrum it is necessary to wait approximately 1 minute after having switched to the gas flow of pure N₂.

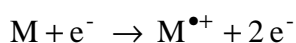
3.4.2. Mass spectrometry (MS spectrometry)

The mass spectrometer is mentioned as “MS” in Fig. 3.1. The device incorporated in the experimental set-up is a 5973Network Mass Selective Detector from Agilent Technologies. It was operated in the electron ionization mode. The device contains three main important parts: a heated electron-ionization ion source, a heated hyperbolic quadrupole mass filter and a high energy dynode (HED) electron multiplier detector. The mass spectrometer was originally designed to work together with a gas chromatograph and its use as a stand alone measurement device has been related with some major problems (see Chap. 3.4.2.2 and 3.4.2.3 for details).

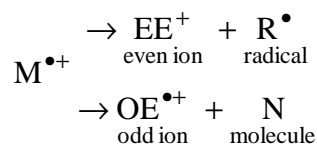
3.4.2.1. General theory of the mass spectrometry

The purpose of this chapter is not to develop the whole theory of the mass spectrometry but only to present the basic principles of this measurement method and mention the purpose of the main components built in the mass spectrometer incorporated in the experimental set-up. Very detailed information about the principles and applications of mass spectrometry can be found in e.g. [56].

In contrast to the FTIR spectrometry, the mass spectrometry is not limited to the detection of certain compounds. The difference is that this method is not based on the absorption of a radiation but on the ionization of the molecules to be detected. The method chosen in the case of this work was the electron ionization. In this case, the electrons used to ionize the molecules in the electron ionization source are produced by a heated filament and accelerated through an anode. This ionization method works fine for gas phase molecules but provokes an intensive fragmentation due to the high energy of the electrons produced. Since the molecules to be detected in the case of this work (CO, O₂ and CO₂) are relatively small and uncomplicated (e.g. non-branched), an extensive fragmentation is not a point of concern. Gas phase ions of the compounds of interest are formed following the path.



The molecular ion $M^{\bullet+}$ then generally splits up in primary product ions:



These primary product ions may also split up and so forth. All these ions are separated in the mass spectrometer by the quadrupole mass filter based on their mass to charge ratio. The detection relative to their abundance is assured by the HED electron multiplier detector. The result obtained is the mass spectrum of the molecule. A typical mass spectrum recorded for a mixture of approximately 4.5 % CO, 0.5 % CO₂ and 25 % O₂ is presented in Fig. 3.14.

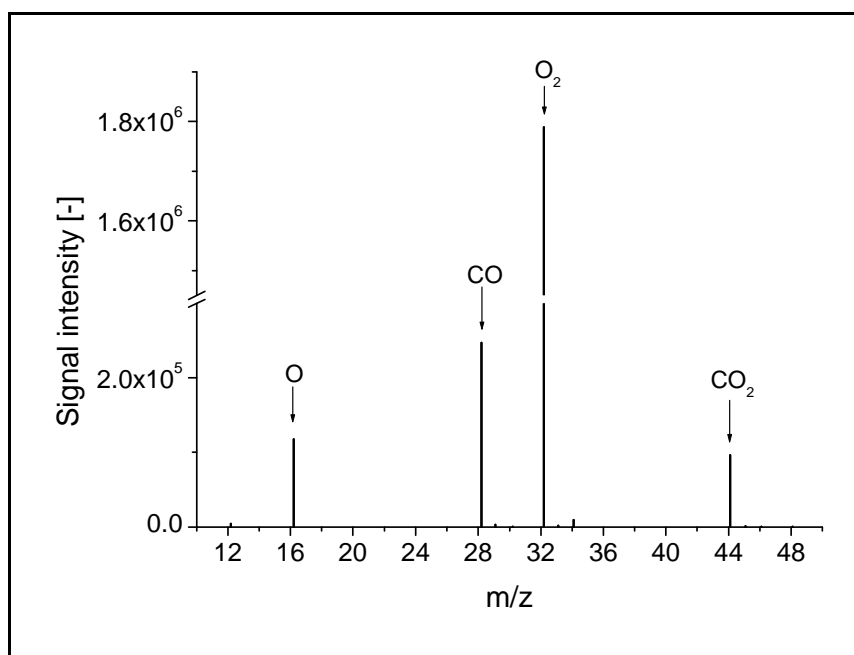


Fig. 3.14 Mass spectrum of 4.5 % CO, 0.5 % CO₂ and 25 % O₂ obtained by electronic ionization

The peak at m/z 32 and 44 are the molecular ions of oxygen and carbon dioxide. The peak at m/z 28 originates mainly from the molecular ion of carbon monoxide but a part of it results of the decomposition of the molecular ion of carbon dioxide. However, it may be seen in [54] that the signal intensity of this secondary ion amounts only approximately 10% of the primary one. Its contribution to the peak at m/z 28 may thus be neglected for the small CO₂ concentration (between 0 and 2%) encountered during this work. The signal at m/z 16 originates mainly from the decomposition of the molecular ion of oxygen and to a small part from the decomposition of the carbon dioxide molecular ion. Based on the signal intensity of the peak at m/z 28, 32 and 44, it is normally possible to calibrate the mass spectrometer using different known concentrations of CO, O₂ and CO₂. However, due to the stability problems mentioned in Chap. 3.4.2.3 it has not been possible to realize a calibration for all the three species. A calibration method has only been found for CO₂ and is described in details in Chap. 3.4.2.3.

3.4.2.2. Development of an inlet setup for the mass spectrometer

As mentioned at the beginning of this chapter, the mass spectrometer used was originally designed to work connected with a gas chromatograph. In this configuration, the end of the chromatographic column was linked with the mass spectrometer inlet and the totality of the gas flow went directly into the mass spectrometer ionization chamber. To make possible the use of the mass spectrometer as a stand alone online measurement device, it was necessary to find a way to link the mass spectrometer with the gas flow pipe directly at the outlet of the reactor. The mass spectrometer working pressure is situated between $2 \cdot 10^{-3}$ and $4.7 \cdot 10^{-5}$ Pa (helium pressure) and a working gas flow between 1 and $2.4 \text{ ml} \cdot \text{min}^{-1}$. The developed inlet set-up should consequently introduce a very high pressure drop between the atmospheric pressure at the reactor outlet and the high vacuum present inside the mass spectrometer. At the same time, the inlet set-up should not introduce any time delay or deform the shape of the concentration changes happening in the main gas flow. For this reasons, the use of e.g. a simple segment of a chromatographic column (even uncoated) as transition piece was not possible.

After some investigations, the use of an orifice plate as the pressure reducer medium, derived from an idea of Quaade et al. [57, 58], was found to be a good solution. The schematic diagram of the developed set-up is shown in Fig. 3.15.

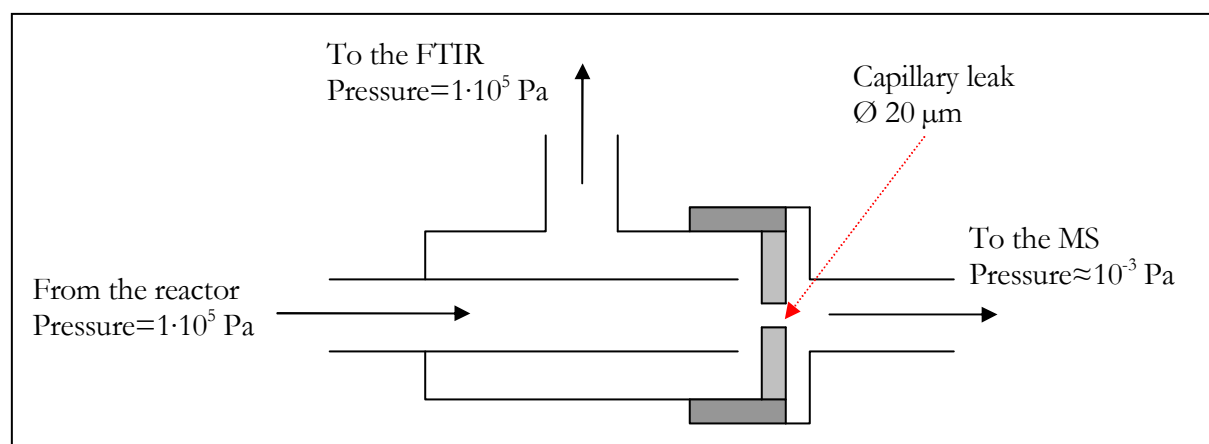


Fig. 3.15 Schematic diagram of the developed mass spectrometer inlet set-up

A very small part of the gas flow is flowing through the capillary leak in the mass spectrometer while the rest (being always at atmospheric pressure) is directed further to the measurement cell of the infrared spectrometer. It is thus possible to measure the gas phase concentration using simultaneously the mass spectrometer and the FTIR spectrometer.

Fig. 3.16 presents a picture of the developed set-up. Fig. 3.17 shows the orifice plate used to reduce the pressure from atmospheric to high vacuum.

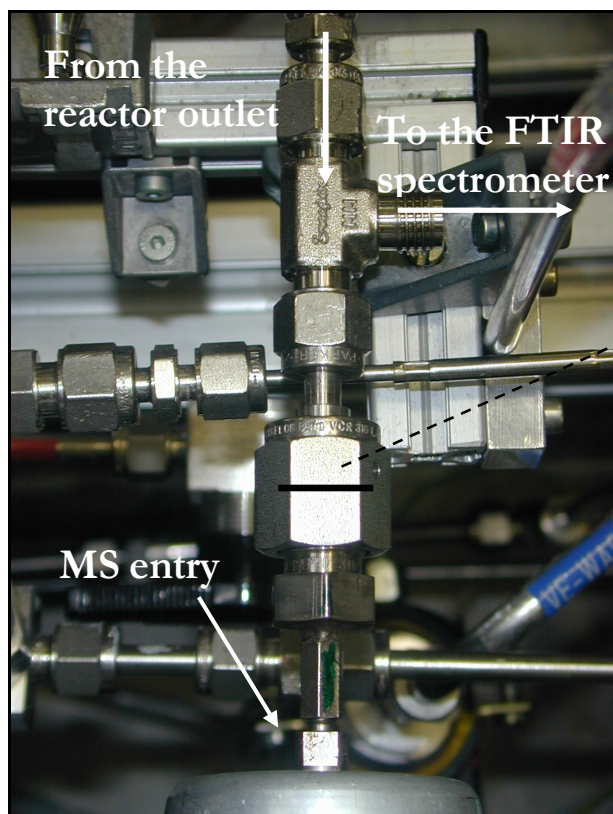


Fig. 3.16 Picture of the developed mass spectrometer inlet set-up

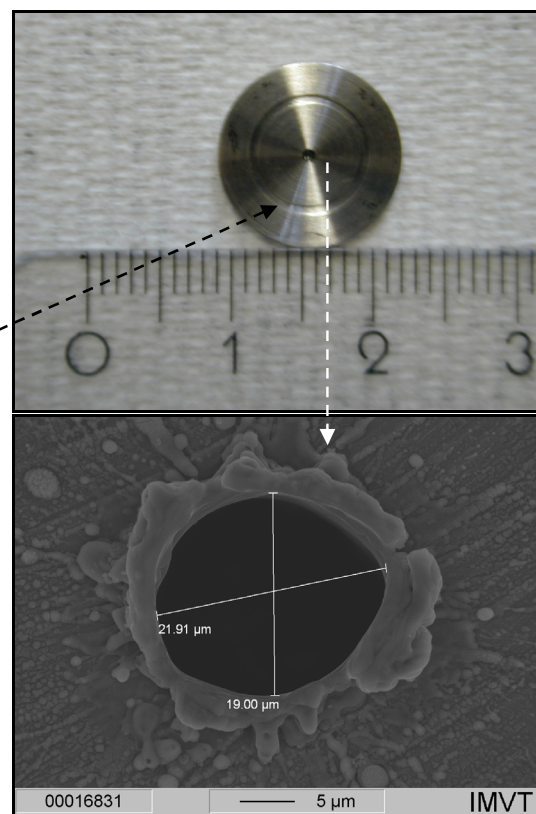


Fig. 3.17 Picture of the orifice plate inserted in the inlet set-up (above) with the laser-drilled capillary leak (below)

The pressure reducing system shown in Fig. 3.16 is made of a VCR pressure screw with a 1/16" nut (for capillary column) welded onto the male part. The interface of the MS is the male part of a pressure screw for a capillary column (1/16"). The airtightness between the pressure reducing system and the MS is realized with a ferrule and a small capillary (2 cm long). The pressure drop between atmospheric pressure and high vacuum is realized using the aperture plate shown in Fig. 3.17. The capillary leak laser-drilled on the aperture plate has a diameter of approximately 20 μm and a length of 100 μm . The pressure inside the mass spectrometer was controlled using the 59864B Gauge Controller from Agilent Technologies.

According to Quaade et al. [58], it is possible to pre-estimate the molar gas flow which will flow through the capillary leak by knowing the pressure at the inlet and at the outlet. In this case, the pressure at the capillary inlet is atmospheric and at the outlet approximately 10^{-3} Pa. At ambient temperature (298 K) and $1.013 \cdot 10^{-5}$ Pa the mean free path " λ " for He is $1.93 \cdot 10^{-7}$ m [59]. The obtained ratio d_{ca}/λ of 52 and 103 for leak diameters values of 10 and 20 μm indicates that the flow inside the leak is of intermediate type and the Knudsen equation allows the calculation of the flow through the capillary leak [57, 59]:

$$\dot{n}_{\text{He}} = \frac{P_{\text{inlet}} - P_{\text{outlet}}}{R \cdot T} \cdot \frac{\pi}{128} \cdot \frac{\bar{P} \cdot d_{\text{ca}}^4}{\eta_{\text{He}} \cdot L_{\text{ca}}} + \frac{1}{3} \cdot \sqrt{2 \cdot \pi} \cdot \frac{d_{\text{ca}}^3}{\varpi(T) \cdot L_{\text{ca}}} \cdot \frac{1 + d_{\text{ca}} \cdot \varpi(T) \cdot \bar{P} / \eta_{\text{He}}}{1 + 1.24 \cdot d_{\text{ca}} \cdot \varpi(T) \cdot \bar{P} / \eta_{\text{He}}} \quad [\text{mol} \cdot \text{s}^{-1}] \quad \text{Eq. 3.6}$$

where $\bar{P} = (P_{\text{inlet}} + P_{\text{outlet}}) / 2$ corresponds to the mean between the inlet and outlet pressure of the capillary leak, η_{He} is the viscosity of helium and $\varpi(T) = \sqrt{M_{\text{He}} / (R \cdot T)}$. The subscribe “ca” indicates the characteristics of the capillary leak (diameter “d” and length “L”).

The results presented in Tab. 3.1 are obtained for molar and volumetric flow of helium through the capillary leak for different diameters and leak lengths.

Diameter [μm] / Length [μm]	Molar flow He [mol·s ⁻¹]	Volumetric flow He [ml·min ⁻¹]
<i>20 / 100</i>	<i>5.76·10⁻⁶</i>	<i>8.5</i>
20 / 200	4.67·10 ⁻⁷	4.26
10 / 100	2.88·10 ⁻⁶	0.7

Tab. 3.1 Molar and volumetric flow of He through the capillary leak calculated for different diameters and lengths at a temperature of 300 K and a pressure of 1.013·10⁵ Pa

It may be seen in Tab. 3.1 that the volumetric flow theoretically calculated using the capillary leak characteristics (italic bold numbers) of the orifice plate used in the inlet set-up exceeds the working gas flow of the mass spectrometer which should not exceed 2 ml·min⁻¹ based on the manufacturer recommendations. To further reduce the flow, it would be necessary to change the leak characteristics. The most effective parameter is the diameter. Dividing it by a factor of two diminishes the flow by a factor of ten where doubling the leak length only halves it. According to Tab. 3.1, a leak with a diameter of 10 μm and a length of 100 μm would be ideal regarding to the mass flow flowing in the mass spectrometer. However, all attempts to laser-drill such a hole were not successful.

Since a better appropriate capillary leak was not available, the mass spectrometer has been operated under these non-ideal conditions. The mass spectrometer principally works but the too high gas flow introduces a signal stability problem which is explained in Chap. 3.4.2.3

3.4.2.3. MS spectrometer stability problem

Despite all the attempts to build an adequate inlet set-up for the mass spectrometer, the operating flow conditions were not completely adequate. This had a bad influence on the stability of the mass spectrometer signal. Ideally the signal recorded for a given concentration of a species should be independent from the composition of the mixture. For example, the signal intensity recorded at

m/z 28 for a mixture of 5 vol% CO and 95 vol% Ar and for a mixture of 5 vol% CO, 5 vol% O₂ and 90 vol% Ar should be identical since the relative concentration of CO does not change. The situation is different in the case of the mass spectrometer used here. Test measurements realized using the above mentioned mixtures have been realized and an example of the results obtained is presented in Fig. 3.18.

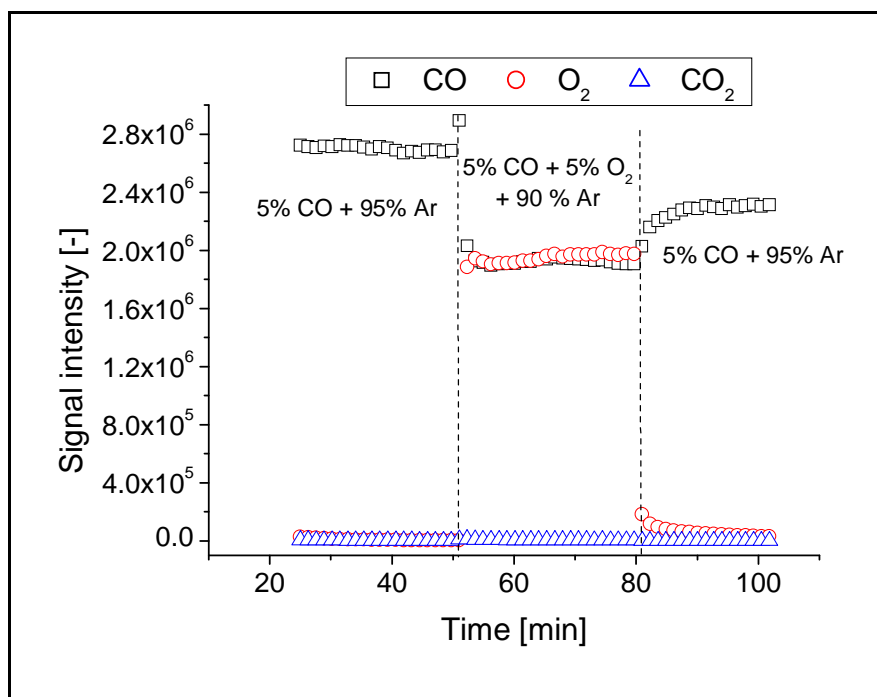


Fig. 3.18 Mass spectrometer signal intensity for CO (m/z 28) (squares), O₂ (m/z 32) (circles) and CO₂ (m/z 44) (triangles) depending from the mixture composition

The squares in Fig. 3.18 represent the signal recorded by the mass spectrometer for an m/z ratio of 28 (CO), the circles an m/z ratio of 32 (O₂) and the triangles an m/z ratio of 44 (CO₂). From 25 to approximately 50 minutes a mixture containing 5 vol% CO and 95 vol% Ar has been measured using the mass spectrometer, from 50 to 80 minutes a mixture containing 5 vol% CO, 5 vol% O₂ and 90 vol% Ar and from 80 to 100 minutes the same mixture as at the beginning. Since the relative CO concentration did not change, the signal intensity for m/z 28 should remain stable independently from the mixture composition. It is clearly to see in Fig. 3.18 that this is not the case. At the moment where oxygen is introduced into the mixture, the signal intensity at m/z 28 decreases. The “disappearance” of CO can not be attributed to the reaction of CO with O₂ to produce CO₂ since no signal at m/z 44 is detected. Moreover, even when the mixture composition is switched back to the initial one, the signal intensity for CO did not reach its original value anymore.

The problem probably results from the too high mass flow which enters the mass spectrometer ionization chamber. In a normal case, the fraction of molecules ionized remains constant so that a given concentration always results in an identical signal, independently of the mixture composition.

In the present situation, since much more molecules enter the ionization chamber, the ionization source is influenced by the mixture composition and is not able to maintain the fraction of ionized molecules constant. It is e.g. thinkable that a strongly oxidative species like oxygen may react with the heated filament of the source and reduce its ionization capacity.

The consequence of the dependence of the signal intensity both with respect to the concentration of the species of interest and with the mixture composition is that it is not possible to calibrate the mass spectrometer in a straightforward way for CO, O₂ and CO₂. Calibration measurements realized using e.g. different mixtures of CO in Ar would lose their validity for mixtures where O₂ and CO₂ are present as in the case of the reaction mixture.

A partially satisfactory solution has been found to calibrate the mass spectrometer for CO₂ in order to get a possibility of comparison to the results obtained with the FTIR spectrometer. The catalytic CO oxidation reaction has been conducted under stationary conditions and concentration measurements were realized with both the FTIR and the mass spectrometer. The CO₂ concentration has been first estimated based on the FTIR measurements. The calculated CO₂ concentration values have then been correlated with the corresponding mass spectrometer signal intensity. This results in a kind of “secondary” calibration curve.

The difference to standard calibration methods as the one used for the FTIR spectrometer is that the other components present during the reaction are also in the calibration mixture. It is reasonable to suppose that these components will influence the ionization capacity of the source approximately in the same way under stationary and non-stationary thermal conditions. Thus calibration measurements are keeping their validity. The limitation of this method is that it is based on a concentration calculated already using another calibration curve (the FTIR spectrometer one) and is accordingly less reliable. The calibration curve determined is presented in Appendix C.

3.4.3. Response time characterization for the FTIR and mass spectrometer

The objective of the mass spectrometer integration in the experimental set-up is to enhance the concentration measurement rate to obtain a better time resolution of the concentration oscillations generated by the cycling of the temperature. To compare the performance of the FTIR and the mass spectrometer, the determination of the response time of both devices is an important parameter. For this purpose a concentration step down of CO₂ has been realized in the gas flow, and the evolution of the recorded signals has been compared. The experimental set-up utilized during this work is not designed to produce sharp concentration changes, and its modification for this purpose is too complicated. To produce the concentration step necessary for the determination of the response time of the two spectrometers, a gas flow of 100 ml·min⁻¹ with 25 vol% O₂, 5 vol% CO, the rest being He, was sent through the reactor heated to 460 K. At this temperature,

approximately 1 vol% CO₂ was produced. The temperature of the reactor was then quenched down within 3 seconds to a temperature where no more CO₂ was produced (400 K). The obtained decrease in the CO₂ concentration is the fastest concentration change obtainable in the experimental set-up used. An example of the results obtained is shown in Fig. 3.19.

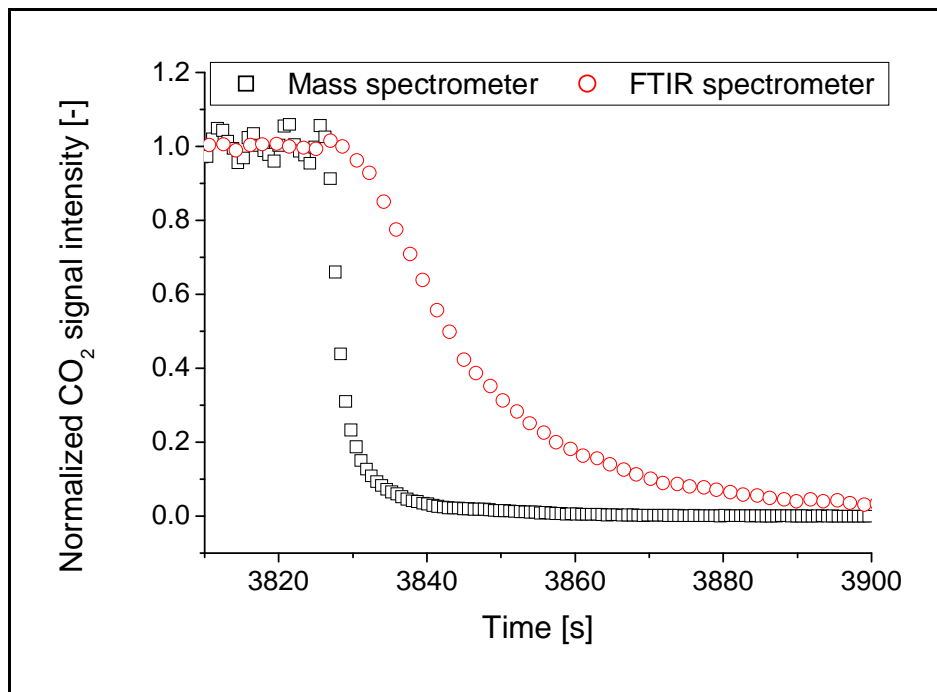


Fig. 3.19 Evolution of the normalized CO₂ signal intensity recorded by the FTIR and mass spectrometer after a CO₂ concentration step down in the gas flow

The squares in Fig. 3.19 represent the signal intensity of CO₂ measured with the mass spectrometer and the circles with the FTIR spectrometer. The comparison of the shape of the two plots obtained shows clearly that the response of the two spectrometers to a concentration step is different. The mass spectrometer responds much faster compared to the FTIR spectrometer. If the response time “ t_{50} ” is defined by the necessary time for the signal to reach 50% of its final value and “ t_{90} ” by the time to reach 90%, values presented in Tab. 3.2 are obtained.

	t_{50} [s]	t_{90} [s]
FTIR spectrometer	15	45
Mass spectrometer	1	4

Tab. 3.2 Response time t_{50} and t_{90} of the FTIR and mass spectrometer to a CO₂ concentration step

The calculated t_{50} and t_{90} for the FTIR spectrometer are between 3 and 4 times longer compared to the ones of the mass spectrometer. Based on the t_{90} calculated, the FTIR spectrometer is able to properly resolve concentration oscillations with a period duration of approximately 90 seconds where the minimal period duration is 8 seconds for the mass spectrometer. Concentration oscillations with a period duration of 30 seconds will be already smoothed to 50% by the FTIR

spectrometer where it is necessary to go down to 2 seconds for the mass spectrometer. Beside the stability problem mentioned in Chap. 3.4.2.3, which may be solved by a modification of the developed inlet set-up, the mass spectrometer is thus better suited to follow online concentration changes generated by the fast periodic variation of the reactor temperature.

3.5. Catalyst preparation and characterization

The catalyst used to effectuate the catalytic CO oxidation is platinum supported on alumina. This catalyst has already been widely experimentally investigated and it is considered as having a good activity towards the CO oxidation reaction, acceptable long term stability and being relatively straightforward to prepare. The method used to prepare the alumina support layer is sol-gel coating of the metallic surface following by wet impregnation of the alumina layer by a platinum solution to deposit the active metal. The detailed procedure and experimental conditions are presented in Chap. 3.5.1 for the FTC-reactor type 2 and in Chap. 3.5.2 for the FTC-reactor type 3.

3.5.1. *FTC reactor type 2*

As mentioned in Chap. 3.1.1, in the case of the FTC reactor type 2 the reaction microchannels are coated once the reactor was fully assembled by diffusion bonding. For this purpose, a sol-gel solution containing approximately $0.55 \text{ mol}\cdot\text{l}^{-1} \text{ Al}_2\text{O}_3$ was pumped through the reaction passage in order to fill the microchannels. The meandric form of the reaction microchannels (presented on Fig. 3.6) prevents the solution from simply going through the channels by placing the reactor vertically and makes the pumping necessary.

The whole reactor is then overnight dried at 340 K, heated from room temperature to 770 K at $3 \text{ K}\cdot\text{min}^{-1}$ and calcinated at 770 K for 5 hours. Platinum is then deposited on the porous alumina layer using the wet impregnation method. Therefore, an aqueous solution of $0.05 \text{ mol}\cdot\text{l}^{-1} \text{ Pt}(\text{NO}_3)_2$ is introduced into the channels and the drying and calcinating steps are repeated under the same conditions as for the alumina coating.

The reduction of the platinum is effectuated by heating the reactor from room temperature to 770 K at $10 \text{ K}\cdot\text{min}^{-1}$ under a gas flow of $1 \text{ l}\cdot\text{min}^{-1}$ Ar flowing through the channels, keeping the temperature at 770 K for 2 hours under $0.5 \text{ l}\cdot\text{min}^{-1} \text{ H}_2$ (0.5 vol%) in Ar and cooling down to room temperature under Ar ($1 \text{ l}\cdot\text{min}^{-1}$).

As mentioned in Chap. 2.1.5, the coating of the microchannels in an assembled reactor does neither allow to measure the surface by BET or checking the quality of the surface of the alumina layer nor to determine the concentration of platinum deposited by a standard chemisorption method. The only way to control how good the channels have been coated is to cut the microstructure reactor in slices perpendicular to the channels. This implies the destruction of the microstructure reactor and can in this case consequently not be applied.

3.5.2. FTC-reactor type 3

In the case of the FTC-reactor type 3, the metallic gauze used can be coated by alumina (Al_2O_3) and impregnated with platinum before being placed in the reaction chamber of the reactor. For this purpose, the Sintered Metal Fibers (SMF) plate (60 x 100 x 0.4 mm) is firstly calcinated at 1170 K for 8 hours. The alumina support layer is prepared by impregnation of the fibers in a aqueous sol [25] containing 3 wt.% Al_2O_3 , drying the fibers plate at room temperature and calcinating it at 770 K for 3 hours in air. The coating operation is repeated three times to ensure a sufficient coverage of the metal fibers. The deposition of platinum is realized by impregnation of the support with an aqueous H_2PtCl_6 solution (1.25 wt. %) followed by drying at room temperature and calcination at 770 K for 3 hours in air. All these operations have been realized at the EPFL by A. Iouranov. The obtained catalyst consists of 0.5 wt.% Pt on 5 wt.% Al_2O_3 deposited on the SMF plates.

Fig. 3.20 and Fig. 3.21 present SEM pictures of the detailed structure of the SMF foil shown in Fig. 3.10 before and after the coating with alumina and impregnation with platinum.

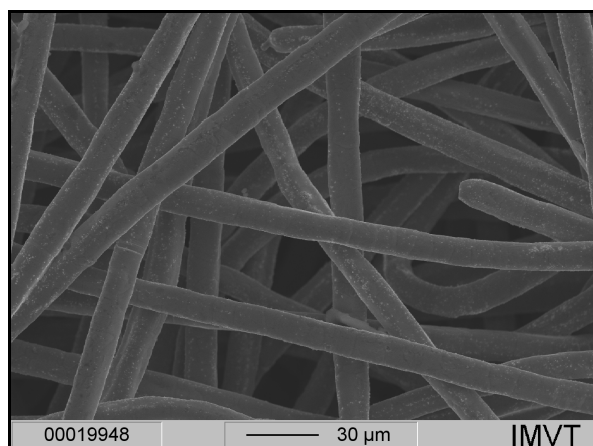


Fig. 3.20 SEM picture of the fibers of a SMF foil before the coating procedure (30 μm scale)

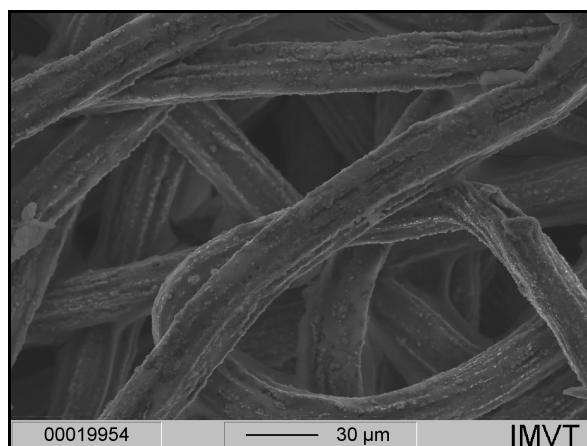


Fig. 3.21 SEM picture of the fibers of a SMF foil after the coating procedure (30 μm scale)

The comparison between Fig. 3.20 and Fig. 3.21 shows that the coating procedure was efficient. The filaments diameter in Fig. Fig. 3.21 is larger due to the alumina coating formed around them. The SEM pictures give, however, no accurate information about the quality of the obtained coating. For this purpose, nitrogen physisorption and hydrogen chemisorption measurements have been realized using a Z10/97-Autosorb-1-C apparatus from Quantachrome GmbH. The physisorption experiments allow to determine the surface of the alumina coating deposited on the fibers of the SMF foil. The chemisorption is used to determine the number of active sites present and the metal dispersion obtained.

The results obtained are given in Tab. 3.3.

BET surface [$\text{m}^2 \cdot \text{g}_{\text{Al}_2\text{O}_3}^{-1}$]	BET surface [$\text{m}^2 \cdot \text{g}_{\text{SMF}}^{-1}$]	Active surface [$\text{m}^2 \cdot \text{g}_{\text{SMF}}^{-1}$]	Metal dispersion [%]
248.2	13.7	4.04	16.36

Tab. 3.3 BET and chemisorption results obtained for the coated SMF foil

The metal dispersion obtained signifies that 16.36% of the platinum deposited on the fibres of the SMF foils is active for a catalytic reaction. This value corresponds approximately with the one mentioned in [60] for a Pd/Al₂O₃ catalyst deposited on sintered metal fibres in the same manner.

3.6. Reactants and chemicals

All the gases were delivered by Messer Griesheim, Germany:

Gas	Purity
Carbon monoxide	99.97 %
Oxygen	99.998 %
Nitrogen	99.996 %
Carbon dioxide	99.995 %
Helium	99.996 %
Argon	99.999 %

The other chemicals used for the catalyst coating of the FTC-type 2 reactor were:

Compounds	Purity	Supplier
Al(OC ₄ H ₉) ₃	≥ 97 %	Merck Schuchardt OHG, Hohenbrunn, Germany
Isopropanol	≥ 99.5 %	Carl Roth GmbH, Karlsruhe, Germany
Acetylacetone	≥ 98 %	Fluka Chemie AG, Buchs, Switzerland
HNO ₃	≥ 65 %	Fluka Chemie AG, Buchs, Switzerland
Pt(NO ₃) ₂	57.50 % Pt	ChemPur Feinchemikalien und Forschungsbedarf GmbH, Karlsruhe, Germany

4. Experimental results: FTC-reactor type 2

Chap. 4 presents the experimental results obtained using the FTC-reactor type 2.

4.1. Flow characterisation

The determination of the flow characteristics (e.g. residence time distribution and flow type) inside the reactor is important as they may have an influence on the behaviour of the studied catalytic reaction. This chapter presents both the experimental measurements realized for the characterization of the flow conditions inside the FTC-reactor type 2 and theoretical calculations effectuated.

4.1.1. *Experimental determination of the flow characteristics*

The experimental determination of the residence time distribution in a reactor is based on the introduction of a tracer into the system and on the measurements of the changes in the shape of the function between the entry and the exit of the system. The tracer must not modify the physical properties of the system (e.g. same viscosity and density) and the injection must not disturb the hydrodynamic conditions. The injection function of the tracer is generally of a known type, like a step or a pulse function.

A detailed theory about residence time distribution measurements may be found e.g. in [61,62], but it is anyway necessary to define some parameters for the comprehension of the following equations.

The mean residence time: τ [s]

The dimensionless time: $\Theta = \frac{t}{\tau}$ [-]

If the dimensionless curve $F(t)$ for the tracer is defined by:

$$F(t) = \frac{C(t)}{C_0} \quad \text{Eq. 4.1}$$

in the particular case of a step function where at $t = 0 \Rightarrow C(t=0) = C_0$

the residence time distribution function $E(t)$ is:

$$E(t) = \frac{dF}{dt} \quad \text{Eq. 4.2}$$

The mean residence time may be determined based on the curve F using:

$$\tau = \int_0^{\infty} t \cdot E(t) dt = \int_0^1 t dF \quad \text{Eq. 4.3}$$

Since the measurements points are normally taken at regular Δt intervals, it is practically simpler to integrate with respect to the time:

$$\tau = \int_0^1 t \, dF = - \int_0^1 t \cdot d(1 - F) = \int_0^\infty (1 - F) \, dt \quad \text{Eq. 4.4}$$

or, with individual points :

$$\tau \cong \sum (1 - F_i) \cdot \Delta t_i \quad \text{Eq. 4.5}$$

In [61, 62], different theoretical plots are illustrated for an ideal plug-flow tubular reactor, an ideal continuous stirred tank reactor and a real reactor with non-ideal flow.

The response curve of the microstructure reactor was measured by switching between a feed of pure nitrogen and a nitrogen feed containing ~ 5 vol.% Ar as tracer. Thus, the inlet function corresponds to a “step” type. To be sure that the hydrodynamic conditions were identical for the two different feeds, the flow rate of each feed was measured prior to each experiment with a soap-bubble column and set to $18.5 \text{ ml} \cdot \text{min}^{-1}$. The concentration of argon was determined every 60 ms by mass spectrometry. The temperature of the reactor was room temperature (20°C) and the pressure was atmospheric (0.099 MPa). A schematic diagram of the experimental set-up used for the measurements is presented in [63] page 62.

To differentiate the effect of the microstructure reactor from the effect of the set-up used for the measurements (tubes, valve, connexions, etc...), the same step function has been performed prior to each experiment without the microstructure reactor connected to the system. Fig. 4.1 presents a typical set of F functions obtained experimentally with the setup only (squares) and with the microstructure reactor connected to the setup (circles):

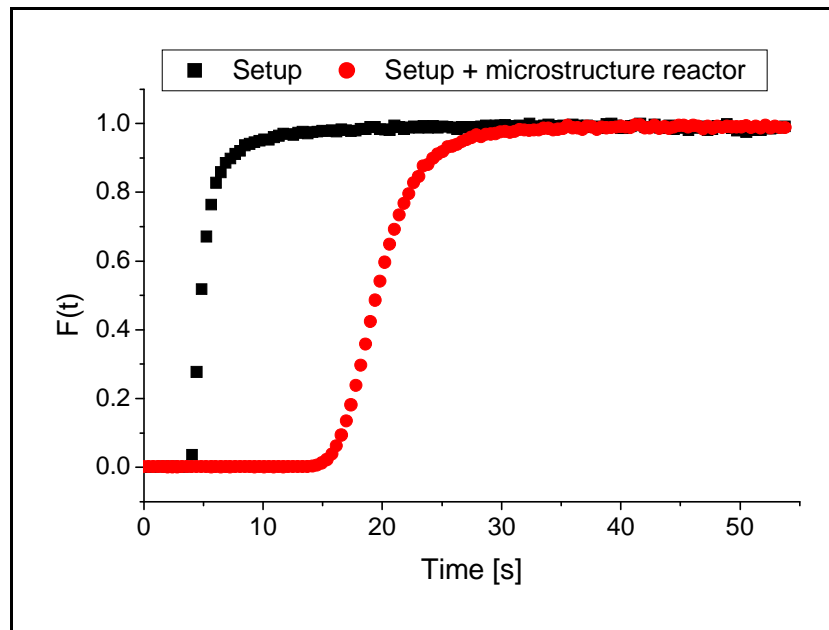


Fig. 4.1 Experimental curves of the residence time distribution of the set-up (squares) and of the set-up with the microstructure reactor connected (circles)

The experimental residence is calculated using the curves presented in Fig. 4.1 and Eq. 4.5. The experimental mean residence time in the whole microstructure reactor (gas connections and microchannels) τ_{reactor} is calculated from the difference between the mean residence time in the setup and the mean residence time in the setup with the microstructure reactor connected.

The experimental curves F allow not only to calculate the mean residence time in the microstructure reactor but also the Bodenstein number (Bo) which characterizes the type of flow inside the reactor. A. Rouge developed during his PhD thesis a simulation program which predicts the response of a closed tubular reactor to an injection of arbitrary shape [64]. This simulation program may be used to fit the experimentally obtained F curve and obtain the corresponding Bodenstein number for the reactor. A copy of the program is presented in Appendix E. The definition of the Bodenstein number is presented in the Chap. 4.1.2. It is sufficient to mention here that a high value of the Bodenstein number (about 100) is an indication that the flow characteristics tend toward a “plug flow” type.

The values presented in Tab. 4.1 are obtained for the experimental mean residence time in the whole microstructured reactor (τ_{reactor}) and the Bodenstein number:

Residence time τ_{reactor} [s]	Bodenstein number [-]
14.4 ± 0.14	110 ± 1

Tab. 4.1 Experimental values of the residence time and Bodenstein number for the FTC-type 2 microstructure reactor

The result for the residence time distribution seems to show that the microstructure reactor behaves like a tubular reactor open to dispersion [61]. The high Bodenstein number value calculated indicates that the axial dispersion is very low. The residence time value was in this case measured with a gas flow of $18.5 \text{ ml}\cdot\text{min}^{-1}$ STP. Under the experimental conditions for the reaction, the total gas flow will be $300 \text{ ml}\cdot\text{min}^{-1}$. This gas flow is 16.2 times higher than the gas flow use during the residence time measurement. If one postulates that the flow conditions stay identical, the measured residence time has consequently to be divided by 16.2 and the effective residence time amounts 0.89 seconds.

4.1.2. Theoretical calculations of the flow characteristics

Using a feed flow rate value of $300 \text{ ml}\cdot\text{min}^{-1}$ (STP) and the channel dimensions given in Chap. 3.1.1, it is possible to calculate a theoretical mean residence time τ_{channels} for the microchannels only:

$$\tau_{\text{channels}} = \frac{\text{channel volume}}{\text{flow rate}} = 0.06 \quad [\text{s}] \quad \text{Eq. 4.6}$$

There is an important size discrepancy between the experimental residence time for the whole microstructure reactor and the residence time in the microchannels only. This difference originates

from the fact that the main volume in the microstructure reactor is built by the gas connexions and the entry chambers and not by the microstructured channels. Since the reaction is taking place only in the microchannels coated with the catalyst, the mean residence time during which the reaction will take place is not the experimental residence time but the one calculated theoretically. It is unfortunately not possible to determine experimentally the mean residence time inside the microchannels only. It is thus necessary to rely on the theoretically calculated value.

Beside the calculation of the theoretical mean residence time, it is also possible to calculate a theoretical Bodenstein number in order to compare it with the one determined experimentally. The Bodenstein number can be theoretically calculated for a circular channel using Eq. 4.7, introducing the Peclet number Pe [65].

$$Bo = Pe \cdot \frac{L}{d_t} \quad [-] \quad \text{Eq. 4.7}$$

$$\begin{aligned} \text{with} \quad L &= \text{length of the channel} & [m] \\ d_t &= \text{diameter of the channel} & [m] \end{aligned}$$

The Peclet number is defined by Eq. 4.8.

$$Pe = \frac{\bar{u} \cdot d_t}{D_{ax}} \quad [-] \quad \text{Eq. 4.8}$$

$$\begin{aligned} \text{with} \quad \bar{u} &= \text{fluid mean linear velocity in a channel} & [m \cdot s^{-1}] \\ d_t &= \text{diameter of the channel} & [m] \\ D_{ax} &= \text{axial dispersion coefficient} & [m^2 \cdot s^{-1}] \end{aligned}$$

Since the microchannels present inside the reactor are not circular but elliptic, the diameter of the channel “ d_t ” in Eq. 4.7 and Eq. 4.8 will be approximated using a hydraulic diameter “ d_h ” defined by:

$$d_h = 4 \cdot \frac{A_c}{p_{ch}} \quad [m] \quad \text{Eq. 4.9}$$

$$\begin{aligned} \text{with} \quad A_c &= \text{cross section of a channel} & [m^2] \\ p_{ch} &= \text{perimeter of a channel} & [m] \end{aligned}$$

For a circular channel, the Peclet number in turn can be calculated using Eq. 4.9 [65].

$$\frac{1}{Pe} = \frac{1}{Re \cdot Sc} + \frac{Re \cdot Sc}{192} \quad [-] \quad \text{Eq. 4.10}$$

The Reynolds number is calculated using Eq. 4.10.

$$Re = \frac{\rho \cdot \bar{u} \cdot d_h}{\mu} \quad [-] \quad \text{Eq. 4.11}$$

$$\begin{aligned} \text{with} \quad \rho &= \text{density of the fluid} & [kg \cdot m^{-3}] \\ \bar{u} &= \text{fluid mean linear velocity in a channel} & [m \cdot s^{-1}] \\ d_h &= \text{hydraulic diameter of a channel} & [m] \\ \mu &= \text{viscosity of the fluid} & [Pa \cdot s] \end{aligned}$$

The Reynolds number varies together with the temperature because if the temperature increases the density of the gas decreases and at the same time the viscosity increases.

The Schmidt number is a ratio between two characteristic properties of a fluid and is defined by:

$$Sc = \frac{\mu}{\rho \cdot D_{12}} = \frac{\nu}{D_{12}} \quad [-] \quad \text{Eq. 4.12}$$

with

μ	=	viscosity of the fluid	[Pa·s]
ρ	=	density of the fluid	[kg·m ⁻³]
ν	=	kinematic viscosity	[m ² ·s ⁻¹]
D_{12}	=	component diffusion coefficient	[m ² ·s ⁻¹]

The values for the viscosity and density of the fluid at 1 bar and different temperatures (300, 375 and 460 K) are taken from the NIST Chemistry WebBook [66]. Values for the diffusion coefficient can be found in the literature for binary mixture only, for example N₂-CO or N₂-O₂. The reactant mixture which is considered here is a tertiary mixture (N₂-O₂-CO), but given that N₂ is the major component and the different diffusion coefficient values for the different gases are quite equivalent, only the binary diffusion coefficient $D_{N_2-O_2}$ and D_{N_2-CO} will be considered. The values of the diffusion coefficient at different temperatures and a pressure of 1.013 bar are taken from the CRC Handbook of Chemistry and Physics [67].

Temperature [K]	D_{N_2-CO} [m ² ·s ⁻¹]	$D_{N_2-O_2}$ [m ² ·s ⁻¹]
293.15	$2.08 \cdot 10^{-5}$	$2.02 \cdot 10^{-5}$
373.15	$3.36 \cdot 10^{-5}$	$3.07 \cdot 10^{-5}$
473.15	$4.91 \cdot 10^{-5}$	$4.62 \cdot 10^{-5}$

Tab. 4.2 Diffusion coefficient for CO and O₂ in N₂ at different temperatures

No values have been found in the literature for diffusion coefficient at a temperature of 300, 375 and 460 K. For the calculations using Eq. 4.12 the values for the diffusion coefficients have been approximated using the values presented in Tab. 4.2 for the temperature of respectively 293.15, 373.15 and 473.15 K. Tab. 4.3 presents the value of the Schmidt number calculated at different temperatures.

Temperature [K]	Schmidt number for CO	Schmidt number for O ₂
300	0.68	0.79
375	0.69	0.78
460	0.67	0.74

Tab. 4.3 Schmidt number for O₂ and CO for different temperatures

Using Eq. 4.7 to Eq. 4.12, and the values presented in Tab. 4.2 and Tab. 4.3, it is now possible to calculate a theoretical value of the Bodenstein number for the microstructured channels. Since the Schmidt number is only slightly dependant on the temperature or the species considered (as it can be seen in Tab. 4.3), a mean value of 0.73 has been taken for the calculation of the Peclet number using Eq. 4.9. As already mentioned, due to the half-elliptic shape of the microstructured channels, the hydraulic diameter “ d_h ” defined in Eq. 4.11 has been substituted for the channel diameter “ d_t ” in Eq. 4.7 and Eq. 4.8.

The values calculated for the Reynolds number, Peclet number and Bodenstein number for three different temperatures are given in Tab. 4.4.

Temperature [K]	Reynolds number [-]	Peclet number [-]	Bodenstein number [-]
300	137	1.88	8535
375	93	2.73	12380
460	65	3.73	16944

Tab. 4.4 Reynolds, Peclet and Bodenstein number for three different temperatures

The values calculated theoretically for the Bodenstein number are clearly above 100. Consequently, the flow in the channels is of “plug flow” type. The theoretical results are confirming the experimental measurements for the whole microstructured reactor. The real value of the Bodenstein number for the channels only will be situated between the value measured experimentally for the whole microstructure reactor ($Bo = 110$, see Chap. 4.1.1) and the values calculated theoretically presented in Tab. 4.4.

4.2. Thermal characterization

Before realizing experimental measurements with the CO oxidation, the pure thermal behaviour of the reactor under temperature cycling conditions has been studied.

4.2.1. *Temperature profile under temperature cycling conditions*

Under stationary thermal conditions, the temperature profile within a microstructure reactor is relatively homogeneous. It becomes, however, rather inhomogeneous under temperature cycling conditions. Using a thermographic camera, Brandner [2] demonstrated that the cooling of a type 1 reactor is not symmetrical. The parts of the reactor near the gas inlet and outlet are not actively cooled and can not follow too fast temperature oscillations. Their temperature remains in this case more or less constant which results in a kind of temperature low pass filter. Léger [68] measured the temperature profile of a specially developed microstructure reactor. This reactor was similar to the type 2 reactor presented in Chap. 3.1.1 but slightly higher (26.5 mm vs. 17.5 mm) in order to give the possibility to incorporate up to 32 thermocouples instead of the 16 available in the type 2

reactor. Léger [68] found temperature differences of up to 50 K between two points inside the device. It was thus necessary to determine the temperature profile developing inside the microstructure reactor type 2 before performing the CO oxidation. For this purpose, the 16 thermocouples were inserted into the device as shown in Fig. 4.2.

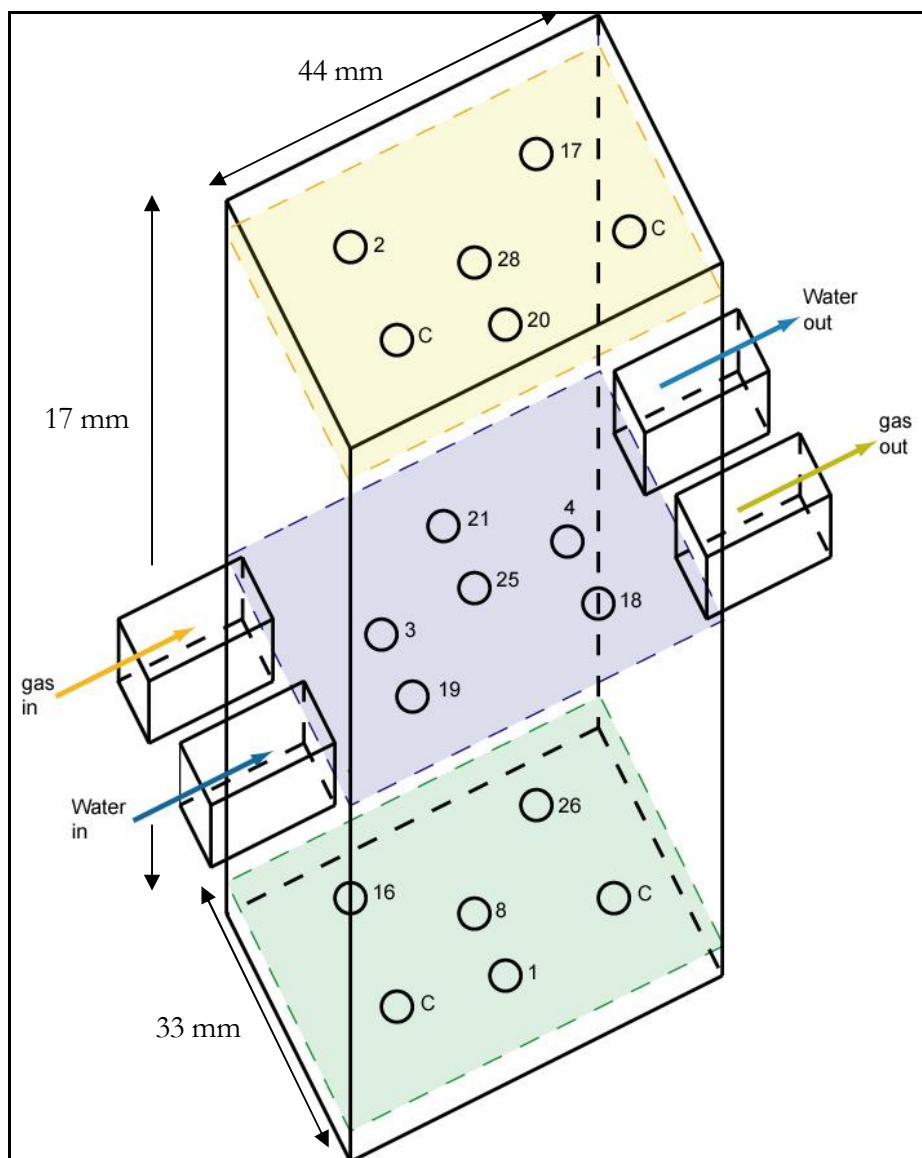


Fig. 4.2 Thermocouples position in the microstructure reactor type 2

The reactor proportions in Fig. 4.2 are not respected. The height of the device has been stretched in order to show better where the thermocouples are placed. Each circle associated with a number represents a thermocouple position. For example, thermocouple 25 is situated precisely in the middle of the reactor. The three planes (marked with the dashed lines) are situated at $\frac{1}{4}$, $\frac{1}{2}$, and $\frac{3}{4}$ of the reactor total height.

When only the plane in the middle is considered, the thermocouples are placed with respect to the reaction plate as shown in Fig. 4.3.

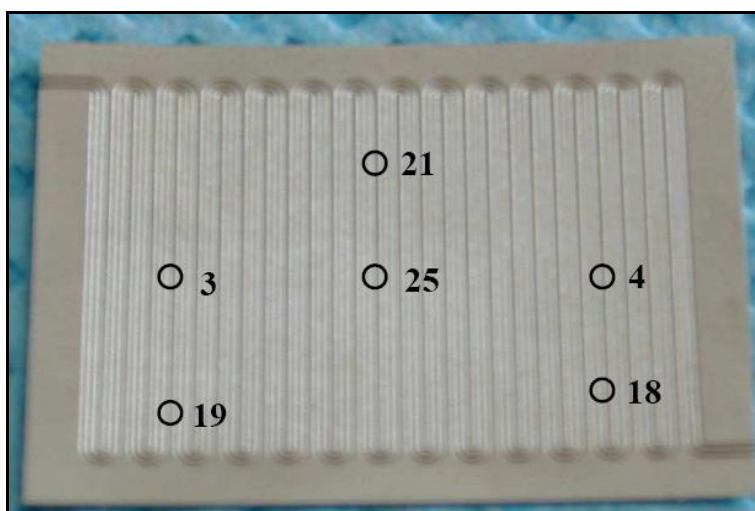


Fig. 4.3 Picture of a reaction plate with the thermocouples position

The circles associated with a number in Fig. 4.3 have the same meaning than those in Fig. 4.2. For practical reasons, it was unfortunately impossible to place a thermocouple directly onto the reaction plate. The temperature was thus not measured directly on the reaction plate but slightly beneath. However, it will be shown in Chap. 4.2.2, that since no heat transfer limitations are present within the device, the measured temperature is really the one present at the surface of the reaction channels where the reaction is taking place.

Fig. 4.4 and Fig. 4.5 present the temperature recorded by the thermocouples illustrated in Fig. 4.3 during two experiments under non-stationary thermal conditions with a gas flow of $300 \text{ ml}\cdot\text{min}^{-1}$ (STP). The period duration is changing from 120 seconds in Fig. 4.4 to 20 seconds in Fig. 4.5.

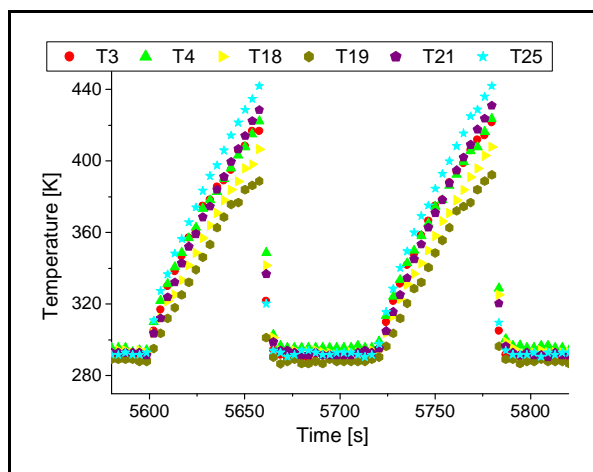


Fig. 4.4 Temperature measured by the thermocouples during temperature oscillations with a period duration of 120 seconds and a mean amplitude of 120 K

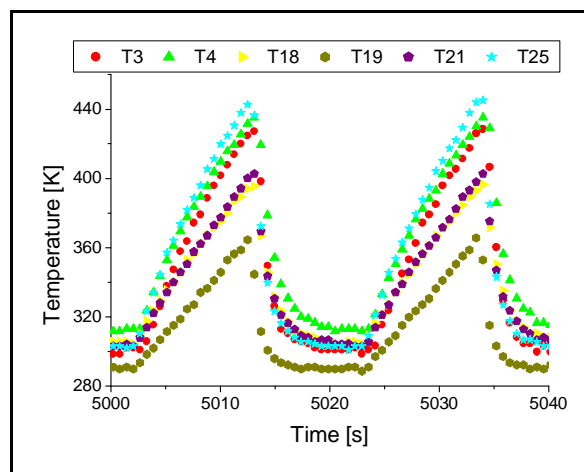


Fig. 4.5 Temperature measured by the thermocouples during temperature oscillations with a period duration of 20 seconds and a mean amplitude of 115 K

The thermocouple numbers given in Fig. 4.4 and Fig. 4.5 correspond with the numbers in Fig. 4.3. For example, the position 3 in Fig. 4.3 corresponds with the thermocouple T3 (points) in Fig. 4.4 and Fig. 4.5.

When the period of the oscillations is relatively long (Fig. 4.4), the reactor temperature profile is relatively homogeneous. There is only the formation of a cold spot (T19) and a hot spot (T25) at the end of a heating half-period. At this time, the temperature difference between these two points in the reactor is 55 K. When the period duration is reduced (Fig. 4.5), the reactor temperature profile becomes less homogeneous. The cold spot and hot spot remain at the same position inside the reactor (T19 and T25) but the temperature difference is now larger and reaches 85 K at the end of the heating half-period.

Some other remarks can also be made from the observation of the Fig. 4.4 and Fig. 4.5. The thermocouple 19, which is situated near the entry of the cooling water, always records a lower temperature than the others, and the amplitude of the oscillations is equally smaller. This region is the reactor cold spot. The thermocouple 25, which is situated in the middle of the reactor, clearly measures a higher temperature than the others. This is where the hot spot is situated. The thermocouples at the position 3 and 4 are showing the same thermal behaviour because they are situated symmetrically in the reactor. The influence of the cooling water entry is not so strong at the position 3 than at the position 19.

The problem related with the development of an inhomogeneous temperature profile under fast periodic temperature oscillations is that the gas flowing through the meandered channels (see Fig. 4.3) will encounter all the temperature values presented in e.g. Fig. 4.5. The reaction rate will thus be different at each point of the reactor. If an apparent activation energy for the CO oxidation between 80 and 100 kJ·mol⁻¹ is supposed, there will be a difference factor between 200 and 800 in the reaction rate value between two points in the reactor at 360 and 450 K. This variation of the reaction rate along the channels will in all cases average the value measured at the reactor outlet and complicate the interpretation of the experimental results. Moreover it is possible that this averaging of the reaction rate reduces the measured effects of the fast temperature cycling conditions. Nevertheless, experimental measurements under fast temperature oscillation conditions using the CO oxidation have been realized in order to verify whether the reactor temperature inhomogeneity was really a relevant problem. The obtained results are presented in Chap. 4.3.5.

4.2.2. Heat transfer characterisation

For the interpretation of the experimental measurements under non-stationary thermal conditions, the correlation between the measured temperature and the corresponding concentration is of primary importance. The introduction of a time delay (presented in Chap. 4.3.5) allows to take into

account the time necessary for the gas to reach the FTIR or mass spectrometer from the reactor outlet. However, since the temperature is not directly measured on the reaction foil but slightly above, it is important to be sure that a temperature change recorded at the measurement position will reach the reaction foil, respectively the reaction channels and the reactive surface without any supplementary time delay.

The dimensionless Fourier number defined in Eq. 4.13 may be described by the ratio of the heat conduction rate with the rate of thermal energy storage. It is useful to determine the time necessary for a temperature change to be “transported” over a given distance [69].

$$Fo = \frac{\alpha \cdot t}{L_c^2} \quad [-] \quad \text{Eq. 4.13}$$

with	α	=	thermal diffusivity	$[m^2 \cdot s^{-1}]$
	t	=	time	$[s]$
	L_c	=	characteristic length	$[m]$

and the thermal diffusivity being defined by:

$$\alpha = \frac{k_c}{\rho \cdot c_p} \quad [m^2 \cdot s^{-1}] \quad \text{Eq. 4.14}$$

with	k_c	=	thermal conductivity	$[W \cdot m^{-1} \cdot K^{-1}]$
	ρ	=	density	$[kg \cdot m^{-3}]$
	c_p	=	specific heat capacity	$[J \cdot m^{-3} \cdot K^{-1}]$

The thermal diffusivity “ α ” for stainless steel is approximately $3.5 \cdot 10^{-6} m^2 \cdot s^{-1}$ and for alumina (catalyst layer) $7 \cdot 10^{-5} m^2 \cdot s^{-1}$ [70]. The distance between the measurement points and the reaction foil “ $L_{c, \text{stainless steel}}$ ” is approximately $2 \cdot 10^{-4} m$ and the thickness of the catalyst layer “ $L_{c, \text{alumina}}$ ” $10^{-9} m$. Due to the extremely small alumina layer thickness, the heat transfer resistance in this layer may be neglected. The Fourier number value is thus given by:

$$Fo = \frac{\alpha_{\text{stainless steel}} \cdot t}{(L_{c, \text{stainless steel}})^2} = \frac{3.5 \cdot 10^{-6} \cdot \text{time}}{(2 \cdot 10^{-4})^2} = 87.5/s \cdot \text{time} \quad [-] \quad \text{Eq. 4.15}$$

After a time duration of 0.1 s, the Fourier number value calculated using Eq. 4.15 is 8.75. In [69] it can be found that a Fourier number value of 1.5 signifies that 97% of a given temperature change has travelled from the border to the centre of a plate. In our case, the value attained for the Fourier number after 0.1 s means that the quasi totality of the temperature change (more than 97%) has moved from the recording position to the surface of the reaction channels within this time. There are thus no heat transfer limitations within the device and no supplementary time delay. The measured temperature is corresponding to the one at the surface of the reaction channels where the catalytic reaction is taking place.

4.3. CO oxidation

This chapter presents the experimental measurements realized using the CO oxidation as a test reaction. First, the results obtained under stationary thermal conditions are shown and then the ones obtained under quasi-stationary and non-stationary conditions are given.

4.3.1. Reaction conditions

All the experimental measurements were conducted under the same reaction conditions in order to compare the obtained results with those measured previously by Brandner [2].

The total reaction gas flow was $300 \text{ ml}\cdot\text{min}^{-1}$ (STP) with 26 % O_2 , 5 % CO, the rest being N_2 . The pressure at the reactor entry was 0.2 MPa and ambient at the outlet. The experiments under stationary thermal conditions were realized at temperatures between 60°C and 190°C . For the non-stationary conditions measurements the temperature has been varied between 20 - 190°C .

Before starting an experimental measurement, the reactor was within 2 minutes heated from room temperature up to 250°C under a flow of $300 \text{ ml}\cdot\text{min}^{-1}$ (STP) of pure nitrogen and then let cool down to the reaction temperature. The objective was to remove all of the adsorbed species from the surface of the catalyst and to get rid of water traces eventually present in the reaction channels.

4.3.2. Stationary thermal conditions

The reaction has been first conducted under stationary thermal conditions in order to get a basis of comparison for the values measured under temperature cycling.

Fig. 4.6 presents the concentration of CO_2 at the reactor outlet with respect to the temperature.

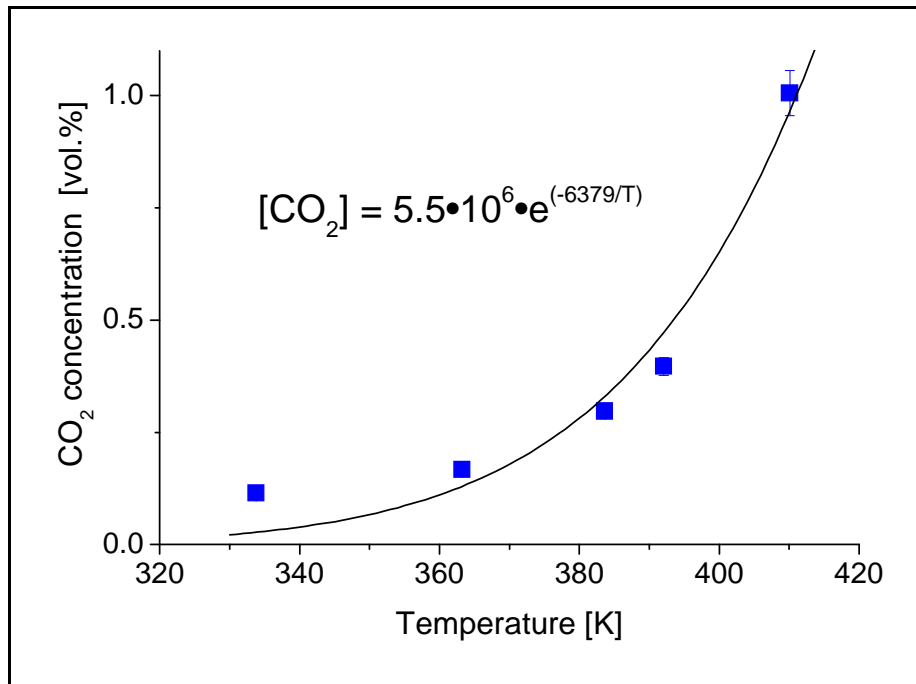


Fig. 4.6 CO_2 concentration at the reactor outlet with respect to the temperature

It can be seen in Fig. 4.6 that the CO_2 concentration depends exponentially from the temperature. This is consistent with the Arrhenius law presented in Eq. 2.1.

If it is assumed that the CO_2 concentration is related to the overall reaction rate constant by

$$[\text{CO}_2] \propto k_{\text{rx}}(T) = k_0 \cdot e^{\left(\frac{-E_a}{R \cdot T}\right)} \quad \text{Eq. 4.16}$$

the exponent of the exponential fit shown in Fig. 4.6 is equal to $-\frac{E_a}{R \cdot T}$. The obtained apparent activation energy for the reaction is thus $53 \text{ kJ} \cdot \text{mol}^{-1}$.

It is equally possible to calculate the activation energy for the overall reaction by taking the logarithm of Eq. 4.16:

$$\ln([\text{CO}_2]) \propto \ln(k_0) - \frac{E_a}{R} \cdot \frac{1}{T} \quad \text{Eq. 4.17}$$

A plot of $\ln([\text{CO}_2])$ with respect to $\frac{1}{T}$ is then giving a straight with a slope of $-\frac{E_a}{R}$. Such a representation is analogue to an Arrhenius plot and is presented in Fig. 4.7.

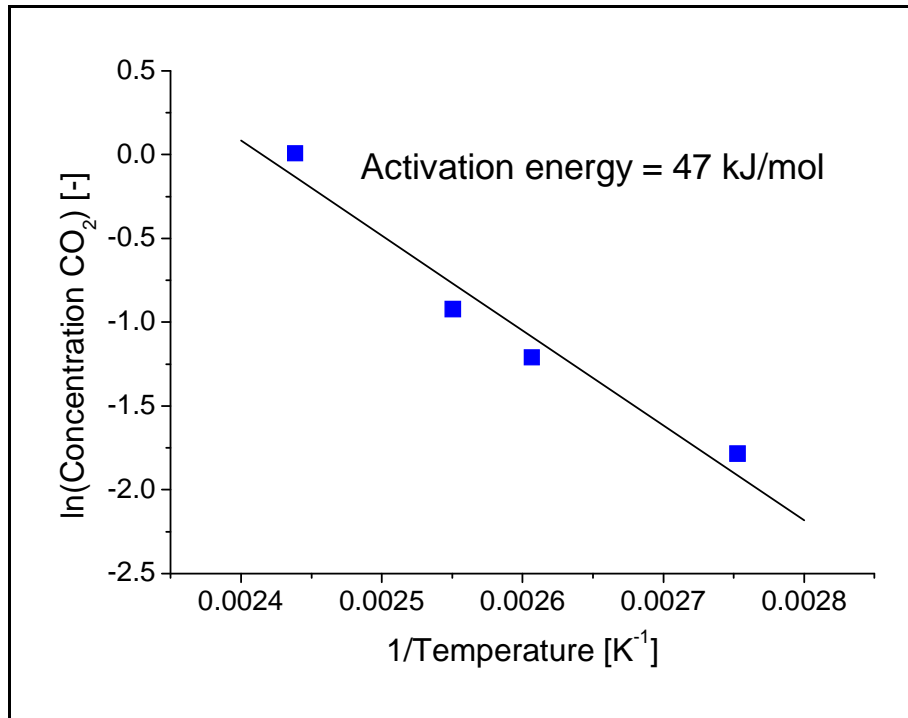


Fig. 4.7 Plot similar to an Arrhenius one for the CO oxidation reaction

The slope of the black straight line in Fig. 4.7 enables to calculate an apparent activation energy (E_a) for the overall CO oxidation reaction of $47 \text{ kJ} \cdot \text{mol}^{-1}$. The straight line in Fig. 4.7 is drawn without the point from Fig. 4.6 at the lowest temperatures where the conversion is very low and the measured CO_2 concentration too weak to be precise.

The values found for the apparent activation energy are considerably lower compared to the values which are usually mentioned in the literature. Values of approximately $100 \text{ kJ}\cdot\text{mol}^{-1}$ can be found for example in [35] or [71]. The relatively low apparent activation energy value estimated here may be due to the influence of transport phenomena on the overall reaction rate. Another possibility may be the influence of the surface coverage of CO, as mentioned by Engel and Ertl [43]. They observed that the activation energy for the CO oxidation on Pd was reduced from 105 to $59 \text{ kJ}\cdot\text{mol}^{-1}$ when the CO coverage on the catalyst surface was changing from a low to a moderate value. They explained their observation by a rearrangement of the adsorbed oxygen adlayer when the CO coverage was increasing. Since the partial pressure of CO in this work is relatively high, a high CO coverage on the surface and consequently a low apparent activation energy is plausible.

The above calculations have been realized by supposing that differential conditions where present inside the reactor. That is, the influence of the development of a concentration profile within the reactor has been neglected. Since the conversion varies between 6 and 20 %, this approximation may not be totally valid for the 20% conversion value. To test the influence of the concentration profile of the reactants, it is also possible to realize similar calculations as above while considering an integral “plug flow” reactor with the corresponding concentration profile.

The material balance in the case of an ideal plug flow reactor may be written by [72]:

$$\frac{\partial c_i}{\partial t} = -\frac{\partial([i] \cdot \bar{u})}{\partial z} + \sum_j \nu_{ij} \cdot r_j \quad \text{Eq. 4.18}$$

with	$[i]$	=	concentration of component “i”	[vol.%]
	\bar{u}	=	linear flow rate	$[\text{m}\cdot\text{s}^{-1}]$
	z	=	coordinate	[m]
	ν_{ij}	=	stoichiometric coefficient of “i” in the j^{th} reaction	[-]
	r_j	=	reaction rate for the j^{th} reaction	$[\text{s}^{-1}]$

Under stationary conditions the time dependency disappears and the balance may be written as

$$\frac{\partial c_i}{\partial t} = -\frac{\partial([i] \cdot \bar{u})}{\partial z} + \sum_j \nu_{ij} \cdot r_j = 0 \quad \text{Eq. 4.19}$$

In our case we will consider that the reaction rate “ r_j ” may be defined by:

$$r_j = R_{\text{CO}_2} = k' \cdot [\text{CO}]^a \cdot \exp\left(\frac{-E_a}{R \cdot T}\right) \quad \text{Eq. 4.20}$$

with $k' = k_0 \cdot [\text{O}_2] \quad [\text{s}^{-1} \cdot (\text{vol.}\%)^{(1-a)}]$ (since the concentration unit is “vol.%”)

For sake of simplicity, the concentration of oxygen $[O_2]$ has been taken as being constant and combined with the pre-exponential factor k_0 . This is a reasonable simplification since oxygen is in a large excess compared to CO and its conversion does not exceed 2% (relative).

By introducing for the case of a constant volumetric flow and supposing that the flow is uniformly distributed over the 12 microchannels of the reactor:

$$\bar{u} = \frac{\dot{V}}{12 \cdot A_c} \quad [m \cdot s^{-1}] \quad \text{Eq. 4.21}$$

$$\begin{array}{llll} \text{with} & \dot{V} & = & \text{volumetric flow} & [m^3 \cdot s^{-1}] \\ & A_c & = & \text{cross section of a channel} & [m^2] \end{array}$$

and combining Eq. 4.19 to Eq. 4.21, the following differential equation is obtained for the evolution of the CO concentration along the reactor:

$$\frac{d[CO]}{dz} = -\frac{\dot{V}}{12 \cdot A_c} \cdot k' \cdot [CO]^a \cdot \exp\left(\frac{-E_a}{R \cdot T}\right) \quad \text{Eq. 4.22}$$

By rearranging:

$$\int_{[CO]_{\text{initial}}}^{[CO]_{\text{final}}} \frac{d[CO]}{[CO]^a} = -\frac{\dot{V}}{12 \cdot A_c} \cdot k' \cdot \exp\left(\frac{-E_a}{R \cdot T}\right) \int_{z=0}^{z_{\text{final}}} dz \quad \text{Eq. 4.23}$$

and integrating the right part:

$$\int_{[CO]_{\text{initial}}}^{[CO]_{\text{final}}} \frac{d[CO]}{[CO]^a} = -\frac{\dot{V}}{12 \cdot A_c} \cdot k' \cdot \exp\left(\frac{-E_a}{R \cdot T}\right) z_{\text{final}} \quad \text{Eq. 4.24}$$

It may be seen in the left part of Eq. 4.24 that the evolution of the CO concentration depends from the value of the partial CO order “a”. To test the influence of this partial order on the apparent activation energy of the reaction, the arbitrary values of -1, 0 and 1 have been chosen. As will be shown in Chap. 5.3.2, the partial order of reaction for CO which is experimentally determined is close to -1.

For a=-1 we have

$$\int_{[CO]_{\text{initial}}}^{[CO]_{\text{final}}} [CO] d[CO] = -\frac{\dot{V}}{12 \cdot A_c} \cdot k' \cdot \exp\left(\frac{-E_a}{R \cdot T}\right) z_{\text{final}} \quad \text{Eq. 4.25}$$

which gives after integration

$$\frac{([\text{CO}]_{\text{final}})^2 - ([\text{CO}]_{\text{initial}})^2}{2} = -\text{Ct} \cdot \exp\left(\frac{-E_a}{R \cdot T}\right) \quad \text{Eq. 4.26}$$

$$\text{with } \text{Ct} = \frac{\dot{V}}{12 \cdot A_c} \cdot k' \cdot z_{\text{final}}$$

Rearranging and taking the logarithm of Eq. 4.26 gives

$$\ln\left(\frac{([\text{CO}]_{\text{initial}})^2 - ([\text{CO}]_{\text{final}})^2}{2}\right) = \ln(\text{Ct}) - \frac{E_a}{R \cdot T} \quad [-] \quad \text{Eq. 4.27}$$

It is clear that a plot of the left part of Eq. 4.27 with respect to $\frac{1}{T}$ gives a straight having a slope of $-\frac{E_a}{R}$.

For $a=0$, there is no dependency of the reaction rate with respect to the CO concentration. The obtained equation after the integration of Eq. 4.24, taking the logarithm and rearranging is

$$\ln([\text{CO}]_{\text{initial}} - [\text{CO}]_{\text{final}}) = \ln(\text{Ct}) - \frac{E_a}{R \cdot T} \quad [-] \quad \text{Eq. 4.28}$$

Since $[\text{CO}]_{\text{initial}} - [\text{CO}]_{\text{final}} = [\text{CO}_2]$, Eq. 4.28 is similar to Eq. 4.17. This is consistent to the fact that in the case of the calculations realized using the differential conditions, the influence of the concentration profile of the reactant on the reaction rate has been neglected.

For $a=1$, Eq. 4.29 is obtained after the integration of Eq. 4.24, rearranging and taking the logarithm.

$$\ln(\ln([\text{CO}]_{\text{initial}}) - \ln([\text{CO}]_{\text{final}})) = \ln(\text{Ct}) - \frac{E_a}{R \cdot T} \quad [-] \quad \text{Eq. 4.29}$$

Here again, a plot of the left part of Eq. 4.29 with respect to $\frac{1}{T}$ gives a straight having a slope of $-\frac{E_a}{R}$.

Since Eq. 4.27, Eq. 4.28 and Eq. 4.29 have no unity, it is possible to represent them in the same graphic in order to better visualize the influence of the partial order of reaction for CO on the apparent activation energy of the reaction. The obtained graphic is presented in Fig. 4.8.

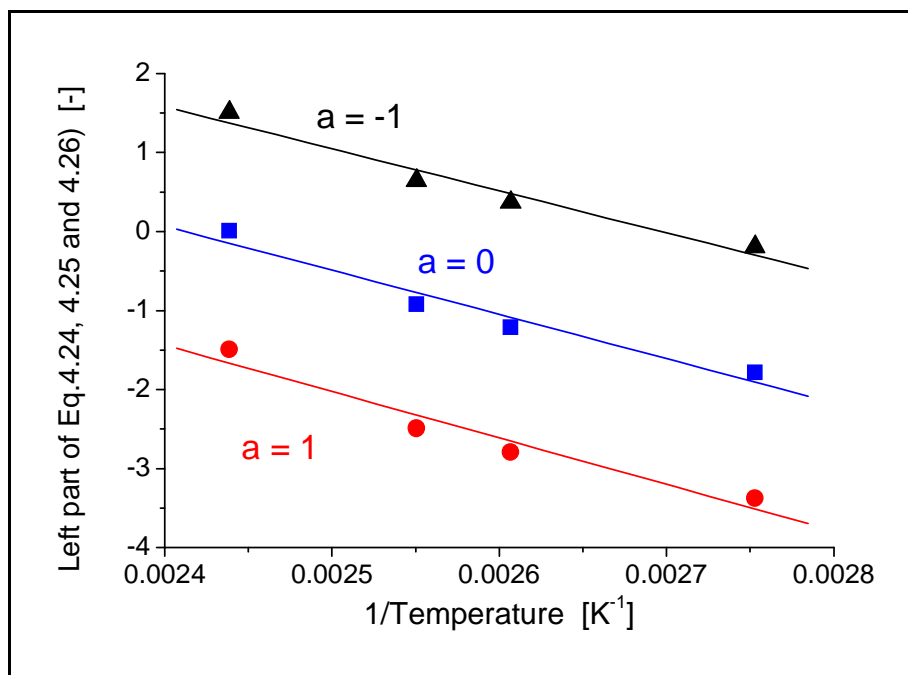


Fig. 4.8 Influence of the partial order of CO “a” on the apparent activation energy of the CO oxidation

It may be seen in Fig. 4.8 that the partial order of CO “a” has no marked influence on the slopes of the straight lines and thus on the apparent activation energy. The obtained numerical values are presented in Tab. 4.5.

Partial CO order “a”	Apparent activation energy E_a [kJ·mol ⁻¹]
-1	44
0	47
1	49

Tab. 4.5 Calculated apparent activation energy in function of the partial order of CO “a”

The calculated values confirm the observation made using the graphic of Fig. 4.8. The partial order in CO “a” has no important influence on the estimation of the apparent activation energy. The difference between a negative partial order and a positive one is not exceeding 5 kJ·mol⁻¹. As awaited, the apparent activation energy calculated using the partial order of CO equal to 0 corresponds to the one calculated using differential conditions and the graphic in Fig. 4.7. As already mentioned, the calculated apparent activation energies are in any case too low compared to the values of the literature. The calculations performed in Chap. 4.3.3 will enable to determine whether any transport limitations are present in the reactor.

4.3.3. Mass transport characteristics

This chapter is devoted to the calculation of parameters for the characterization of the transport phenomena within the microstructure reactor.

4.3.3.1. External mass transfer rate

The calculation of the external transfer rate of the reactive species from the bulk to the catalyst surface and the comparison with the reaction rate is one possibility to rule out external transport limitations. An empirical correlation allowing the Sherwood number calculation has been developed by van Male [73] for microchannels with a square section. This correlation will be used as an approximation, although the reaction channels are not perfectly square but elliptic.

$$\text{Sh} = 2.43 \cdot \left(1 + \left(\frac{\text{Gz}_m}{132} \right)^{0.835} \right) \quad [-] \quad \text{Eq. 4.30}$$

where Gz_m is the Graetz number for mass transport defined by

$$\text{Gz}_m = \text{Re} \cdot \text{Sc} \cdot \frac{d}{z} \quad [-] \quad \text{Eq. 4.31}$$

with

Re	=	Reynolds number	[-]
Sc	=	Schmidt number	[-]
d	=	side of a square cross section	[m]
z	=	coordinate	[m]

The microchannels wet chemically etched onto the reaction foils are more half-elliptic, respectively rectangular, than square. Consequently, the side of the square section “d” has been replaced for the calculations with Eq. 4.31 by the hydraulic diameter “ d_h ” defined in Eq. 4.9.

Tab. 4.6 presents calculated values for the Sherwood number for O_2 and CO at different temperatures and coordinates in the reactor using Eq. 4.30 and Eq. 4.31. The values for the Reynolds and Schmidt number used for the calculations are presented in Tab. 4.3 and Tab. 4.4.

Coordinate z [mm]	Temperature = 300 K		Temperature = 375 K		Temperature = 460 K	
	Sh O_2 [-]	Sh CO [-]	Sh O_2 [-]	Sh CO [-]	Sh O_2 [-]	Sh CO [-]
0.001	214.4	189.7	152.5	138.7	109.5	101.2
0.01	33.4	29.8	24.4	22.3	18.1	16.9
0.1	6.96	6.43	5.64	5.34	4.72	4.54
1	3.09	3.02	2.90	2.86	2.76	2.74
10	2.53	2.52	2.50	2.49	2.48	2.48
100	2.44	2.44	2.44	2.44	2.44	2.44
764	2.43	2.43	2.43	2.43	2.43	2.43

Tab. 4.6 Sherwood number for O_2 and CO for different temperatures and coordinates along a microchannel

Tab. 4.6 shows that the channel length (764 mm) is sufficient to reach the asymptotic value 2.43 for the Sherwood number. This asymptotic value is different from the one mentioned in e.g. [74] which is 3.74 for channels of elliptic form. The value of 2.43 which is giving the lowest transfer coefficient is used for the further calculations. This ensures that the transfer rate is not overestimated. Eq. 4.32 relates the overall mass transfer coefficient k_c with the Sherwood number.

$$Sh = \frac{k_c \cdot L_c}{D_{12}} \quad [-] \quad \text{Eq. 4.32}$$

with

k_c	=	overall mass transfer coefficient	$[m \cdot s^{-1}]$
L_c	=	characteristic length	$[m]$
D_{12}	=	component diffusion	$[m^2 \cdot s^{-1}]$

By choosing a characteristic length value of half of the hydraulic diameter (in the worst case a molecule has to travel from the middle to the side of the channel), the mass transfer coefficient from the bulk to the catalyst surface can be calculated for each of the reactive species. The values for the component diffusion D_{12} used in Eq. 4.31 can be found in Tab. 4.2.

Temperature [K]	k_c for O_2 [$m \cdot s^{-1}$]	k_c for CO [$m \cdot s^{-1}$]
300	0.58	0.67
375	0.89	0.97
460	1.34	1.42

Tab. 4.7 Overall mass transfer coefficient for O_2 and CO at different temperature

The calculated overall mass transfer coefficient can be used in Eq. 4.33 for the calculation of the transfer rate for the species “j”.

$$R_{tr,j} = k_{c,j} \cdot A_c \cdot ([j]_{bulk} - [j]_{surface}) \quad [mol \cdot s^{-1}] \quad \text{Eq. 4.33}$$

with

$k_{c,j}$	=	overall mass transfer coefficient for the species “j”	$[m \cdot s^{-1}]$
A_c	=	area of the channels	$[m^2]$
$[j]_{bulk}$	=	concentration of the species “j” in the bulk	$[mol \cdot m^{-3}]$
$[j]_{surface}$	=	concentration of the species “j” on the surface	$[mol \cdot m^{-3}]$

When the surface reaction rate is fast, the surface concentration of the reactants $C_{j,surface}$ may be postulated equal to zero. The values of the transfer rate $R_{tr,j}$ for the different species can thus be calculated using the overall mass transfer coefficient presented in Tab. 4.7 and Eq. 4.33. The values of the transfer rate calculated for different temperatures are presented in Tab. 4.8.

Temperature [K]	Transfer rate O_2 [$mol \cdot s^{-1}$]	Transfer rate CO [$mol \cdot s^{-1}$]
300	$8.89 \cdot 10^{-2}$	$1.27 \cdot 10^{-2}$
375	$1.35 \cdot 10^{-1}$	$1.85 \cdot 10^{-2}$
460	$2.03 \cdot 10^{-1}$	$2.70 \cdot 10^{-2}$

Tab. 4.8 Transfer rate for O_2 and CO from the bulk to the surface at different temperature

As can be seen in Fig. 4.6, the maximal CO₂ concentration measured at the reactor outlet is approximately 1 vol%, corresponding to a conversion of 20%, at a reactor temperature of 410 K. Based on Brandner [2], it is reasonable to postulate a gas flow temperature of approximately 320 K for this reactor temperature. With the reactor outlet at atmospheric pressure, the use of the perfect gas law allows to calculate a global reaction rate $R_{\text{CO}_2, \text{glob}}$ based on Eq. 4.34.

$$R_{\text{CO}_2, \text{glob}} = \frac{P_{\text{outlet}} \cdot [\text{CO}_2] \cdot \text{Flow}_{\text{outlet}}}{100 \cdot R \cdot T_{\text{gas outlet}}} \quad [\text{mol} \cdot \text{s}^{-1}] \quad \text{Eq. 4.34}$$

with	P_{outlet}	=	pressure at the reactor outlet	[Pa]
	$[\text{CO}_2]$	=	CO ₂ concentration	[vol. %]
	Flow_{tot}	=	reaction gas flow	[m ³ ·s ⁻¹]
	R	=	perfect gas constant	[m ³ ·Pa·K ⁻¹ ·mol ⁻¹]
	$T_{\text{gas outlet}}$	=	gas flow temperature at the reactor outlet	[K]

The maximal global reaction rate value obtained using Eq. 4.34 is $1.9 \cdot 10^{-6} \text{ mol} \cdot \text{s}^{-1}$. Compared with the transfer rate presented in Tab. 4.8, the global reaction rate value is at least three orders of magnitude smaller. Even if the supposition of zero concentration of the reactive species at the surface is not true, a concentration gradient of only 1% ($C_{\text{surface}} = 0.99 \cdot C_{\text{bulk}}$) is sufficient for the transfer rate of the reactive species to be 30 times faster than the reaction rate. Based on these calculations, a limitation or influence of the measured reaction rate by external transport phenomena is excluded.

4.3.3.2. Mears criterion

Another criterion which can be calculated in order to determine whether the measured reaction rate is influenced by external transport phenomena is the Mears criterion. Eq. 4.35 must be satisfied [75] for no external transport limitation to be present in the case of a porous catalyst.

$$\omega = \frac{\Re \cdot r_p}{C_b \cdot k_{c,p}} < \frac{0.15}{|n|} \quad [-] \quad \text{Eq. 4.35}$$

for a chemical reaction with a kinetic of type

$$\Re = k \cdot C_s^n \quad [\text{g} \cdot \text{mol} \cdot \text{s}^{-1} \cdot \text{cm}^{-3}] \quad \text{Eq. 4.36}$$

with	\Re	=	observed reaction rate per unit particle volume	[g·mol·s ⁻¹ ·cm ⁻³]
	r_p	=	particle radius	[cm]
	C_b	=	concentration of reactant in the bulk fluid	[g·mol·cm ⁻³]
	$k_{c,p}$	=	mass transfer coefficient between gas and particle	[cm·s ⁻¹]
	n	=	integer exponent in the power law equation	[-]
	k	=	reaction rate constant	[s ⁻¹]
	C_s^n	=	reactant concentration at the surface of the particle	[mol·cm ⁻³]

In the case of microchannels, Eq. 4.34 can be transformed in Eq. 4.36 to correspond to the parameters of the system [76].

$$\omega = \frac{R_{v,CO_2} \cdot d_c}{C_{CO} \cdot k_{c,CO}} < \frac{0.15}{|n|} \quad [-] \quad \text{Eq. 4.37}$$

with	R_{v,CO_2}	=	observed reaction rate per reaction volume	$[\text{mol} \cdot \text{s}^{-1} \cdot \text{m}^{-3}]$
	d_c	=	channel diameter	$[\text{m}]$
	C_{CO}	=	CO concentration in the gas phase	$[\text{mol} \cdot \text{m}^{-3}]$
	$k_{c,CO}$	=	mass transfer coefficient for CO	$[\text{m} \cdot \text{s}^{-1}]$

The Mears criterion is calculated for the CO molecule because its concentration and mass transfer coefficient values are smaller than those of O_2 . The criterion value calculated this way is the highest obtainable and thus the more unfavourable. Using the highest CO_2 concentration measured and the volume of the channels, a maximum reaction rate value of $12.7 \text{ mol}_{CO_2} \cdot \text{m}^{-3} \cdot \text{s}^{-1}$ can be calculated. With the CO concentration decreasing to $1.14 \text{ mol} \cdot \text{m}^{-3}$ at the reactor outlet, the Mears criterion calculated is:

$$\omega = \frac{12.7 \cdot 0.32 \cdot 10^{-3}}{1.14 \cdot 0.67} = 5.3 \cdot 10^{-3} < \frac{0.15}{|n|}$$

Since values of the exponent “n” may vary for the CO oxidation between -0.5 and 2, the Mears criterion will be satisfied in all cases and the influence of the reaction rate by external transport phenomena may be excluded. This is consistent with the result obtained in Chap. 4.3.3.1.

The relatively low value for the activation energy measured is thus not due to transport limitations.

4.3.4. Quasi-stationary thermal conditions

After having characterized the reaction behaviour under stationary thermal conditions, slow temperature ramps have been applied to the reactor. These measurements were realized in order to test whether slow temperature changes were sufficient to observe some difference compared to the stationary thermal conditions. The temperature ramps have been applied to the reactor with a heating rate of $10 \pm 2 \text{ K} \cdot \text{min}^{-1}$ and a cooling rate of $6 \pm 1 \text{ K} \cdot \text{min}^{-1}$. The difference between the heating and cooling rate is due to the fact that the cooling is in this case not active. The heater cartridges are simply turned off and the reactor cooled down passively. It is thus not possible to regulate the cooling rate. The CO_2 concentration was monitored online together with the temperature. Fig. 4.9 presents an example of the obtained results.

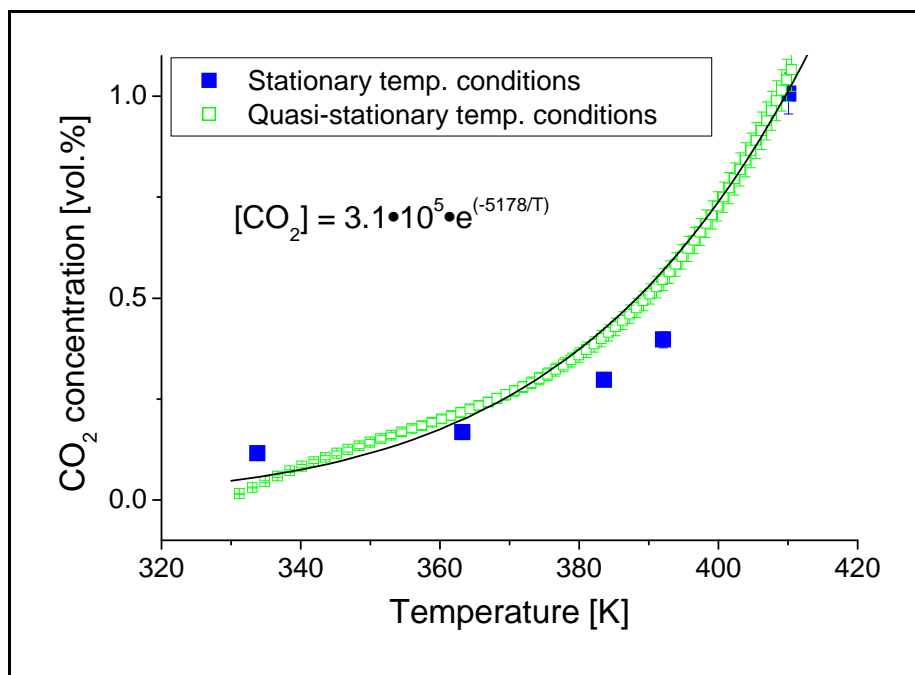


Fig. 4.9 CO₂ concentration measured by FTIR at the FTC-type 2 reactor outlet under stationary thermal conditions (full squares) and quasi-stationary thermal conditions (empty squares)

As can be seen in Fig. 4.9, there is no significant difference in the temperature dependence of the CO₂ concentration under stationary and quasi-stationary temperature conditions. The apparent activation energy for the reaction calculated using the exponent of the exponential fit presented in Fig. 4.9 is 43 kJ·mol⁻¹. This value is comparable to the one calculated in Chap. 4.3.2 under stationary temperature conditions. The temperature change rate is not high enough to perturb the reaction behaviour, which is still predicted by the Arrhenius law (exponential dependence with respect to the temperature).

4.3.5. *Non-stationary thermal conditions*

Since slow temperature changes were not sufficient to break the classical exponential dependence given by the Arrhenius law, the effect of faster temperature variations has been investigated.

In order to minimize the development of the inhomogeneous temperature profile presented in Fig. 4.5 only relatively slow periodic temperature variations have been applied to the microstructure reactor for the first series of measurements under non-stationary thermal conditions.

Fig. 4.10 presents the results obtained with a period duration of 120 s and an amplitude of 120 Kelvin.

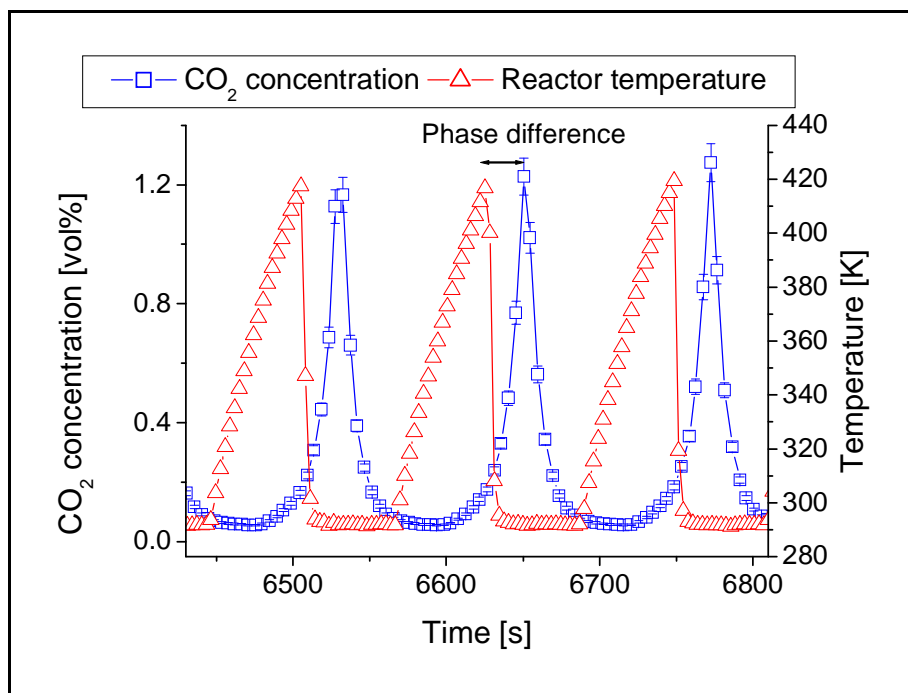


Fig. 4.10 Measured mean reactor temperature (triangles) and CO_2 concentration (squares) under forced temperature oscillations with a period of 120 s and an amplitude of 120 Kelvin

In Fig. 4.10 the squares represent the CO_2 concentration measured using the FTIR spectrometer and the triangles the mean temperature of the reactor. This mean temperature is defined by the sum of all the recorded values of the 14 thermocouples (see Fig. 4.2) divided by the number of thermocouples.

As it can be seen in Fig. 4.10 the curves formed by the squares and the triangles are shifted with respect to the time. That is, when the temperature reached its maximum value, the CO_2 concentration measured at the same time is still rising and reaches its maximum afterwards. This effect is denoted “phase difference” in Fig. 4.10 and may have two different causes. For one part, the measurement of the concentration does not take place directly at the reactor outlet. The gas has to pass through a certain length of pipes to reach the FTIR spectrometer measurement cell. Moreover, the correlation of the temperature measurements with the concentration measurements is not trivial. It is possible that a systematic error has been introduced from e.g. a slightly different sampling rate of the temperature regulation program compared to the FTIR spectrometer control program.

In this case of relatively slow temperature cycling, it is reasonable to postulate that the maximum of the two lines should correspond. By subtraction of the two points in time where the maximum values are recorded a phase difference (or shift) of 25 s can be calculated. If the 25 seconds are subtracted from the time of the CO_2 concentration curve, the result presented in Fig. 4.11 is obtained.

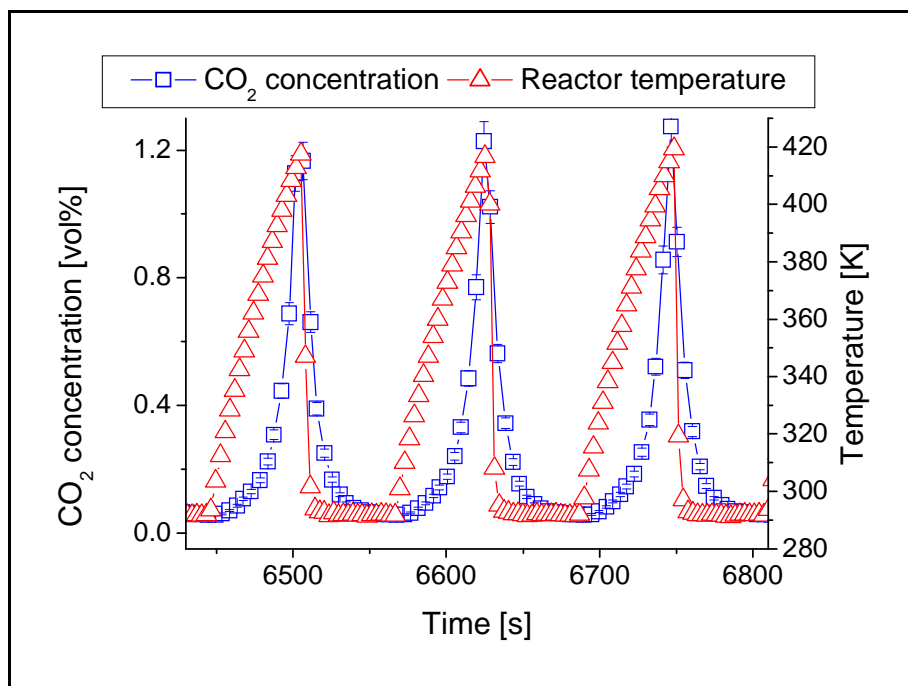


Fig. 4.11 Measured mean reactor temperature (triangles) and CO₂ concentration (squares) under forced temperature oscillations with a period of 120 s and an amplitude of 120 Kelvin after phase difference correction

The squares and triangles have in Fig. 4.11 and Fig. 4.10 the same meaning. After subtraction of the phase difference the maximum and minimum of the temperature and concentration curves are now corresponding. During the heating half-period the reactor temperature varies relatively linearly while the concentration increase is more of exponential type. This exponential increase of the concentration with respect to the linear increase of the temperature is predicted by the Arrhenius law (Eq. 2.1) and is an indication that the reaction behaves like under stationary thermal conditions. During the first part of the cooling half-periods, the temperature change rate is too high ($9 \text{ K}\cdot\text{s}^{-1}$) compared to the response time of the FTIR spectrometer. This prevents the proper resolution of the concentration changes during the cooling half periods. Consequently, the effect of the temperature oscillations will be characterized using the concentration values measured during the heating half-periods only.

To compare the measurements realized under non-stationary thermal conditions with the ones under stationary conditions more easily, it is useful to represent the concentration values with respect to the temperature as it is done in Fig. 4.6 and Fig. 4.9. The plot presented in Fig. 4.12 is obtained.

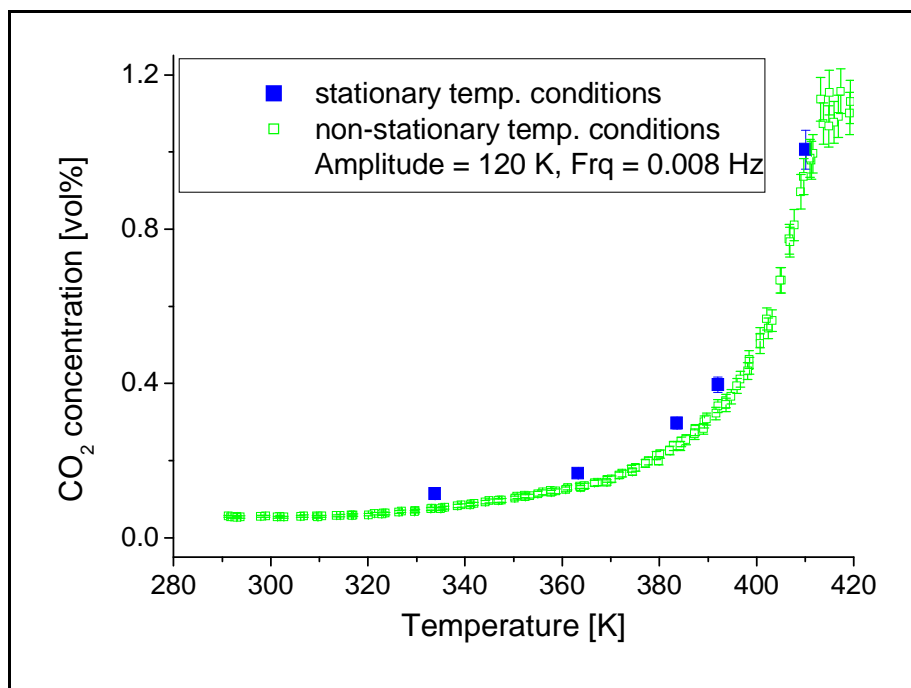


Fig. 4.12 Comparison of the measured CO_2 concentration under stationary thermal conditions (full squares) and non-stationary thermal conditions (empty squares)

As it can be seen in Fig. 4.12, there is again no noticeable difference between the concentration values measured under non-stationary temperature conditions (empty squares) and the reference values obtained under stationary conditions (full squares). The reaction rate follows constantly the classical exponential dependence with respect to the temperature given by the Arrhenius law. The heating rate of approximately $1 \text{ K}\cdot\text{s}^{-1}$ is not sufficient to produce the theoretically awaited reaction rate increase under forced temperature oscillations. It is thus necessary to raise the frequency of the oscillations.

The results obtained for the CO_2 concentration at the reactor outlet and the measured reactor temperature under a frequency of 0.025 and 0.05 Hz are presented in Fig. 4.13 and Fig. 4.14.

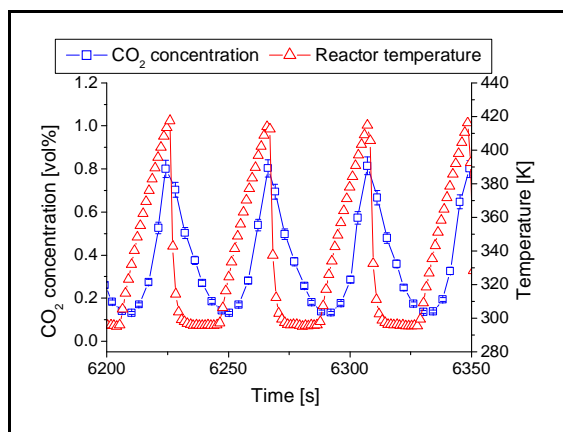


Fig. 4.13 Measured mean reactor temperature (triangles) and CO_2 concentration (squares) under forced temperature oscillations with a period duration of 40 s and an amplitude of 120 Kelvin

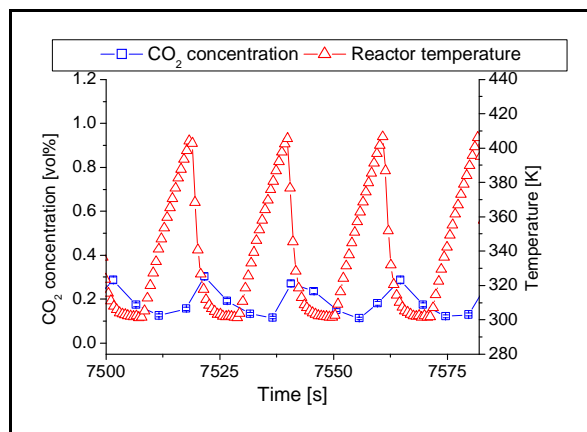


Fig. 4.14 Measured mean reactor temperature (triangles) and CO_2 concentration (squares) under forced temperature oscillations with a period duration of 20 s and an amplitude of 110 Kelvin

In Fig. 4.13 and Fig. 4.14 the squares represent the CO_2 concentration measured using the FTIR spectrometer and the triangles the mean temperature of the reactor.

The effect obtained by increasing the frequency (reduction of the period duration) is at the contrary to the one which was hoped. Although the mean temperature amplitude remains approximately the same, the measured CO_2 concentration amplitude is clearly reduced when the frequency increases. For a period duration of 20 s (Fig. 4.14), the concentration oscillations are nearly negligible. If the concentration curve in Fig. 4.13 and Fig. 4.14 is plotted with respect to the temperature, Fig. 4.15 and Fig. 4.16 are obtained.

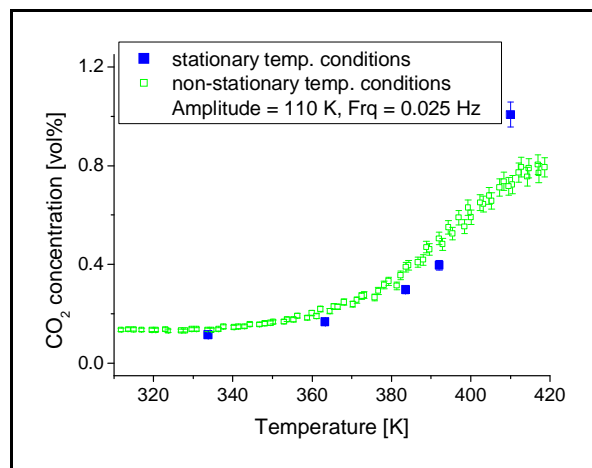


Fig. 4.15 Comparison of the measured CO_2 concentration under stationary (full squares) and non-stationary conditions (empty squares). Amplitude = 120 K, Frequency = 0.025 Hz

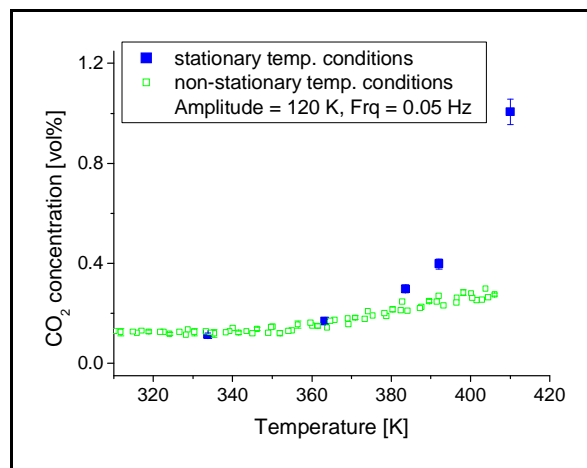


Fig. 4.16 Comparison of the measured CO_2 concentration under stationary (full squares) and non-stationary conditions (empty squares). Amplitude = 110 K, Frequency = 0.05 Hz

As supposed in Chap. 4.2.1, the thermal inhomogeneity of the microstructure reactor under temperature cycling conditions is strongly influencing the measured reaction rate (proportional to the CO_2 concentration). Especially at high temperatures (see e.g. Fig. 4.16), the CO_2 concentration values are not reaching the values attained under stationary temperature conditions any more. It seems that fast temperature oscillations are diminishing the reaction rate instead of increasing it. This effect is due to the influence of the zones of the reactor remaining at a relatively constant low temperature even when the mean reactor temperature is increasing. These reactor regions attenuate the temperature oscillations and thus decrease the measured CO_2 concentration oscillations. The high thermal inhomogeneity of the microstructure reactor type 2 under fast temperature cycling conditions makes it thus only suitable to a limited extent for the study of the effect of non-stationary thermal conditions on a catalytic reaction. Combined with the difficulties, if not the impossibility, to characterize the catalyst deposited inside the microstructured channels, these limitations are imposing the development and the use of another device for the continuation of this experimental study.

The chosen microstructure device is called FTC-reactor type 3 and has been presented above in Chap. 3.1.2. The experimental results obtained using this reactor are presented in Chap. 5.

5. Experimental results: FTC-reactor type 3

5.1. Flow characterization

As for the FTC-reactor type 2, experimental measurements and theoretical calculations have been realized for the determination of the flow conditions present within the device. This chapter present the results obtained.

5.1.1. *Experimental determination of the flow characteristics*

The experimental determination of the flow behaviour in the FTC-reactor type 3 is based on the same principles as already presented in Chap. 4.1.1. The measurements have been realized at the Swiss Federal Institute of Technology. The response curve of the microstructure reactor was measured by switching between a feed of pure He and a feed containing $\sim 5\%$ N_2 as a tracer. The entry function was of type “step”. The flow rate was set to $100 \text{ ml}\cdot\text{min}^{-1}$ which correspond to the flow used afterwards for the measurements with the CO oxidation reaction. The reactor was at room temperature (20°C) and the pressure was atmospheric (1.02 MPa). Fig. 5.1 presents a set of experimental F curves (see Chap. 4.1.1 for details) obtained for the measurement set-up only (squares) and with the microstructure reactor connected to the system (circles).

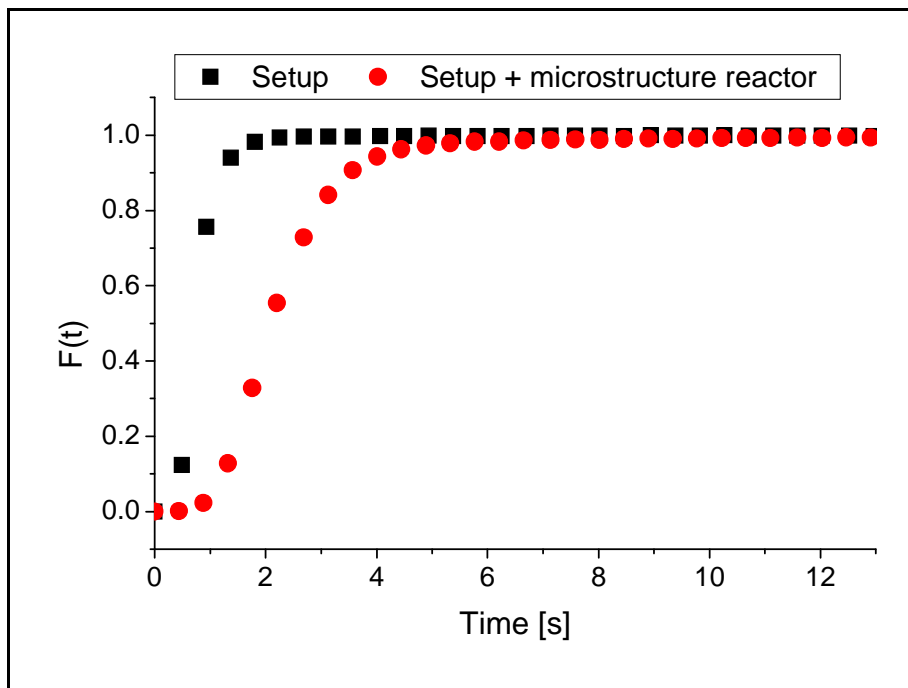


Fig. 5.1 Experimental F curves for the set-up only (squares) and for the set-up including the microstructure reactor (circles)

The experimental mean residence time in the whole microstructure reactor (gas connections and reaction chamber) τ_{reactor} is calculated from the difference between the mean residence time measured for the set-up including the reactor and for the set-up only. The F curves allow, as

mentioned in Chap. 4.1.1, to calculate the Bodenstein number (Bo) which characterizes the type of flow present in the reactor. The experimental values determined are given in Tab. 5.1.

Mean residence time τ_{reactor} [s]	Bodenstein number [-]
1.52 ± 0.08	4.1 ± 0.2

Tab. 5.1 Experimental values of the residence time τ_{reactor} and Bodenstein number for the FTC-type 3 reactor

Some measurements have been realized at a higher temperature than the room temperature (between 100 and 200°C) with the same volumetric flow in order to approach more closely the experimental conditions used during the experiments with the catalytic CO oxidation. However, the measured curves under these conditions do not allow to calculate a mean residence time or a Bodenstein. The mean residence time values become too low at the highest temperatures compared to the sampling rate of the mass spectrometer used for the measurements.

If the residence time distribution obtained for the FTC-reactor type 2 and 3 (diamonds) in Fig. 4.1 and Fig. 5.1, are compared, it is observed that the tailing of the measured curve for the type 3 is much more pronounced in comparison with the one of the type 2. This tailing is compatible with the very low Bodenstein number calculated. The hydrodynamic conditions are far away from a “plug flow” type. This is due to the random structure built by the single filaments composing the metallic gauze present in the reaction chamber through which the gas flows. There are many paths of different length, and thus different residence time, which the gas molecules may take for passing through the sintered metal filter plate.

5.1.2. Theoretical calculations of the flow characteristics

Using the feed flow rate of 100 ml·min⁻¹ (STP) and knowing the sintered fibres plate dimensions, it is possible to calculate the theoretical mean residence time within the reaction chamber τ_{chamber} . If a homogenous repartition of the gas flow within the sintered metal fibres plate is assumed, the theoretical residence time is given by:

$$\tau_{\text{chamber}} = \frac{\text{SMF plate volume} \cdot \text{porosity}}{\text{flow rate}} = 0.06 \quad [\text{s}] \quad \text{Eq. 5.1}$$

The porosity value used for the calculation is 70% [49].

A large discrepancy exists between the measured mean residence time and the theoretical one. This is because the theoretical residence time value is calculated only for the reaction chamber where the sintered metal plate is placed. The main volume of the reactor, responsible for the higher value of the experimental residence time, is built by the connexions and entry channels where no catalytic material is present. The time period during which a reaction will take place is thus not the

measured mean residence time but the one calculated theoretically. As in the case of the FTC-reactor type 2, it is unfortunately impossible to determine the mean residence time within the reaction chamber experimentally due to its very small value and the fact that it is impossible to eliminate the effect of the connexions without perturbing the gas hydrodynamics. It is thus necessary to rely on the value estimated theoretically.

Due to the random structure built by the single filaments composing the sintered metal fibres plate, it is not clear what kind of fluid hydrodynamic conditions prevails. The theoretical estimation of the Bodenstein number using the equations presented in Chap. 4.1.2 is not feasible because these equations are valid for a circular microchannel only.

5.2. Thermal characterization

5.2.1. *Temperature profile under temperature cycling conditions*

It has been shown in Chap. 4 that the strongly inhomogeneous temperature profile developing inside the FTC-reactor type 2 under non-stationary thermal conditions was a handicap for the study of the temperature effects on the catalytic CO oxidation. It is thus necessary to verify whether the temperature profile of the FTC-reactor type 3 remains more homogeneous under the non-stationary thermal conditions.

The temperature is measured using two thermocouples introduced into the gas inlet and outlet connexions. The thermocouple ends are pressed inside the sintered metal fibres plate by the reactor top plate in order to ensure a good contact. This guarantees that the measured temperature is really the one at the surface of the sintered metal plate respectively at the catalytic surface where the reaction is taking place. Fig. 5.2 presents a schematic drawing of the temperature measurement configuration.

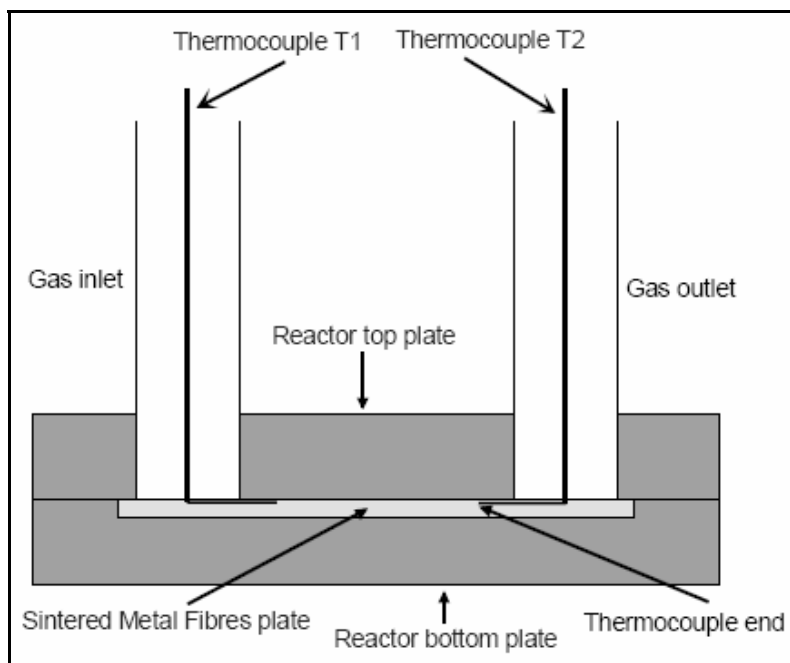


Fig. 5.2 Schematic drawing of the thermocouple configuration. The ends are pressed between the reactor top plate and the SMF foil to ensure a good temperature measurement

Fig. 5.2 shows the end of the thermocouples being pressed under the top plate of the reactor to ensure a good contact between them and the SMF plate and thus a reliable temperature measurement. The temperature measurements were realized under a gas flow of $100 \text{ ml}\cdot\text{min}^{-1}$ corresponding to the one used afterwards during the experiments with the CO oxidation reaction. The pressure drop and hydrodynamic conditions remain thus identical between the different experiments.

Fig. 5.3 and Fig. 5.4 present examples of temperature plots recorded by the thermocouples placed inside the microstructure reactor under non-stationary thermal conditions with a maximum amplitude of the temperature oscillations of 68 Kelvin. The period duration is 24 seconds in Fig. 5.3 and 16 seconds in Fig. 5.4.

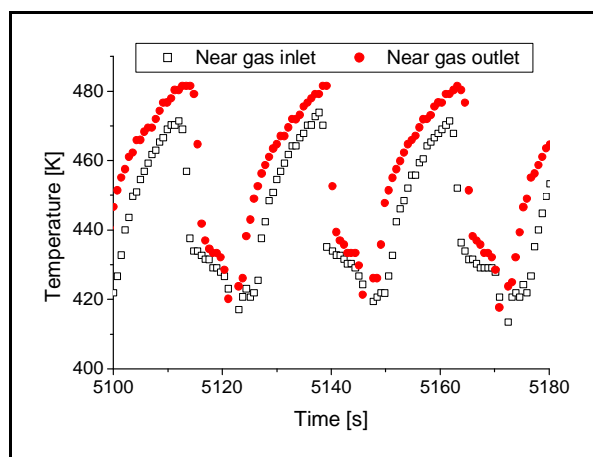


Fig. 5.3 Temperature measured by the thermocouples during temperature oscillations with a period duration of 24 seconds and a mean amplitude of 60 K

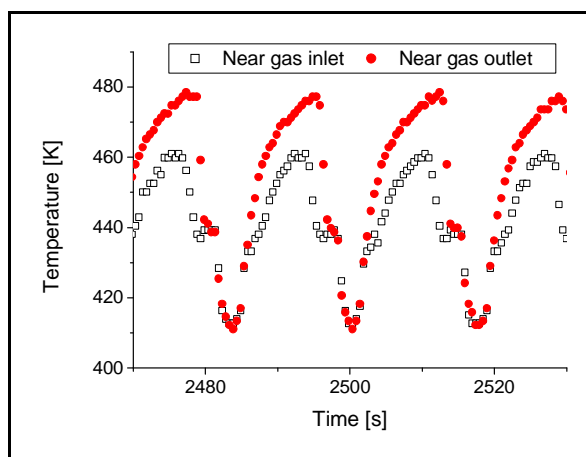


Fig. 5.4 Temperature measured by the thermocouples during temperature oscillations with a period duration of 16 seconds and a mean amplitude of 58 K

The empty squares in Fig. 5.3 and Fig. 5.4 represent the temperature measured on the SMF foil near the gas inlet and the full circles the one near the outlet.

The shortest time period (16 seconds) induces again the development of a temperature profile as in the case of the FTC-reactor type 2. The temperature values recorded near the gas inlet are always lower than near the gas outlet. This is because the measurement position at the gas inlet is simultaneously situated near the entry of the cooling water. This reactor section is cooled down directly by the cooling water flow during the cooling half-period but equally by conduction through the cold water pipes even during the heating half period. Moreover, the reactor section near the gas outlet (and thus near the cooling water outlet) is slightly worse cooled down due to the partial evaporation of the cooling water along the channels. Water vapour has a smaller heat capacity and a lower heat transfer coefficient with respect to the channel walls compared to liquid water and restrains thus the cooling efficiency.

In this case, the temperature difference measured at the end of a heating half-period did not exceed 10 to 15 Kelvin. Compared with the 85 Kelvin temperature difference recorded within the FTC-type 2 device, the gain in temperature homogeneity is non-negligible. The observed reaction rate during the experiments with the catalytic CO oxidation will be less-strongly influenced by the temperature inhomogeneity and the FTC-type 3 reactor is thus better suited for the continuation of the experimental study.

Although the clamping of the thermocouples end between the reactor top plate and the SMF foil ensures a reliable temperature measurement, this may have an influence on the hydrodynamic conditions within the reaction chamber. Indeed, the pressed thermocouples are slightly deforming the SMF foil as may be seen in Fig. 5.5.

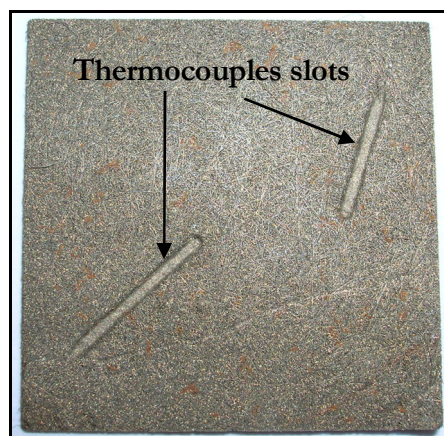


Fig. 5.5 Picture of a SMF foil with the two slots created by the clamping of the thermocouples

The two slots present on the SMF foil shown in Fig. 5.5 are the result of the clamping of the thermocouples by the reactor top plate. Even if they are filled by the thermocouples end themselves during the reaction, they may be responsible for the introduction of inhomogeneity like a by pass along the borders of the slots. For this reason, it may be preferable to realize the

temperature measurements with the thermocouples end simply pressed to the surface of the SMF foil. Fig. 5.6 presents the schematic drawing of the thermocouples new configuration.

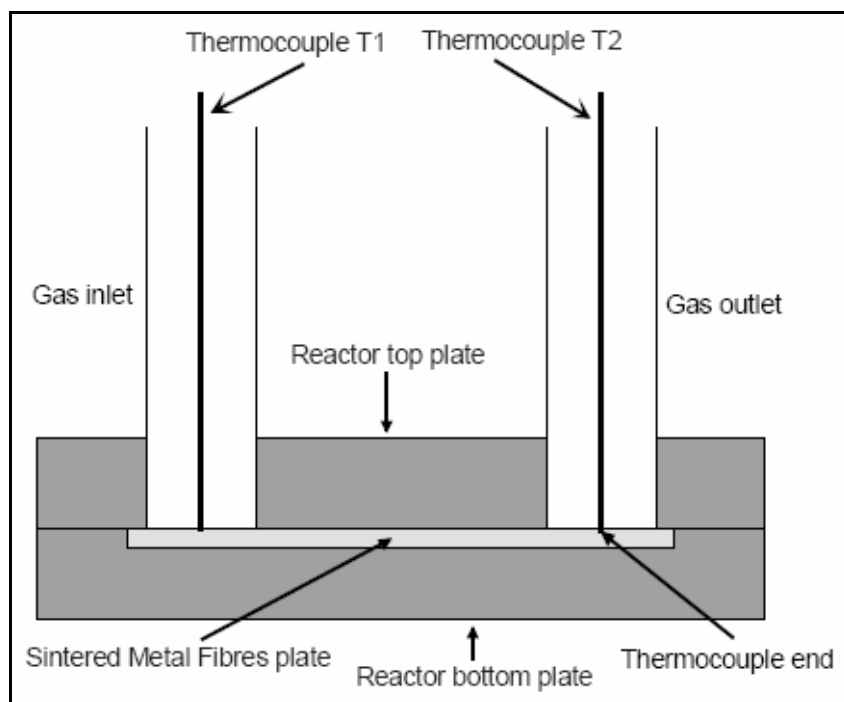


Fig. 5.6 Schematic drawing of the second configuration of the thermocouples. The ends are now simply pressed to the surface of the SMF foil

With their end only pressed to the surface of the SMF foil, the thermocouples are not anymore deforming its surface and introduce less hydrodynamic inhomogeneities. However, before performing the CO oxidation by using this temperature measurement method, it is necessary to control that the configuration change did not influence the reliability of the temperature recording by the thermocouples. For this purpose, the temperature has been measured under the same non-stationary thermal conditions (amplitude and frequency) and the recorded temperature compared. The obtained results are presented in Fig. 5.7 and Fig. 5.8.

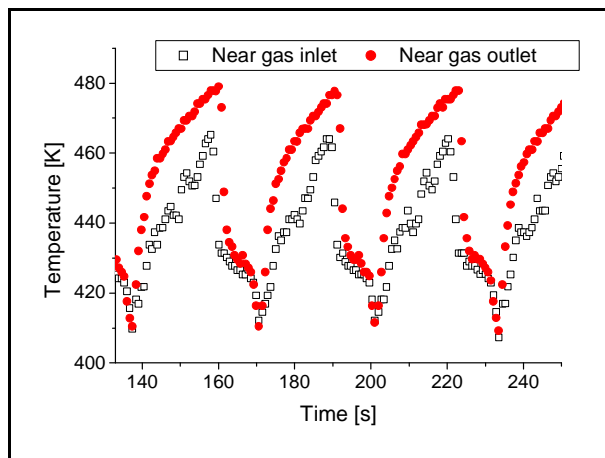


Fig. 5.7 Temperature recorded with the ends of the thermocouples pressed into the SMF foil. Period duration = 31 s, Amplitude max = 70 K

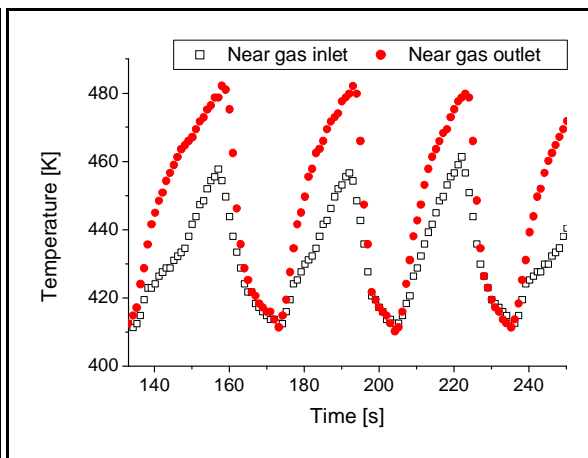


Fig. 5.8 Temperature recorded with the ends of the thermocouples pressed onto the surface of the SMF foil. Period duration = 31 s, Amplitude max = 70 K

The empty squares in Fig. 5.7 and Fig. 5.8 represent the temperature measured on the SMF foil near the gas inlet and the full circles the one near the outlet. The temperature plots shown in Fig. 5.7 were recorded with the ends of the thermocouples clamped between the reactor top plate and the SMF foil. In Fig. 5.8 the temperature was measured with the ends of the thermocouples only pressed onto the surface of the SMF foils. The same non-stationary thermal conditions were applied for the two series of measurements. The maximal amplitude of the oscillations was 70 K and the period duration 31 seconds.

The comparison of the curves of Fig. 5.7 and Fig. 5.8 shows that the different thermocouples configuration introduces only small differences. The temperature measured either with the ends of the thermocouples pressed inside the SMF foil or only at the surface shows the same tendency. The measured temperature values are approximately the same within the temperature error range. The temperature is in both configurations lower at the gas inlet and the maximal difference at the end of a heating half-period is approximately 15 Kelvin. Since the thermocouples configuration has not an important influence on the recorded temperature, the one presented in Fig. 5.6 (introducing less hydrodynamics perturbations) has been chosen for the temperature measurement during the experimental measurements with the catalytic CO oxidation.

The variation of the period duration (or frequency) of the temperature oscillations is an important parameter for the investigation of the effects of non-stationary thermal conditions on the catalytic CO oxidation. For the comparison and interpretation of the experimental results, it is crucial that when the period duration is varied while keeping the amplitude constant, the temperature profile which develops inevitably did not change. Indeed, if the temperature profile would change, this may have a non-negligible influence on the observed reaction rate and will lead to incorrect conclusions. To rule out this possibility, variations of the period duration of the temperature oscillations have been realized while keeping the amplitude constant. The obtained results are presented in Fig. 5.9 for three different periods.

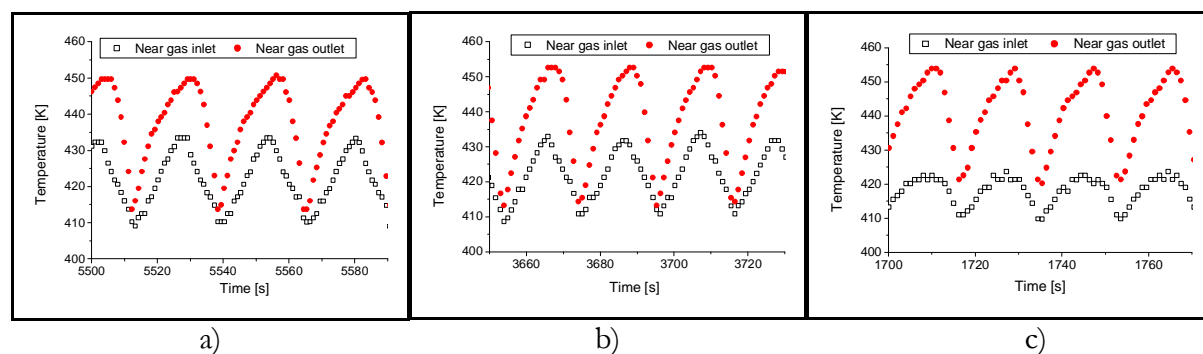


Fig. 5.9 Temperature recorded under non-stationary thermal conditions with a maximal amplitude of 40 Kelvin and a period duration of a) 26 seconds b) 21 seconds and c) 19 seconds

The squares in Fig. 5.9 a), b) and c) represent the temperature recorded by the thermocouple placed on the SMF foil at the reactor gas inlet and the circles by the thermocouple placed on the

SMF foil at the reactor gas outlet. The variation of the period duration from 26 to 19 seconds has only a marginal influence on the temperature of the reactor section situated near the gas inlet. The importance of this influence may be however better assessed if the plots of Fig. 5.9 a) to c) were placed in a dimensionless plot with respect to the time. This allows to get rid of the different period duration.

By defining a dimensionless time for the m^{th} period

$$t_{\text{adim},m} = \frac{\text{time}}{m \cdot t_p} \quad [-] \quad \text{Eq. 5.2}$$

with	time	=	measurement time	[s]
	m	=	number of the period	[-]
	t_{period}	=	period duration	[s]

the plot presented in Fig. 5.10 is obtained.

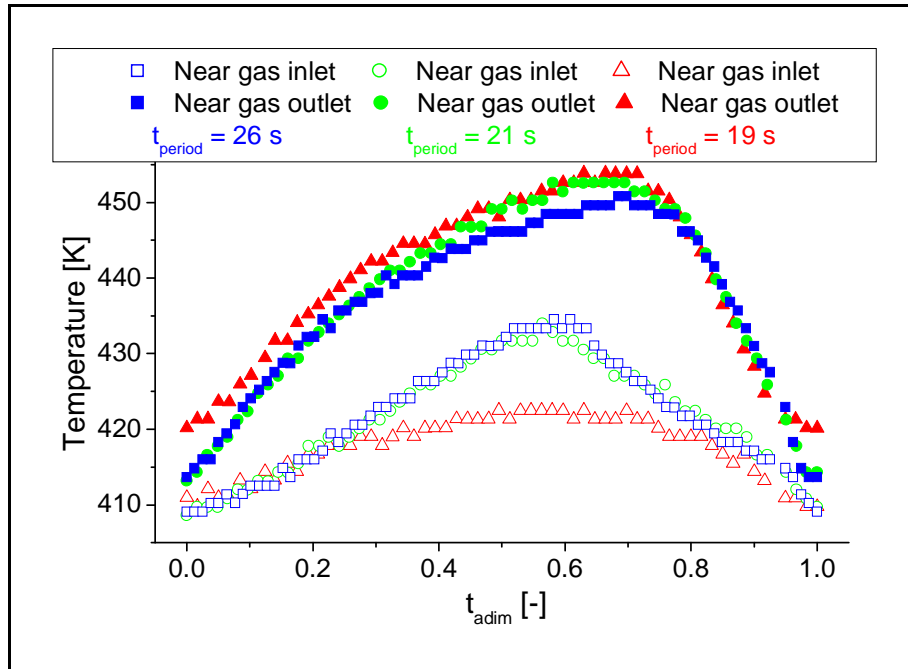


Fig. 5.10 Evolution of the temperature measured during a period represented using a dimensionless time for three different period durations.

The squares in Fig. 5.10 represent the temperature measured for a period duration of 26 seconds, the circles for 21 seconds and the triangles for 19 seconds. The empty symbols represent the temperature of the reactor near the gas inlet connexion and the full symbols near the gas outlet. This presentation allows a better comparison of the temperature curves obtained for the different period durations. The diminution of the period duration has no noticeable influence on the temperature measured near the reactor gas outlet. The situation is slightly different for the temperature measured near the reactor gas inlet. In the case of the shortest period duration the temperature did not reach the value attained at the end of a heating period for the two lower frequencies. However even in this case, this difference represents only 10 Kelvin and should not

have a too strong influence on the results obtained when performing the catalytic CO oxidation. In the worst case, this slightly colder section will marginally diminish the observed reaction rate and thus the eventual positive effects of the non-stationary thermal conditions.

5.3. CO oxidation

This chapter presents the experimental measurements performed with the FTC-reactor type 3 using the CO oxidation reaction as test reaction. In Chap. 5.3.2 the results obtained under the classical stationary thermal conditions are given. Chap. 5.3.3 and 5.3.4 respectively present the experiments realized under quasi-stationary and non-stationary thermal conditions.

5.3.1. *Reaction conditions*

All the experiments were realized using the conditions presented hereafter. This allows a straightforward comparison of the results obtained under stationary and non-stationary thermal conditions.

The total reaction gas flow was $100 \text{ ml}\cdot\text{min}^{-1}$ (STP) with 25% O_2 , 5% CO, the rest being He. The pressure at the reactor entry was 0.11 MPa and ambient at the outlet. The experiments under stationary thermal conditions have been realized between 90°C and 200°C . The lower limit of the temperature range used for the measurements under non-stationary thermal conditions was 140°C and the upper one 190°C .

The gas flow has been reduced from $300 \text{ ml}\cdot\text{min}^{-1}$ to $100 \text{ ml}\cdot\text{min}^{-1}$ in order to get a comparable conversion in the FTC-type 2 and FTC-type 3 reactors. The two different gas flows result in the same theoretical residence time in the microstructured channels of the FTC-type 2 reactor and in the reaction chamber of the FTC-type 3 reactor (see Chap. 4.1.2 and 5.1.2). The carrier gas has been changed from N_2 to He due to the use of mass spectrometry as a complimentary measurement method. Indeed, the mass spectrometer signals of CO and N_2 are both situated at the mass 28. Because of the overlapping of the signal, the use of N_2 as a carrier gas would prevent to measure the CO concentration in the gas flow. He, which MS signal is at the mass 4, is in this case a suitable substitute for N_2 .

Before starting an experimental measurement, the FTC-type 3 reactor was pre-treated similarly as the FTC-type 2. The device was heated within 2 minutes up to 250°C under a flow of $100 \text{ ml}\cdot\text{min}^{-1}$ of pure He and cooled down to the reaction temperature in order to get rid of water traces eventually adsorbed on the SMF foil.

5.3.2. *Stationary thermal conditions*

The reaction has been first conducted under stationary thermal conditions to get a basis of comparison for the results which will be obtained when applying the temperature oscillations.

Fig. 5.11 presents the CO₂ concentration measured with the FTIR spectrometer at the reactor outlet with respect to the temperature.

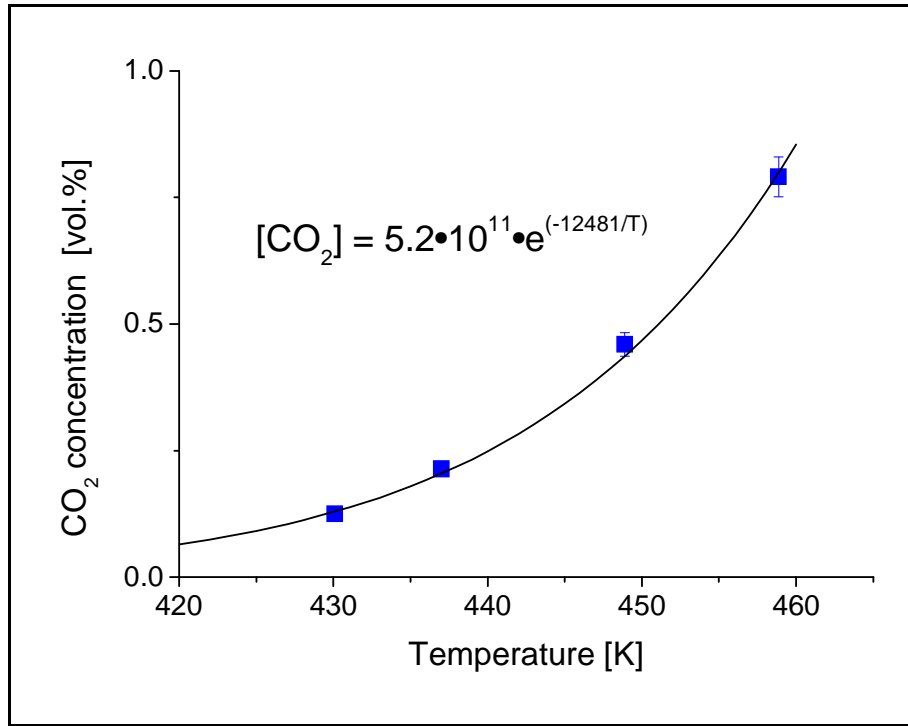


Fig. 5.11 CO₂ concentration measured with the FTIR spectrometer at the FTC-type 3 reactor outlet under stationary thermal conditions represented with respect to the temperature

The dependence of the CO₂ concentration presented in Fig. 5.11 with respect to the temperature is clearly exponential. This was theoretically awaited and consistent with the Arrhenius law presented in Eq. 2.1. As in Chap. 4.3.2, the exponent of the exponential fit shown in Fig. 5.11 is equal to $-\frac{E_a}{R \cdot T}$. The obtained apparent activation energy for the reaction is 104 kJ·mol⁻¹.

The characterization of the platinum catalyst deposited on the SMF foil by the BET measurements presented in Chap. 3.5.2 and the use of the perfect gas law allows to calculate an observed reaction rate $R_{CO_2,obs}$ per gram of active catalyst.

$$R_{CO_2,obs} = \frac{P_{outlet} \cdot [CO_2] \cdot Flow_{outlet}}{R \cdot T_{gas\ flow} \cdot M_{SMF} \cdot Cat_{load} \cdot Dispersion} \quad [mol \cdot g_{cat}^{-1} \cdot s^{-1}] \quad \text{Eq. 5.3}$$

with	P_{outlet}	=	pressure at the reactor outlet	[Pa]
	$[CO_2]$	=	Volume fraction CO ₂ in the gas flow	[vol.%]
	$Flow_{outlet}$	=	reaction gas flow at the reactor outlet	[m ³ ·s ⁻¹]
	R	=	perfect gas constant	[m ³ ·Pa·K ⁻¹ ·mol ⁻¹]
	$T_{gas\ flow}$	=	gas flow temperature at the reactor outlet	[K]
	M_{SMF}	=	mass of the SMF plate	[g]
	Cat_{load}	=	percentage of catalyst deposited	[wt.%]
	$Disp$	=	catalyst dispersion	[%]

By using a gas flow temperature $T_{\text{gas flow}}$ of 320 K and the catalyst loading and dispersion values presented in Chap. 3.5.2, the graphic presented in Fig. 5.12 is obtained for the observed reaction rate with respect to the temperature. The reactor model used for the calculations is differential due to the relatively low conversion values measured between 410 and 460 K (0 to 16%).

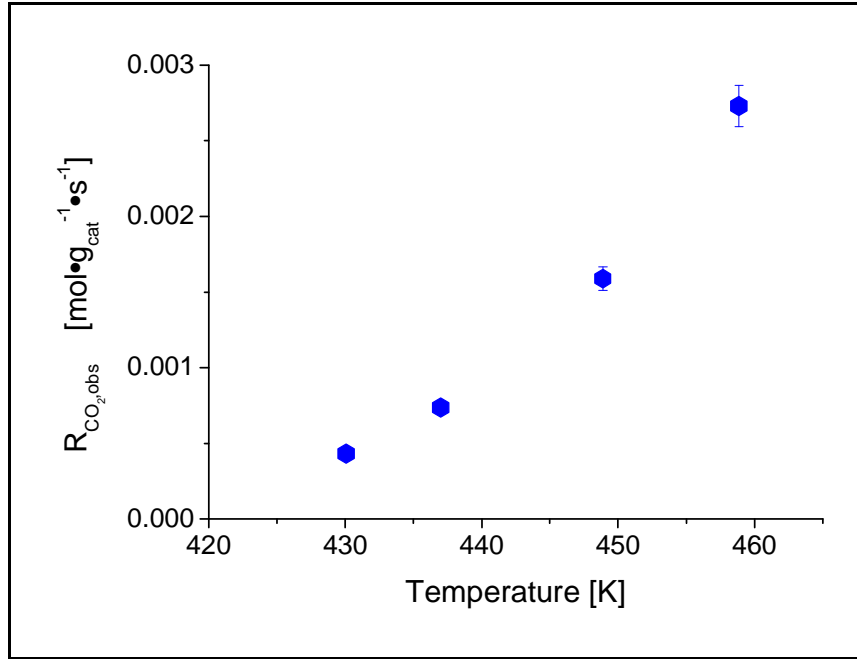


Fig. 5.12 Observed reaction rate under stationary thermal conditions represented with respect to the temperature

Since the FTC-type 3 reactor seems to be more suitable to study the catalytic CO oxidation under non-stationary conditions than the FTC-type 2 reactor, a slightly more detailed kinetic study has been realized using this device in order to better characterize the reaction behaviour under stationary thermal conditions. The information collected may also be useful for the simulations presented in Chap.6.2.

A simple formal reaction rate equation may be proposed for the catalytic CO oxidation:

$$R_{\text{CO}_2} = k_{\text{rx}} \cdot [\text{CO}]^a \cdot [\text{O}_2]^b \quad [\text{mol} \cdot \text{g}_{\text{cat}} \cdot \text{s}^{-1}] \quad \text{Eq. 5.4}$$

Since the conversion is maintained relatively low (2.4 to 16%), the concentration gradient along the reactor may be neglected and the reaction rate “ R_{CO_2} ” may be simply calculated using Eq. 5.3.

The differential conditions allow to determine the partial order “a” for CO using Eq. 5.5

$$\ln(R_{\text{CO}_2}) = a \cdot \ln([\text{CO}]) + \ln(k_{\text{rx}} \cdot [\text{O}_2]^b) \quad [-] \quad \text{Eq. 5.5}$$

By varying the CO concentration and keeping the O_2 concentration constant, a plot of $\ln(R_{\text{CO}_2})$ with respect to $\ln([\text{CO}])$ results in a straight line which slope is giving the partial order “a” for CO. As a first approach, the CO concentration has been varied only for the O_2 concentration used during the experiments under non-stationary thermal conditions (25%). A very

detailed kinetic study would also request to vary the CO concentration for different O₂ concentration in order to verify whether this influences the calculated partial order. This would, however, exceed the purpose of the measurements realized here. The graphic presented in Fig. 5.13 has been obtained at a reaction temperature of 463 Kelvin. The reactant concentration used and corresponding reaction rate values calculated are presented in Appendix F. The total volumetric flow and pressure are identical with the conditions presented in Chap. 5.3.1.

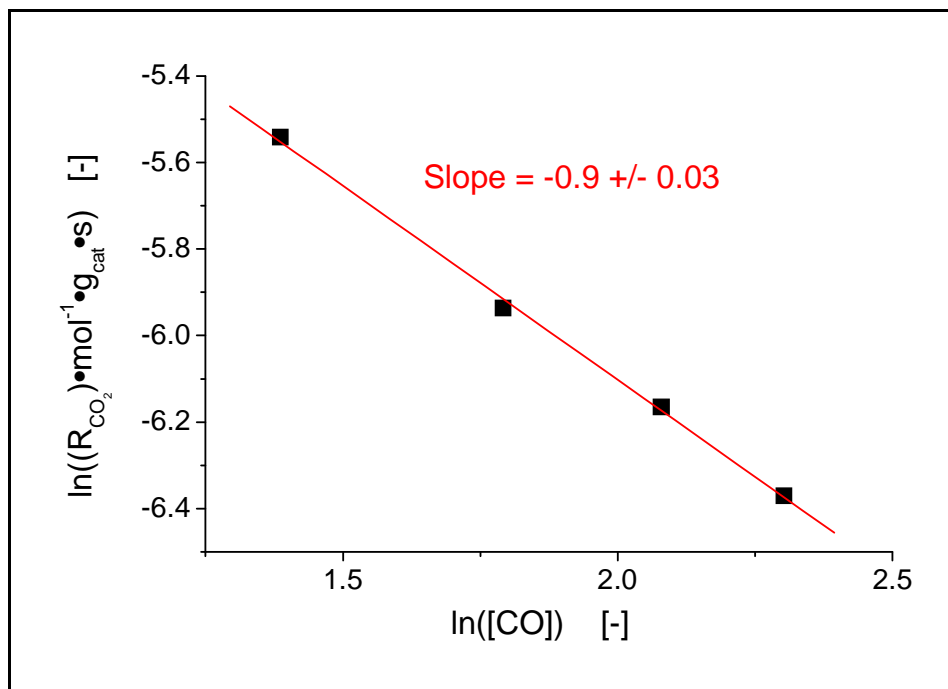


Fig. 5.13 Graphic used for the determination of the partial order for CO. Reaction temperature 463 K

Based on Eq. 5.5 and Fig. 5.13, a partial order of -0.9 for CO is determined for the reaction temperature of 463 Kelvin. This negative order near unity is consistent with values found in the literature [77, 78]. The negative order indicates that the CO molecule acts as an inhibitor for the reaction.

Based on the same assumptions, the partial order for O₂ may be determined using Eq. 5.6.

$$\ln(R_{CO_2}) = b \cdot \ln([O_2]) + \ln(k_{rx} \cdot [CO]^a) \quad [-] \quad \text{Eq. 5.6}$$

A plot of $\ln(R_{CO_2})$ with respect to $\ln([O_2])$ with a constant CO concentration gives a straight line with a slope “b”, the partial order for O₂. As for CO, the O₂ concentration has only been varied at a temperature of 462 Kelvin with the CO concentration used for the experiments under non-stationary thermal conditions (5%). The detailed reactant concentration used and corresponding reaction rate values calculated are presented in Appendix F. The plot presented in Fig. 5.14 has been obtained.

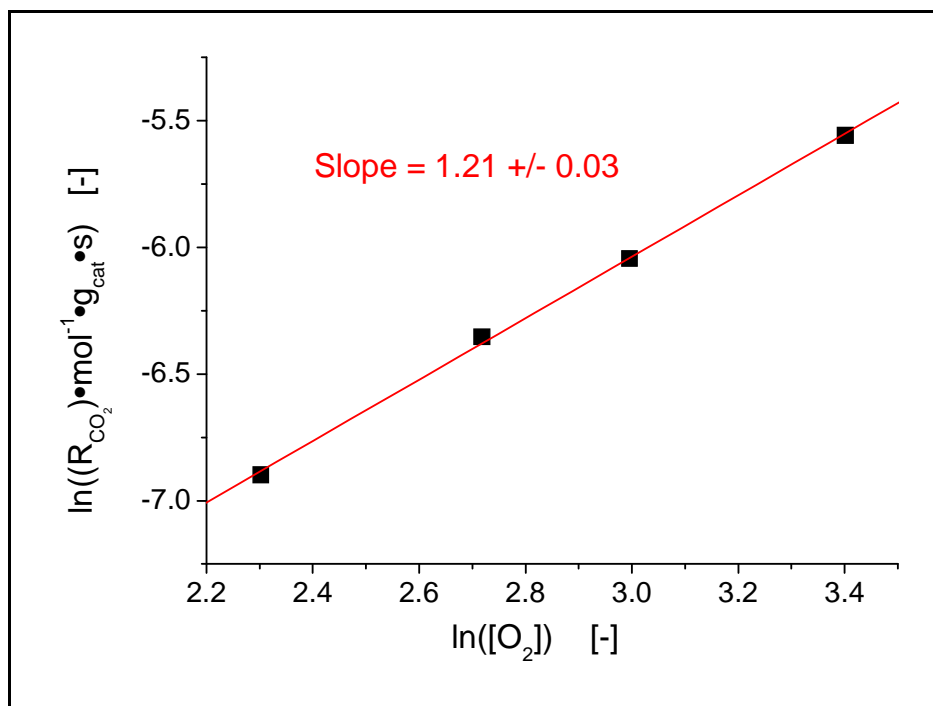


Fig. 5.14 Graphic used for the determination of the partial order for O_2 . Reaction temperature 463 K

Based on Eq. 5.6 and Fig. 5.14, a partial order “b” of 1.21 has been determined. This positive order near the unity is consistent with the values found in the literature [77, 79].

The determined partial orders allow to rewrite the reaction rate law:

$$R_{CO_2} = k_{rx} \cdot [CO]^{-0.9} \cdot [O_2]^{1.2} \quad [\text{mol} \cdot \text{g}_{\text{cat}}^{-1} \cdot \text{s}^{-1}] \quad \text{Eq. 5.7}$$

The differential method applied here for the determination of the partial orders allows formally not to calculate the reaction rate constants for the different temperatures. The conversion and thus the reactant concentration is varying from one temperature to the other and this has in turn an influence on the reaction rate. However, since the conversion is kept very low (below 16%), it may be assumed in a first approximation that the varying conversion (or reactant concentration) and temperature have only a negligible effect. By taking the reactant concentration equal to the initial concentration, the observed reaction rate values (presented in Fig. 5.12) calculated using Eq. 5.3 and substituted in Eq. 5.7 allow to calculate the reaction rate constant for the different temperatures.

Temperature [K]	Reaction rate constant [$10^{-5} \cdot \text{mol} \cdot \text{g}_{\text{cat}}^{-1} \cdot \text{s}^{-1}$]
430	4.9
437	8.4
448	18.1
458	31.1

Tab. 5.2 Reaction rate constant for different temperature

The reaction rate constants presented in Tab. 5.2 allow to calculate the apparent activation energy for the catalytic CO oxidation using the Arrhenius method. Based on Eq. 5.8

$$\ln(k_{rx}(T)) = \ln(k_{\infty}) - \frac{E_a}{R} \cdot \frac{1}{T} \quad [-] \quad \text{Eq. 5.8}$$

a plot of the logarithm of the apparent reaction rate constant with respect to the inverse of the temperature results in a straight line which slope is equal to $-\frac{E_a}{R}$. Fig. 5.15 presents the Arrhenius plot obtained using this method for a conversion between 2.4 and 16 %.

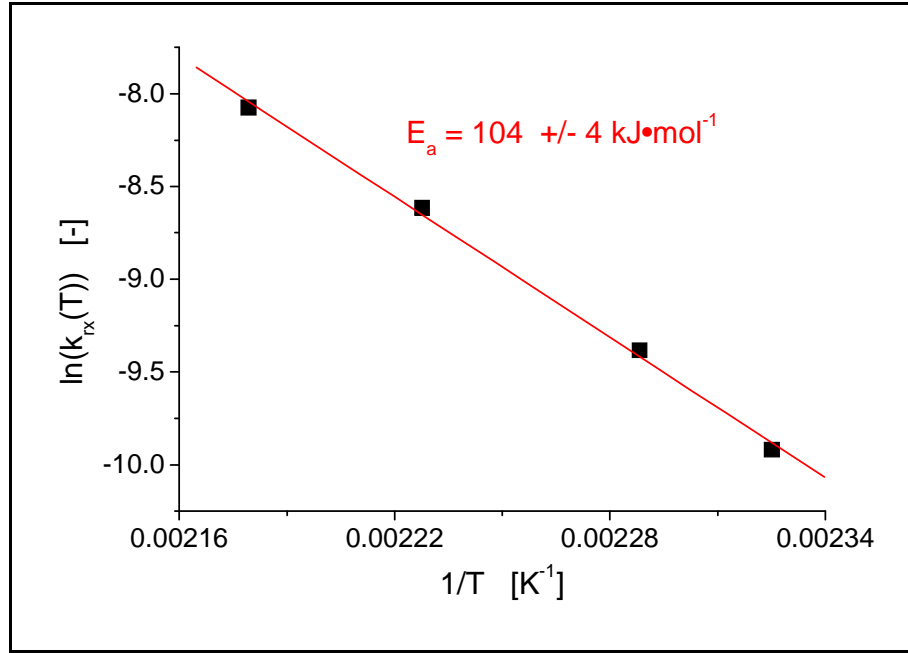


Fig. 5.15 Arrhenius plot for the determination of the apparent activation energy of the CO oxidation

The calculated value of the apparent activation energy for the catalytic CO oxidation based on the slope of the red straight line in Fig. 5.15 is $104 \text{ kJ}\cdot\text{mol}^{-1}$. This corresponds with the values mentioned in the literature by e.g. Rinnemo et al. [35] or Chorkendorff and Niemantsverdriet [71]. The corresponding values are an indication that no transfer limitations influence the observed reaction rate. The limiting step is, in this case, the surface reaction. This situation is favourable for the study of the effects of non-stationary thermal conditions since the objective is to influence the surface coverage of the reactive species. An influence of transport phenomena would considerably complicate the theoretical interpretation of the experimental results.

5.3.3. Quasi-stationary thermal conditions

After the reaction behaviour under stationary thermal conditions has been characterized, the effect of slow temperature changes has been investigated. The measurements have been realized, as in the case of the FTC-type 2 reactor, to verify whether already relatively slow temperature changes are sufficient to break the classical temperature dependence given by the Arrhenius law. For this

purpose, temperature ramps have been applied to the reactor with a heating rate of $14 \pm 2 \text{ K}\cdot\text{min}^{-1}$ and a cooling rate of $7 \pm 1 \text{ K}\cdot\text{min}^{-1}$. The difference between the heating and cooling rate is due to the fact that the cooling is in this case not active. The heater cartridges are simply turned off and the reactor cooled down passively. It is not possible to obtain slow cooling rates by using the water cooling. Using the reaction conditions presented in Chap. 5.3.1 the results presented in Fig. 5.16 have been obtained.

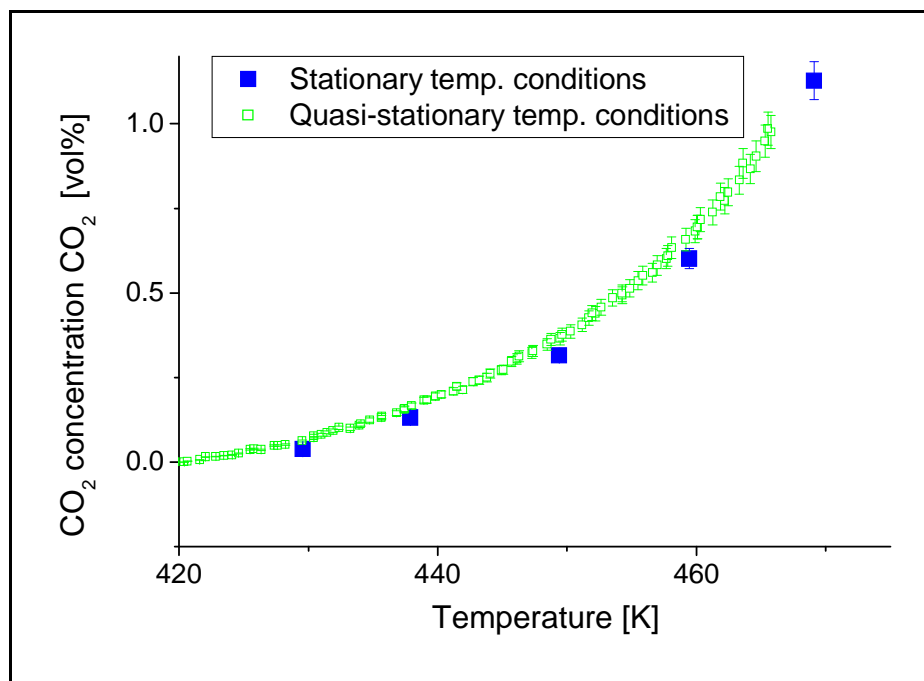


Fig. 5.16 CO₂ concentration measured by FTIR at the FTC-type 3 reactor outlet under stationary thermal conditions (full squares) and quasi-stationary thermal conditions (empty squares)

The full squares in Fig. 5.16 represent the CO₂ concentration measured under stationary thermal conditions and the open squares the one when slow temperature ramps were applied to the reactor. The CO₂ concentration was measured using the FTIR spectrometer because the concentration changes are in this case slow enough (due to the slow temperature change rate) for the sampling rate of the FTIR spectrometer to be sufficient. Since the calibration of the FTIR spectrometer is more reliable compared to the mass spectrometer, it is advantageous to use it when a not too fast concentration measurement rate is required.

As can be seen in Fig. 5.16, there is no difference between the concentration values measured under stationary and quasi-stationary temperature conditions. The dependence with respect to the temperature is in both cases exponential as predicted by the Arrhenius law. These results are similar with the one obtained using the FTC-type 2 reactor. They show that a temperature change rate in the order of magnitude of about ten Kelvin per minute is not sufficient to perturb the surface coverage of the reactive species. The phenomena involved in the catalytic CO oxidation are sufficiently rapid to follow the temperature changes. The system behaves as being always under quasi-stationary state.

The influence of faster temperature changes has then been investigated and the related results presented in Chap. 5.3.4.

5.3.4. *Non-stationary thermal conditions*

Since slow temperature variations were not sufficient to observe any non-classical effects of the temperature on the behaviour of the catalytic CO oxidation, oscillations of higher frequencies have been applied to the microstructure reactor. The experimental CO₂ concentration and temperature plots presented in Fig. 5.17 have been obtained using an amplitude of 35 Kelvin and a frequency of 0.05 Hz.

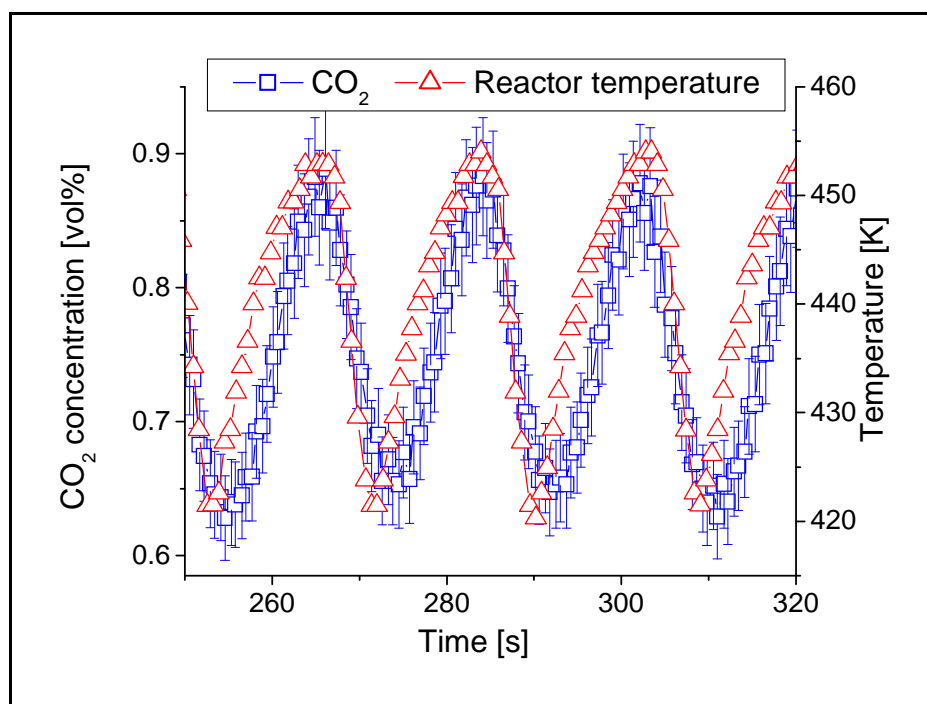


Fig. 5.17 Measured temperature near the reactor outlet (triangles) and CO₂ concentration (squares) under forced temperature oscillations with an oscillation frequency of 0.05 Hz and an amplitude of 34 Kelvin.

The squares in Fig. 5.17 represent the CO₂ concentration measured at the reactor outlet using the FTIR spectrometer. As it can be seen, the CO₂ concentration plot is in phase with the temperature plot. The CO₂ production rate is, as awaited theoretically, maximal when the temperature passes through a maximum. The triangles represent the temperature measured near the reactor outlet (see Fig. 5.6). This corresponds to the maximum temperature measured within the microstructure reactor. The maximum reactor temperature has been chosen as a basis of comparison based on a “worst case approach”. If the chosen reference temperature was the mean temperature of the microstructure reactor, potential non-trivial effects of the non-stationary thermal conditions could be attributed to the slightly higher temperature of some reactor areas with respect to the presented mean temperature value. Choosing directly the highest temperature value as a basis of comparison allows to rule out a possible “artificial” influence of the slightly

inhomogeneous reactor temperature. The effects of the fast temperature oscillations will thus be in the worst case slightly diminished and not artificially increased.

Fig. 5.17 shows that the CO_2 concentration oscillates together with the temperature. It is however relatively difficult to compare the results obtained under non-stationary thermal conditions with the ones under stationary conditions in such a graphic. The representation of the concentration with respect to the temperature is much more adequate for this comparison. The CO_2 concentration curve of Fig. 5.17 plotted with respect to the temperature is presented in Fig. 5.18.

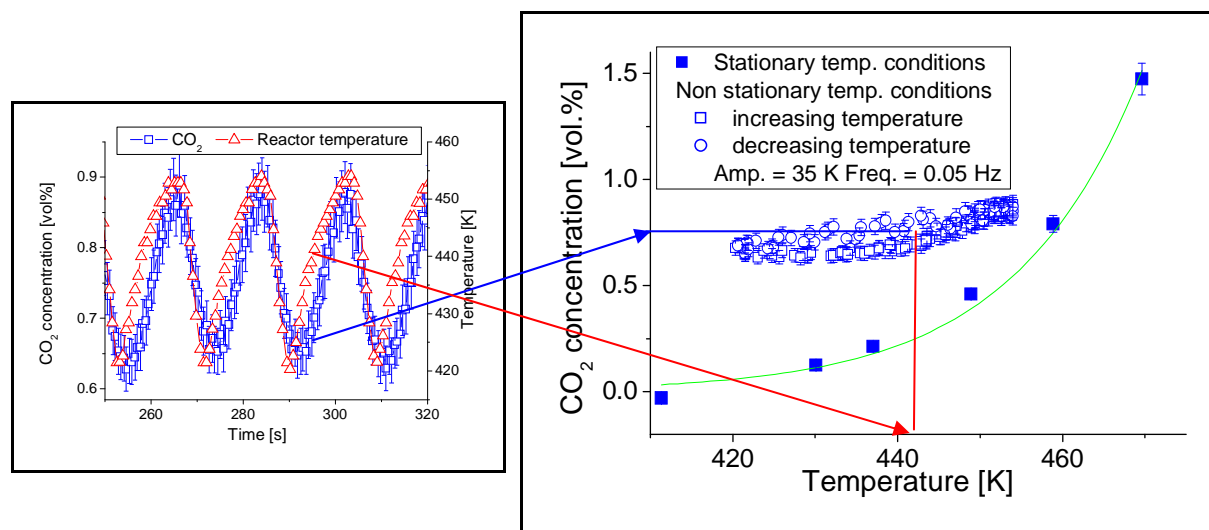


Fig. 5.18 Comparison of the measured CO_2 concentration with respect to the temperature under stationary (full squares) and non-stationary (empty squares) thermal conditions (Amplitude = 35 K, Frequency = 0.05 Hz)

The full squares in the right graphic of Fig. 5.18 represent the CO_2 concentration measured under stationary thermal conditions at the given temperature. The empty squares and circles correspond to the instantaneous CO_2 concentration measured under non-stationary thermal conditions correlated with the corresponding reactor temperature during 6 temperature cycles. The difference in the right graphic of Fig. 5.18 between the points taken during a heating and a cooling half-cycle is due to the fact that the temperature oscillations are not totally symmetrical. The cooling rate is higher than the heating rate ($5 \text{ K}\cdot\text{s}^{-1}$ vs. $3 \text{ K}\cdot\text{s}^{-1}$) and the correlation of the temperature with the corresponding CO_2 concentration is not so good during a cooling half-cycle as during a heating half-cycle. The difference in the heating and cooling rate is due to the difficult regulation of the water cooling.

Fig. 5.18 shows that for a given temperature, the measured CO_2 concentration value is higher under non-stationary thermal conditions compared to the one under stationary conditions. The fast temperature oscillations are increasing the observed reaction rate. In order to better characterize the obtained effect, the experimental measurements have been repeated using different frequencies and amplitudes. The range of frequencies and amplitude are, however, limited by the experimental

set-up. Very high frequencies induce the development of a temperature profile within the microstructure reactor. It has been seen in Chap. 4.3.5 that temperature inhomogeneities reduce, respectively eliminate, the positive effects of the temperature oscillations. Due to this limitation, the microstructure reactor type 3 does not allow to study the effects of temperature oscillations with a period length below ten seconds. Moreover, the amplitude of the oscillations is not totally independent from the frequency. Because of the finite heating and cooling capacity of the microstructure reactor, the maximum attainable temperature decreases with increasing frequency [2].

Fig. 5.19 and Fig. 5.20 present an example of the results obtained for the CO_2 concentration measured at the reactor outlet when the frequency of the temperature oscillations is varied while the amplitude is maintained constant.

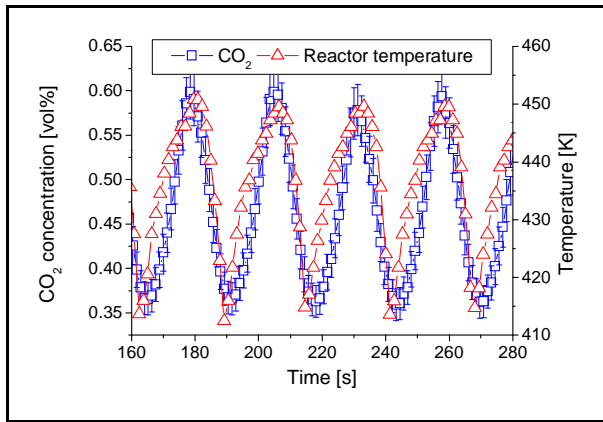


Fig. 5.19 Measured highest reactor temperature (triangles) and CO_2 concentration (circles) under forced temperature oscillations with a period duration of 26 seconds and an amplitude of 37 Kelvin.

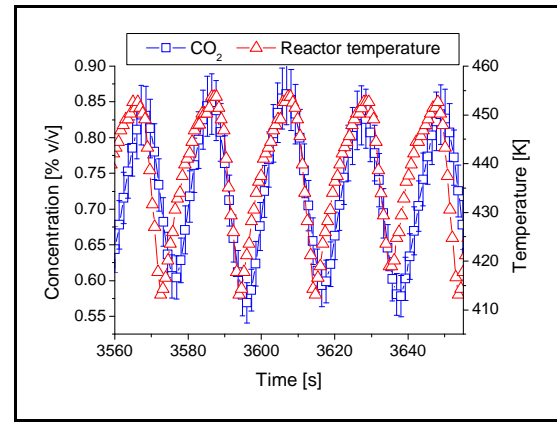


Fig. 5.20 Measured highest reactor temperature (triangles) and CO_2 concentration (circles) under forced temperature oscillations with a period duration of 21 seconds and an amplitude of 41 Kelvin.

The squares and triangles in Fig. 5.19 and Fig. 5.20 represent the same variables as in Fig. 5.17. The amplitude of the temperature oscillations is kept identical between the two measurements within the range or error but the period duration is reduced from 26 to 21 seconds. Although the maximal temperature value stays the same (approximately 450 K), the CO_2 concentration curve seems to have drifted towards higher values.

The representation of the concentration curves of Fig. 5.19 and Fig. 5.20 with respect to the maximal temperature of the reactor allows to better visualize in Fig. 5.21 the obtained effect.

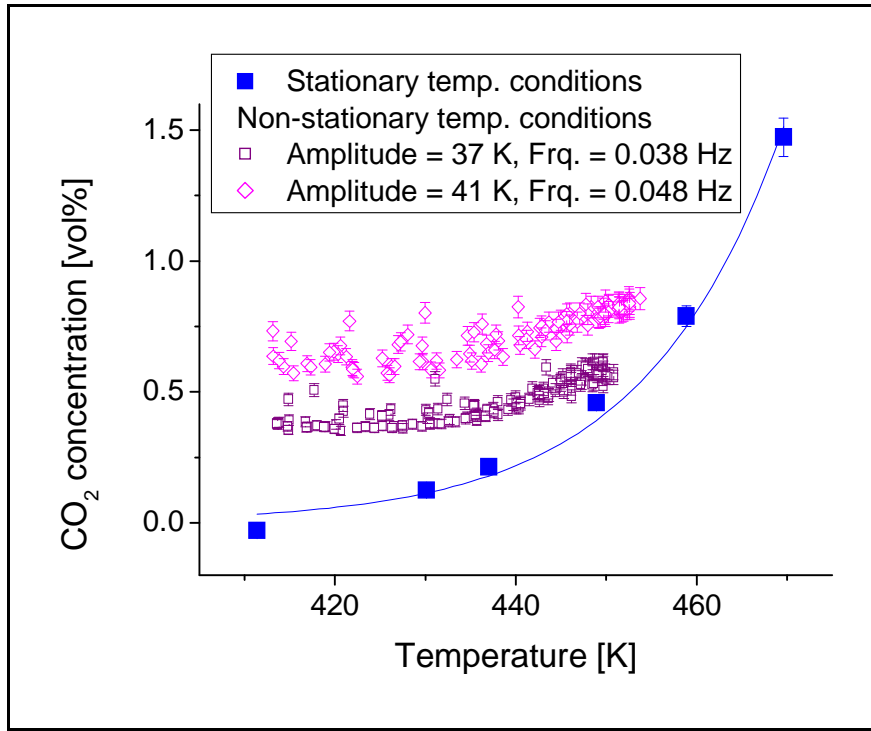


Fig. 5.21 Comparison of the measured CO_2 concentration with respect to the temperature under stationary thermal conditions (full squares) and non-stationary thermal conditions (empty squares: Amplitude = 39 K, Freq. = 0.05 Hz; empty diamonds: Amplitude = 38 K, Freq. = 0.048 Hz)

The full squares in Fig. 5.21 represent the CO_2 concentration measured under stationary thermal conditions at the given temperature. The empty squares and diamonds represent the instantaneous CO_2 concentration measured under non-stationary thermal conditions and correlated with the corresponding reactor temperature for two different frequencies of temperature oscillations. Fig. 5.21 reveals clearly that the CO_2 concentration measured under temperature cycling conditions is higher for any given temperature in the oscillation range. Moreover, for a given temperature amplitude, an increasing frequency has the tendency to amplify the effects of the temperature oscillations.

Besides the online measurement of the concentration, it is also interesting to determine the mean value obtained during a certain period of time under non-stationary thermal conditions. This value can be compared with the mean value which would have been obtained under quasi-stationary thermal conditions in order to quantify the obtained difference. Since the measured CO_2 concentration is directly proportional to the observed reaction rate, Eq. 2.4 to Eq. 2.6 are transformed into Eq. 5.9 to Eq. 5.11 to calculate the gain obtained for the mean reaction rate. With the temperature periodically oscillating between a low and a high temperature, the mean CO_2 concentration under quasi-stationary thermal conditions is defined by

$$[\text{CO}_2]_{\text{meanQSC}} = \frac{[\text{CO}_2]_{T_{\text{low}}} + [\text{CO}_2]_{T_{\text{high}}}}{2} \quad [\text{vol}\%] \quad \text{Eq. 5.9}$$

For the calculation of $[\text{CO}_2]_{\text{meanQSC}}$, the highest temperature has been chosen slightly higher (≈ 10 K) than the maximal temperature measured during the oscillations to take into account the slight asymmetry of the temperature oscillations. This slight asymmetry implies that the mean temperature is slightly higher than in the case of perfectly symmetrical oscillations. Taking the highest temperature being slightly higher under quasi-stationary conditions allows to obtain the same mean temperature as under non-stationary conditions. This avoids an overestimation of the gain obtained under non-stationary conditions.

The mean CO_2 concentration under non-stationary thermal conditions is defined by the mean over all the “g” measurements points recorded between 2 maximums or minimums of the concentration and temperature plots. With “g” being the number of measurement points recorded we have:

$$[\text{CO}_2]_{\text{meanNSC}} = \frac{\sum [\text{CO}_2]_g}{g} \quad [\text{vol}\%] \quad \text{Eq. 5.10}$$

and the gain obtained by

$$\text{Gain} = \left(\frac{[\text{CO}_2]_{\text{meanNSC}}}{[\text{CO}_2]_{\text{meanQSC}}} - 1 \right) \cdot 100 \quad [\%] \quad \text{Eq. 5.11}$$

The method used to calculate the mean CO_2 concentration under non-stationary conditions is identical to a numerical integration and is presented graphically in Fig. 5.22.

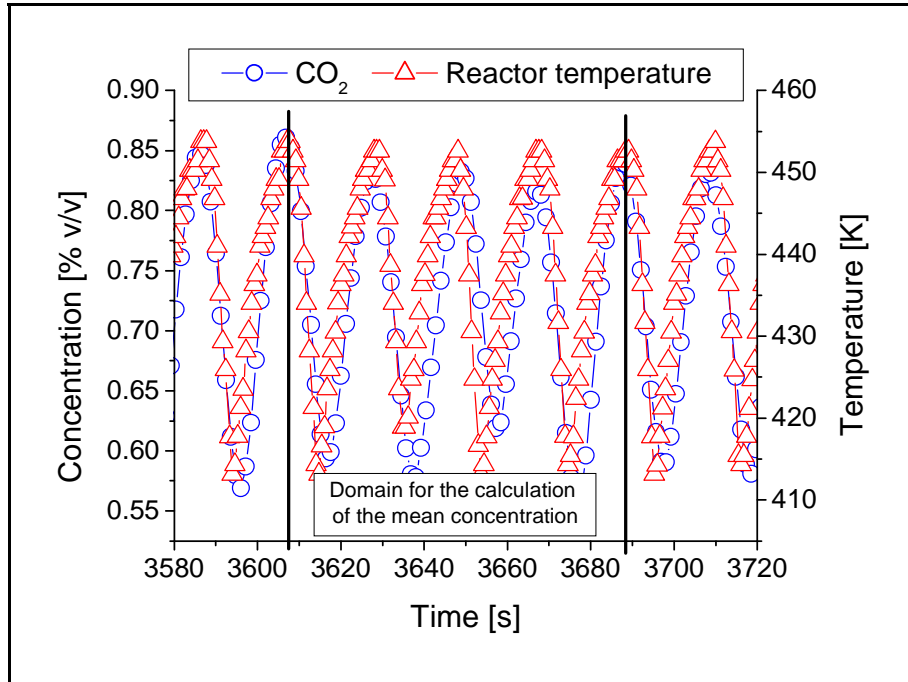


Fig. 5.22 Illustration of the method used to calculate the mean CO_2 concentration under non-stationary conditions with temperature oscillations with a period duration of 21 seconds and an amplitude of 41 Kelvin.

Fig. 5.22 presents an illustration of a domain used to calculate the mean CO_2 concentration under non-stationary conditions with temperature oscillations having a period length of 21 seconds and an amplitude of 41 K. As may be seen in Fig. 5.22, the domain is symmetrical. That is, the lower and upper borders of the domain have been chosen to correspond to a maximum in the temperature and concentration plot. This ensures that the mean concentration calculated is representative for all the cycles.

For a better comprehension, it is possible to represent the mean CO_2 concentration calculated using Eq. 5.10 and the domain illustrated in Fig. 5.22 in a graphic similar to the one presented in Fig. 2.10. The obtained results are presented in Fig. 5.23.

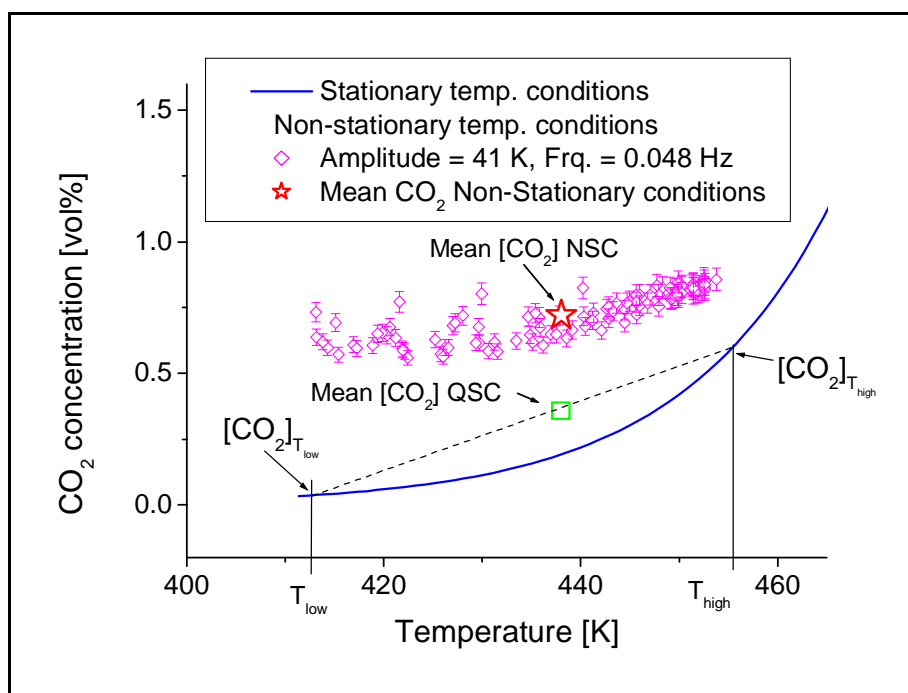


Fig. 5.23 Graphical illustration of the mean CO_2 concentration obtained under quasi-stationary temperature conditions (square) and under non-stationary conditions (star).

As in Fig. 5.21, the full line in Fig. 5.23 represents the evolution of the CO_2 concentration with respect to the temperature under stationary conditions and the diamonds the concentration measured under non-stationary conditions with the temperature oscillating between 413 and 454 K at a period length of 21 s. The empty square corresponds to the mean CO_2 concentration which would have been obtained if the reaction had been conducted under quasi-stationary conditions. The empty star corresponds to the mean CO_2 concentration obtained under the non-stationary temperature conditions.

It is clearly seen that the mean concentration under non-stationary conditions is considerably higher compared to the value obtainable under quasi-stationary conditions. The observed CO_2 concentration is even higher than the concentration measured under stationary temperature conditions at the highest reactor temperature used during the oscillations (454 K).

To quantify the improvement, the obtained gain has then been calculated using Eq. 5.11 for different frequencies of oscillations while the amplitude was kept constant as good as possible. Fig. 5.24 presents an example of the gain obtained in the mean reaction rate using temperature oscillations with an amplitude of 39 Kelvin (± 2 K) while the frequency being varied between 0.038 and 0.051 Hz.

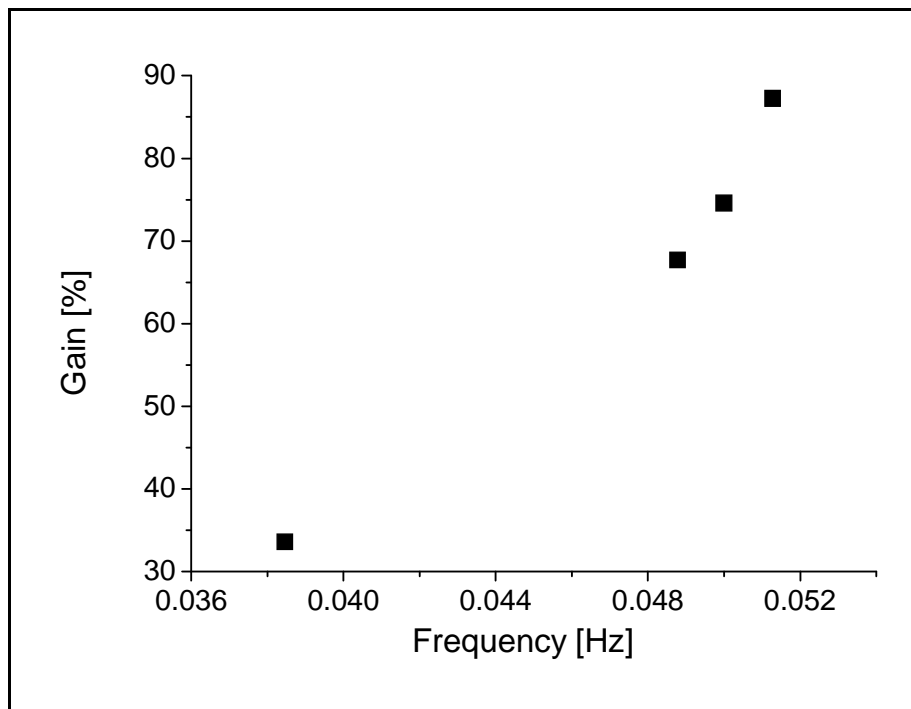


Fig. 5.24 Gain obtained calculated using Eq. 5.11 for different frequencies of temperature oscillations and a constant amplitude of 37.5 K (± 3.5 K)

The squares in Fig. 5.24 represent the gain obtained calculated using Eq. 5.11. The gain is increasing together with the frequency of the temperature oscillations. The faster the periodic temperature changes are, the more pronounced are the effects on the behaviour of the reaction. These results are similar with those obtained by Hansen et al. [38] using a silicon microstructure reactor. Since the phenomena involved in a heterogeneously catalyzed reaction (e.g. adsorption-desorption equilibrium, surface reaction) are in general very rapid, this dependency is logical. The faster the reaction conditions changes are, the more probable it is that one of the individual steps may not be able to reach a new equilibrium state. It is conceivable that the fast temperature variations of the catalytic surface are able to modify the composition of the surface coverage and thus increase the surface reaction compared to the steady state. A theoretical interpretation of the experimental results and a tentative determination of the phenomena which may be responsible are presented in Chap. 6.2.

On the other hand, the results obtained using the FTIR spectrometer to measure the CO_2 concentration are not completely satisfactory. It seems in Fig. 5.21 that the effect of the temperature oscillations is especially marked in the low temperature domain and the concentration

oscillations measured are indeed relatively small. It has been seen in Chap. 3.4.3 that the response time “ t_{50} ” of the FTIR spectrometer is in the order of magnitude of 15 seconds and the response time “ t_{90} ” is approximately 45 seconds. Since the period duration is between 9 and 13 seconds, the measured concentration oscillations are attenuated. This attenuation may complicate the theoretical interpretation of the results and the subsequent comparison with the simulations.

The response time calculated in Chap. 3.4.3 for the mass spectrometer is smaller than the one of the FTIR spectrometer. The use of the mass spectrometry as a concentration measurement method should thus solve, at least partially, the problem of the attenuation of the concentration oscillations. The reduced response time is not the only advantage of the mass spectrometer. It is also possible to measure the O_2 concentration and thus to follow online the signal of all the reactants (O_2 and CO) and the product (CO_2).

Fig. 5.25 presents an example of MS spectrometer signal for O_2 , CO and CO_2 obtained under non-stationary thermal conditions with the amplitude of the temperature oscillations equal to 38 Kelvin and the period length equal to 19 seconds.

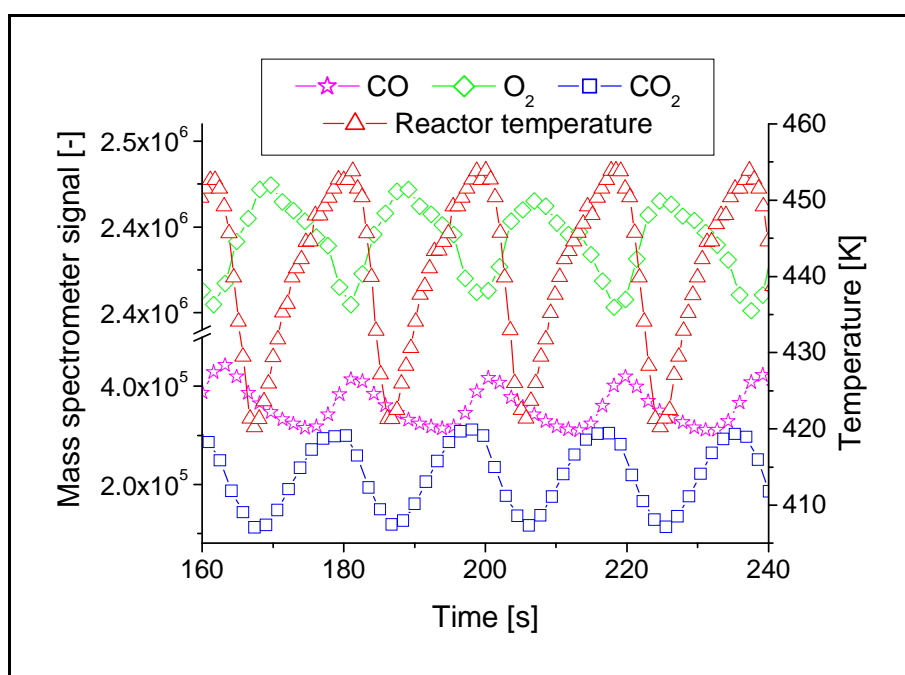


Fig. 5.25 Mass spectrometer signals intensity for CO (stars), O_2 (diamonds) and CO_2 (squares) and reactor temperature (triangles) under forced temperature oscillations with an amplitude of 38 K and a period duration of 19 seconds.

The stars in Fig. 5.25 represent the signal intensity measured for CO , the diamonds for O_2 and the squares for CO_2 . The triangles represent the maximal temperature measured inside the reactor.

Although the stability problems mentioned in Chap. 3.4.2.3 prevent to calibrate the mass spectrometer signals for CO and O_2 in a reliable way, Fig. 5.25 allows at least to make some qualitative comments on the characteristics of the measured plots. The CO_2 plot is, as in Fig. 5.17, in phase with the temperature. The production rate of CO_2 is maximal when the temperature is

maximal. When the signal intensity of CO_2 is at this maximum, there is a corresponding minimum in the intensity of the oxygen signal. This corresponds to the consumption of oxygen by the surface reaction to produce CO_2 . The fact that the two curves are exactly out of phase by one half period is an indication that no desorption effect from the surface of the catalyst influences the evolution of the concentration of the two species in the gas phase. The situation is slightly different for the CO. The periodic maxima and minima of the CO concentration curve are shifted with respect to the oxygen curve. Since CO is consumed by the surface reaction together with oxygen (even if not at the same rate), the curves should follow the same progression. On the other side, if it is assumed that the adsorption of CO on the catalyst surface is a reversible process where CO adsorbs when the temperature decreases and desorbs by increasing temperature, this could explain the increases in the gas phase CO concentration observed at the end of a heating half-period. These observations are analogous with the ones of e.g. Nibbelke et al. [42] who propose a mechanism for the CO oxidation including an adsorption-desorption equilibrium for CO and an irreversible dissociative adsorption step for the oxygen.

Based on the calibration method described in Chap. 3.4.3, it was also possible to determine an approximate CO_2 concentration using the recorded mass spectrometer signal. In Fig. 5.26 the CO_2 concentration oscillations measured using the FTIR and mass spectrometer under identical non-stationary thermal conditions (temperature amplitude = 39 K, period duration 26 seconds) are compared.

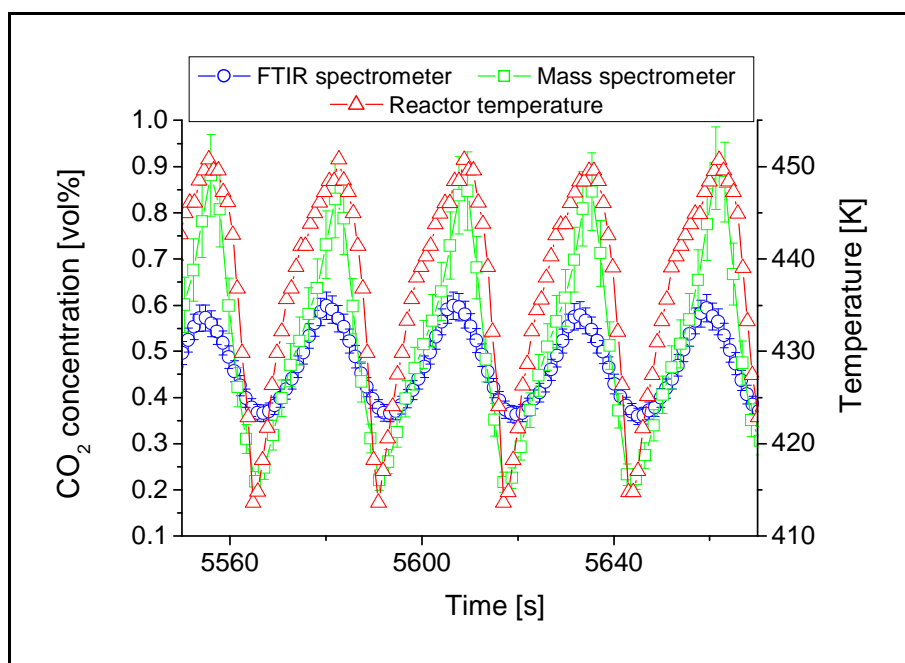


Fig. 5.26 CO_2 concentration measured under non-stationary thermal conditions using the FTIR spectrometer (circles) and the mass spectrometer (squares). Temperature amplitude = 39 K, Period duration = 26 seconds

The circles in Fig. 5.26 represent the CO₂ concentration measured using the FTIR spectrometer and the squares the one measured using the mass spectrometer. The two concentration curves are both in phase with the temperature (higher CO₂ production rate at higher temperature) but the amplitude of the oscillations recorded by the mass spectrometer is much more important (0.6 vol% versus 0.25 vol%). The comparison between the two measured curves shows that the infrared spectrometer acts, as supposed previously, as an attenuator towards the concentration oscillations. The infrared spectrometer used here is thus not a completely adequate measurement apparatus to follow online the gas phase concentration changes induced by the fast cycling of the reactor temperature.

However, even if only the mean CO₂ concentration value measured under non-stationary conditions is considered, a quantitative increase toward the value obtained under stationary conditions has been demonstrated. The first experimental measurements realized by Brandner, basis for this work, have thus been confirmed. The qualitative and quantitative information collected during the experimental work are also used in Chap. 6.2 for the theoretical interpretation of the experimental results.

6. Simulations and theoretical interpretation of the experimental results

This chapter is devoted to the theoretical investigation of the effects of non-stationary temperature conditions on heterogeneously catalyzed reactions and on the research of a possible explanation for the experimentally observed reaction rate increase presented in Chap. 5.3.4. The objective of the simulations is not to exactly reproduce the results obtained experimentally. The developed simulation programs, based for sake of simplicity on differential conditions, are not adequate for this kind of investigations. The differential conditions imply that no reactant or product concentration variations are considered and reactor parameters like the residence time or catalyst quantity do not need to be integrated in the program.

The aim is rather to reproduce the trends observed and to show that the experimentally measured reaction rate increase under non-stationary thermal conditions is theoretically conceivable. The developed simulation programs are given in Appendix G.

6.1. Monomolecular reaction

A monomolecular reaction is the simplest conceivable reaction and is therefore suitable to show if fast periodic temperature changes may actually have some non-trivial effects on the behaviour of a heterogeneously catalyzed reaction. Such a reaction may be e.g. an isomerisation or a decomposition reaction.

The following model is taken into account:



with the kinetic equations related to the model:

$$r_a = k_a \cdot C_A \cdot (1 - \Theta_A) \quad [s^{-1}] \quad \text{Eq. 6.3}$$

$$r_d = k_d \cdot \Theta_A \quad [s^{-1}] \quad \text{Eq. 6.4}$$

$$R_r = k_r \cdot \Theta_A \quad [s^{-1}] \quad \text{Eq. 6.5}$$

with

$$k_i = k_{0,i} \cdot \exp\left(\frac{-E_{a,i}}{R \cdot T}\right) \quad \text{Eq. 6.6}$$

with

$$\begin{aligned} k_{0,i} &= \text{pre-exponential factor for the step "i"} & [m^3 \cdot mol^{-1} \cdot s^{-1}] \text{ or } [s^{-1}] \\ E_{a,i} &= \text{Activation energy for the step "i"} & [kJ \cdot mol^{-1}] \end{aligned}$$

Under stationary conditions, by using the quasi-steady state approximation (QSSA)

$$\frac{d(\Theta_A)}{dt} = 0 \quad \text{Eq. 6.7}$$

the surface coverage of A “ Θ_A ” is given by

$$\Theta_A = \frac{K_A \cdot C_A}{1 + K_A \cdot C_A} \quad \text{Eq. 6.8}$$

with

$$K_A = \frac{k_a}{k_d + k_r} \quad \text{Eq. 6.9}$$

if the adsorption, desorption and surface reaction rate are of same order of magnitude. The surface reaction rate is then defined by

$$R_r = \frac{k_r \cdot K_A \cdot C_A}{1 + K_A \cdot C_A} \quad \text{Eq. 6.10}$$

Under non-stationary conditions, after a temperature change, the surface coverage evolution with the time follows

$$\frac{d(\Theta_A)}{dt} = r_a - r_d - R_r \quad \text{Eq. 6.11}$$

The consequence of Eq. 6.3 to 6.11 is that a priori no special effects are awaited from the application of fast periodic temperature changes. However, by simulating Eq. 6.3 to 6.11 under non-stationary thermal conditions and under certain conditions, it appears that a non-trivial increase in the reaction rate may be observed. For the first series of simulations, the temperature variations have been modelled using a periodic function of type step, as shown in Fig. 6.1.

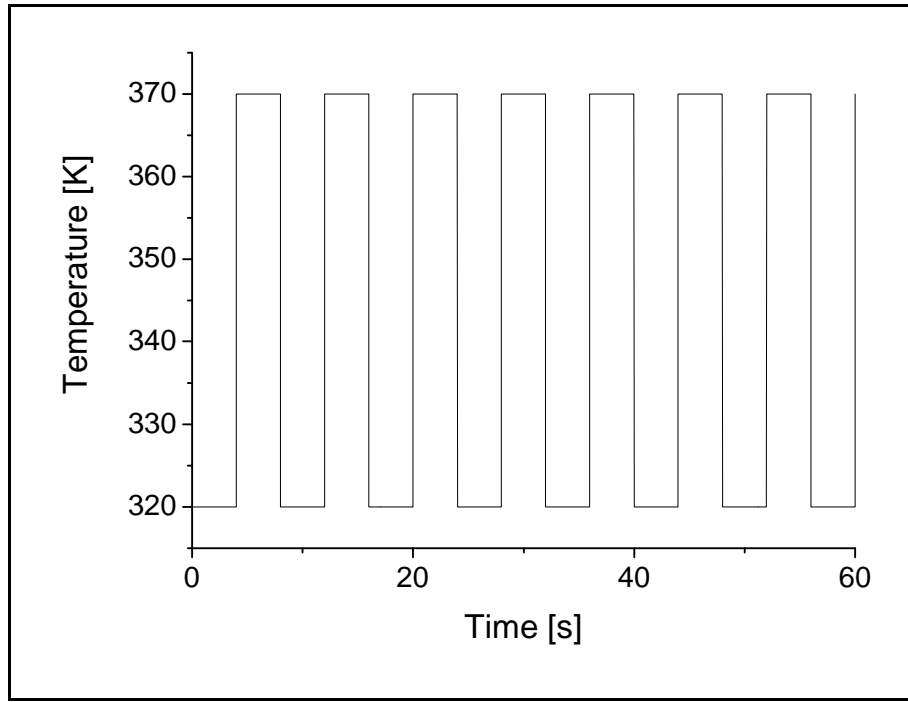


Fig. 6.1 Periodic temperature variations of type step according to the time

The choice of the kinetic parameters employed during the simulations is of crucial importance. For the simulations to have any significance, it is important to choose them as close as possible to real ones. The example of simulation results presented in Fig. 6.2 has been obtained using a set of kinetic parameters substituted in Eq. 6.3 to Eq. 6.11. Their values are mentioned in the legend at the bottom of Fig. 6.2.

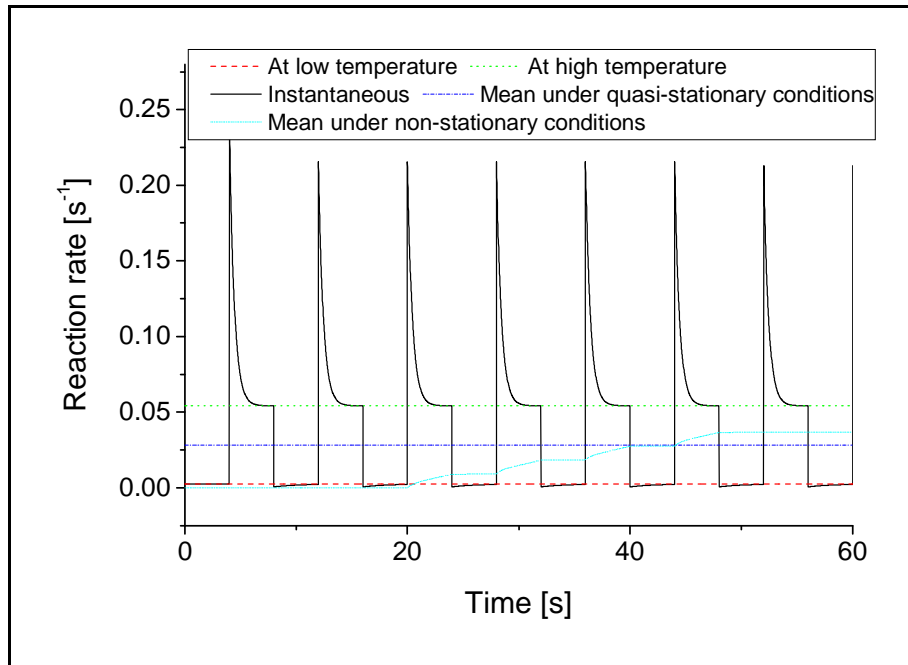


Fig. 6.2 Reaction rate at low temperature (dash), at high temperature (short dash), instantaneous (plain), mean under quasi-stationary conditions (dash-dot) and mean under non-stationary temperature conditions (dot); $k_{0,a} = 5 \text{ m}^3 \cdot \text{mol}^{-1} \cdot \text{s}^{-1}$, $E_{a,a} = 0 \text{ kJ} \cdot \text{mol}^{-1}$, $k_{0,d} = 2 \cdot 10^{14} \text{ s}^{-1}$, $E_{a,d} = 100 \text{ kJ} \cdot \text{mol}^{-1}$, $k_{0,r} = 1.25 \cdot 10^{12} \text{ s}^{-1}$, $E_r = 90 \text{ kJ} \cdot \text{mol}^{-1}$

The dashed, short dashed and dash-dotted lines in Fig. 6.2 represent the reaction rate at low temperature, high temperature and the mean under stationary state conditions, respectively. The plain line is the instantaneous reaction rate and the dotted one the mean value calculated under periodic temperature cycling conditions.

Fig. 6.2 shows that the mean reaction rate under periodic temperature variations is higher than the one which would be obtained under quasi-stationary conditions using the reaction rate at low temperature ($R_{rx}(T_{low})$) and at high temperature ($R_{rx}(T_{high})$):

$$R_{rx,meanQSC} = \frac{R_{rx}(T_{low}) + R_{rx}(T_{high})}{2} \quad [s^{-1}] \quad \text{Eq. 6.12}$$

For the chosen parameters the increase amounts to approximately 30 % and is due to the presence of a peak in the instantaneous reaction rate. This non-trivial effect can be explained with the exponential increase of the surface reaction with the temperature and the slow variation of the surface coverage as presented in Fig. 6.3.

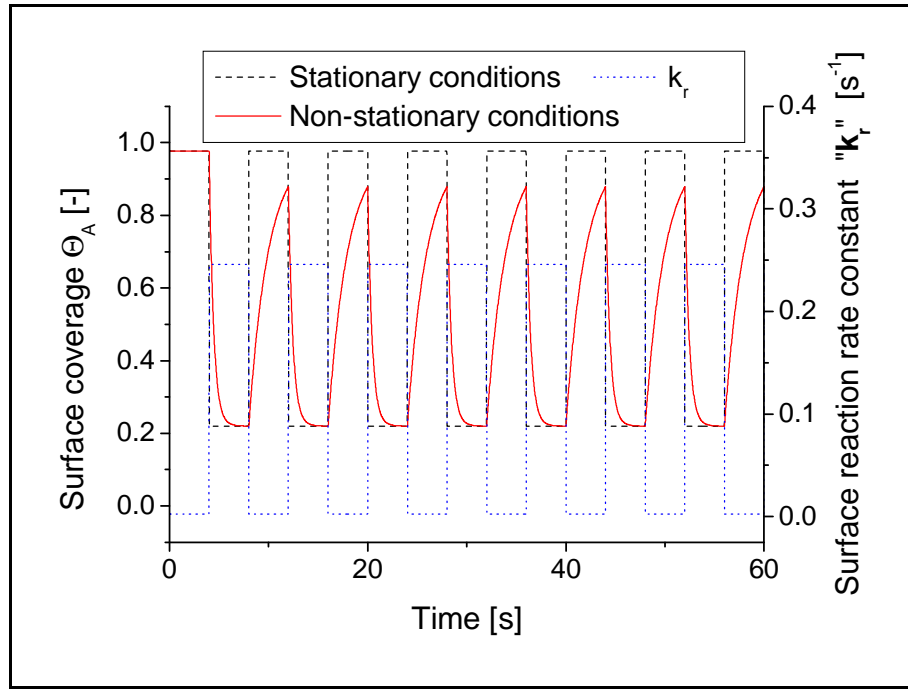


Fig. 6.3 Surface coverage of the catalyst under stationary (dash) and non-stationary (plain) temperature conditions and surface reaction rate constant k_r (dots); kinetic parameters value as in Fig. 6.2

The dashed and plain lines in Fig. 6.3 represent the surface coverage of A under stationary and non-stationary temperature conditions, respectively. The dotted line corresponds to the surface reaction rate constant.

Under stationary temperature conditions, as seen in Fig. 6.3, when the temperature is high, the value of the reaction rate constant is also high. At the same time, the surface coverage of A is low due to the displacement of the adsorption-desorption equilibrium towards the desorption. The consequence is that the surface reaction rate value is higher for the high temperature but anyway limited by the relatively low surface coverage of the reacting species.

Under non-stationary temperature conditions Fig. 6.3 shows that the change of the surface coverage value after a temperature change is not instantaneous but tends slowly towards the new equilibrium value. At the contrary, there is no inertia in the evolution of the reaction rate constant which reach instantaneously its new value. Therefore, at the beginning of a high temperature half-period, when the temperature is changed to the higher value, there is a short time period where both the surface reaction rate constant and the surface coverage are high. This results in the peak in the instantaneous reaction rate curve represented in Fig. 6.2. After a certain time, the surface coverage reaches its equilibrium value for the high temperature and the reaction rate becomes identical with the one under stationary temperature conditions.

On the contrary, during the low temperature half-period, the instantaneous surface reaction rate is slightly lower than the one at the low temperature under stationary conditions. The surface coverage is at the beginning almost equal to the one at high temperature (very low) and this, correlated with the low value of the reaction rate constant, slows down the reaction rate. The reaction rate increases then slowly together with the surface coverage of the reacting species. However, in this case it never reaches the new equilibrium value at low temperature because the next high temperature half-period starts before.

The increase of the mean reaction rate under non-stationary thermal conditions is extremely dependent on the choice of the kinetic parameters, the period or shape of the temperature oscillations and of the low and high temperature values. Fig. 6.4 illustrates what happens when the adsorption and desorption rates are both multiplied by a factor ten.

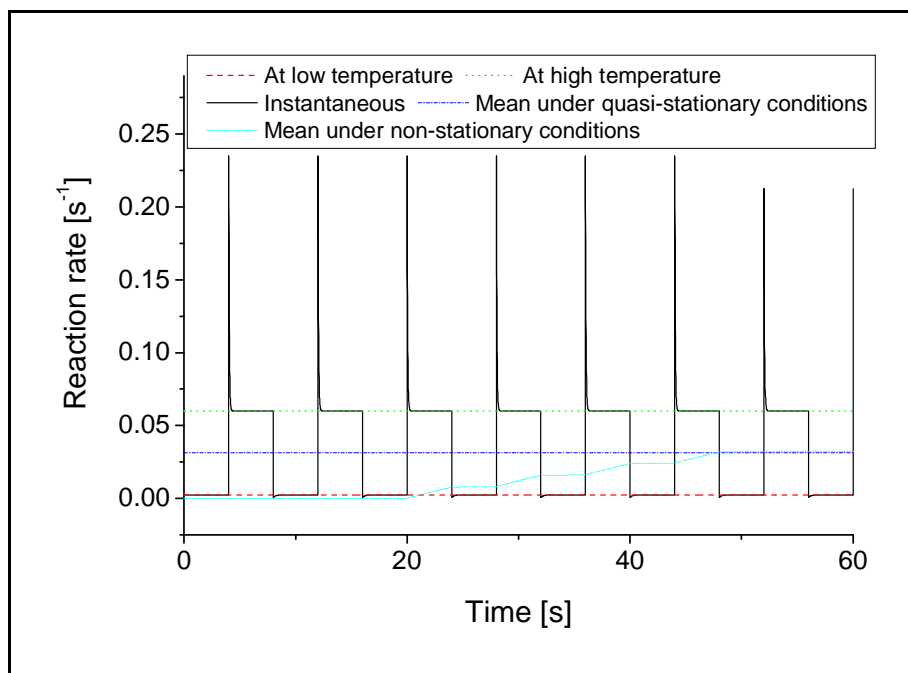


Fig. 6.4 Reaction rate at low temperature (dash), at high temperature (short dash), instantaneous (plain), mean under quasi-stationary conditions (dash-dot) and mean under non-stationary temperature conditions (dot); kinetic parameters identical with the ones in Fig. 6.2 excepting $k_{0,a} = 50 \text{ m}^3 \cdot \text{mol}^{-1} \cdot \text{s}^{-1}$ and $k_{0,d} = 2 \cdot 10^{15} \text{ s}^{-1}$

The plots in Fig. 6.4 have the same signification as in Fig. 6.2.

The mean reaction rate under non-stationary temperature conditions is now only negligibly higher compared with the one under stationary conditions ($\approx 3\%$). This is due to the fact that the peak observed in the instantaneous reaction rate curve at the beginning of a high temperature half-period is yet considerably shorter. This can be correlated with the evolution of the surface coverage presented in Fig. 6.5.

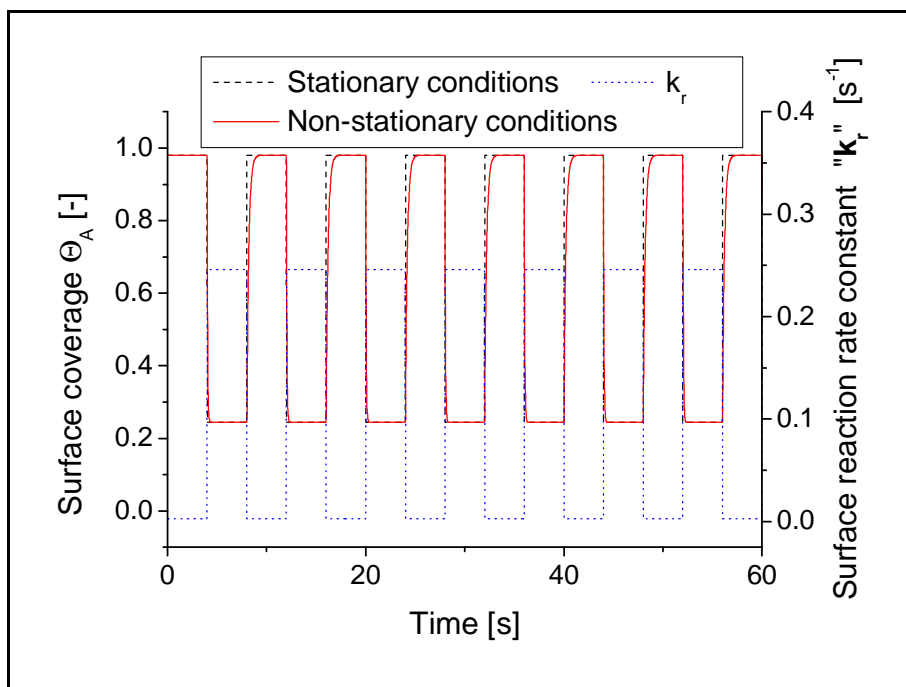


Fig. 6.5 Surface coverage of the catalyst under stationary (dash) and non-stationary (plain) temperature conditions and surface reaction rate constant k_r (dots); kinetic parameters value has in Fig. 6.4

The plots in Fig. 6.5 have the same signification as in Fig. 6.3.

The comparison of the surface coverage evolution in Fig. 6.3 and Fig. 6.5 after a temperature change shows two important differences. On one hand, during the low temperature half-period, because of the faster adsorption rate, the surface coverage can now reach the equilibrium value for the low temperature. On the other hand, when the temperature is switched to its high value, the surface coverage reaches now quasi-instantaneously its equilibrium value for the high temperature. The inertia in the surface coverage evolution is in this case quasi not existent. This explains the shortened peak in the instantaneous reaction rate curve and the reduced effect of the temperature oscillations.

Temperature changes of the type presented in Fig. 6.1 are not really realistic. The shape of the temperature changes which can be realized using a microstructure reactor is more like an exponential curve as shown in Fig. 6.6.

For the case shown here, the length of the period under periodic temperature oscillations must be in the range of the characteristic desorption rate of the reactant in order to get a measurable effect on the mean reaction rate.

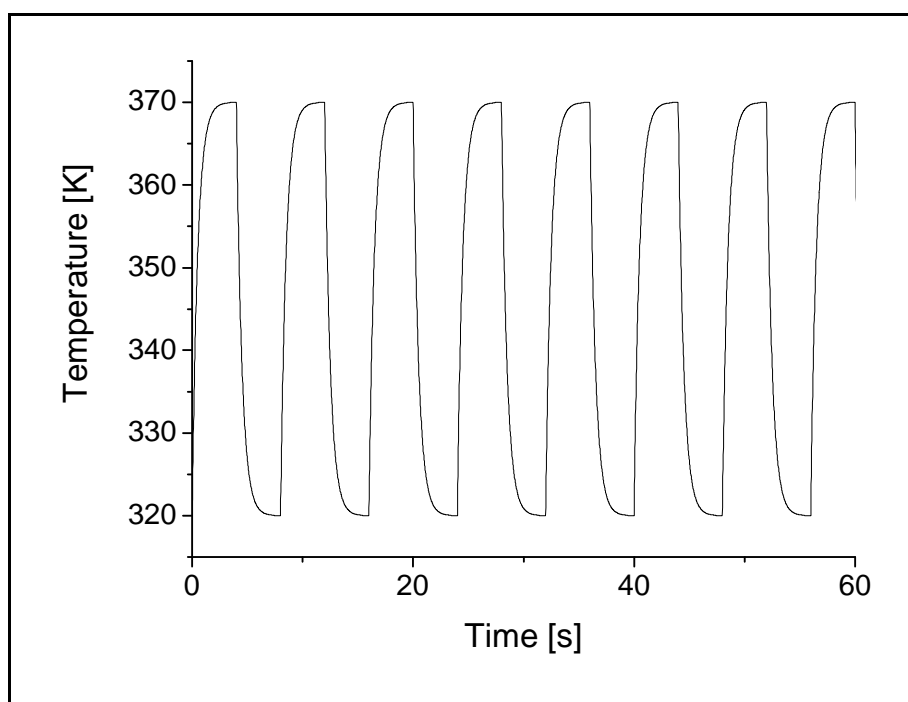


Fig. 6.6 Periodic temperature variation of exponential type according to the time

It is thus interesting to investigate what influence the type of periodic temperature changes has on the effect on the behaviour of the model reaction. Fig. 6.7 presents an example of the simulations results obtained using the same set of kinetic parameters as in Fig. 6.2 but under periodic temperature variations of exponential type instead of step type.

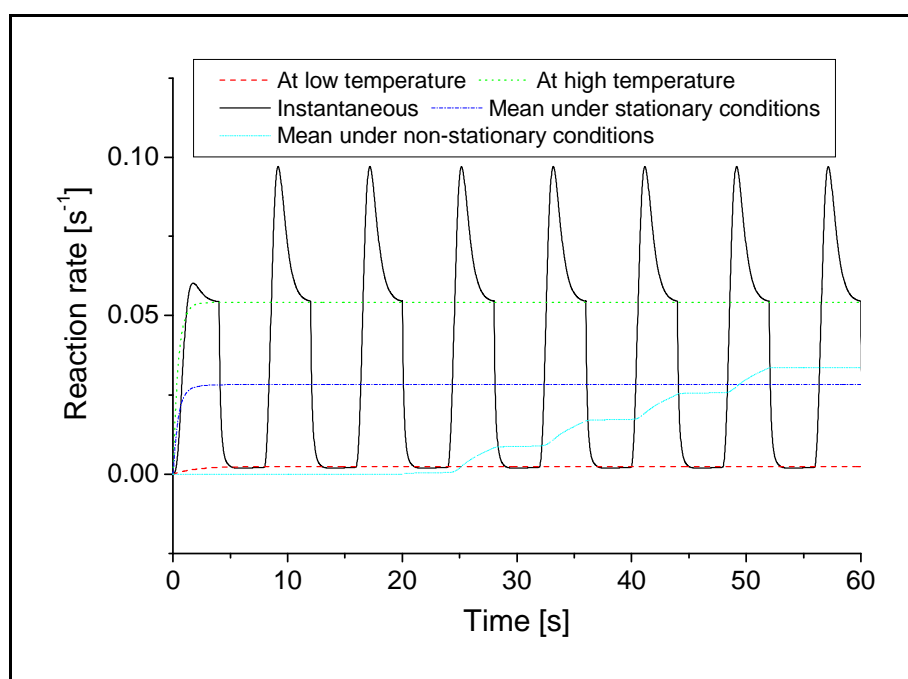


Fig. 6.7 Reaction rate at low temperature (dash), at high temperature (short dash), instantaneous (plain), mean under stationary conditions (dash-dot) and mean under non-stationary temperature conditions (dot); kinetic parameters identical with Fig. 6.2

The plots in Fig. 6.7 have the same signification as in Fig. 6.2.

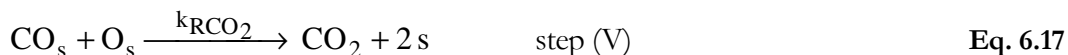
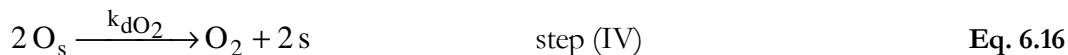
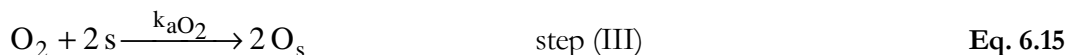
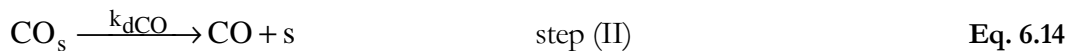
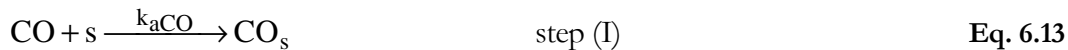
Although the temperature change rate applied to the kinetic system is now smaller, there is still a peak in the instantaneous reaction rate curve. The corresponding calculated increase of the mean reaction rate under non-stationary conditions compared to the one under quasi-stationary conditions is in this case approximately 20 %. The temperature changes are still rapid enough to take advantage from the inertia in the surface coverage evolution after a temperature change.

The preliminary simulations realized using the simple case of a monomolecular reaction have theoretically shown that temperature cycling conditions may lead to a non-trivial increase in the mean reaction rate compared to the one obtained under quasi-stationary conditions. To obtain this increase, it is necessary that at least one step implied in the kinetic scheme is slow enough to be influenced by the temperature changes. In the case of the monomolecular reaction studied here, if the desorption rate is too rapid, the surface coverage of the reactive species will reach too quickly the low equilibrium value for the high temperature and no beneficial transient state occurs on the catalyst surface.

For a more complex reaction like a bimolecular one as the CO oxidation, a much more complex behaviour is awaited. However, the main principle remains the same. It is necessary that at least one phenomenon implied in the reaction scheme is slow enough to be influenced by the temperature changes. Chap. 6.2 is dedicated to the simulations of the CO oxidation under non-stationary thermal conditions to tentatively explain the experimentally observed increase presented in Chap. 5.3.4.

6.2. CO oxidation reaction

The CO oxidation is one of the most studied catalytic reactions during the past decade and many mechanism propositions may be found in the literature. Despite its apparent simplicity, this reaction is well known to show self-sustained oscillations under certain conditions [47, 48]. Although the mechanism explaining the presence of these self-oscillations is still not undoubtedly determined, the following steps are widely accepted as basic mechanism [35, 42, 43].



The kinetic equations related to this model are

$$r_{aCO} = k_{aCO} \cdot P_{CO} \cdot \Theta_v \quad \text{Eq. 6.18}$$

$$r_{dCO} = k_{dCO} \cdot \Theta_{CO} \quad \text{Eq. 6.19}$$

$$r_{aO_2} = k_{aO_2} \cdot P_{O_2} \cdot (\Theta_v)^2 \quad \text{Eq. 6.20}$$

$$r_{dO_2} = k_{dO_2} \cdot (\Theta_O)^2 \quad \text{Eq. 6.21}$$

$$R_{CO_2} = k_{RCO_2} \cdot \Theta_{CO} \cdot \Theta_O \quad \text{Eq. 6.22}$$

with

$$\begin{aligned} \Theta_i &= \text{surface coverage of the "i" species} & [-] \\ \Theta_v &= \text{surface coverage of the vacant active sites} & [-] \end{aligned}$$

The balance on the active site of the catalyst is given by

$$1 = \Theta_v + \Theta_{CO} + \Theta_O \quad \text{Eq. 6.23}$$

The rate constant of the individual steps is calculated using the Arrhenius law shown in Eq. 6.6.

The model is of Langmuir-Hinshelwood type with a reversible adsorption of CO and O₂ on the catalyst surface followed by a surface reaction between adsorbed CO molecules and oxygen atoms. The model considers a competitive adsorption for CO and O₂ with only one type of active site on the surface where CO and O₂ adsorb. The CO₂ formed interacts only weakly with the surface [43, 46] and thus desorbs immediately from the catalyst surface. Its surface coverage may be considered to be zero.

To explain the appearance of self-oscillations, it would be necessary to include a relatively slow and non linear feed-back step [48] into the above mechanism. The Langmuir-Hinshelwood mechanism itself is not sufficiently non-linear to show a complex dynamic behaviour. The situation in the case of forced temperature oscillations is slightly different. Due to the strongly non-linear temperature dependence of the rate constant of the different steps, oscillations are easily induced without the need to introduce any supplementary step.

To perform the simulations, it is necessary to attribute a numerical value to each of the kinetic parameters of the model. One solution would be to take the parameter values from the literature. A broad variety is available about the CO oxidation reaction. However, generally applicable kinetic parameters for the individual steps are missing even for the basic reaction mechanism. The kinetic parameters are very much dependent on the experimental conditions like the catalyst studied, partial pressure of the reactants or whether the reaction had been performed under Ultra High Vacuum or atmospheric pressure. Moreover, in general, kinetic constants determined under

stationary thermal conditions can not be applied under non-stationary thermal conditions without any restrictions [80]. To illustrate the wide range of values, some kinetic parameters found in the literature are listed in Tab. 6.1.

Step	$k_{0,j}$ [see footer*]	$E_{a,j}$ [kJ·mol ⁻¹]	Reference
(I)	$1.6 \cdot 10^8$	0	[35]
	$6.02 \cdot 10^4$	0	[47]
(II)	$3.0 \cdot 10^{14}$	150.7	[81]
	$1 \cdot 10^{14}$	134	[69]
(III)	$7.2 \cdot 10^6$	0	[35]
	$1.5 \cdot 10^{11}$	21	[82]
	$1.9 \cdot 10^5$	4.2	[47]
	$3.3 \cdot 10^6$	0	[83]
(IV)	$2.2 \cdot 10^8$	240	[80]
	$1.0 \cdot 10^{13}$	213.2	[84]
(V)	$1.0 \cdot 10^{12.7}$	103	[69]
	$1.0 \cdot 10^{7.3}$	67	[69]

Tab. 6.1 Different kinetic parameters values found in the literature for the CO oxidation reaction

Even if the values presented in Tab. 6.1 are much dispersed for each step, they are useful to get an idea about the proper order of magnitude and sequence. The activation energies of the different steps are a priori following the sequence $E_{a,(I)} \approx E_{a,(III)} < E_{a,(V)} < E_{a,(II)} < E_{a,(IV)}$ with the activation energy of steps (I) and (III) being relatively close or equal to zero. This type of information is useful to assess whether the parameters determined using the simulations presented hereafter are plausible or not.

The model has been first simulated under stationary thermal conditions to test whether it was adequate to quantitatively reproduce the experimentally measured reaction rate and to determine the adequate kinetic parameters for the individual steps. Fig. 6.8 presents the comparison of the simulation curve with the experimental results.

* Pre-exponential factors of step (I) and (III) are in [s⁻¹·bar⁻¹], the rest of pre-exponential factors in [s⁻¹]

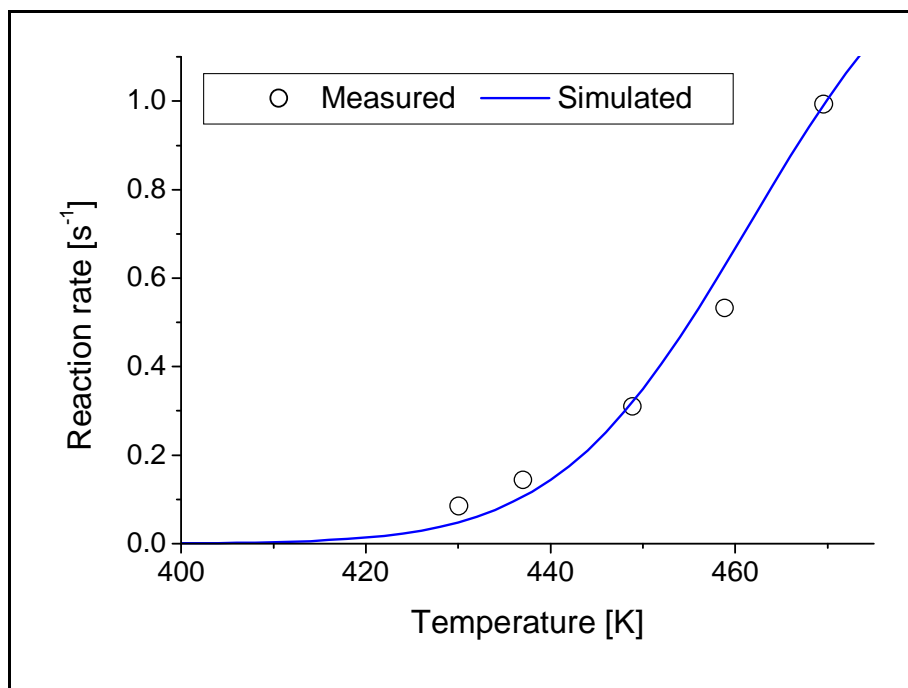


Fig. 6.8 Comparison of the experimental reaction rate (circles) with the simulated one (line).

The circles in Fig. 6.8 represent the experimental reaction rate and the line the simulated one. The comparison shows that the simulated simple model reproduces in a satisfying way the temperature dependence of the reaction rate. This model is, thus, adequate to investigate the effects of non-stationary thermal conditions. The fitting of the experimental results under stationary conditions has been realized using the parameters given in Tab. 6.2.

Step	$k_{0,j}$ [see footer [†]]	$E_{a,j}$ [kJ·mol ⁻¹]
(I)	$5.9 \cdot 10^5$	0
(II)	$4.8 \cdot 10^{13}$	102
(III)	$3.4 \cdot 10^5$	0
(IV)	$2 \cdot 10^{13}$	213
(V)	$3.8 \cdot 10^{10}$	89

Tab. 6.2 Parameters used in the simulations based on the basic model

The kinetic parameters determined are consistent with that presented in Tab. 6.1. The adsorption of CO and O₂ is nearly non-activated and the activation energies of the remaining steps are following the sequence mentioned on p. 93. The orders of magnitude of the pre-exponential factors are also similar to the ones shown in Tab. 6.1.

Before investigating the behaviour of the reaction under non-stationary conditions, it is useful to examine the evolution of the surface coverage and reaction rate under stationary conditions with

[†] Pre-exponential factors of step (I) and (III) are in [s⁻¹·bar⁻¹], the rest of pre-exponential factors in [s⁻¹]

respect to the temperature. The simulation results presented in Fig. 6.9 have been obtained by varying the temperature between 380 and 540 K.

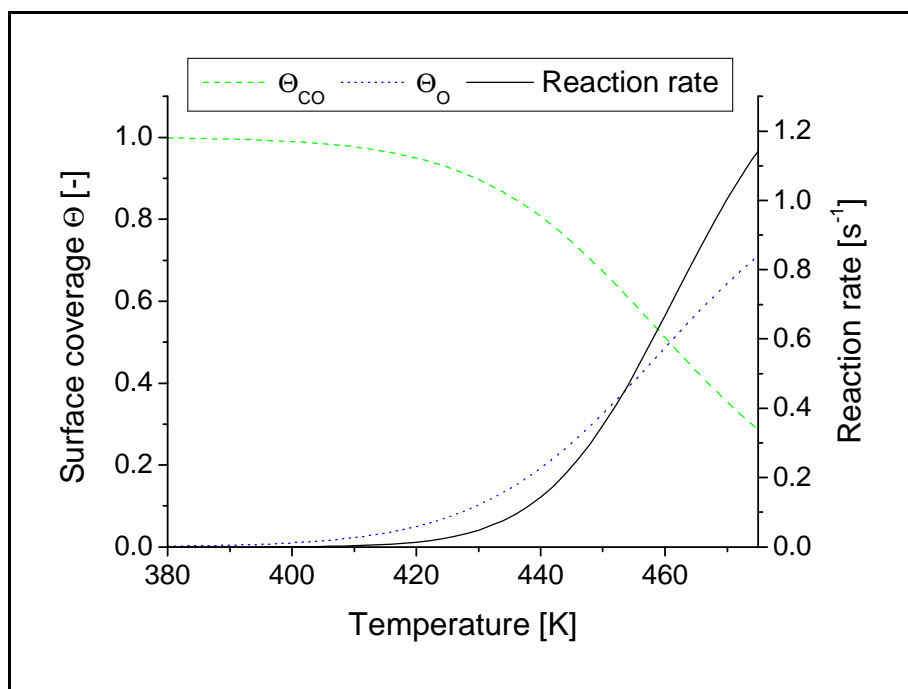


Fig. 6.9 Evolution of the surface coverage of CO (dashed line), oxygen atoms (dotted line) and reaction rate (plain line) with respect to the temperature under stationary temperature conditions.

The dashed line in Fig. 6.9 represents the surface coverage of CO and the dotted line the one of the oxygen atoms. The plain line corresponds to the surface reaction rate.

As may be seen in Fig. 6.9, the surface coverage of CO is near the unity at low temperature and goes down when the temperature increases. The surface coverage of the oxygen atoms behaves exactly in the contrary way, starting with a low value at low temperature and going towards a high value at high temperature. This is due to the lower activation energy of the desorption of CO compared to the one for the desorption of oxygen. At low temperature, CO is preferably adsorbed on the surface due to the highest value of the adsorption rate compared to the oxygen one. When the temperature increases, the desorption rate of CO becomes non negligible and the desorbing CO molecules let some place on the catalyst surface for the adsorption of oxygen. Due to the very high value of the activation energy for the oxygen desorption, only a negligible amount desorbs even at high temperature. The oxygen atoms occupy thus much more active sites of the catalyst at high temperature.

Based on Eq. 6.21, it is obvious that the optimal surface coverage value for the surface reaction rate is 0.5 for the CO molecules and 0.5 for the oxygen atoms. However, in Fig. 6.9, the reaction rate curve still increases above 460 K which is the temperature where the surface coverage of the molecules is theoretically optimal ($\Theta = 0.5$ for the CO molecules and O atoms). This happens because not only the surface coverage values are changing with the temperature but equally the surface reaction rate constant which is increasing with the temperature. Under non-stationary

thermal conditions the surface coverage of the reacting species oscillates probably between the values at the high and low temperature. It would be thus possible for the instantaneous surface coverage to get some values which are more favourable than the coverage at the optimal steady-state temperature and increase thus the maximal reaction rate obtained.

The validity of this supposition has been tested by simulated the same model under non-stationary thermal conditions using the kinetic parameters presented in Tab. 6.2. The simulations have been realized using periodic temperature changes of exponential type (as in Fig. 6.6) between 430 and 470 K. The temperature changes of exponential type are closer to the form of the experimental temperature changes than the step type ones. Fig. 6.10 presents an example of the simulation results obtained with an oscillation period of 10 seconds.

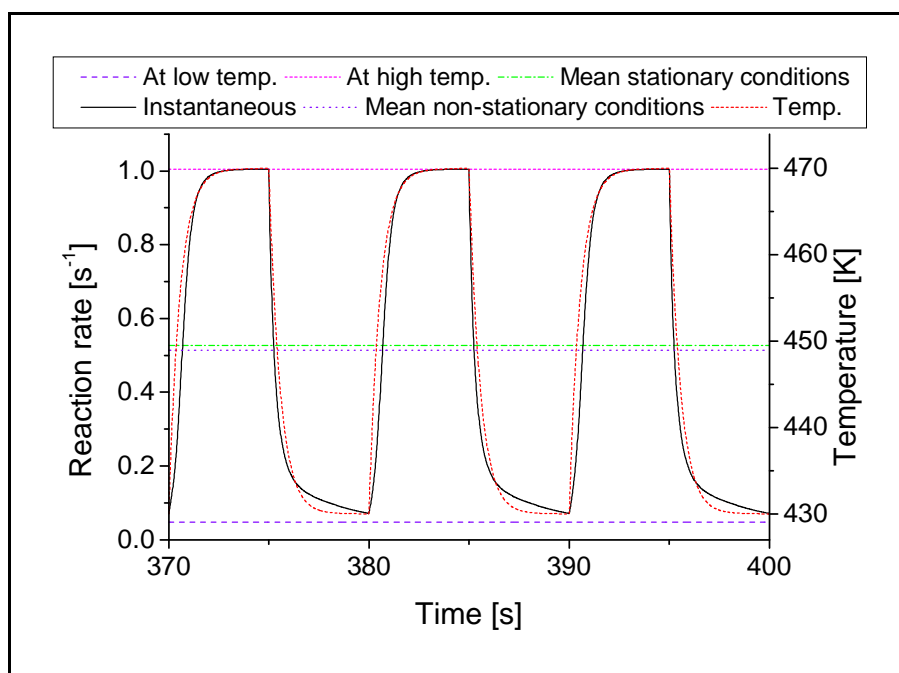


Fig. 6.10 Simulated reaction rates at low temperature (dashed line), at high temperature (short dashed line), instantaneous (plain line), mean under stationary conditions (dash-dotted line) and mean under non-stationary temperature conditions (dotted line) and temperature (short-dashed line)

The dashed, short dashed and dash-dotted lines in Fig. 6.10 represent respectively the reaction rate at low temperature, high temperature and the mean under stationary state conditions. The plain plot is the instantaneous reaction rate and the dotted one the mean value calculated under periodic temperature cycling conditions. The short-dashed line is the temperature plot.

Fig. 6.10 shows that the mean reaction rate value under non-stationary temperature conditions is close to the mean reaction rate value under stationary temperature conditions. There is no noticeable increase due to the application of the periodic temperature changes. This is due to the fact that the instantaneous reaction rate follows closely the temperature plot without any non-trivial effects. The fact that the mean reaction rate under non-stationary conditions is even slightly lower than the mean reaction rate under stationary conditions is due to the very small shift observed

between the evolution of the temperature and reaction rate plots when the temperature increases. Otherwise, it seems that the system behaves as being always under stationary conditions. This may be verified by looking at the evolution of the surface coverage of CO and oxygen under the non-stationary conditions represented in Fig. 6.11.

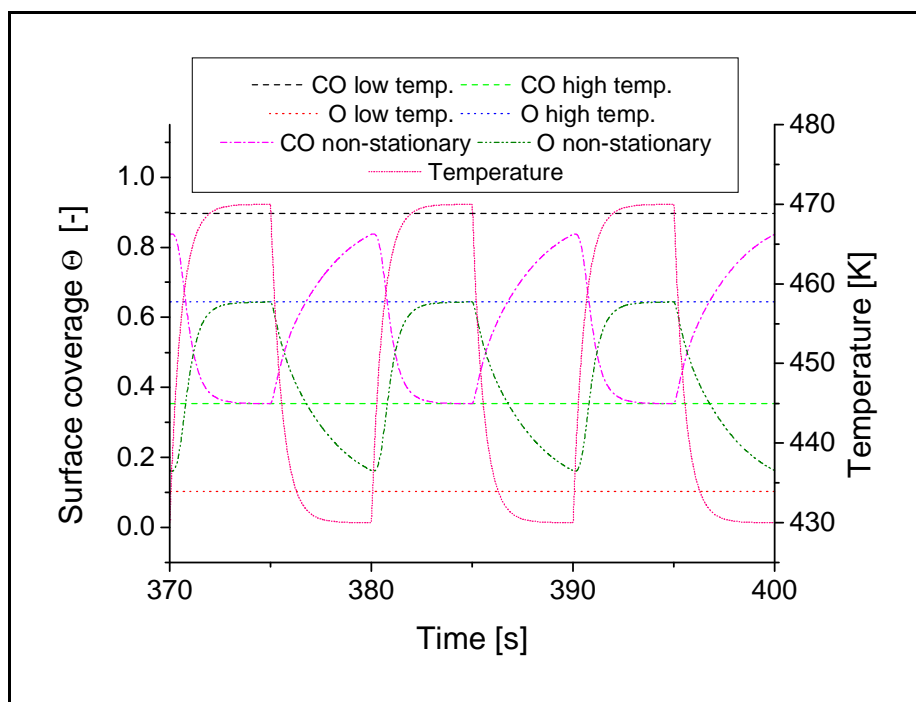


Fig. 6.11 Simulated surface coverage of CO (dashed lines) and O (dotted lines) under stationary temperature conditions, under non-stationary temperature conditions (CO dash dotted line and O dash-dot-dotted line) and reaction rate constant (short-dotted line).

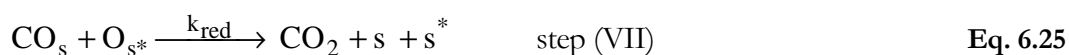
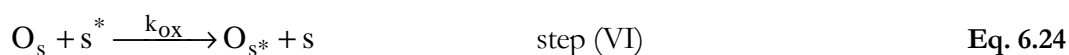
The dashed lines in Fig. 6.11 represent the CO coverage under stationary conditions at the low temperature (high coverage value) and at the high temperature (low coverage value). The dotted lines are the O atoms surface coverage under stationary temperature conditions at the low temperature (low coverage value) and at the high temperature (high coverage value). The dash-dotted and dash-dot-dotted lines are respectively the surface coverage of CO and O atoms under non-stationary temperature conditions. The short dotted plot corresponds to the temperature. As in Fig. 6.10, the period of the oscillations is 10 seconds and the temperature varies between 430 and 470 K using an exponential periodic function.

As supposed by observing the evolution of the reaction rate curve in Fig. 6.10, no special effect is obtained by applying the temperature oscillations. The surface coverage of the reactive species oscillates simply between the value at high temperature and near the value at low temperature. The surface coverage changes are fast enough to follow the temperature changes and thus no non-trivial effect is obtained through the temperature oscillations. The fact that during the cooling period (when the temperature decreases) the surface coverage does not have the time to reach the stationary state value for the low temperature is due to the slower CO and O₂ adsorption-desorption equilibria at the low temperatures. A slightly longer time would be needed to reach the

new equilibrium value after the temperature change. This has however no noticeable influence on the reaction rate. At the high temperature, the adsorption-desorption equilibria are faster and 5 seconds are sufficient for the surface coverage to reach the stationary value for the high temperature.

Even if the period of the temperature oscillations is reduced to 0.01 seconds, no increase of the mean reaction rate is observed. The adsorption-desorption equilibria phenomena are still fast enough to follow the temperature changes and the system behaves as being always in steady-state. Since the reaction rate increase was experimentally observed for a period duration of approximately 20 seconds, one may conclude that the simple Langmuir-Hinshelwood is adequate to reproduce the experimental results under stationary conditions but not under thermal non-stationary conditions. The implied phenomena are definitely too fast compared to the duration of the temperature oscillations. The introduction of a feedback step in the theoretical model similar with the one explaining the self-oscillations observed by e.g. Yuranov et al. [47] or van Neer et al. [48] is thus necessary.

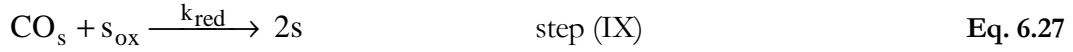
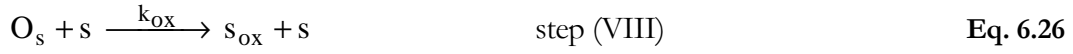
To explain the self-sustained oscillations observed during the CO oxidation over Pd supported on glass fibres, Yuranov et al. [47] proposed, based on the work of Sales et al. [85] and Basset et al. [86], the addition of a step of oxidation-reduction of the palladium. They also took into account the possible reaction of adsorbed CO on the palladium surface with subsurface oxygen atoms. The two supplementary steps added to the basic mechanism already presented on p. 99 were [47]:



where s and s^* represent a vacant active site respectively at the surface and in the subsurface layer of the catalyst. The indicises “ s ” and “ s^* ” indicate an adsorbed molecule or atom on an active site either at the surface or in the subsurface layer.

Yuranov et al. [47] mentioned that the oxidized catalyst had a low activity and the reduced one a high activity toward the CO oxidation. They showed also that the reduction step which has an activation energy of approximately $42 \text{ kJ}\cdot\text{mol}^{-1}$ [85] is more influenced by a variation of the temperature than the oxidation step which activation energy is only $4.2 \text{ kJ}\cdot\text{mol}^{-1}$. The only limitation of the proposed mechanism is that the observed self-sustained oscillations had a period between 0.5 and 6 hours. The proposed oxidation-reduction steps are very slow with a rate constant in the order of magnitude of 10^{-4} s^{-1} at 483 K [47].

To test if the oxidation-reduction of the catalyst may be an explanation to the observed phenomena, the following steps have been added, based on Sales et al. [85], to the simple mechanism presented on page 100:



where the index “s” denotes an adsorbed species, s a vacant active site and s_{ox} an active blocked by the formation of an oxide.

The kinetic equations which have to be added to the ones of page 101 are thus [83]:

$$r_{\text{ox}} = k_{\text{ox}} \cdot \Theta_{\text{O}} \cdot (1 - \Theta_{\text{ox}}) \quad \text{Eq. 6.28}$$

$$r_{\text{red}} = k_{\text{red}} \cdot \Theta_{\text{CO}} \cdot \Theta_{\text{ox}} \quad \text{Eq. 6.29}$$

and the balance on the active sites becomes

$$1 = \Theta_v + \Theta_{\text{CO}} + \Theta_{\text{O}} + \Theta_{\text{ox}} \quad \text{Eq. 6.30}$$

To form an oxide, it is necessary that an oxygen atom is adsorbed on the surface and that an active site is free for the oxidation. Since the surface coverage of oxidized sites is given by Θ_{ox} , the surface coverage of sites which may be oxidized is given by $1 - \Theta_{\text{ox}}$. The reaction rate of reduction is proportional to the surface coverage of CO and oxidized active site. Eq. 6.30 illustrates that the oxidized sites are blocked for the adsorption of CO and O_2 and reduce thus the catalytic activity.

As in the case of the simple Langmuir-Hinshelwood mechanism, the model has been first simulated under stationary thermal conditions to test whether it was adequate to quantitatively reproduce the experimentally measured reaction rate and to determine the adequate kinetic parameters for the individual steps. Fig. 6.12 presents the comparison of the simulation curve with the experimental results.

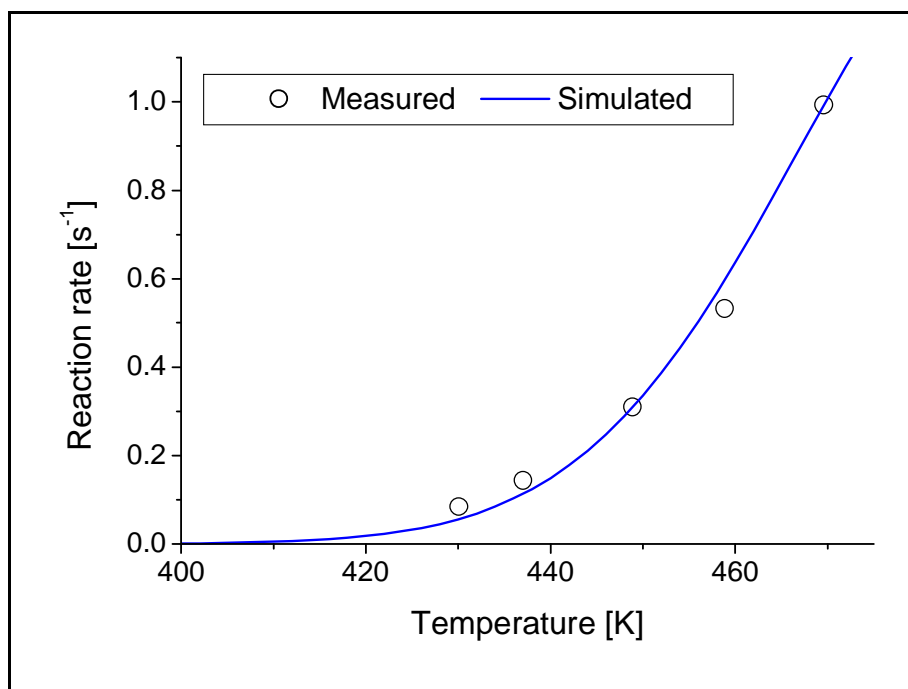


Fig. 6.12 Comparison of the experimental reaction rate (circles) with the simulated one (line).

The circles in Fig. 6.12 represent the experimental reaction rate and the plain plot the simulated one. The comparison shows that the simulated simple model reproduces in a satisfying way the temperature dependence of the reaction rate. This model is thus equally adequate to investigate the effects of non-stationary thermal conditions. The fitting of the experimental results under stationary conditions has been realized using the parameters given in Tab. 6.3.

Step	$k_{0,j}$ [see footer [‡]]	$E_{a,j}$ [kJ·mol ⁻¹]
(I)	$2.9 \cdot 10^5$	0.03
(II)	$1.1 \cdot 10^{13}$	100
(III)	$7.1 \cdot 10^5$	0.02
(IV)	$1.6 \cdot 10^{13}$	203
(V)	$5.2 \cdot 10^{11}$	88
(VIII)	0.1	4.2
(IX)	130	42

Tab. 6.3 Parameters used in the simulations based on the model with the oxidation-reduction step

The kinetic parameters determined for the steps (I) to (V) are consistent with the ones presented in Tab. 6.1 and similar to the one used in the simple Langmuir-Hinshelwood model. The adsorption of CO and O₂ is nearly non-activated and the activation energies of the remaining steps are following the sequence mentioned on p. 110. The activation energy for the steps (VIII) and

[‡] Pre-exponential factors of step (I) and (III) are in [s⁻¹·bar⁻¹], the rest of pre-exponential factors in [s⁻¹]

(IX) has been taken identical to the value mentioned by Sales et al. [85]. The order of magnitude of the pre-exponential factor determined for these two steps is equally consistent with the value in [85].

As for the simple model, the evolution of the surface coverage and reaction rate with respect to the temperature has been simulated under stationary conditions. The results are shown in Fig. 6.13 for a variation of the temperature between 380 and 540 K.

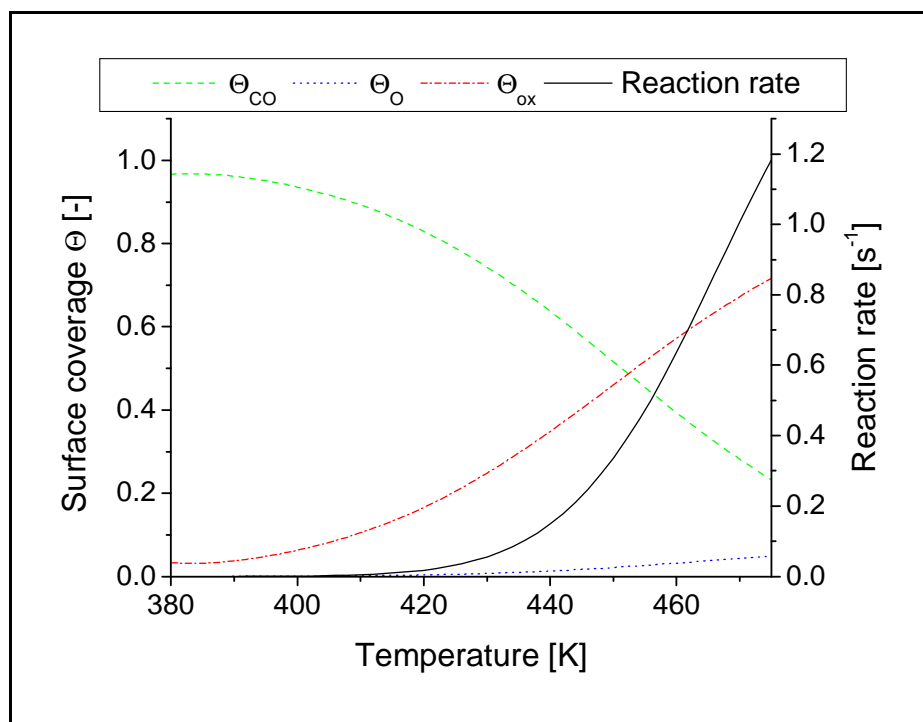


Fig. 6.13 Evolution of the surface coverage of CO (dash), oxygen atoms (dot), oxidized active sites (dash-dot) and reaction rate (plain) with respect to the temperature under stationary temperature conditions.

The dashed plot in Fig. 6.13 represents the surface coverage of CO, the dotted plot the one of the oxygen atoms and the dash-dotted plot the surface coverage of the oxidized active sites. The plain plot corresponds to the surface reaction rate.

As may be seen in Fig. 6.13 the surface coverage of CO is near the unity at low temperature and goes down when the temperature increases. This behaviour is similar to what happens in the case of the simple Langmuir-Hinshelwood model. The major difference comes from the behaviour of the oxygen atoms surface coverage. When the temperature increases, it does not equally increase as in the case of the previous model but stay at a low value. At the contrary the fraction of the oxidized active sites strongly increases together with the temperature. In the high temperature region, where the reaction rate should be very high, it is limited by the very high fraction of active sites which are oxidized and thus not available for the adsorption of CO and oxygen and the subsequent reaction.

If the applied temperature oscillations are influencing the oxidation-reduction steps of the catalyst so that the catalyst surface spends more time in the reduced state with the high activity this could account for the observed increase in the mean CO_2 concentration under non-stationary conditions.

This supposition has been tested by simulated the model under non-stationary conditions using the kinetic parameters presented in Tab. 6.3. The simulations have been realized using the same temperature change of exponential type between 430 and 470 K as for the simple model. The results presented in Fig. 6.14 are obtained with an oscillation period of 10 seconds.

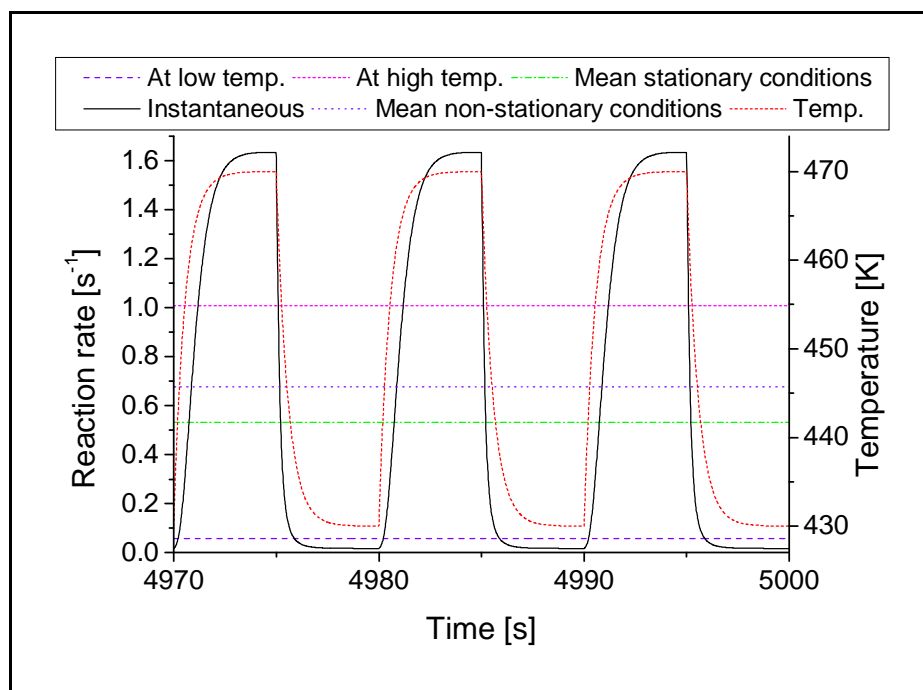


Fig. 6.14 Simulated reaction rates at low temperature (dash), at high temperature (short dash), instantaneous (plain line), mean under stationary conditions (dash-dot) and mean under non-stationary temperature conditions (dot) and temperature (short-dash)

The dashed, short dashed and dash-dotted plots in Fig. 6.14 represent respectively the reaction rate at low temperature, high temperature and the mean under stationary state conditions. The plain plot is the instantaneous reaction rate and the dotted one the mean value calculated under periodic temperature cycling conditions. The short-dashed line is the temperature curve.

Fig. 6.14 shows that with the parameters used the mean reaction rate under thermal non-stationary conditions is clearly higher than the mean reaction rate under stationary conditions. The gain obtained, calculated based on Eq. 5.11 while replacing the CO_2 concentration with the reaction rate, amounts approximately 27%. This pronounced increase is due to the very high value reached by the instantaneous reaction rate during the heating period. This value is clearly higher than the one obtained at the highest temperature under stationary conditions. The high value of the instantaneous reaction rate under thermal non-stationary conditions may be explained by observing

the evolution of the surface coverage of the reactive species during the temperature as shown in Fig. 6.15.

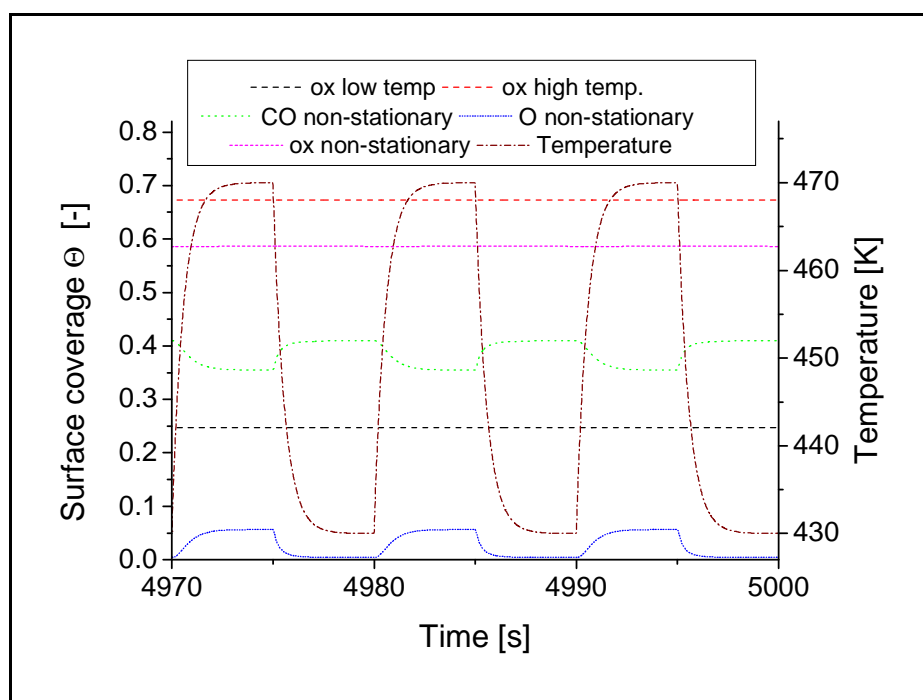


Fig. 6.15 Simulated surface coverage of oxidized sites (dash) under stationary temperature conditions, CO, O and oxidized sites (dot, short-dot and short dash) under non-stationary conditions and temperature (dash-dot).

The dashed lines in Fig. 6.15 represent the surface coverage of the oxidized sites at low temperature (low value) and at high temperature (high value). The dotted, short-dotted and short dashed plots are respectively the surface coverage of CO, oxygen atoms and oxidized sites under non-stationary conditions. The dash-dotted plot is the temperature.

Two characteristics of the surface coverage evolution explain why the instantaneous reaction rate reaches under thermal non-stationary conditions some values higher than the stationary high temperature value. It may be seen in Fig. 6.15 that the surface coverage of the oxidized sites (short dashed line slightly below 0.6) quasi does not vary with the temperature at the contrary of the surface coverage of CO and the oxygen atoms. The surface coverage value of the oxidized sites varies only between 0.586 and 0.587 what is not good to discern in Fig. 6.15. This is because the oxidation-reduction phenomena are very slow and the period duration of 10 seconds is sufficiently short so that a nearly relaxed steady-state is obtained. The surface coverage of the oxidized sites stays permanently below its high temperature value which would be 0.68. Fewer sites are blocked by the oxidation even when the temperature is high and more sites are thus available for the adsorption of CO and oxygen. Fig. 6.13 and Fig. 6.15 show that in the temperature range, the surface coverage of the oxygen atoms is very low (below 0.05) and limits the reaction rate value obtainable. Under non-stationary temperature conditions, the oxygen atoms coverage increases up to 0.057. This increase of the oxygen atoms surface coverage is directly responsible for the high

value of the instantaneous reaction rate observed under non-stationary temperature conditions. The evolution of the surface coverage of the reactive species for different oscillations frequencies is equally presented in Fig. 6.17.

It has been shown in Chap. 5.3.4 that the gain obtained in the mean reaction rate was increasing with the frequency of the temperature oscillations. It is thus interesting to investigate whether it is although the case for our theoretical model. For this purpose, the gain obtained in the mean reaction rate has been calculated based on Eq. 5.11 for different frequencies while the temperature was varied using the same exponential changes between 430 and 470 K. The result obtained is presented in Fig. 6.16.

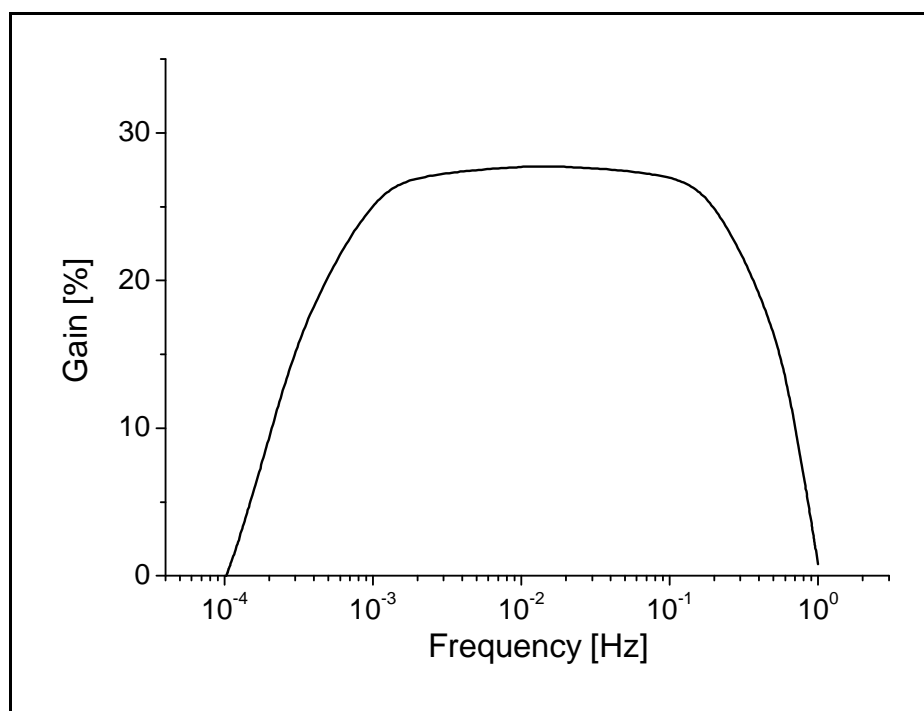


Fig. 6.16 Gain obtained in the mean reaction rate with respect to the frequency of the temperature oscillations.

The plot in Fig. 6.16 shows three domains. At low frequency the gain increases together with the frequency, reaches a plateau and then diminishes. The evolution of the gain is related to the changes in the surface coverage of the reactive species, as may be seen in Fig. 6.17.

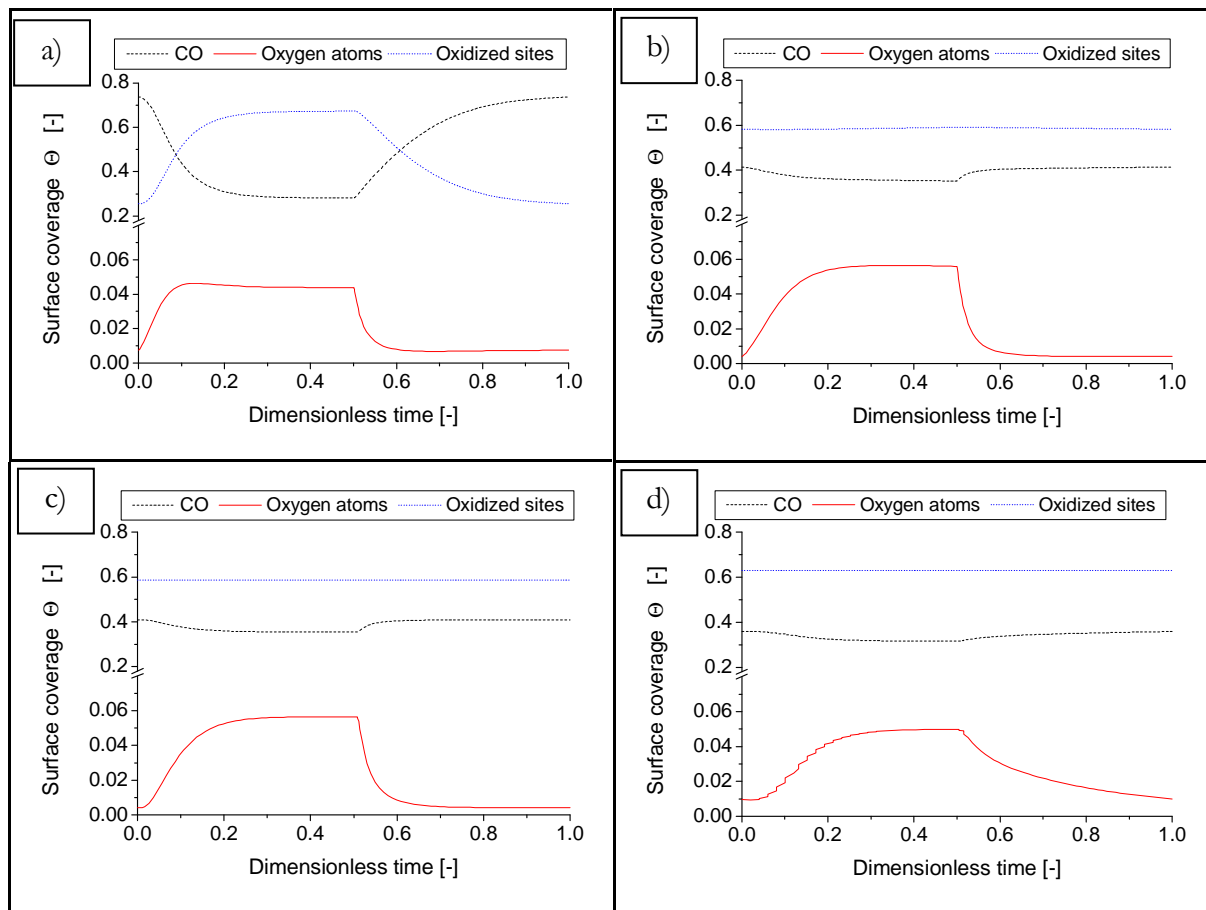


Fig. 6.17 Evolution of the surface coverage of CO (dash) oxygen atoms (plain) and oxidized sites (dot) under non-stationary temperature conditions during one period of oscillations with respect to the dimensionless time. Freq. = a) $1 \cdot 10^{-4}$ Hz, b) $1 \cdot 10^{-2}$ Hz c) 0.1 Hz and d) 1 Hz.

The dashed, plain and dotted plots in Fig. 6.17 represent respectively the evolution of the surface coverage of CO, oxygen atoms and oxidized active sites during one period of oscillations with respect to a dimensionless time. Between 0 and 0.5 the temperature increases and decreases between 0.5 and 1. The temperature change type is always of exponential type between 430 and 470 K.

At the very low frequency (see Fig. 6.17 a)), the surface coverage of CO, oxygen atoms and oxidized sites is simply closely following the temperature changes and no advantage is obtained through the temperature oscillations. The system behaves as being always under stationary temperature conditions. At $1 \cdot 10^{-2}$ Hz the surface coverage of the oxidized sites becomes approximately invariant at a value lower than the value at the highest stationary temperature. Since fewer sites are oxidized, the surface coverage of the oxygen atoms reaches values during the heating half-period higher than at the highest stationary temperature. Since the oxygen atoms surface coverage is the reaction rate limiting factor, the instantaneous reaction rate becomes greater than at the highest stationary temperature. Between $1 \cdot 10^{-2}$ and 0.1 Hz (see Fig. 6.17 b) and c)) the surface coverage of the reactive species doesn't change and the effect of the temperature oscillations stays identical. At 1 Hz, the surface coverage of the oxidized sites reaches its relaxed steady state value

which is higher than the value at $1 \cdot 10^{-2}$ and 0.1 Hz. The maximal surface coverage of the oxygen atoms during the heating period diminishes again (see Fig. 6.17 c)). Since the effect of the temperature oscillations was based on a higher surface coverage of the oxygen atoms reached during the heating half-period, the positive effect disappears.

The addition to the simple Langmuir-Hinshelwood mechanism for the catalytic CO oxidation of a slow feed-back step in a form of an oxidation-reduction of the active sites of the catalyst has allowed to demonstrate an increase of the mean reaction rate under non-stationary temperature conditions compared to the one obtained under stationary conditions. This increase is due to the variations of the surface coverage of the reactive species during the temperature oscillations. Above a certain frequency of oscillation, the reactive species surface coverage did not reach the new equilibrium value instantaneously but a transient surface coverage develops. If during the transient phase the surface coverage of the reactive species is more favourable than the one obtained under stationary state conditions at the highest temperature, the instantaneous reaction rate will go through a maximum higher than the maximum reaction rate value obtained under stationary state conditions. In the case of the simulations presented above, it is the surface coverage of the oxygen atoms which reaches a higher value under non-stationary temperature conditions than the value at the highest stationary temperature in the oscillation range.

The effect of the temperature oscillations on the reaction behaviour is very complex since all the reaction steps (adsorption, desorption, surface reaction, etc.) are influenced by the temperature simultaneously. This effect may not be predicted by considering only the reactive species surface coverage values under stationary state conditions but have to be investigated using the simulation of the reaction behaviour under non-stationary conditions.

Although the simulations have demonstrated the possible existence of a non-trivial increase of the catalytic CO oxidation mean reaction rate under non-stationary thermal conditions, the simulation results were not totally consistent with the experimental ones. The experimental measurements have shown a gain of up to 80% under temperature oscillations with a frequency of approximately $5 \cdot 10^{-2}$ Hz and an amplitude of 40 K. The simulation results of the catalytic CO oxidation under non-stationary temperature conditions have only demonstrated a gain of 27% for a frequency between 10^{-3} and 10^{-1} Hz and an amplitude of 40 K. Moreover, the simulations have shown an effect of the temperature oscillations already at a frequency of 10^{-3} Hz while a frequency of 10^{-2} Hz was not sufficient to see experimentally any increase in the reaction rate. The experimental results may thus not totally be explained using the oxidation-reduction feedback step. These two phenomena are probably too slow to be alone responsible for the observed increase in the mean CO_2 concentration.

Van Neer et al. [48] arrived equally at the conclusion that the oxidation-reduction of the catalyst only was not completely adequate to explain the self-oscillations they observed during the CO

oxidation over a supported Pt catalyst. They mention in their publication that the metal catalyst may experience some surface restructuring together with a partial oxidation. Since the characteristic time of the phase transformations is thought to be in the order of some seconds [87], it is thinkable that temperature oscillations having a period duration in the same order of magnitude are able to influence this type of phenomena.

However, van Neer et al. [48] pointed out that the development of a theoretical model for the surface restructuring of a supported catalyst is very difficult. Since the ambition of the presented simulations was only to demonstrate the existence of a non-trivial effect of temperature oscillations on the catalytic CO oxidation in principle, it has been decided to renounce in the frame of this work to the development of such a model.

7. Conclusions and perspectives

7.1. Conclusions

The effect of fast temperature oscillations on the behaviour of a catalytic reaction has been investigated using two different types of microstructure reactors. The devices were permanently heated using electrical heater cartridges and periodically cooled down by water flowing through cooling channels incorporated inside the reactors. The test reaction chosen was the catalytic CO oxidation on a platinum catalyst supported on alumina (Pt/Al₂O₃). In the first device (FTC-type 2), the reaction was taking place in microstructured channels with the catalyst layer deposited on their walls. The reaction area in the second device (FTC-type 3) consisted of a piece of Sintered Metal Fibres plate placed in a reaction chamber inside the microstructure reactor. The catalyst was deposited on the filaments of the SMF plate.

The experimental measurements realized in both devices at different temperatures under stationary conditions have shown that the reaction behaved as it is predicted by the Arrhenius law. The classical exponential dependence of the measured CO₂ concentration at the reactor outlet (proportional to the reaction rate) with respect to the temperature was observed.

The application of slow temperature changes to the microstructure devices (between 7 and 14 K·min⁻¹) has had no special influence on the reaction behaviour which was always predicted by the Arrhenius law. The CO₂ concentration measured at the reactor outlet was identical under quasi-stationary thermal conditions with the one under stationary conditions for every temperature. A temperature change rate in the order of magnitude of about ten Kelvin per minute is not sufficient to perturb the surface coverage of the reactive species. The phenomena involved in the catalytic CO oxidation are sufficiently rapid to follow the slow temperature changes and the system behaves as being always under steady-state conditions.

The results obtained under non-stationary thermal conditions were different for the two types of microstructure devices. The FTC-type 2 reactor allowed temperature changes of up to 120 K within around ten seconds but these very fast temperature changes were related with a pretty high temperature inhomogeneity of the device. A temperature difference of up to 80 K was measured between two points inside the reactor. Due to their very low local reaction rate, the colder areas of the reactor were greatly attenuating the measured CO₂ concentration oscillations at the reactor outlet which should have been created by the temperature oscillations. No positive effects of the non-stationary thermal conditions could be shown using this device under these conditions.

The FTC-type 3 reactor allowed only temperature changes of up to 50 Kelvin within approximately ten seconds, but its temperature homogeneity was much better. The maximal temperature difference between a cold and a hot spot inside the reactor was approximately 15 K. Under temperature oscillations, the measured instantaneous CO₂ concentration was higher for any

given temperature within the oscillating temperature range compared to the one recorded under stationary thermal conditions. The increase obtained in the mean CO_2 concentration was ranging from 34% for a frequency of the oscillations of 0.035 Hz to 85% for a frequency of 0.052 Hz. The amplitude of the oscillations was kept constant at approximately 40 K and the mean temperature value at 437 K.

Simulations using a simple Langmuir-Hinshelwood mechanism of the catalytic CO oxidation have failed to demonstrate an increase of the mean reaction rate under non-stationary temperature conditions compared to the one obtained under quasi-stationary conditions. The phenomena implicated are too fast compared to the length of the temperature oscillation period and the system behaves as being always under steady state.

The addition to the simple Langmuir-Hinshelwood mechanism of a slow feed-back step in a form of an oxidation-reduction of the active sites of the catalyst has allowed to demonstrate an increase of the mean reaction rate under non-stationary temperature conditions compared to the one obtained under quasi-stationary conditions.

Above a certain frequency, the temperature oscillations are fast enough compared to the characteristic time of the feedback step and are able to perturb the stationary established reactive species surface coverage. The formation of a transient surface coverage more favourable for the reaction than the surface coverage at high temperature allows during the transient period to reach an instantaneous surface reaction rate values higher than the one at high temperature. In the particular case of the simulations realized, it is the surface coverage of the oxygen atoms which reaches a higher value under non-stationary temperature conditions than the value at the highest stationary temperature. The related highest value of the instantaneous reaction rate is then responsible for the increase of the mean reaction rate under non-stationary thermal conditions. A discrepancy is however observed in the frequency from which a positive effect of the temperature oscillations is observed. Consequently, for a quantitative explanation of the experimental results, the use of the oxidation-reduction step is not sufficient. The addition of a supplementary feedback step like a surface restructuring together with a partial oxidation of the catalyst is necessary.

7.2. Perspectives

Both the experimental measurements realized during this work and the presented simulations have confirmed that fast temperature oscillations were able to increase the mean reaction rate value of a catalytic reaction above the one obtained under quasi-stationary conditions under certain conditions. There is, however, still room for an improvement of the experimental set-up and for further theoretical and experimental investigations.

The experimental concentration data collected during this work are only partially suitable for theoretical investigations due to the influence of the FTIR spectrometer used for the quantitative

measurements. It has been demonstrated that a mass spectrometer would less deform the concentration oscillations generated than the FTIR spectrometer and allow to record all the involved species (CO , O_2 and CO_2). Some efforts have already been made for the incorporation of such a device in the experimental set-up. The mass spectrometer signal stability problem could, however, not be solved during this work. Further modifications of the inlet set-up have to be performed.

Real instantaneous concentration data without any modification due to the measurement method would allow to develop and test the validity of a theoretical model incorporated one or more extra step(s) than the basic one presented here. The development of such a model is necessary for the quantitative reproduction of the experimental results

Moreover, it is still unclear up to which frequency the gain experimentally observed in the mean reaction rate still increases and whether there is a frequency above which it might even decrease. To answer this question, oscillations of much higher frequencies have to be realized. This is, using the actual microstructure reactor, unfortunately not possible. It would be necessary to develop a new microstructure device allowing to produce temperature oscillations of higher frequencies while keeping a good thermal homogeneity.

8. Symbols and abbreviations

a	Partial order for CO in the power law equation	$[-]$
A_c	Area of a channel	$[m^2]$
Asb	Absorbance	$[-]$
b	Partial order for O ₂ in the power law equation	$[-]$
Bo	Bodenstein number	$[-]$
c	Sample concentration	$[mol \cdot l^{-1}]$
$[c]_{bulk}$	Concentration of reactant in the bulk fluid	$[g \cdot mol \cdot cm^{-3}]$
C_A	Concentration of A	$[mol \cdot m^{-3}]$
Cat_{load}	Percentage of catalyst deposited	$[vol\%]$
$[CO]$	Concentration of CO	$[vol. \%]$
$[CO_2]$	Concentration of CO ₂ in the gas flow	$[vol. \%]$
C_s^n	Reactant concentration at the surface of the particle	$[mol \cdot cm^{-3}]$
CSTR	Continuous Stirred Tank Reactor	
d	Side square of a channel cross section	$[m]$
d_l	Sample layer thickness	$[cm]$
D_{12}	Component diffusion coefficient	$[m^2 \cdot s^{-1}]$
D_{ax}	Axial diffusivity	$[m^2 \cdot s^{-1}]$
d_c	Channel diameter	$[m]$
d_h	Hydraulic diameter of a channel	$[m]$
Disp	Catalyst dispersion	$[\%$
d_t	Diameter of a channel	$[m]$
$E(t)$	Residence time distribution	
$E(\theta)$	Dimensionless residence time distribution	
E_a	Activation energy	$[kJ \cdot mol^{-1}]$
$E_{a,i}$	Activation energy for the step “i”	$[kJ \cdot mol^{-1}]$
$Flow_{outlet}$	Reaction gas flow at the reactor outlet	$[m^3 \cdot s^{-1}]$
Fo	Fourier number	$[-]$
$F(t)$	Response curve to the tracer	
FTC	Fast temperature cycling	
FTIR	Fourier transform infrared	
g	Number of measurement points	$[-]$
Gz_m	Graetz number for mass transport	$[-]$
I	Radiation intensity	$[-]$
$[i]$	Concentration of Component “i”	$[vol. \%]$
$[j]_{bulk}$	Concentration of the species “j” in the bulk	$[mol \cdot m^{-3}]$
$[j]_{surface}$	Concentration of the species “j” at the surface	$[mol \cdot m^{-3}]$
k	Reaction rate constant	$[s^{-1}]$
k_0	Pre-exponential factor	$[s^{-1}]$
$k_{0,i}$	Pre-exponential factor for the step “i”	$[m^3 \cdot mol^{-1} \cdot s^{-1}]$ or $[s^{-1}]$
k_a	Adsorption rate constant	$[m^3 \cdot mol^{-1} \cdot s^{-1}]$
K_A	Equilibrium constant of A	
k_{aCO}	Adsorption rate constant for CO	$[s^{-1} \cdot bar^{-1}]$
k_{aO_2}	Adsorption rate constant for O ₂	$[s^{-1} \cdot bar^{-1}]$
k_c	Overall mass transfer coefficient	$[cm \cdot s^{-1}]$
$k_{c,CO}$	Mass transfer coefficient for CO	$[m \cdot s^{-1}]$
$k_{c,p}$	Mass transfer coefficient between gas and particle	$[cm \cdot s^{-1}]$
k_d	Desorption rate constant	$[s^{-1}]$
k_{dCO}	Desorption rate constant for CO	$[s^{-1}]$
k_{dO_2}	Desorption rate constant for O ₂	$[s^{-1}]$
k_r	Reaction rate constant	$[s^{-1}]$

k_{RCO_2}	Surface reaction rate constant	$[\text{s}^{-1}]$
L	Length of a channel	$[\text{m}]$
L_c	Characteristic length	$[\text{m}]$
m	Period number	$[-]$
MFC	Mass flow controller	
MS	Mass spectrometer	
M_{SMF}	Mass of the SMF plate	$[\text{g}]$
n	Integer exponent in the power law equation	$[-]$
NSC	Non-stationary conditions	
Pe	Peclet number	$[-]$
p_{ch}	Perimeter of a channel	$[\text{m}]$
P_{outlet}	Pressure at the reactor outlet	$[\text{Pa}]$
QSC	Quasi-stationary conditions	
R	Perfect gas constant	$[\text{J}\cdot\text{mol}^{-1}\cdot\text{K}^{-1}]$
\mathfrak{R}	Observed reaction rate per unit particle volume	$[\text{g}\cdot\text{mol}\cdot\text{s}^{-1}\cdot\text{cm}^{-3}]$
Re	Reynolds number	$[-]$
r_j	reaction rate for the j^{th} reaction	$[\text{s}^{-1}]$
r_p	particle radius	$[\text{cm}]$
R_{v,CO_2}	Observed reaction rate per reaction volume	$[\text{mol}\cdot\text{s}^{-1}\cdot\text{m}^{-3}]$
Sc	Schmidt number	$[-]$
Sh	Sherwood number	$[-]$
SMF	Sintered metal fibres	
t	Time	$[\text{s}]$
t_{50}	50% signal change response time	$[\text{s}]$
t_{90}	90% signal change response time	$[\text{s}]$
t_c	Characteristic time of a system	$[\text{s}]$
T	Temperature	$[\text{K}]$
$T_{\text{gas flow}}$	Gas flow temperature at the reactor outlet	$[\text{K}]$
T_J	Thermocouple number J	
t_p	Duration of an oscillation period	$[\text{s}]$
\bar{u}	Gas linear velocity in a channel	$[\text{m}\cdot\text{s}^{-1}]$
z	Coordinate	

Greek letters

α	Thermal diffusivity	$[\text{m}^2\cdot\text{s}^{-1}]$
ϵ	Extinction coefficient	$[\text{l}\cdot\text{cm}^{-1}\cdot\text{mol}^{-1}]$
μ	Viscosity	$[\text{Pa}\cdot\text{s}]$
ν	Kinematic viscosity	$[\text{m}^2\cdot\text{s}^{-1}]$
ν_{ij}	stoichiometric coefficient	$[-]$
θ	Dimensionless time	$[-]$
Θ_A	Surface coverage of A	$[-]$
Θ_{CO}	Surface coverage of CO	$[-]$
Θ_{O}	Surface coverage of the oxygen atoms	$[-]$
Θ_v	Surface coverage of the free active sites	$[-]$
ρ	Density	$[\text{kg}\cdot\text{m}^{-3}]$
τ	Residence time	$[\text{s}]$
τ_{exp}	Experimental residence time	$[\text{s}]$
τ_{channels}	Theoretical residence time in the microchannels	$[\text{s}]$
ω	Mears criterion	$[-]$

BIBLIOGRAPHY

- 1 F.J.M. Horn, R.C. Lin; Periodic processes: a variational approach; I&EC Process Design and Development 6 (1), pp. 21-30, 1967
- 2 J.J. Brandner; Entwicklung von Mikrostrukturreaktoren zum thermisch instationären Betrieb chemischer Reaktionen; Thesis work; IMVT, Forschungszentrum Karlsruhe, FZKA-6891, 2003
- 3 M. Abraham, W. Ehrfeld, V. Essel, K.P. Kämper, M. Lacher, A. Picard; Microsystem Technology: Between Research and Industrial Application; Microelectronic Engineering 41/42 , pp. 47-52, 1998
- 4 W. Ehrfeld, V. Hessel, H. Löwe; Microreactors, New Technology for Modern Chemistry; Wiley-VCH, Weinheim, 2000
- 5 V. Hessel, H. Löwe; Microchemical engineering: Components, plant concepts, user acceptance; Chemical Engineering Communications 26 (1), pp. 13-24, 26 (4), pp. 540-559, 26 (5), pp. 531-544, 2003
- 6 M. Vorbach, L. Bohn, M. Kotthaus, M. Kraut, P. Pöchlauer, A. Wenka, K. Schubert; First Large-Scale Application of Microreaction Technology within Commercial Chemical Production of DSM; Proceedings of the 28th international Exhibition-Congress on Chemical Engineering, Environmental Protection and Biotechnology, AIChE 2006, Frankfurt am Main, 15-19 May 2006, p. 89, 2006
- 7 K.F. Jensen; Microreaction engineering – is small better?; Chemical Engineering Science 56, pp. 293-303, 2001
- 8 O. Brand, G.K. Fedder, C. Hierold, J.G. Korvink, O. Tabata (Eds); Advanced Micro and Nanosystems Vol.5. Microprocess Engineering; Wiley-VCH, Weinheim, pp. 267-319, 2006
- 9 M. Madou; Fundamentals of microfabrication; CRC Pres, Boca Raton, London, New-York, Washington, 1997
- 10 W. Benzinger, J.J. Brandner, U. Schygulla, K. Schubert; Anti Fouling Investigations in a Microstructured Heat Exchanger; Proceedings of the 28th international Exhibition-Congress on Chemical Engineering, Environmental Protection and Biotechnology, AIChE 2006, Frankfurt am Main, 15-19 May 2006
- 11 W. Ehrfeld; Design Guidelines and Manufacturing Methods for Microreaction Devices; Chimia 56, pp. 598-604, 2002
- 12 W. Beitz, K.-H. Grote; Dubbel, Taschenbuch für den Maschinenbau, 19. Auflage; Springer-Verlag, 1997
- 13 V. Hessel, H. Löwe, F. Schönfeld; Micromixers-a review on passive and active mixing principles; Chemical Engineering Science, 60, pp. 2479-2501, 2005
- 14 J.J. Brandner, E. Anurjew, L. Bohn, E. Ansjosten, T. Henning, U. Schygulla, A. Wenka; Concepts and realization of microstructure heat exchangers for enhanced heat transfer; Experimental Thermal and Fluid Science 30, pp. 801-809, 2006
- 15 K. Schubert, J. Brandner, M. Fichtner, G. Linder, U. Schygulla, A. Wenka; Microstructure devices for applications in thermal and chemical process engineering; Microscale Thermophysical Engineering 5, pp. 17-39, 2001
- 16 V. Hessel, H. Löwe, A. Müller, G. Kolb; Chemical Micro Process Engineering, Processing and Plants; Wiley-VCH Verlag, KGaA, Weinheim, 2005
- 17 T. Zech, G. Bohner, J. Klein; High-throughput screening of supported catalyst in massively parallel single-bead microreactors: Workflow aspects related to reactor bonding and catalyst preparation; Catalysis today 110, pp. 58-67, 2005
- 18 C. Horny, L. Kiwi-Minsker, A. Renken; Micro-structured string-reactor for autothermal production of hydrogen; Chemical Engineering Journal 101, pp. 3-9, 2004
- 19 B.N. Chapman, J.C. Anderson; Science and technology of surface coatings; Academic Press London, 1974
- 20 R. Wunsch, M. Fichtner, K. Schubert; Anodic Oxidation Inside Completely Manufactured Microchannel Reactors Made of Aluminium; Proceeding of the 4th International Conference On Microreaction Technology, AIChE, March 5-9, 2000, Atlanta, USA, pp. 481-487

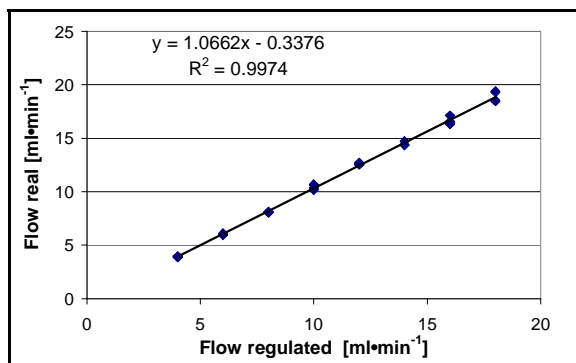
- 21 M. Janicke, H. Kestenbaum, U. Hagendorf, F. Schüth, M. Fichtner, K. Schubert; The Controlled Oxidation of Hydrogen from an Explosive Mixture of Gases Using a Microstructured Reactor/Heat Exchanger and Pt/Al₂O₃ Catalyst; *Journal of Catalysis* 191, pp. 282-293, 2000
- 22 P. Pfeifer, K. Schubert, G. Emig; Preparation of copper catalyst washcoats for methanol steam reforming in microchannels based on nanoparticles; *Applied Catalysis A: General* 286, pp. 175-185, 2005
- 23 K. Haas-Santo, M. Fichtner, K. Schubert; Preparation of sol-gel synthesis for catalysis coatings; *Applied Catalysis A. General* 220, pp. 79-92, 2001
- 24 L. Kiwi-Minsker, A. Renken; Microstructured reactors for catalytic reactions; *Catalysis Today* 110, pp. 2-14, 2005
- 25 Y. Kobayashi, T. Ishizak, Y. Kurokawa; Preparation of alumina films by the sol-gel method; *Journal of Material Science* 40, pp. 263-283, 2005
- 26 C.J. Brinker, G.W. Scherer; *Sol-gel science: the physics and chemistry of sol-gel processing*; Boston Academic Press, 1990
- 27 S. Brunauer, P.H. Emmett, E. Teller; Adsorption of Gases in Multimolecular Layers; *Contribution from the Bureau of Chemistry and Soils and George Washington University*, pp. 309-319, 1938
- 28 D. Truyen, M. Courty, P. Alphonse, F. Ansart; Catalytic coatings on stainless steel prepared by sol-gel route; *thin solid films* 495, pp. 257-261, 2006
- 29 G. Li, L. Hu, J.m. Hill; Comparison of reducibility and stability of alumina-supported Ni catalysts prepared by impregnation and co-precipitation; *Applied Catalysis A: General* 301, pp. 16-24, 2006
- 30 J.J. Brandner, M. Fichtner, U. Schygulla, K. Schubert; Improving the Efficiency of Micro Heat Exchangers and Reactors; *Proceedings of the 4th Int. Conf on Microreaction Technology, IMRET 4*, March 5-9, 2000, Atlanta, GA, USA, pp. 244-249
- 31 M.B. Cutlip; Concentration forcing of catalytic surface rate processes, Part I. Isothermal carbon monoxide oxidation over supported platinum; *AIChE Journal* 25 (3), pp. 502-508, 1979
- 32 G. Rambeau, H. Amaglio; Improvement of the catalytic performance of a ruthenium powder in ammonia synthesis by the use of a cyclic procedure; *Applied Catalysis* 1 (5), pp. 291-302, 1981
- 33 F.J.R. van Neer, A.J. Kodde, H. den Uil, A. Blik; Understanding of resonance phenomena on a catalyst under forced concentration and temperature oscillations; *The Canadian Journal of Chemical Engineering* 74, pp. 664-673, 1996
- 34 H.Kayode Abdul-Kareem, R.R. Hudgins, P.L. Silveston; Forced cycling of the catalytic oxidation of CO over a V₂O₅ catalyst – II Temperature cycling; *Chemical Engineering Science* 35, pp. 2085-2088, 1980
- 35 M. Rinnemo, D. Kulginov, S. Johansson, K.L. Wong, V. P. Zhdanov, B. Kasemo; Catalytic ignition in the CO-O₂ reaction on platinum: experiment and simulations; *Surface Science*, 376, pp. 297-309, 1997
- 36 J.E. Bailey; Periodic operation of chemical reactors: a review; *Chemical Engineering Communications* 1, pp. 111-124, 1973
- 37 A. Renken; Unsteady-state operation of continuous reactors; *International Chemical Engineering* 24 (2), pp.202-213, 1984
- 38 H. A. Hansen, J. L. Olsen, S. Jensen, O. Hansen, U. J. Quaade; Rate enhancement in microfabricated chemical reactors under fast forced temperature oscillations; *Catalysis Communications* 7, pp. 272-275, 2006
- 39 E. Gulari, X. Zhou, C. Sze; Catalytic oxidation of carbon monoxide under periodic and transient operation; *Catalysis Today* 25, pp. 145-157, 1995
- 40 H. Kayode Abdul-Kareem, P.L. Silveston, R.R. Hudgins; Forced cycling of the catalytic CO oxidation over a V₂O₅ catalyst – I Concentration cycling; *Chemical Engineering Science* 35, pp.2077-2084, 1980
- 41 X. Zhou, Y. Barshad, E. Gulari; CO oxidation on Pd/Al₂O₃. Transient response and rate enhancement through forced concentration cycling; *Chemical Engineering Science* 41 (5), pp. 1277-1284, 1986
- 42 R. H. Nibbelke, M. A. J. Campman, J. H. B. J. Hoebink, G. B. Marin; Kinetic study of the CO oxidation over Pt/g-Al₂O₃ and Pt/Rh/CeO₂/g-Al₂O₃ in the presence of H₂O and CO₂; *Journal of Catalysis* 171, pp. 358-373, 1997
- 43 T. Engel, G. Ertl; A molecular beam investigation of the catalytic oxidation of CO on Pd(111); *The Journal of Chemical Physics*, 69, pp. 1267-1281, 1978

- 44 J. R. Engstrom, W. H. Weinberg; Surface reaction dynamics via Temperature modulation: Applications to the oxidation of carbon monoxide on the Pt(110)-(1x2) surface; *Physical Review Letters*, 55, pp. 2017-2020, 1985
- 45 A. Holmgren, D. Duprez, B. Andersson; A model of oxygen transport in Pt/Ceria Catalysts from isotope exchange; *Journal of Catalysis*, 182, pp. 441-448, 1999
- 46 O. Dulaurent, D. Bianchi; Adsorption isobars for CO on a Pt/Al₂O₃ catalyst at high temperatures using FTIR spectroscopy: isosteric heat of adsorption and adsorption model; *Applied Catalysis A: General*, 196, pp. 271-280, 2000
- 47 I. Yuranov, L. Kiwi-Minsker, M. Slin'ko, E. Kurkina, E.D. Tolstunova, A. Renken; Oscillatory behavior during CO oxidation over Pd supported on glass and mathematical modeling; *Chemical Engineering Science* 55, pp. 2827-2833, 2000
- 48 F. van Neer, A. Blik; The feedback mechanism in self-oscillations for CO oxidation over EUROPT-3; *Chemical Engineering Science* 54, pp. 4483-4499, 1999
- 49 I. Yuranov, A. Renken, L. Kiwi-Minsker; Zeolite/sintered metal fibers composites as effective structured catalysts; *Applied Catalysis A: General*, 281, pp. 55-60, 2005
- 50 M. J. Kahlich, H. A. Gasteiger, R. J. Behm, Kinetics of the selective CO oxidation in H₂-Rich Gas on Pt/Al₂O₃; *Journal of Catalysis* 171, pp. 93-105, 1997
- 51 V. Cominos, V. Hessel, C. Hofmann, G. Kolb, R. Zapf, A. Ziogas, E.R. Delsman, J.C. Schouten, Selective oxidation of carbon monoxide in a hydrogen-rich fuel cell feed using a catalyst coated microstructured reactor, *Catalysis Today* 110, pp. 140-153, 2005
- 52 H. Guenzler, H.-U. Gremlich, M.-J. Bluemich (Traduction); *IR spectroscopy : an introduction*; Wiley-VCH, 2002
- 53 W. Gottwald, G. Wachter; *IR-Spektroskopie für Anwender*; Wiley-VCH, 1997
- 54 S.E. Stein, NIST Mass Spec Data Center, "Infrared Spectra", WebBook de Chimie NIST, Base de Données Standard de Référence NIST Numéro 69, Eds. P.J. Linstrom and W.G. Mallard, National Institute of Standards and Technology, Gaithersburg MD, 20899, 2005 (<http://webbook.nist.gov>)
- 55 P.R. Griffiths, J.A. de Haseth, *Fourier Transform Infrared Spectroscopy*, A Wiley-Interscience publication, John Wiley & Sons, 1986
- 56 E. de Hoffmann, V. Stroobant; *Mass Spectrometry: Principles and Applications*; John Wiley & Sons Ltd, 2001
- 57 U.J. Quaade, S. Jensen, O. Hansen; Microsystem with integrated capillary leak to mass spectrometer for high sensitivity temperature programmed desorption; *Review of Scientific Instruments* 75 (10), pp. 3345-3347, 2004
- 58 U.J. Quaade, S. Jensen, O. Hansen ; Fabrication and modeling of narrow capillaries for vacuum system gas inlets; *Journal of Applied Physics* 97, pp. 044906-1-4, 2005
- 59 A. Roth, *Vacuum Technology*, Elsevier Science Publishers B.V, Amsterdam, The Netherlands, 1990
- 60 I. Yuranov, L. Kiwi-Minsker, A. Renken; Structured combustion catalysts based on sintered metal fibre filters; *Applied Catalysis B: Environmental* 43, pp. 217-227, 2003
- 61 Albert Renken; *Technique de réaction, Conception et calcul de réacteurs chimiques* ; LGRC, Lausanne EPF, octobre 2001, pp. 132-155
- 62 Manuel Jakubith; *Chemische Verfahrenstechnik, Einführung in Reaktionstechnik und Grundoperationen*; VCH Verlagsgesellschaft mBH, pp. 197-214, 1991
- 63 P. Reuse; Production d'hydrogène dans un réacteur microstructuré. Couplage thermique entre le steam reforming et l'oxydation totale du méthanol ; Thesis work, LGRC, École Polytechnique Fédérale de Lausanne, 2003
- 64 André Rouge; Periodic Operation of a Microreactor for Heterogeneously catalyzed Reactions: the Dehydration of Isopropanol; Thesis work; Chemistry Department, EPF Lausanne, 2001
- 65 M. Baerns, H. Hofmann, A. Renken; *Chemische Reaktionstechnik, Lehrbuch der Technischen Chemie Band 1*, Georg Thieme Verlag Stuttgart New York, pp. 339-342, 1992

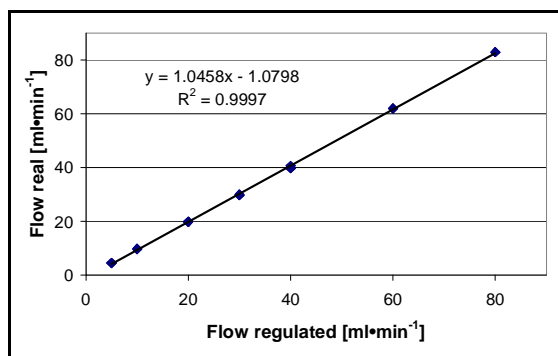
- 66 E.W. Lemmon, M.O. McLinden and D.G. Friend; Thermophysical Properties of Fluid Systems in NIST Chemistry WebBook, NIST Standard Reference Database Number 69, Eds. P.J. Linstrom and W.G. Mallard, National Institute of Standards and Technology, Gaithersburg MD, 20899, June 2005
- 67 CRC Handbook of Chemistry and Physics; 79th Edition (1998-1999); CRC Press LLC; pp. 6-179 to 6-180
- 68 P. Léger; Thermal and pressure drop characterization of a microreactor for fast temperature cycling; Diploma work; IMVT, Forschungszentrum Karlsruhe, 2005
- 69 H. Tautz; Wärmeleitung und Temperatenausgleich; Verlag Chemie GmbH, Weinheim/Bergstr., 1971
- 70 Y.S. Touloukian, C.Y. Ho; Thermophysical properties of matter, Vol. 10, Thermal diffusivity; IFI/Plenum, New York-Washington, 1979
- 71 I. Chorkendorff, J.W. Niemantsverdriet; Concept of modern catalysis and kinetics; Wiley-VCH, 2003
- 72 M. Baerns, H. Hofmann, A. Renken; Chemische Reaktionstechnik; Georg Thieme Verlag Stuttgart New-York, pp. 297-299, 1992
- 73 P. van Male, M.H.J.M. de Croon, R.M. Tiggelaar, A. van den Berg, J.C. Schouten; Heat and mass transfer in a square microchannel with asymmetric heating; International Journal of Heat and Mass transfer, 47, pp. 87-99, 2004
- 74 O. Brand, G.K. Fedder, C. Hierold, J.G. Korvink, O. Tabata (Eds); Advanced Micro and Nanosystems Vol.5. Microprocess Engineering; Wiley-VCH, Weinheim, pp. 173-201, 2006
- 75 D.E. Mears; Tests for Transport Limitations in Experimental Catalytic Reactors; Industrial and Engineering Chemistry Process Design and Development, 10, pp. 541-547, 1971
- 76 O. Görke, P. Pfeifer, K. Schubert; Determination of kinetic data of exothermic reactions in the isothermal microstructure reactor based on the example of catalyzed oxidation of hydrogen; Microreaction Technology : Proceedings of the 6th Internat. Conf. on Microreact. Eng., New Orleans, La.; March 10-14, 2002 ; AIChE Spring Meeting; AIChE Publication (164), pp. 267-272
- 77 G. S. Zafiris, R. J. Gorte; CO Oxidation on Pt/ α -Al₂O₃(0001): Evidence for Structure Sensitivity; Journal of Catalysis 140 (2), pp. 418-423, 1993
- 78 J. A. Rodriguez, D. W. Goodman; High pressure catalytic reactions over single-crystal metal surface; Surface Science Report 14 (1-2), pp. 1-107, 1991
- 79 H. Muraki, S. Matunaga, H. Shinjoh, M. S. Wainwright, D. L. Trimm; The effect of steam and hydrogen in promoting the oxidation of carbon-monoxide over a platinum on alumina catalyst; Journal of Chemical Technology and Biotechnology 52 (3), pp. 415-424, 1991
- 80 A. Renken, R. Doepper, M. Schmid; Application of non-stationary and Periodic Processes in the Study of Heterogeneous Catalytic Kinetics; Dechema-Monographs, vol. 120, VCH Verlagsgesellschaft, pp. 273-290, 1989
- 81 J. R. Engstrom, W.H. Weinberg; Analysis of gas-surface reactions by surface temperature modulation: experimental applications to the adsorption and oxidation of carbon monoxide on the Pt(110)-(1x2) surface; Surface Science 201, pp. 145-170, 1988
- 82 A. Holmgren, D. Duprez, B. Andersson; A model of oxygen transport in Pt/Ceria catalysts from isotope exchange; Journal of Catalysis 182, pp. 441-448, 1999
- 83 C. T. Campbell, G. Ertl, H. Kuipers, J. Segner; A molecular beam study of the adsorption and desorption of oxygen from a Pt(111) surface; Surface Science 107, pp. 220-236, 1981
- 84 Y. K. Park, P. Aghalayam, D. G. Vlachos; A generalized approach for predicting coverage-dependent reaction parameters of complex surface reactions: Application to H₂ oxidation over platinum; Journal of Physical Chemistry A. 103, pp. 8101-8107, 1999
- 85 B.C. Sales, J.E. Turner, M.B. Maple; Oscillatory oxidation of CO over Pt, Pd and Ir catalysts: Theory; Surface Science 114, pp. 381-394, 1982
- 86 M.R. Basset, R. Imbihl; Mathematical modeling of kinetic oscillations in the catalytic CO oxidation on Pd(110): The subsurface oxygen model; Journal of Chemical Physics 93 (1), pp. 811-821, 1990
- 87 D. T. Lynch, G. Emig, S. E. Wanke; Oscillations during CO Oxidation over Supported Metal Catalysts III. Mathematical Modeling of the Observed Phenomena; Journal of Catalysis 97, pp. 456-468, 1986

APPENDICES

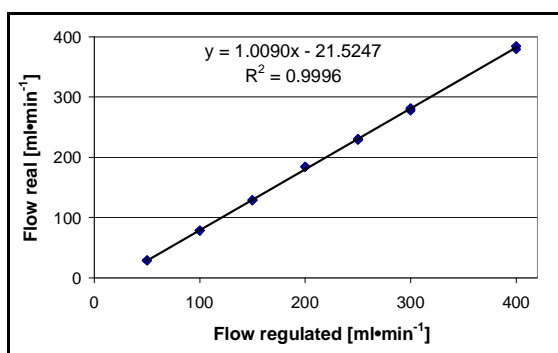
Appendix A: Calibration curves of the mass flows



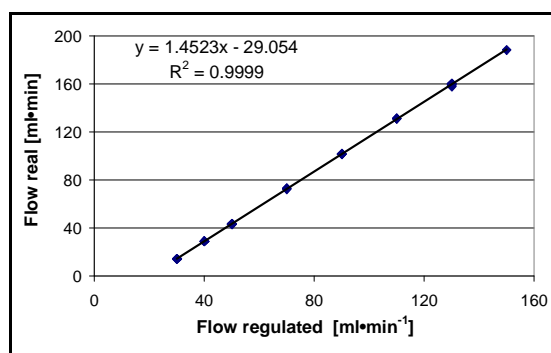
Calibration curve for mass flow CO with CO



Calibration curve for mass flow O₂ with O₂

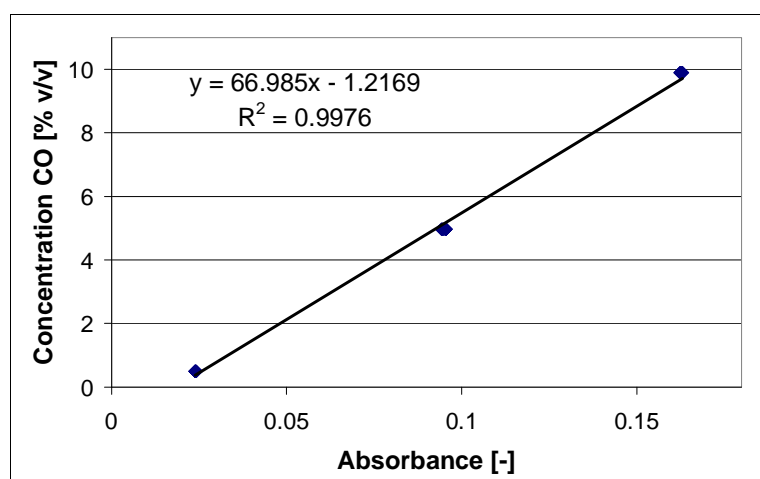


Calibration curve for mass flow N₂ with N₂

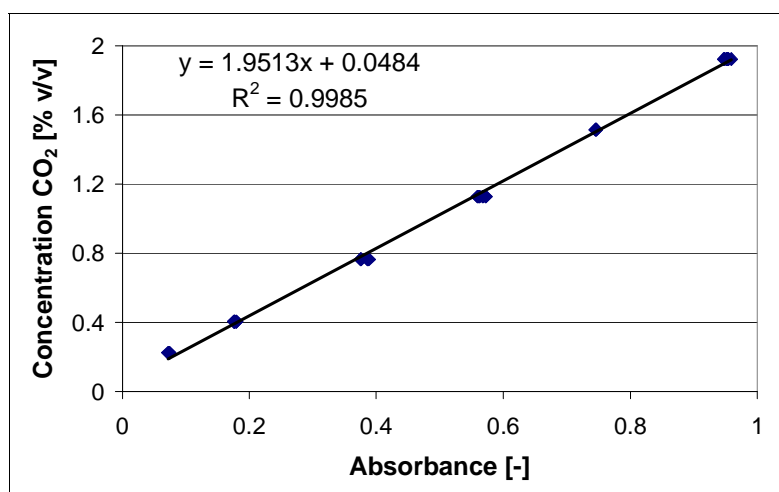


Calibration curve for mass flow N₂ with He

Appendix B: FTIR spectrometer calibration curves

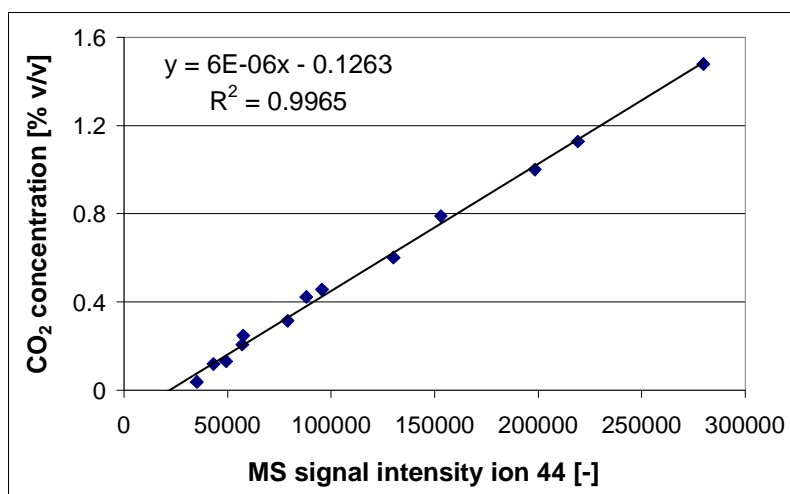


Calibration curve for CO



Calibration curve for CO₂

Appendix C: Mass spectrometer calibration curve



Calibration curve for CO₂

Appendix D: Error estimation

When assessing the effects of Fast Temperature Cycling on the CO oxidation reaction, it is important to know how precise and reliable the measured reactive species concentration values are. In fact, to have a real significance, the measured effects have to lie above the estimated uncertainty of the experimental values.

The total uncertainty on a measured value depending from different variables can be estimated by using the Gauß error propagation law.

Giving

$$y = f(x_i) \quad \text{Eq. A-1}$$

$$|\sigma_y| = \sum_{i=1}^N |\sigma_{x_i}| \cdot \left| \frac{\partial f(x_i)}{\partial x_i} \right| \quad \text{Eq. A-2}$$

with σ_y = absolute deviation from $y = f(x_i)$

σ_{x_i} = absolute deviation from the variable x_i

The mass flow controllers are calibrated using a bubble column and the following formula:

$$\dot{V}_{\text{real}} = \frac{V_{\text{reference}} \cdot 60}{\text{time}} \quad \text{Eq. A-3}$$

with $V_{\text{reference}}$ = volume of the bubble column chosen for the calibration [ml]

time = time necessary for the bubble to go through the reference volume [s]

The absolute uncertainty on the gas flow regulated by the mass flow controllers is then given by:

$$|\sigma_{\dot{V}_{\text{real}}}| = |\sigma_{V_{\text{reference}}}| \cdot \left| \frac{60}{\text{time}} \right| + |\sigma_{\text{time}}| \cdot \left| -\frac{V_{\text{reference}} \cdot 60}{\text{time}^2} \right| \quad [\text{ml} \cdot \text{min}^{-1}] \quad \text{Eq. A-4}$$

The FTIR and Mass spectrometers are calibrated for CO₂ and O₂ with different gas mixtures prepared on site using the mass flow controllers and not with calibrated gas. The concentration of the “j” species in a given gas mixture is given by:

$$C_j = \frac{\dot{V}_{\text{real}, j}}{\dot{V}_{\text{real}, j} + \dot{V}_{\text{real}, \text{carrier gas}}} \cdot 100 \quad [\%] \quad \text{Eq. A-5}$$

The absolute uncertainty on the concentration of the component “j” in a given gas mixture used for the calibration of the component “j” is then given by:

$$\left| \sigma_{C_j, \text{calibration}} \right| = \frac{100}{\left(\dot{V}_{\text{real}, j} \right)^2 + 2 \cdot \dot{V}_{\text{real}, j} \cdot \dot{V}_{\text{real}, \text{carrier gas}} + \left(\dot{V}_{\text{real}, \text{carrier gas}} \right)^2} \cdot \left(\left| \sigma_{\dot{V}_{\text{real}, j}} \right| \cdot \left| \dot{V}_{\text{real}, \text{carrier gas}} \right| + \left| \sigma_{\dot{V}_{\text{real}, \text{carrier gas}}} \right| \cdot \left| -\dot{V}_{\text{real}, j} \right| \right) \quad \text{Eq. A-6}$$

The absolute uncertainty $\sigma_{\text{abs}, j, \text{calibration}}$ on the measured absorbance during the calibration measurements for the species “j” is simply taken as the standard deviation of the absorbance values measured during 10 minutes. The absolute uncertainty of the measured absorbance $\sigma_{\text{abs}, j, \text{calibration}}$ is always much smaller compared to the uncertainty on the gas mixture compositions $\sigma_{C_j, \text{calibration}}$ used for the calibration and can be consequently neglected.

The relative error being defined by:

$$\sigma_R = \frac{\sigma_y}{y} \quad [\%] \quad \text{Eq. A-7}$$

The evolution of the relative error on the CO₂ concentration value is presented as an example in Fig. A-1.

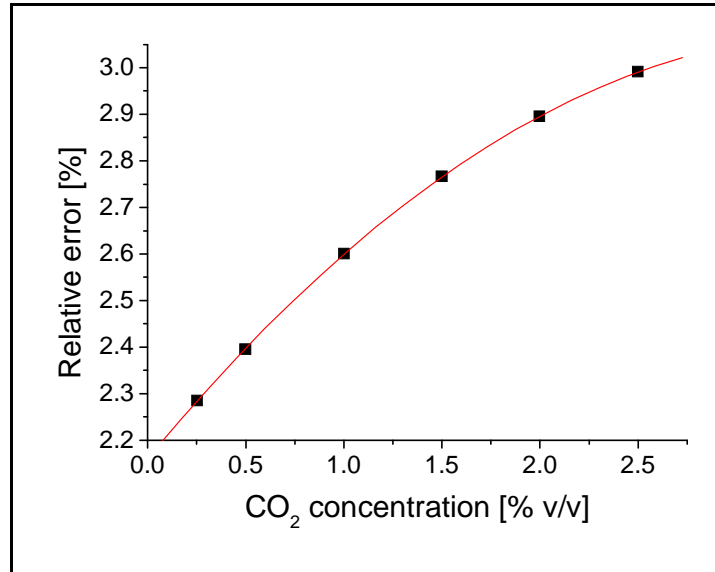


Fig. A-1 Evolution of the relative error on the CO₂ concentration

The relative error is slightly increasing together with an increasing CO₂ concentration due to the method used for the calibration of the mass flow controllers. The FTIR and Mass spectrometer have been calibrated for CO with calibrated gas, the error on the CO calibration will be much lower than in the case of CO₂ and O₂ and is now dominated by the standard deviation of the absorbance values measured during 10 minutes for the calibration. For the sake of simplicity a relative error of 5% has been chosen for all the concentration error bars in the graphics.

Appendix E: Simulation program for the Bodenstein number evaluation

Program in the madonna environment (Macey, R. and G. Oster, *Madonna 7.0*, University of California, Berkeley, 1999) developed by A. Rouge during his PhD thesis [64]

Simulation program for convoluting a known distribution function with the response of a closed tubular reactor

{model predicting the response of a closed tubular reactor to an injection of arbitrary shape (given as experimental points)}

{with an infinite Bodenstein, the model behaves as a tank-in-series model (NELEM is the number of tanks)}

METHOD stiff
STARTTIME = 0
STOPTIME= 10
dtmax= 10
dtout= 0.01

tampon = 0.01
the
synchronisation}}

{time delay to be applied to the experimental inlet curve (if experimental data let suppose a problem of

cin=delay(#indata(time) ,tampon)
dataset

{definition of the entering concentration, indata is the containing the experimental points}

nelem=100
numbers give

{number of elements used for the integration (high more precise results)}

tau=3

{residence time}

Bo=40

{Bodenstein number}

init c [1. .nelem] =0
dz=1/nelem

d/dt(c[1])=(-c[1]+cin)/tau/dz+(c[2]-C[1])/tau/Bo/dzA2

d/dt (c [2. .nelem-1]) = (c [i-1] -c [i]) /tau/dz+ (c [i+1] +c [i-1] -2*C [i]) /tau/Bo/dzA2

d/dt (c [nelem])=(c[nelem-1]-c[nelem])/tau/dz+(c[nelem-1]- C[nelem])/tau/Bo/dzA2

cfin=c[nelem] {cfin is the outlet concentration}

Appendix F: Concentration and reaction rate values for the kinetic study

$[\text{CO}]_{\text{inlet}}$ [vol. %]	$[\text{O}_2]_{\text{inlet}}$ [vol. %]	$[\text{CO}_2]_{\text{outlet}}$ [vol. %]	Conversion [-]	R_{CO_2} [$\text{mol} \cdot \text{g}_{\text{cat}}^{-1} \cdot \text{s}^{-1}$]
4	25	1.13	0.28	$3.9 \cdot 10^{-3}$
6	25	0.76	0.13	$2.6 \cdot 10^{-3}$
8	25	0.60	0.08	$2.1 \cdot 10^{-3}$
10	25	0.50	0.05	$1.7 \cdot 10^{-3}$
5	10	0.29	0.06	$1.0 \cdot 10^{-3}$
5	20	0.69	0.14	$2.4 \cdot 10^{-3}$
5	30	1.12	0.22	$3.9 \cdot 10^{-3}$
5	15.15	0.50	0.1	$1.7 \cdot 10^{-3}$

The volumetric flow used for all the experiments was $300 \text{ ml} \cdot \text{min}^{-1}$ (STP).
 The temperature used for the experiments at constant $[\text{O}_2]_{\text{inlet}}$ was 463 K.
 The temperature used during the experiments at constant $[\text{CO}]_{\text{inlet}}$ was 462 K.
 The pressure at the reactor entry was 0.11 MPa and ambient at the outlet.

Appendix G: Simulation programs for the temperature oscillations

All the simulation programs have been developed using the program Berkeley Madonna, Version 8.0.1, ©1997-2000 Robert I. Macey & George F. Oster, University of California, Berkeley

Program developed for the monomolecular reaction with temperature changes of step type.

```

METHOD stiff
STARTTIME = -20
STOPTIME= 100
DT = 0.001
dtmax=0.01
k0a1 = 50          {adsorption of A}          {[m3/mol/s]}
Ea1 = 0            {kJ/mol}
k0d1 = 2e15        {desorption of A}          {[s-1]}
Ed1 = 100          {kJ/mol}
k0r = 1.25e12       {surface reaction}         {[s-1]}
Er = 90            {kJ/mol}
R = 8.314          {perfect gases constant [J/mol/K]}
C1 = 0.1           {entry concentration of reactant A [mol/m3]}
T1 = 320           {initial temperature [K]}
T2 = 370           {final temperature [K]}
x=0
period=8
split=0.5
a=((time+x)/period-int((time+x)/period))-1+split
b=-int(a)
c=1+int(a)
T = If Time < 0 Then T1 Else (b*T1+c*T2)
ka1 = k0a1*exp(-Ea1*1000/R/T)
kd1 = k0d1*exp(-Ed1*1000/R/T)
kr = k0r*exp(-Er*1000/R/T)
K1= ka1/kd1
K1r=ka1/(kd1+kr)
teta1s=K1r*C1/(1+K1r*C1)
ra1 = ka1*C1*(1-teta1)
rd1 = kd1*teta1
Rx = kr*teta1
Init teta1 = 0
Init Rxmean=0
d/dt (teta1) = (ra1-rd1-Rx)
n = 10
m = 6
d= if (time>(stoptime-n*period) and time<(stoptime-m*period)) then 1 else 0
d/dt(Rxmean)=d*Rx/period/(n-m)
{reaction rate under QSSA}
{low temperature, T1}
ka1s1 = k0a1*exp(-Ea1*1000/R/T1)
kd1s1= k0d1*exp(-Ed1*1000/R/T1)
krs1 = k0r*exp(-Er*1000/R/T1)
ra1s1 = ka1s1*C1*(1-teta1s1)
rd1s1 = kd1s1*teta1s1
Rxs1 = krs1*teta1s1
Init teta1s1 = 0
d/dt (teta1s1) = (ra1s1-rd1s1-Rxs1)
{high temperature, T2}
ka1s2 = k0a1*exp(-Ea1*1000/R/T2)

```

```

kd1s2= k0d1*exp(-Ed1*1000/R/T2)
krs2 = k0r*exp(-Er*1000/R/T2)
ra1s2 = ka1s2*C1*(1-teta1s2)
rd1s2 = kd1s2*teta1s2
Rxs2 = krs2*teta1s2
Init teta1s2 = 0
d/dt (teta1s2) = (ra1s2-rd1s2-Rxs2)
Rxsmean=Rxs2*split+Rxs1*(1-split)
Gain = If time > (stoptime-m*period) then (Rxmean/Rxsmean-1)*100 else 0

```

Program developed for the monomolecular reaction with temperature changes of exponential type.

```

METHOD stiff
STARTTIME = 0
STOPTIME= 100
DT = 0.001
dtmax=0.01
k0a1 = 5           {adsorption of A}           {[m3/mol/s]}
Ea1 = 0             {kJ/mol}
k0d1 = 2e14         {desorption of A}          {[s-1]}
Ed1 = 100           {kJ/mol}
k0r = 1.25e12       {surface reaction}         {[s-1]}
Er = 90             {kJ/mol}
R = 8.314           {perfect gases constant [J/mol/K]}
C1 = 0.1            {entry concentration of reactant A [mol/m3]}
period = 8
Fraction = 0.5
tc1 = 2
tc2 = 2
T1 = 320            {initial temperature [K]}
DeltaT = 50         {Temp. difference [K]}
T2 = T1+ deltaT
T = IF (Mod(Time, Period)<=Fraction*Period) Then (DeltaT*(1-exp(-tc1*Mod(Time, Period)))+T1) Else
(DeltaT*(exp(-tc2*(Mod(Time, Period)-Period*Fraction)))+T1)
ka1 = k0a1*exp(-Ea1*1000/R/T)
kd1 = k0d1*exp(-Ed1*1000/R/T)
kr = k0r*exp(-Er*1000/R/T)
K1= ka1/kd1
K1r=ka1/(kd1+kr)
teta1s=K1r*C1/(1+K1r*C1)
ra1 = ka1*C1*(1-teta1)
rd1 = kd1*teta1
Rx = kr*teta1
Init teta1 = 0
Init Rxmean=0
d/dt (teta1) = (ra1-rd1-Rx)
n = 10
m = 6
d= if (time>(stoptime-n*period) and time<(stoptime-m*period)) then 1 else 0
d/dt(Rxmean)=d*Rx/period/(n-m)
                                     {reaction rate under QSSA}
                                     {low temperature, T1}

ka1s1 = k0a1*exp(-Ea1*1000/R/T1)
kd1s1= k0d1*exp(-Ed1*1000/R/T1)
krs1 = k0r*exp(-Er*1000/R/T1)
ra1s1 = ka1s1*C1*(1-teta1s1)
rd1s1 = kd1s1*teta1s1

```

```

Rxs1 = krs1*teta1s1
Init teta1s1 = 0
d/dt (teta1s1) = (ra1s1-rd1s1-Rxs1)

```

{high temperature, T2}

```

ka1s2 = k0a1*exp(-Ea1*1000/R/T2)
kd1s2= k0d1*exp(-Ed1*1000/R/T2)
krs2 = k0r*exp(-Er*1000/R/T2)
ra1s2 = ka1s2*C1*(1-teta1s2)
rd1s2 = kd1s2*teta1s2
Rxs2 = krs2*teta1s2
Init teta1s2 = 0
d/dt (teta1s2) = (ra1s2-rd1s2-Rxs2)
Rxsmean=Rxs2*Fraction+Rxs1*(1-Fraction)
Gain = If time > (stoptime-m*period) then (Rxmean/Rxsmean-1)*100 else 0

```

Program developed for the catalytic CO oxidation reaction with temperature changes of step type.

```

METHOD stiff
STARTTIME = 0
STOPTIME= 80
DT = 0.0000001
dtmax=0.01
k0aCO = 5.9e5           {CO adsorption parameters}      {[bar-1*s-1]}
EaCO= 0                 {kJ/mol}
k0dCO =4.8e13           {CO desorption parameters}      {[s-1]}
EdCO = 102              {kJ/mol}
k0aO2 = 3.4e5           {O2 adsorption parameters}      {[bar-1*s-1]}
EaO2 = 0                 {kJ/mol}
k0dO2 = 2e+13           {O2 desorption parameters}      {[s-1]}
EdO2 = 213              {kJ/mol}
k0RCO2 = 3.8e10          {surface reaction parameters}   {[s-1]}
ERCO2 = 89              {kJ/mol}
R = 8.314               {perfect gases constant}
[J/mol/K]}
CCO = 0.05              {pressure of CO [bar]}
CO2 = 0.25              {pressure of O2 [bar]}
T1 = 430                {initial temperature [K]}
T2 = 470                {final temperature [K]}
x=0
period=4
split=0.5
a=((time+x)/period-int((time+x)/period))-1+split
b=-int(a)
c=1+int(a)
T = If Time < 0 Then T1 Else (b*T1+c*T2)

{Non-stationary temperature conditions}

kaCO = k0aCO*exp(-EaCO*1000/R/T)
kdCO = k0dCO*exp(-EdCO*1000/R/T)
kaO2 = k0aO2*exp(-EaO2*1000/R/T)
kdO2 = k0dO2*exp(-EdO2*1000/R/T)
kRCO2 = k0RCO2*exp(-ERCO2*1000/R/T)
raCO = kaCO*CCO*(1-tetaCO-tetaO)

```

```

rdCO = kdCO*tetaCO
raO2 = kaO2*CO2*(1-tetaCO-tetaO)*(1-tetaCO-tetaO)
rdO2 = kdO2*tetaO*tetaO
RCO2 = kRCO2*tetaCO*tetaO
Init tetaCO = 0
Init tetaO = 0
Init RCO2mean=0
d/dt (tetaCO) = raCO-rdCO-RCO2
d/dt (tetaO) = 2*raO2-RCO2-2*rdO2
n = 5
m = 2
d= if (time>(stoptime-n*period) and time<(stoptime-m*period)) then 1 else 0
d/dt(RCO2mean)=d*RCO2/period/(n-m) {Calculation mean reaction rate non-
stationary}

{reaction rate under QSSA}
{low temperature, T1}

kaCOs1 = k0aCO*exp(-EaCO*1000/R/T1)
kdCOs1 = k0dCO*exp(-EdCO*1000/R/T1)
kaO2s1 = k0aO2*exp(-EaO2*1000/R/T1)
kdO2s1 = k0dO2*exp(-EdO2*1000/R/T1)
kRCO2s1 = k0RCO2*exp(-ERCO2*1000/R/T1)
raCOs1 = kaCOs1*CCO*(1-tetaCOs1-tetaOs1)
rdCOs1 = kdCOs1*tetaCOs1
raO2s1 = kaO2s1*CO2*(1-tetaCOs1-tetaOs1)*(1-tetaCOs1-tetaOs1)
rdO2s1 = kdO2s1*tetaOs1*tetaOs1
RCO2s1 = kRCO2s1*tetaCOs1*tetaOs1
Init tetaCOs1 = 0
Init tetaOs1 = 0
d/dt (tetaCOs1) = raCOs1-rdCOs1-RCO2s1
d/dt (tetaOs1) =2*raO2s1-RCO2s1-2*rdO2s1

{high temperature, T2}

kaCOs2 = k0aCO*exp(-EaCO*1000/R/T2)
kdCOs2 = k0dCO*exp(-EdCO*1000/R/T2)
kaO2s2 = k0aO2*exp(-EaO2*1000/R/T2)
kdO2s2 = k0dO2*exp(-EdO2*1000/R/T2)
kRCO2s2 = k0RCO2*exp(-ERCO2*1000/R/T2)
raCOs2 = kaCOs2*CCO*(1-tetaCOs2-tetaOs2)
rdCOs2 = kdCOs2*tetaCOs2
raO2s2 = kaO2s2*CO2*(1-tetaCOs2-tetaOs2)*(1-tetaCOs2-tetaOs2)
rdO2s2 = kdO2s2*tetaOs2*tetaOs2
RCO2s2 = kRCO2s2*tetaCOs2*tetaOs2
Init tetaCOs2 = 0
Init tetaOs2 = 0
d/dt (tetaCOs2) = raCOs2-rdCOs2-RCO2s2
d/dt (tetaOs2) = 2*raO2s2-RCO2s2-2*rdO2s2
RCO2smean=RCO2s2*0.5+RCO2s1*(1-0.5) {Calculation mean reaction rate stationary}

Gain = If time > (stoptime-m*period) then (RCO2mean/RCO2smean-1)*100 else 0 {Calculation gain}

```

Program developed for the catalytic CO oxidation reaction with temperature changes of exponential type.

METHOD stiff

STARTTIME = 0
STOPTIME= 5000
DT = 1e-6
dtmax=0.1

k0aCO = 2.9e5	{CO adsorption parameters}	{[bar-1*s-1]}
EaCO= 0.03		{kJ/mol}}
k0dCO =1.1e13	{CO desorption parameters}	{[s-1]}
EdCO = 100		{kJ/mol}}
k0aO2 = 7.07e5	{O2 adsorption parameters}	{[bar-1*s-1]}
EaO2 = 0.02		{kJ/mol}}
k0dO2 = 1.6e+13	{O2 desorption parameters}	{[s-1]}
EdO2 = 203		{kJ/mol}}
k0RCO2 = 5.2e11	{surface reaction parameters}	{[s-1]}
ERCO2 = 88		{kJ/mol}}
k0ox = 0.11	{oxidation catalyst parameters}	{[s-1]}
Eaox = 4.2		{kJ/mol}}
k0red = 130	{reduction catalyst parameters}	{[s-1]}
Eared = 42		{kJ/mol}}
R = 8.314	{perfect gases constant}	{[J/mol/K]}
CCO = 0.05	{entry concentration of reactant A}	{[mol/m3]}
CO2 = 0.25	{entry concentration of reactant B}	{[mol/m3]}

period = 10
Fraction = 0.5
tc1 = 1.8
tc2 = 1.8

T1 = 430	{initial temperature}	{[K]}
DeltaT = 40	{Temperature difference}	{[K]}
T2 = T1+ deltaT		

{Temperature curve}

T = IF (Mod(Time, Period)<=Fraction*Period) Then (DeltaT*(1-exp(-tc1*Mod(Time, Period)))+T1) Else (DeltaT*(exp(-tc2*(Mod(Time, Period)-Period*Fraction)))+T1)

{Non-stationary temperature conditions}

kaCO = k0aCO*exp(-EaCO*1000/R/T)
kdCO = k0dCO*exp(-EdCO*1000/R/T)
kaO2 = k0aO2*exp(-EaO2*1000/R/T)
kdO2 = k0dO2*exp(-EdO2*1000/R/T)
kRCO2 = k0RCO2*exp(-ERCO2*1000/R/T)
kox = k0ox*exp(-Eaox*1000/R/T)
kred = k0red*exp(-Eared*1000/R/T)
raCO = kaCO*CCO*tetafree
rdCO = kdCO*tetaCO
raO2 = kaO2*CO2*tetafree*tetafree
rdO2 = kdO2*tetaO*tetaO
RCO2 = kRCO2*tetaCO*tetaO
Rox = kox*TetaO*(1-Tetaox)
Rred = kred*TetaCO*tetaox
tetafree = 1-tetaCO-tetaO-tetaox
Init tetaCO = 0
Init tetaO = 0

```

Init RCO2mean=0
Init tetaox = 0
d/dt (tetaCO) = raCO-rdCO-RCO2-Rred
d/dt (tetaO) = 2*raO2-RCO2-2*rdO2-Rox
d/dt(tetaox) = Rox-Rred
n = 10
m = 2
d= if (time>(stoptime-n*period) and time<(stoptime-m*period)) then 1 else 0
d/dt(RCO2mean)=d*RCO2/period/(n-m) {Calculation mean reaction rate non-stationary}

```

{reaction rate under QSSA}
{low temperature, T1}

```

kaCOs1 = k0aCO*exp(-EaCO*1000/R/T1)
kdCOs1 = k0dCO*exp(-EdCO*1000/R/T1)
kaO2s1 = k0aO2*exp(-EaO2*1000/R/T1)
kdO2s1 = k0dO2*exp(-EdO2*1000/R/T1)
kRCO2s1 = k0RCO2*exp(-ERCO2*1000/R/T1)
koxs1 = k0ox*exp(-Eaox*1000/R/T1)
kreds1 = k0red*exp(-Eared*1000/R/T1)
raCOs1 = kaCOs1*CCO*tetafrees1
rdCOs1 = kdCOs1*tetaCOs1
raO2s1 = kaO2s1*CO2*tetafrees1*tetafrees1
rdO2s1 = kdO2s1*tetaOs1*tetaOs1
RCO2s1 = kRCO2s1*tetaCOs1*tetaOs1
Roxs1 = koxs1*TetaOs1*(1-Tetaoxs1)
Rreds1 = kreds1*tetaCOs1*tetaoxs1
tetafrees1 = 1-tetaCOs1-tetaOs1-tetaoxs1
Init tetaCOs1 = 0
Init tetaOs1 = 0
Init tetaoxs1 = 0
d/dt (tetaCOs1) = raCOs1-rdCOs1-RCO2s1-Rreds1
d/dt (tetaOs1) = 2*raO2s1-RCO2s1-2*rdO2s1-Roxs1
d/dt (tetaoxs1) = Roxs1-Rreds1

```

{high temperature, T2}

```

kaCOs2 = k0aCO*exp(-EaCO*1000/R/T2)
kdCOs2 = k0dCO*exp(-EdCO*1000/R/T2)
kaO2s2 = k0aO2*exp(-EaO2*1000/R/T2)
kdO2s2 = k0dO2*exp(-EdO2*1000/R/T2)
kRCO2s2 = k0RCO2*exp(-ERCO2*1000/R/T2)
koxs2 = k0ox*exp(-Eaox*1000/R/T2)
kreds2 = k0red*exp(-Eared*1000/R/T2)
raCOs2 = kaCOs2*CCO*tetafrees2
rdCOs2 = kdCOs2*tetaCOs2
raO2s2 = kaO2s2*CO2*tetafrees2*tetafrees2
rdO2s2 = kdO2s2*tetaOs2*tetaOs2
RCO2s2 = kRCO2s2*tetaCOs2*tetaOs2
Roxs2 = koxs2*TetaOs2*(1-Tetaoxs2)
Rreds2 = kreds2*TetaCOs2*tetaoxs2
tetafrees2 = 1-tetaCOs2-tetaOs2-tetaoxs2
Init tetaCOs2 = 0
Init tetaOs2 = 0
Init tetaoxs2 = 0
d/dt (tetaCOs2) = raCOs2-rdCOs2-RCO2s2-Rreds2
d/dt (tetaOs2) = 2*raO2s2-RCO2s2-2*rdO2s2-Roxs2
d/dt (tetaoxs2) = Roxs2-Rreds2
RCO2smean=RCO2s2*0.5+RCO2s1*(1-0.5)

```

{Calculation mean reaction rate stationary}

Gain = If time > (stoptime-m*period) then (RCO2mean/RCO2smean-1)*100 else 0 {Calculation gain}

Martin Luther
Karl-Wilhelm-Str. 22
D-76131 Karlsruhe
Germany
0049 179 9607135
martin_luther60@hotmail.com

Swiss
Born 09.05.1980 in Moutier, Switzerland

Education and professional experience

- 11.2006 - Scientific researcher at the Karlsruhe Research Centre, Institute for Micro Process Engineering. Work on the Federal Ministry of Education and Research (BMBF) project icefuel® - integrated cable energy system for fuel and power
- 11.2003 – 2008 PhD Thesis directed by Pr. Renken (Swiss Federal Institute of Technology of Lausanne (EPFL), Switzerland). Thesis work made at the Karlsruhe Research Centre, Institute for Micro Process Engineering. Dissertation topic: Fast Temperature Cycling of the Catalytic CO Oxidation using Microstructure Reactors
- 1998 – 2003 Diploma of chemical engineer EPFL (Swiss Federal Institute of Technology, Lausanne). Diploma work: Cinétique de semihydrogénation catalytique d'un alcyne
- 1995 – 1998 Swiss federal maturity type C (scientific) at the cantonal high-school of Neuchâtel (Switzerland)

Languages

French: Mother tongue
German: Fluent
English: Very good

Publications

Publications

M. Luther, J.J. Brandner, L. Kiwi-Minsker, A. Renken, K. Schubert; *New opportunities for enhanced microreactor performance by forced thermal oscillations*; Proceedings of the 28th International Exhibition-Congress on Chemical Engineering, Environmental Protection and Biotechnology,ACHEMA, Frankfurt-am-Main, Germany, p. 97, 2006

M. Luther, J.J. Brandner, L. Kiwi-Minsker, A. Renken, K. Schubert; *Microstructure reactors for forced temperature oscillations of catalytic chemical reactions*; Proceedings of the 9th International Conference on Microreaction Technology, IMRET 9, Potsdam, Germany, pp. 144-145, 2006

M. Luther, J.J. Brandner, L. Kiwi-Minsker, A. Renken, K. Schubert; *Forced periodic temperature cycling of chemical reactions in microstructure devices*; Proceedings of the 5th International Conference on Unsteady-State Processes in Catalysis, USPC5, SuitaCity, Japan, pp. 35-36, 2006

M. Luther, J.J. Brandner, L. Kiwi-Minsker, A. Renken, K. Schubert; *Enhanced microstructured reactor performance under forced temperature oscillations*; International Journal of Chemical Reactor Engineering Vol. 5: A49, 2007

M. Luther, J.J. Brandner, L. Kiwi-Minsker, A. Renken, K. Schubert; *Novel design of a microstructured reactor allowing fast temperature oscillations*; Chemical Engineering Journal, 135S, pp. 254-258, 2008

M. Luther, J.J. Brandner, L. Kiwi-Minsker, A. Renken, K. Schubert; *Forced periodic temperature cycling of chemical reactions in microstructure devices*; Chemical Engineering Science, article in press, 2008

Oral presentations

M. Luther, J.J. Brandner, L. Kiwi-Minsker, A. Renken, K. Schubert; *Thermisch instationärer Betrieb heterogen katalysierter Gasphasenreaktionen*; Internal seminar of the Institute for Microprocess Engineering, Karlsruhe Research Center, Germany, 2005

M. Luther, J.J. Brandner, L. Kiwi-Minsker, A. Renken, K. Schubert; *New opportunities for enhanced microreactor performance by forced thermal oscillations*; AICHE, Frankfurt-am-Main, Germany, 2006

M. Luther, J.J. Brandner, L. Kiwi-Minsker, A. Renken, K. Schubert; *Microstructure Reactors for Forced Temperature Oscillations of Catalytic Chemical Reactions*; IMRET 9, Potsdam, Germany, 2006

M. Luther, J.J. Brandner, L. Kiwi-Minsker, A. Renken, K. Schubert; *Enhanced microstructured reactor performance under forced temperature oscillations*; Green Chemical Reactor Engineering conference, Bilbao, Spain, 2007

Posters

M. Luther, J.J. Brandner, L. Kiwi-Minsker, A. Renken, K. Schubert; *Fast Temperature Cycling of Catalytic Reactions using Microreactors*; IMRET 8, Atlanta, USA, 2005

M. Luther, J.J. Brandner, L. Kiwi-Minsker, A. Renken, K. Schubert; *Fast Temperature Cycling of the Catalytic CO Oxidation*; Summer school, séminaire hors-ville en Chimie I, Villars, Switzerland, 2005

M. Luther, J.J. Brandner, L. Kiwi-Minsker, A. Renken, K. Schubert; *Enhanced microstructured reactor performance under forced temperature oscillations*; Green Chemical Reactor Engineering conference, Bilbao, Spain, 2007